Microbunching and Coherent Synchrotron Radiation in Linear Free Electron Lasers

Thesis submitted in accordance with the requirements of the University of Liverpool for the degree of Doctor in Philosophy by

Alexander Darius Brynes

June 2021

Contents

Declaration

I confirm that I have read and understood the University's PGR Policy on Plagiarism and Dishonest Use of Data. I have acted honestly, ethically and professionally in conduct leading to assessment for the programme of study. I have not copied material from another source nor committed plagiarism nor fabricated, falsifed or embellished data when completing the attached material. I have not colluded with any other student in the preparation and production of this material. If an allegation of suspected academic malpractice is made, I give permission to the University to use source-matching software to ensure that the submitted material is all my own work.

Acknowledgements

Firstly, I would like to thank my supervisor Andy Wolski, who has been a constant source of guidance, motivation and support throughout this project. His help has greatly improved the quality (and grammar!) of this thesis, and I am very grateful that he has dedicated his time to my development.

My colleagues at ASTeC have also been a great source of help during this process, professionally and otherwise. In particular I would like to thank Deepa Angal-Kalinin for supporting me in beginning this journey, along with James Jones, Bruno Muratori and Julian McKenzie, among others, who have provided a lot of help with the technical work. Special thanks go to Peter Williams, without whom I would not have had the opportunity to visit FERMI and participate in the experimental work. He has been available, and more importantly willing, to help and to push me further in order to achieve the best scientific results.

I would also like to extend my thanks to our international collaborators, including the FERMI accelerator physics team, and our collaborators from ASML who worked on the FEL project. Simone Di Mitri and Irwan Setija in particular have spent a great deal of time working with me on this project, and I will always be grateful for their inspiration and assistance. In addition, Peter Smorenburg and Bas van der Geer have been very supportive with the simulation and theoretical work.

To my family: thank you. You have encouraged and supported me throughout my life in everything that I have done. Finally, to my partner Jemimah and my daughter Saskia, thank you for everything.

Alexander Darius Brynes

Microbunching and Coherent Synchrotron Radiation in Linear Free Electron Lasers

Abstract

The optimal performance of short-wavelength free-electron lasers (FELs), driven by high-energy bunches of electrons, is limited by collective interactions that occur due to the self-fields of particles within the bunch. An understanding of these collective effects is therefore crucial for current and future machines. In particular, it is important when designing and operating such a machine that these effects are understood, and mitigated as much as possible. In order to achieve such an understanding, a correspondence between the theory of the impact of these collective effects, their calculation using computer-based simulation codes, and experimental measurements of the effects, is essential. This thesis presents a study of two such collective effects: coherent synchrotron radiation (CSR) and the microbunching instability. An extension to the 1D theory of CSR is derived, which correctly takes account of effects arising due to the electron bunch entering and exiting a bending magnet. Theoretical predictions of these CSR transient effects are then compared with results from simulation codes. The CSR-induced emittance growth is then studied experimentally in the FERMI FEL across a range of electron bunch parameters, showing good agreement between theory, simulation and experiment in most cases, and some divergence during more extreme bunch compression scenarios. In addition, the microbunching instability in the FERMI FEL has been studied extensively. A new method of characterising the instability using 2D Fourier analysis has been developed, which uncovers previously unseen parameters, and demonstrates the necessity of performing a thorough analysis in order to understand fully this effect. The microbunching instability has also been induced, by imposing periodic modulations on electron bunches across a number of accelerator lattice configurations. Comparisons between theory, simulation and experiment are also shown in this case, demonstrating an improved understanding of the development of these collective effects.

List of Figures

List of Tables

Chapter 1

Introduction

Particle accelerators have long been used both as tools for developing an understanding of fundamental physical processes, and as machines for facilitating scientific discovery in a wide range of fields, including the life sciences, chemistry and technology development. The emission of synchrotron radiation [1, 2, 3] by high-energy electron accelerators led to the development of accelerators which generate some of the brightest man-made sources of light, and have provided the opportunity for the investigation of matter at an unprecedented spatial and temporal scale [4]. These accelerators are able to provide a narrow spectral bandwidth of light and tunability of photon wavelength and brilliance, giving rise to a flexibility and wavelength range that is unavailable to other light sources, such as conventional lasers.

Free-electron lasers (FELs) [5] are able to produce light with better coherence properties than those which can be achieved by circular synchrotrons, and modern FEL user facilities provide beams to users in wavelengths ranging from the infra-red to the hard x-ray. A number of these machines are not based on a recirculating accelerator (as in a more conventional synchrotron light source), but on a single-pass linear accelerator (linac). This type of machine allows for the brightness of the light produced to increase by orders of magnitude, in addition to decreasing the spectral and temporal bandwidth close to the Fourier limit [6]. An FEL-based light source can allow for the probing of structures on a smaller scale than conventional synchrotron-based light sources, and the short pulse lengths produced provide the opportunity to study the dynamics of pro-

cesses within complex materials and molecules on an unprecedented temporal scale [7]. FELs can therefore not only complement the investigations that can be made by synchrotrons; a wide range of other processes can be studied only by using the photon wavelength, bandwidth, pulse length and intensity that FELs are able to produce, such as chemical processes, plasma physics, matter under extreme conditions and astrophysics.

All accelerator-based light sources are dependent on the interaction between charged particles and magnetic fields. This is achieved in an FEL by propagating a bunch of electrons along the axis of an array of alternating magnetic dipole fields, in an arrangement known as an undulator, or a wiggler (depending on the strength and periodicity of the magnetic fields). These fields cause the transverse position of particles in the bunch to oscillate. This then results in the emission of radiation with a wavelength proportional to the period of the magnet and the inverse of the particle energy squared [8, 9]. If the electrons within a bunch are considered as isolated sources of radiation, then the synchrotron emission is incoherent, and the power of the radiation scales linearly with the number of emitting particles. If, however, the ensemble of particles is considered as a whole, and if the wavelength of the light emitted is longer than the overall longitudinal density distribution (or length) of the bunch, then coherent emission takes place, with an intensity proportional to the square of the number of particles in the bunch. It has also been demonstrated that the radiation emitted can act back on the emitting electrons, causing them to bunch together into so-called 'microbunches' with a length proportional to the wavelength of the radiation. This causes a process to take place which further amplifies the emission of radiation, giving rise to a greater intensity of synchrotron emission. This process, which initially begins with noisy emission from individual particles, can then can then lead to an exponential growth in the radiation intensity by many orders of magnitude until the process eventually saturates [10, 11, 12].

The quality of the photon beams produced by FELs (i.e. their spectral and temporal properties) is highly dependent on the properties of the electron bunches driving the FEL process. Therefore, a deep understanding of the physical processes which can affect these bunches of electrons is necessary in order

to optimise the performance of these machines. A number of these processes are driven by the interactions between the electrons within a bunch, known broadly under the umbrella term 'collective effects'. Charged particles produce electromagnetic fields which interact with their surrounding environment, including other particles within an ensemble. In a typical short wavelength FEL, the number of electrons within a bunch can exceed 10^9, and so providing analytic or computational calculations of these effects for this number of particles can be very difficult. Developing an understanding of these processes, and how they translate to effects on a real machine, however, is of fundamental importance to improving the beam quality of an FEL. As with all scientific endeavour, the goal in studying collective effects is to bring together theory and experiment, and in accelerator physics this is generally possible only with the additional use of simulation codes which approximate the physical processes in a real machine.

This thesis will present an analysis of two such collective effects in an FEL: coherent synchrotron radiation (CSR) and the microbunching instability. The thesis is laid out as follows. Chapter 2 will give a brief overview of beam dynamics in accelerator physics, discussing the aspects pertinent to the study of CSR and microbunching, such as the concept of emittance and longitudinal bunch compression. The theory of CSR emission is presented, and expressions are derived which show the impact of CSR when a bunch of electrons enters and exits a bending magnet – the so-called 'transient' regimes. A discussion of the theory surrounding the development, propagation and amplification of the microbunching instability is also presented. The mitigation of the microbunching instability through a device known as a laser heater is discussed, as is the possibility of stimulating and controlling the instability through the use of a temporally modulated laser pulse.

Chapter 3 gives an introduction to the computation of collective effects using simulation codes. The methods used for three of these codes are discussed, along with their limitations. Some benchmarking studies are undertaken in order to compare the accuracy of the simulation codes with theoretical predictions of the impact of these collective effects. In particular, the extended theory of CSR transients mentioned above is compared with results from a simulation code for

a simple test case, showing good agreement between the two.

In Chapter 4 the influence of CSR on the transverse emittance of electron bunches in the FERMI FEL [13] is studied. CSR causes the emittance of a bunch to increase as it travels on a curved trajectory, such as that required for magnetic bunch compression. The emittance of bunches in FERMI was measured as a function of bunch compression factor and transverse beam size, and compared with simulated and theoretical predictions. It is shown that simulation codes which take the transverse extent of the bunch into account, rather than taking a simpler 1D approximation of the CSR effect, can produce better agreement with the experimental measurements.

Chapter 5 details extensive measurements of the microbunching instability, also in the FERMI FEL, for three different bunch compression schemes. The longitudinal phase space of a microbunched beam exhibits fragmentation in energy and time, rather than the smooth distribution that is required for the nominal application of a short wavelength FEL. In order to improve the understanding of this instability, a technique based on 2D Fourier analysis has been developed that can characterise accurately the modulation amplitude in time and energy, and also the frequency of these modulations. It is also demonstrated that, by increasing the uncorrelated energy spread of the bunch in the low-energy section of the machine, through the use of a so-called 'laser heater', the modulations at higher energy can be suppressed. Finally, the laser heater is used in a non-standard configuration; by modifying the longitudinal intensity profile of the pulse in the laser heater, modulations in energy can be imposed onto the bunch, thereby stimulating the microbunching instability at a known frequency. This flexible technique allows for the probing of the microbunching instability in unprecedented detail by imposing a range of amplitude and frequency modulations onto the bunch. In addition to providing the means to compare the development of the microbunching instability experimentally with theoretical predictions and estimates from simulation, this technique could prove to be useful for a wider range of accelerator applcations, such as the generation of THz radiation or for future plasma-based accelerators.

Chapter 2

Theory of CSR and Microbunching

This chapter will give a theoretical outline of two important collective effects in high-energy particle accelerators: coherent synchrotron radiation (CSR) and the microbunching instability. First, in Sec. 2.1 some general concepts in accelerator physics, including the theory of beam dynamics, transport matrices, and bunch compression, will be introduced.

Much of the published theory concerning the emission of CSR on curved trajectories is based on a 1D approximation, in which the electron beam distribution is projected onto the longitudinal dimension. Experimental and computational studies [14, 15, 16, 17] have demonstrated good agreement between the 1D CSR theory and its impact on the beam, particularly in terms of its projected and slice emittance. However, the theory based on Ref. [18] fails to take full account of the CSR radiation emitted as the bunch enters and exits a bending magnet, as will be demonstrated in Sec. 2.2. An extension of the 1D CSR field will be derived for these so-called 'entrance' and 'exit transient' regimes.

The conditions which give rise to the microbunching instability [19, 20, 21, 22] will also be investigated in this chapter. This phenomenon, observed at a number of high-energy FELs [23, 24, 25], causes modulations in energy and/or density to develop within an electron bunch, which can result in a reduction in FEL performance. Three main sources which can cause the instability to develop and increase in severity – shot noise, longitudinal space charge (LSC) and CSR – are

recognised. The theory behind these effects will be outlined in Sec. 2.3, along with some methods for mitigating the instability, such as the so-called 'laser heater' [20], the most common device employed at the majority of X-ray FELs for this purpose [26, 27, 28, 29, 30]. A number of proposed alternatives to the laser heater are also discussed.

Recent interest in the ability to manipulate the longitudinal phase space of an electron beam for the generation of THz radiation [31, 32, 33, 34] has resulted in the application of temporally modulated laser beams to induce microbunching. Results from theory and simulation will provide an insight into how lasers and undulator magnets can interact with an electron beam to manipulate its properties – this is discussed in Sec. 2.4.

2.1 Accelerator Physics

This section will provide a brief overview of beam dynamics in particle accelerators, including some of the theoretical descriptions pertinent to developing an understanding of the collective effects explored in this thesis. Comprehensive derivations of the physics of beam dynamics in particle accelerators will not be given here, as they can be found elsewhere [35, 36, 37]. The electron bunches studied in this thesis are generally in the ultra-relativistic regime, where the particle energies are sufficiently high that the approximation can be made that velocity $v = \beta c \approx c$, where c is the speed of light and β is the relativistic velocity of the particle – this will simplify some of these preliminary discussions. The motion of an electron in the presence of electric and magnetic fields $\vec{E}$ and $\vec{B}$, and with charge $q = -e \approx -1.6 \times 10^{-19}\,\mathrm{C}$ is described by the Lorentz force [1]:

$$\vec{F} = q\left(\vec{E} + \vec{v} \times \vec{B}\right). \tag{2.1}$$

2.1.1 Beam Dynamics and Transfer Matrices

In conventional accelerators, electric fields are typically used to accelerate particle bunches, and magnetic fields focus and steer them. Since the majority of high-energy particle accelerators do not follow a completely straight trajectory, the

motion of particles in an accelerator is generally described using a Frenet-Serret co-ordinate system with a non-zero curvature, and with zero torsion [36]. In this system, three spatial co-ordinates represent the position of a particle – x, y and s, where s is the direction of motion, and x and y are orthogonal to this trajectory in the horizontal and vertical directions, respectively. Complementary to these positional co-ordinates are the momenta of each co-ordinate, for example p_x, p_y for the transverse momenta. These six co-ordinates specify both the location of a given particle, and its trajectory. We will use the notation $\mathbf{X} = (x, p_x, y, p_y, z, \delta)$ for the full 6D phase space, where $\delta = \Delta p/p$ is the normalised deviation from the design momentum p, and z is the longitudinal position of the particle. This 6D vector is generally sufficient to describe the motion of any particle through accelerator components by using so-called 'transfer matrices' which transform the beam position in a step-wise fashion. The full arrangement of accelerator components which describe the layout of the machine is often referred to as a 'lattice'. These transfer matrices are based on the Lorentz force applied to a particle as it propagates through an electric or magnetic field.

In order to compute the evolution of the 6D vector describing the position and motion of a particle travelling through a given accelerator element with transfer matrix $\mathbf{R}$, the following notation is used:

$$\mathbf{X_1} = \mathbf{R}\mathbf{X_0}, \tag{2.2}$$

where the subscripts $_{0,1}$ denote the initial and final particle vectors, respectively. Multiple accelerator elements can be combined within this formalism such that successive elements in the accelerator lattice are multiplied together to give an overall transfer matrix $\mathbf{R_{tot}}$:

$$\mathbf{X_1} = \mathbf{R_{tot}}\mathbf{X_0} = \mathbf{R_n}\mathbf{R_{n-1}} \cdots \mathbf{R_2}\mathbf{R_1}\mathbf{X_0} \tag{2.3}$$

with n the total number of elements in the lattice. The explicit form of the evolution of particle motion through a given accelerator element, beginning at

position s_0 and ending at position s_1 is as follows:

$$\mathbf{X_1} = \begin{pmatrix} x \\ p_x \\ y \\ p_y \\ z \\ \delta \end{pmatrix}_{s_1} = \mathbf{R}\mathbf{X_0} = \mathbf{R} \begin{pmatrix} x \\ p_x \\ y \\ p_y \\ z \\ \delta \end{pmatrix}_{s_0} . \tag{2.4}$$

It should also be noted that, in cases where a linear approximation is not sufficient to model the effects of an electromagnetic field, second-, third-, and higher-order expansions of the fields can also be incorporated into the transfer matrix computations [37]. For the purposes of this thesis, only a small number of different types of accelerator element need to be considered: drift spaces, sector dipole magnets, quadrupole magnets, and radiofrequency (RF) cavities. The motion of particles travelling in a lattice without coupling between the horizontal and vertical planes, and with bending in the horizontal plane, can be described using Hill's equation [36]:

$$\frac{d^2x}{ds^2} + \left(\frac{1}{\rho(s)^2} + k(s) \right) x(s) = \frac{\delta}{\rho(s)}, \tag{2.5a}$$

$$\frac{d^2y}{ds^2} + k(s)y(s) = 0. \tag{2.5b}$$

Here, $k(s)$ describes the focusing in the beamline, and $\rho(s)$ gives the bending radius of a dipole magnet. Omitting the derivations for standard accelerator beamline components (which can be found in most standard accelerator physics textbooks [35, 36]), the transfer matrices for a drift space, dipole magnet and quadrupole magnet are given below.

For a drift space – that is, a straight beamline section with no electric or

magnetic fields and a length l_d – the transfer matrix is:

$$R_{drift} = \begin{pmatrix} 1 & l_d & 0 & 0 & 0 & 0 \\ 0 & 1 & 0 & 0 & 0 & 0 \\ 0 & 0 & 1 & l_d & 0 & 0 \\ 0 & 0 & 0 & 1 & 0 & 0 \\ 0 & 0 & 0 & 0 & 1 & \frac{l_d}{\beta^2\gamma^2} \\ 0 & 0 & 0 & 0 & 0 & 1 \end{pmatrix}, \tag{2.6}$$

where $\gamma = [1 - \beta^2]^{-\frac{1}{2}}$ is the relativistic Lorentz factor of the particle.

The FERMI accelerator, which is studied in this thesis, uses sector dipole magnets for bending the beam, in which the design trajectory of the particles enters and exits normal to the edge of the magnetic field (assuming that the field stops abruptly at the edge of the magnet pole face – the 'hard-edge' model). For a sector dipole magnet with length l_d and bending angle for the reference particle (i.e. a particle with the intended design momentum for that magnet) $\theta = l_d/\rho$, with ρ the radius of the bend, the linear transfer matrix is as follows:

$$R_{dip} = \begin{pmatrix} \cos\theta & \rho\sin\theta & 0 & 0 & 0 & \rho(1-\cos\theta) \\ -\frac{1}{\rho}\sin\theta & \cos\theta & 0 & 0 & 0 & \sin\theta \\ 0 & 0 & 1 & 0 & 0 & 0 \\ 0 & 0 & 0 & 1 & 0 & 0 \\ \sin\theta & \rho(1-\cos\theta) & 0 & 0 & 1 & \rho(\theta-\sin\theta) \\ 0 & 0 & 0 & 0 & 0 & 1 \end{pmatrix}. \tag{2.7}$$

Quadrupole magnets are used to focus the beam transversely. Due to the nature of quadrupole magnetic fields for a magnet with field strength k, focusing occurs in one plane while the beam is defocused in the transverse plane orthogonal to it. For a horizontally focusing quadrupole, with $k > 0$ and length l_q, the

transfer matrix is:

$$R_{fquad} = \begin{pmatrix} \cos\theta & \frac{1}{\sqrt{k}}\sin\theta & 0 & 0 & 0 & 0 \\ -\sqrt{k}\sin\theta & \cos\theta & 0 & 0 & 0 & 0 \\ 0 & 0 & \cosh\theta & \frac{1}{\sqrt{k}}\sinh\theta & 0 & 0 \\ 0 & 0 & \sqrt{k}\sinh\theta & \cosh\theta & 0 & 0 \\ 0 & 0 & 0 & 0 & 1 & 0 \\ 0 & 0 & 0 & 0 & 0 & 1 \end{pmatrix}, \tag{2.8}$$

with $\theta = \sqrt{k}l_q$. This type of quadrupole, with focusing in the horizontal plane, will from here on be called a focusing quadrupole. A defocusing quadrupole, which focuses in the vertical plane, has $k < 0$, and its transfer matrix is as follows:

$$R_{dquad} = \begin{pmatrix} \cosh\theta & \frac{1}{\sqrt{|k|}}\sinh\theta & 0 & 0 & 0 & 0 \\ \sqrt{|k|}\sinh\theta & \cosh\theta & 0 & 0 & 0 & 0 \\ 0 & 0 & \cos\theta & \frac{1}{\sqrt{|k|}}\sin\theta & 0 & 0 \\ 0 & 0 & -\sqrt{|k|}\sin\theta & \cos\theta & 0 & 0 \\ 0 & 0 & 0 & 0 & 1 & 0 \\ 0 & 0 & 0 & 0 & 0 & 1 \end{pmatrix}. \tag{2.9}$$

with $\theta = \sqrt{|k|}l_q$. It should also be noted that the transfer matrices given above for dipoles and quadrupoles do not take fringe fields into account [38] – that is, they assume that the fields exist only inside the magnet, and that the field strength within the magnet is constant throughout its length. In reality, this is an oversimplification; the strength of a magnet reaches its maximum value in its central point, and decays smoothly to a point outside of the physical magnet. Dipole fringe fields will be included in most of the simulation work that follows (see Chapter 3), but for higher-order multipole magnets, these will not be included.

2.1.2 Phase Spaces and Transverse Emittance

The transfer matrices given in the section above determine how a single particle is transported through an accelerator lattice. Most problems in accelerator physics require an understanding of the transport of a large number of particles in a beam, in which case it would be impractical to calculate the single-particle transport of each particle individually. In order to gain an understanding of such bunches of particles, it is instructive to consider the bulk properties of a beam. As above (Sec. 2.1.1), the statistical properties of an ensemble of particles can be represented in a six-dimensional phase space, using three orthogonal elements each for position and momentum.

The particle motion in $x - p_x$ space (where p_x is the horizontal momentum) can be expressed in terms of the Courant-Snyder (or Twiss) parameters [39] and the action variable J_x [35]:

$$J_x = \frac{1}{2}\left(\gamma_x x^2 + 2\alpha_x x p_x + \beta_x p_x^2\right), \tag{2.10}$$

where J_x is invariant for linear motion. The motion in the horizontal phase space can be described in terms of x and p_x, or in terms of the action-angle variables J_x and ϕ_x, where $\tan(\phi_x) = -\beta_x \frac{p_x}{x} - \alpha_x$. The horizontal emittance ϵ_x is defined as the statistical average of the action for an ensemble of particles:

$$\epsilon_x = \langle J_x \rangle. \tag{2.11}$$

The Courant-Synder parameters β_x, α_x and γ_x, also known as Twiss parameters, are defined as follows:

$$\langle x^2 \rangle = \beta_x \epsilon_x, \tag{2.12a}$$

$$\langle x p_x \rangle = -\alpha_x \epsilon_x, \tag{2.12b}$$

$$\langle p_x^2 \rangle = \gamma_x \epsilon_x, \tag{2.12c}$$

and the condition $\beta_x \gamma_x - \alpha_x^2 = 1$ is also imposed. These definitions are valid in the

absence of energy deviations in the particles in the bunch – for a discussion of how such deviations can affect the transverse distribution, see Sec. 2.1.3 below. The Courant-Snyder parameters vary in such a way that the action J_x is a constant of the motion in the absence of radiation and collective effects. It then follows that the emittance can be written as:

$$\epsilon_x = \sqrt{\langle x^2 \rangle \langle p_x^2 \rangle - \langle x p_x \rangle^2}. \tag{2.13}$$

A similar set of expressions can be derived for vertical and longitudinal motion. Given that, as a particle is accelerated, the transverse momenta p_x and p_y (which are inversely proportional to the particle momentum) becomes proportionally smaller, most single-pass FEL machines utilise the concept of normalised emittance $\epsilon_N = \gamma\epsilon$, with γ the relativistic (or 'Lorentz') factor, defined as:

$$\gamma = \frac{1}{\sqrt{1-\beta^2}}, \tag{2.14}$$

where $\beta = v/c$, with v the velocity of the particle and c the speed of light. The energy of a particle with mass m has an energy $E = \gamma mc^2$. Under the condition of linear, symplectic transport, the normalised emittance remains constant irrespective of changes in beam energy. As mentioned above, the motion of particles under the influence of electric and magnetic fields is given by the Lorentz force (Eq. 2.1), and this motion through standard accelerator elements can be described using a Hamiltonian [35]. As such, according to Liouville's theorem, the area occupied by the beam in 6D phase space is conserved in the absence of external forces. One such force that can cause a dilution in the beam transverse phase space is the coherent synchrotron radiation (CSR) that arises due to the collective interactions of particles, as described below (Sec. 2.2).

2.1.3 Dispersion

The dispersion $\eta(s)$ of a beamline relates the momentum of a particle to its trajectory in a given direction. After passing through a horizontal bending magnet, a particle i with momentum deviation δ_i from the nominal momentum has the

following horizontal position (to first order) [35]:

$$x_i(s) = \eta_i(s)\delta_i(s). \tag{2.15}$$

The dispersion function determines the offset of a particle from the reference trajectory for a given momentum deviation, and it is typically corrected using quadrupole magnets after a beam passes through a bending magnet. If uncorrected, then the dispersion function can contribute to an increase in beam size and transverse momentum.

2.1.4 Bunch Compression

RF photoinjectors (also known as 'guns') used for single-pass FELs tend to produce electron bunches with a peak current on the order of 100 A or less [40, 41, 42, 43, 44]. The peak current is defined as the local charge density in the core of the bunch, projected along the longitudinal axis, multiplied by the bunch velocity. In order to achieve the required peak currents for FEL operation, which tends to be on the order of up to 1 kA or more, the electron bunch must be compressed longitudinally. In most FELs, this is achieved through a chicane-like bunch compressor system consisting of four dipole magnets. Bunch compression is typically done at a relatively high energy (greater than 100 MeV), in order to mitigate the respulsive Coulomb force (also known as 'space charge') which scales with a factor $1/\gamma^2$ [45], and which increases with increasing charge density.

Longitudinal compression is often achieved using a four-dipole magnetic chicane, by forcing the time of flight of the tail of the bunch to be shorter than that of the head – this can be done by giving particles at the back of the bunch a larger energy than those at the front. The linear component of the variation in particle energy along the longitudinal axis of a particle bunch is known as the 'energy chirp', and in the case of particles at the back of the bunch having larger energy than particles at the head, this is referred to as a negative energy chirp. Since the electric field of an RF cavity – used for accelerating particles – varies sinusoidally, the timing of electrons within the bunch with respect to the phase of the cavity has an influence on the amplitude of the field that they experience.

The phase of the cavity can be tuned such that particles at the back of the bunch experience a larger field than those at the front, thus imparting a negative energy chirp. As the bunch propagates through the chicane, the tail of the bunch then follows a trajectory that has a smaller deflection from the dipoles, and is able to catch up with the head. The overall compression of the bunch in a compressor chicane, then, is related to both the longitudinal energy chirp of the bunch and the longitudinal dispersion (known as the R_{56} parameter – see Eq. 2.7) of the chicane. See Fig. 2.1 for a schematic of an example four-dipole bunch compressor chicane, and the longitudinal compression undergone by a bunch travelling through it.

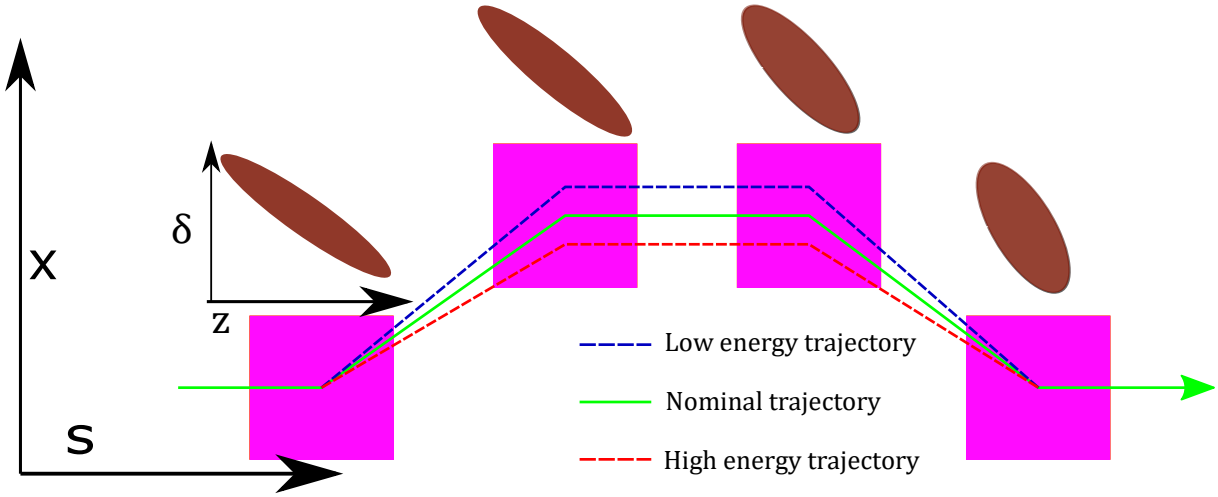

Figure 2.1: A schematic of a typical four-dipole bunch compressor chicane (with dipoles as blue squares) bending in the horizontal (x) direction, with the $z - \delta$ phase space of a bunch (red) propagating through it.

The total path length of a particle travelling through a four-dipole chicane with distance between the centres of the first and second, and the third and fourth dipoles defined as L_1, and the distance between the centres of the second and third dipoles defined as L_2, is:

$$L_{tot} = \frac{2L_1}{\cos\theta_0} + L_2, \tag{2.16}$$

where θ_0 are the bend angles of the dipoles. A particle with relative momentum deviation from the reference particle δ will experience a different bending angle

θ:

$$\theta = \frac{\theta_0}{1+\delta}. \tag{2.17}$$

Under the small-angle approximation ($\theta \ll 1$), which is generally true for bunch compressor chicanes in FELs, we find:

$$\cos\theta \approx 1 - \frac{\theta^2}{2}, \tag{2.18}$$

and therefore the path length difference is now:

$$L_{tot} \approx 2L_1 + L_1\left(\frac{\theta_0}{1+\delta}\right)^2 + L_2. \tag{2.19}$$

Now, given that the R_{56} of the chicane transfer matrix describes the path-length difference with respect to the energy deviation:

$$R_{56} = \frac{dL_{tot}}{d\delta} = -2L_1\theta_0^2, \tag{2.20}$$

the total path-length difference is now found to be:

$$\Delta z = L_{tot}(\delta) - L_{tot}(0) = L_1\left(\frac{\theta_0}{1+\delta}\right)^2 - L_1\theta_0^2 = \frac{1}{2}R_{56}\left(1 - \frac{1}{(1+\delta)^2}\right). \tag{2.21}$$

Finally, performing a Taylor expansion around $\delta = 0$, the expression for Δz is as follows:

$$\Delta z \approx \frac{1}{2}R_{56}\left(1 - 1 + 2\delta - 3\delta^2 + 4\delta^3 + ...\right) = R_{56}\delta - T_{566}\delta^2 + U_{5666}\delta^3, \tag{2.22}$$

where $T_{566} = -\frac{3}{2}R_{56}$ and $U_{5666} = 2R_{56}$ are, respectively, the second- and third-order terms describing the path-length difference with respect to the energy deviation [37].

In order for a bunch to be compressed in a chicane, a time-energy correlation (i.e. a negative linear chirp) must be imposed on the bunch before it enters the compressor. This can be achieved with an accelerating cavity. A particle

travelling through an RF cavity with initial and final position $s_{0,1}$, and an initial energy deviation $\delta(s_0)$ will experience an energy deviation at the exit of the cavity $\delta(s_1)$, defined as:

$$\delta(s_1) = \delta(s_0) + \frac{qV_{RF}}{E_0}\cos\left(\frac{\omega_{RF}z(s_0)}{c} + \phi_{RF}\right), \tag{2.23}$$

with q the electron charge, V_{RF}, ω_{RF} and ϕ_{RF} the RF cavity voltage, frequency and phase, respectively, and E_0 the energy of the reference particle. Depending on the RF phase setting, a time-energy correlation, otherwise known as an energy chirp, can be imposed on a bunch in the cavity. In the limit of small δ, Eq. 2.23 can be expanded as:

$$\delta(s_1) \approx \delta\left(1 + E' \cdot s_1 + \frac{E'}{2} \cdot s_1^2 + \frac{E''}{6} \cdot s_1^3 + ...\right), \tag{2.24}$$

where a prime denotes the derivative with respect to s. The linear energy chirp factor h is defined as:

$$h = E' = -\frac{qV_{RF}}{E_0}\frac{\omega_{RF}}{c}\sin\left(\phi_{RF}\right), \tag{2.25}$$

and in the limit $\left|\left(\omega_{RF}s_1\right)/c\right| \ll 1$, the relative energy deviation of a particle at position z in an energy-chirped bunch is $\Delta E/E \approx hz$ [46]. Once the bunch passes through the chicane and reaches position s_2, the relationship between longitudinal co-ordinate and relative energy deviation is given as follows:

$$z(s_2) = z(s_1) + R_{56}\delta(s_1) + T_{566}\delta(s_1)^2 + U_{5666}\delta(s_1) + ... \tag{2.26a}$$

$$\delta(s_2) = \delta(s_1). \tag{2.26b}$$

Now, the combined transfer map for the longitudinal phase space of the linac and bunch compressor is given by [35]:

$$\begin{pmatrix} z \\ \delta \end{pmatrix}_{s_2} = \begin{pmatrix} 1 & R_{56} \\ 0 & 1 \end{pmatrix}\begin{pmatrix} 1 & 0 \\ R_{65} & 1 \end{pmatrix}\begin{pmatrix} z \\ \delta \end{pmatrix}_{s_0} = \begin{pmatrix} 1 + R_{65}R_{56} & R_{56} \\ R_{65} & 1 \end{pmatrix}\begin{pmatrix} z \\ \delta \end{pmatrix}_{s_0}. \tag{2.27}$$

For a fully compressed bunch, i.e. with no final energy chirp, the rms bunch length at the exit of the chicane can be calculated as:

$$\begin{aligned}\sigma_z(s_2) = \left\langle z(s_2)^2 - \langle z(s_2)\rangle \right\rangle^2 = \sqrt{\left(1 + R_{56}R_{65}\right)^2 \sigma_z(s_1)^2 + R_{56}^2 \sigma_\delta(s_1)^2} \\ \approx \left(1 + hR_{56}\right) \sigma_z(s_1),\end{aligned} \tag{2.28}$$

and the overall compression factor is the ratio between the initial and final bunch length, or (in the linear approximation):

$$CF = \frac{\sigma_z(s_1)}{\sigma_z(s_2)} \approx \frac{1}{1 + hR_{56}}. \tag{2.29}$$

One of the major factors limiting the overall compression achievable in a single bunch compressor chicane is the emittance degradation of the bunch due to coherent synchrotron radiation (CSR); as the bunch becomes shorter, and the compression in a given dipole magnet becomes larger, the CSR power emitted becomes higher. This means that, in short-wavelength FELs, bunch compression is generally done in two or three stages, thus mitigating, to a certain extent, the degradation of the beam emittance due to CSR and nonlinearities (see Sec. 2.2.4).

These nonlinearities in the compressed longitudinal phase space can arise due to the higher-order terms in the energy deviation (Eq. 2.24). The higher-order terms can then result in a curvature in the longitudinal phase space, and the final bunch length will be larger than the value predicted using only the linear terms [35]. By using multiple compression stages, the required energy chirp at each chicane will be reduced, and the nonlinear effects can be mitigated to some extent [47, 48].

2.1.5 Free-Electron Lasers

The principle of the generation of FEL radiation is based on the extraction of electromagnetic radiation from relativistic electron beams travelling through a periodic magnetic lattice, using a sequence of short dipoles with alternating field polarity (known as an undulator). Full theoretical treatments of the principles behind the generation of FEL radiation can be found in Refs. [8, 9, 49]. The

radiation emitted by an ultrarelativistic electron is highly concentrated in its direction of travel, into an opening angle approximately equal to $1/\gamma^2$, with γ the relativistic Lorentz factor (see Eq. 2.14). The fundamental wavelength λ_f emitted by a particle travelling through an FEL is proportional to λ_u/γ^2, with λ_u the period of the undulator – that is, twice the length of each undulator pole in the lattice.

The brilliance of a photon pulse produced by an accelerator is defined as the number of photons n_p with a spectral bandwidth BW emitted by the particles in the accelerator per unit phase space area of the source (for a non-diffraction limited source – see below). The units of brilliance (otherwise known as brightness) are usually given as $n_p/\mathrm{s}/\mathrm{mm}^2/\mathrm{mrad}^2/0.1\%\mathrm{BW}$. For many users of light sources, a larger brightness leads to the possibility of studying processes at shorter time and length scales, and with greater accuracy. For a beam of radiation that has a Gaussian distribution in both the spatial and angular planes with a width of σ_r and $\sigma_{r'}$ respectively, the photon beam emittance is defined as follows:

$$\epsilon_{ph,x,y} = \frac{1}{2}\sigma_r\sigma_{r'} = \frac{\lambda_f}{4\pi}, \tag{2.30}$$

where λ_f is the wavelength of the radiation. This is known as the diffraction-limited photon emittance, and this diffraction limit can be reached when the electron beam emittance is smaller than $\epsilon_{ph,x,y}$ [36].

One requirement for optimising the brightness of an FEL is a small relative momentum spread of the electrons travelling through the undulator lattice. A single electron with momentum p can have a deviation δ from the nominal design momentum p_0 for producing light at a wavelength λ_f. The relative momentum spread of the electron bunch can be defined as the rms width of the distribution of δ for all electrons in the bunch. Since the wavelength of an emitted photon λ_f is dependent on γ, it is desirable, in order to reduce the spectral bandwidth of the radiation pulse produced, to aim towards minimising the momentum spread of the beam on entrance to the undulator. An additional requirement for optimising the transfer of energy from electrons in the bunch to the radiation that they produce is the spatial overlap of photons and electrons. This overlap is maintained using quadrupole magnets in between undulator sections, which control

the beam divergence in the transverse plane. The energy transfer between photons and electrons improves when the beams overlap spatially, as this enhances the probability of their interaction, and this optimal spatial overlap between the electron and photon beams is achieved when the transverse emittance of the electron beam is smaller than the diffraction limit of the photon beam [50, 51].

All accelerator-based light sources are based on the transfer of energy from particles to radiation, but the brightness of an FEL can be ten orders of magnitude larger (or more) than synchrotron-based light sources. This remarkable increase in performance has partly been made possible by improvements in RF photoinjectors and emittance preservation for linear machines. Therefore, preserving the electron beam emittance during the acceleration process, and through the undulator, is highly desirable for optimising the performance of FELs.

2.1.6 Self-Fields

This thesis will investigate collective interactions among particles within an electron bunch used as a driver for a free-electron laser. These collective effects arise due to the electric and magnetic fields (or 'self-fields') of charged particles interacting with either each other or their environment. Particles in an accelerator driving an FEL often reach ultrarelativistic energies in a short distance after the source (the electron gun). In this regime, in a straight section of beamline, a particle in the beam will only experience the fields of particles that are ahead of it, or of its close neighbours. As such, these fields are generally known as 'wake fields' [45]. In the case of coherent synchrotron radiation (CSR) – discussed below in Sec. 2.2 – the curved trajectory of the beam in a dipole magnet allows the field of particles in the beam to affect particles ahead of it, but this is often still referred to as a wake field.

The wake field of an ensemble of particles within an accelerator vacuum chamber depends on the geometry and materials of the system (thorough treatments of these wake fields can be found in Refs. [45, 52]). For example, in the case of a perfectly conducting accelerator vacuum chamber with a geometry that varies longitudinally, the calculation of the wake field involves solving Maxwell's equations with the boundary conditions provided by the cavity geometry [53]

– such a wake field is known as a 'geometric' wake field. The resulting 'wake function' describes the field experienced by a single particle at a specified distance from an emitting particle, giving rise to a delta-function distribution. A wake field refers to the electromagnetic field produced by a particle bunch, and it depends on the properties of both the bunch and the vacuum chamber surrounding it. The impedance of the resulting wake function can be solved in the frequency domain by calculating its Fourier transform. As will be shown later (Sec. 2.3), this approach proves useful when describing the propagation and amplification of small-scale modulations on a particle bunch. Geometric wake fields, and those arising due to accelerator elements with some electrical resistance ('resistive' wake fields) will not be considered in detail in this thesis; rather, only those which arise due to the direct collective interaction of particles will be considered.

2.2 Theory of CSR

Short electron bunches, such as those used to drive ultraviolet and X-ray FELs, can be susceptible to emittance degradation due to coherent synchrotron radiation (CSR) [18, 14, 16, 54]. This phenomenon occurs when the bunch travels through a bending magnet, and the radiation emitted by the bunch has a wavelength comparable to, or larger than, the bunch length. Since the bunch is travelling on a curved trajectory, and given that the radiation is emitted in a cone following the particle motion [1], the radiation from the back of the bunch is able to catch up with the head of the bunch, thus giving the particles at the head a kick in energy. When the force is applied to all particles in a bunch that receive such a kick, the relative energy spread of the bunch increases. It should also be noted that the characteristic wavelength of CSR, which is related to the total bunch length, may become shorter if there is some substructure within the longitudinal bunch distribution.

Magnetic bunch compressors, which are often used to reduce the electron bunch length used for driving an FEL, usually comprise a four-dipole chicane (see Sec. 2.1.4), which is designed to produce zero dispersion at the exit. The

kick in energy received by a particle travelling on a curved trajectory can cause it to travel along a different path through the bunch compressor, which then changes the transverse co-ordinate of the electron at the exit of the chicane. When this effect is taken into account for all particles in the bunch that have received a kick in energy due to CSR, this results in an overall emittance growth.

This section will outline some of the theory concerning the impact of an energy kick induced by CSR on curved trajectories, providing some new insights into the CSR field in the entrance and exit transient regimes, which apply when the bunch is traversing the magnetic field boundary. These results will become useful when addressing the accuracy of models used in simulation (Sec. 3.2), and for comparison with experimental measurements of emittance growth in a bunch compressor (Sec. 4.5).

2.2.1 1D Theory

We first consider the case of a bunch of electrons on a curved trajectory at time t through a bending magnet of bending radius R and bending angle ϕ_m. The electromagnetic field acting upon any particular electron in the bunch comprises the fields emitted by electrons at earlier times $t' < t$ on this curved path. In the following derivation, the subscripts 0 and 1 will refer to the emitting and receiving particle, respectively, and a prime indicates retarded time or position; that is, the point at which the field was emitted. To calculate the total field, we first consider the field emitted by a single electron at position $\vec{r_0}'$ inside the magnet at time t' and observed by another electron at position $\vec{r_1}$ at time t. For simplicity, in this section we neglect the transverse extent and energy spread of the electron bunch, and thereby assume that all electrons travel exactly along the reference trajectory. The electromagnetic field at $\vec{r_1}$ due to the electron at $\vec{r_0}'$ is given by the Liénard-Wiechert field [1] at time t:

$$\vec{E}(\vec{r},t) = \frac{e}{4\pi\epsilon_0}\left(\frac{\vec{n}-\vec{\beta}'}{\gamma^2(1-\vec{n}\cdot\vec{\beta}')^3\rho^2} + \frac{\vec{n}\times\left(\left(\vec{n}-\vec{\beta}'\right)\times\dot{\vec{\beta}}'\right)}{c\left(1-\vec{n}\cdot\vec{\beta}'\right)^3\rho}\right), \tag{2.31}$$

where e is the electron charge, ϵ_0 is the vacuum permittivity, c is the speed of light, γ is the relativistic Lorentz factor, $\vec{\beta}'$ is the velocity of the emitting electron (normalised to c), $\dot{\vec{\beta}}'$ is the normalised acceleration of the emitting electron, $\rho = |\vec{r_1} - \vec{r_0}'|$ is the distance between the emission site and point of observation, and $\vec{n} = (\vec{r_1} - \vec{r_0}')/\rho$. From now on, the first term on the right hand side of Eq. 2.31, which does not depend on $\dot{\vec{\beta}}'$, will be referred to as the 'Coulomb' field, and the second term will be designated the 'acceleration' field. Conventionally, several regimes of CSR forces are identified according to the positions of the emitting and observing particles [18]. Initially, the particle in front is inside the magnetic field of the dipole and the particle behind has not yet entered it, in which case $\dot{\vec{\beta}} = 0$ and only the first term of Eq. 2.31 contributes. This is the 'entrance transient' regime. When both particles are inside the magnet, both terms in Eq. 2.31 contribute to the CSR field, and this is known as the 'steady-state' regime. Finally, when the emitter is still in the magnet and the receiver has exited it, this is known as the 'exit transient' regime. Eq. 2.31 describes the electric field due to a single point particle, and so to calculate the entire CSR field requires a convolution of this expression with the charge density of the entire bunch. To simplify further analysis, the longitudinal field component $E_{||}$ can be expressed in terms of a wake function $w(z - z')$:

$$E_{||}(z) = \int w(z - z')\lambda(z')dz', \tag{2.32}$$

where $\lambda(z)$ is the longitudinal charge distribution, with the normalisation condition $\int \lambda(s)ds = Q$ (with Q the total bunch charge), and $w(z - z')$ is the parallel component of the field in Eq. 2.31 at position z in the bunch due to a particle at position z' in the bunch. In the following derivation of the CSR field in these three regimes, we will project the charge density onto the reference trajectory, neglecting the effects of the transverse bunch size.

2.2.1.1 Steady-State Regime

As shown in [18, 55], the electric field observed at position z for a line charge $\lambda(z)$ due to the motion on a circular arc of radius R is given by:

$$E_{||}^{SS}(z) = \frac{Ne\beta^2}{8\pi\epsilon_0 R}\int_0^{\phi} \frac{\beta - \cos(u/2)}{\left(1-\beta\cos(u/2)\right)^2}\lambda(z-\Delta z(u))du, \tag{2.33}$$

where ϕ is the angle from the entrance of the magnet to the observation point, $\Delta z(u) = R\,(u - 2\beta\sin(u/2))$, N is the number of particles in the bunch and u is the retarded angle between the emitter at time of emission and the observer at time of observation. A schematic of this scenario is shown in Fig. 2.2. Note that both the position of the emitting electron at time of emission $\vec{r_0}'$ and at time of observing $\vec{r_0}$ have been drawn, reflecting the fact that the bunch travels a considerable distance during the time required for the electromagnetic field to travel from emitter to observer. This formula is valid for a rigid line charge, using the ultrarelativistic approximation ($\beta \approx 1$). This model also does not take account of any effects due to dipole fringe fields. The transition to the steady-state regime takes place at a distance D^{SS} from the entrance to the magnet [18]:

$$D^{SS} \approx \left(24R^2\sigma_z\right)^{1/3}, \tag{2.34}$$

with σ_z the rms bunch length.

2.2.2 Entrance and Exit Transients (1D Model)

2.2.2.1 Derivation of CSR Entrance Transient

In this regime, the condition D^{SS} has not been reached, and a significant portion of the emitting particles have not yet entered the magnetic field. This means that their contribution comes entirely from the Coulomb field (the first term) of Eq. 2.31. We begin by calculating a number of distances shown in Fig. 2.3. For the full derivation of the total CSR field in this regime, see Appendix A.1. The

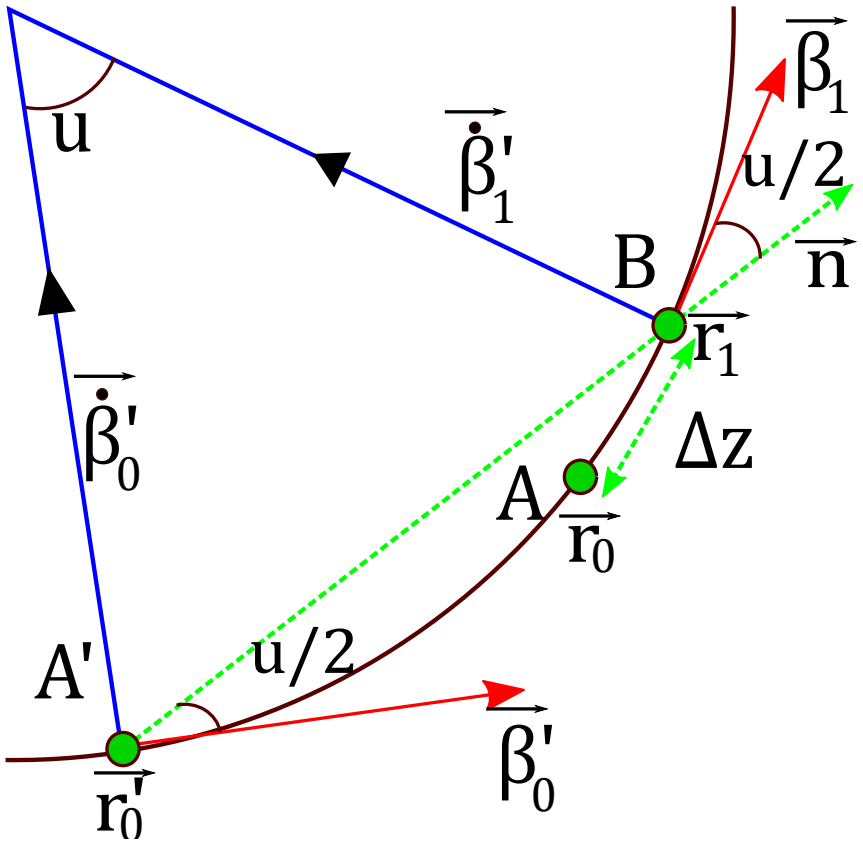

Figure 2.2: Schematic of the CSR interaction in the 1D model in the steady-state regime. The positions of the emitter and receiver at the time of interaction are shown as A and B, the the position of the emitter at the time of emission is A'. The acceleration and velocity vectors of the particles are shown as blue and red lines, respectively; the distances used in the derivation of the CSR field are shown as green dashed lines.

resulting expression for this field is:

$$E_{||}^{ent}(z) = E_{||}^{SS}(z) + \frac{Ne}{4\pi\epsilon_0\gamma^2}\int_0^d \frac{(y-\beta\rho(y))\cos(\phi)+R\sin(\phi)}{(\rho(y)-\beta(y+r\sin(\phi)))^2\rho(y)}\lambda(z-\Delta(y))dy, \tag{2.35}$$

where $\rho(y) = \sqrt{y^2+2Ry\sin(\phi)+4R^2\sin^2(\phi/2)}$ and $\Delta(y) = y+R\phi-\beta\rho(y)$, with y the distance between the emitting particle and the entrance of the magnet, and d the length of the drift before the magnet taken into account for the calculation of the CSR field. A representation of this regime is shown in Fig. 2.3. The contributions to the field from $E_{||}^{SS}$ arise from the radiative emission of particles on the curved trajectory, while the other term comes from particles which have not yet reached the magnet at the time of emission. Both terms of Eq.2.35

partially cancel, and the net CSR field has a lower amplitude than either term. In the limit $d \to \infty$, in the small-angle and ultrarelativistic approximations [18], this field reduces to:

$$E_{\parallel}^{ent} = \frac{Ne}{24^{1/3}\pi\epsilon_0 R^{2/3}} \left(\left(\frac{24}{R\phi^3}\right)^{1/3} \left[\lambda\left(z - \frac{R\phi^3}{24}\right) - \lambda\left(z - \frac{R\phi^3}{6}\right) \right] + \int_{z-R\phi^3/24}^{z} \frac{d\lambda(z')}{dz'} \frac{dz'}{(z-z')^{1/3}} \right). \quad (2.36)$$

However, without taking this limit, that is, by taking only a short drift length before the entrance of the dipole, the Coulomb term can dominate up until the steady-state regime has been reached, invalidating the usual 1D approximation.

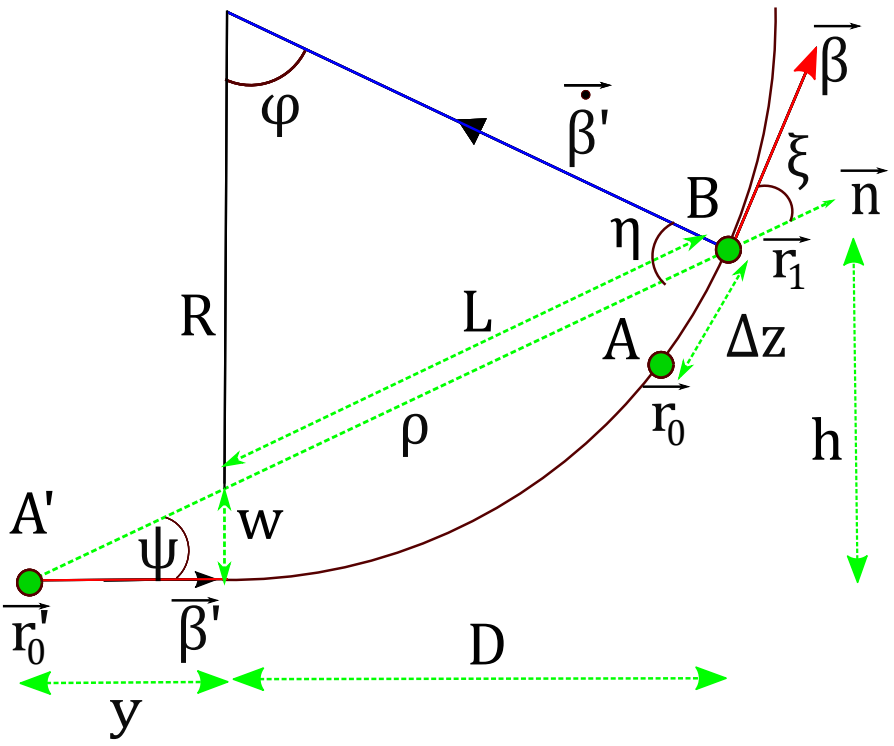

Figure 2.3: Geometry of CSR interaction between an emitting electron at $\vec{r}_0'$ before the magnet and a receiving electron at $\vec{r}_1$ within the magnet. ψ is the angle between the emitter at time t' and the receiver at time t, and ξ is the angle between $\vec{\beta}$ and $\vec{n}$. The colour scheme is the same as Fig. 2.2.

This result – that the Coulomb component of the Liénard-Wiechert field can provide a non-negligible contribution to the CSR field in the entrance transient

regime, even in the ultrarelativistic limit – can be understood in the following way, as illustrated by Fig. 2.4. The Coulomb field of a particle on a straight trajectory is confined to a narrow disk, and it appears to be produced instantaneously by the electron at position r_0, at time t_0 to an observer, whereas in fact the field was produced at a retarded time t_0' (Fig. 2.4a). Even if the electron subsequently moves onto a different trajectory between t_0' and t_0, this will not change the field at the observation point r_1, and the Coulomb field is still travelling along the straight path (Fig. 2.4b). For a bunch of electrons beginning to enter a curved path, the electrons at the head will observe this Coulomb field generated by the tail of the bunch, as the field has been able to 'catch up' with the head. This is because electrons at the head of the bunch have taken a longer time to travel a longitudinal distance z than the field (Fig. 2.4c). This model suggests that, for a given angle ϕ into the magnet, there exists a characteristic drift length d_c needed to generate Coulomb fields at that position – that is, to have an entrance transient effect. This distance can be estimated by calculating the required distance in front of the magnet that the field would need in order to be observed by the observing electron, giving:

$$d_c \approx \frac{\gamma R \phi^2}{\sqrt{2}}. \tag{2.37}$$

The effect of the entrance transient will depend on the length of the drift section preceding the bend, so it is necessary to take d_c into account in order to correctly account for this. In a circular machine, bending magnets will not necessarily have drift lengths of tens of metres in front of them, as is often the case for a linear accelerator. This means that errors can be made if the formula Eq. 2.36 is applied in these scenarios, or if a sufficient drift is not taken into account before the entrance to a dispersive region. In Sec. 3.2, this will be demonstrated by simulating two test cases with different values of the drift length before a bending magnet.

2.2.2.2 Derivation of CSR Exit Transient

Consider the situation at time t, when an electron bunch has traveled through a bending magnet of bending radius R and bending angle ϕ_m and is currently a

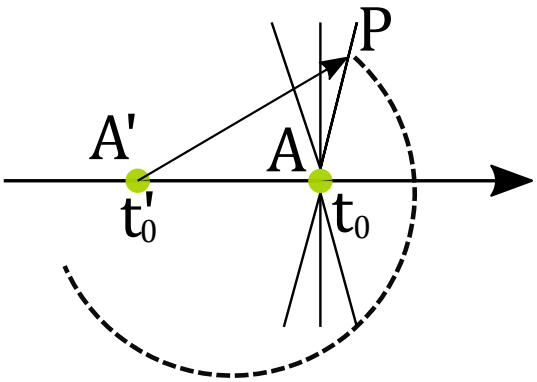

(a) Although Coulomb field lines align with the current position, the field actually originates from the retarded position.

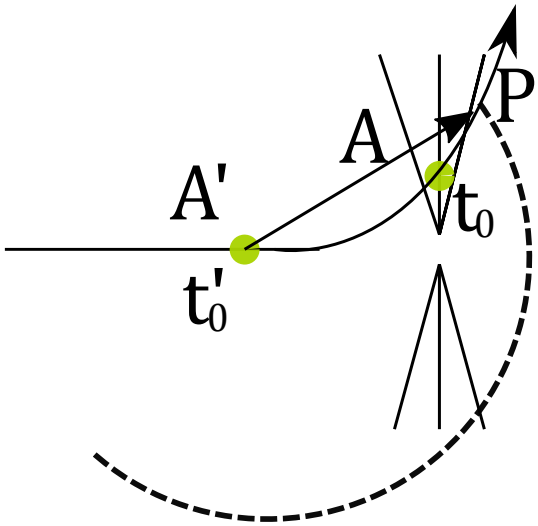

(b) Consequently, if the emitting electron A' electron enters the curved trajectory between the retarded time t_0' and the current time t_0, the field at the observation point is not affected.

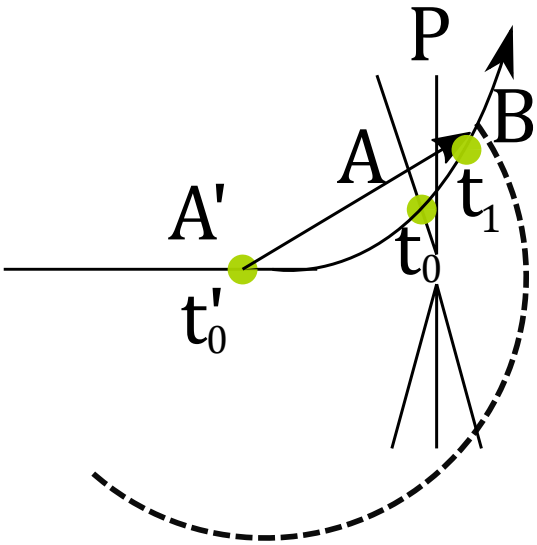

(c) This allows electrons (B) in front of the source electron (A') to end up inside the high-field region due to A'.

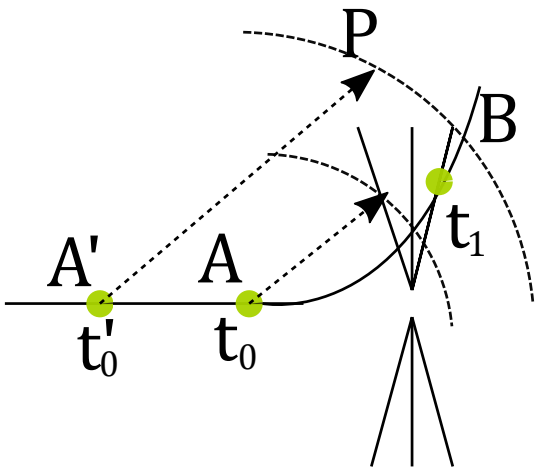

(d) Whether the high-field region exists at time t_1 depends on the length of the drift on which the source electron has been moving.

Figure 2.4: Schematic representation of the CSR entrance transient field. The observation point P due to the Liénard-Wiechert field of the emitter A' at a retarded time t_0' is shown as the dashed circle.

distance x_c past the exit edge of the magnet. The electromagnetic field acting upon any particular electron in the bunch is comprised of the fields emitted by electrons at earlier times $t' < t$ when they were still inside the magnet. To calculate the total field, we first consider the field emitted by a single electron

at position $\vec{r_0}'$ inside the magnet at time t' and observed by another electron at position $\vec{r_1}$ past the magnet at time t. The geometry of this case is sketched in Fig. 2.5.

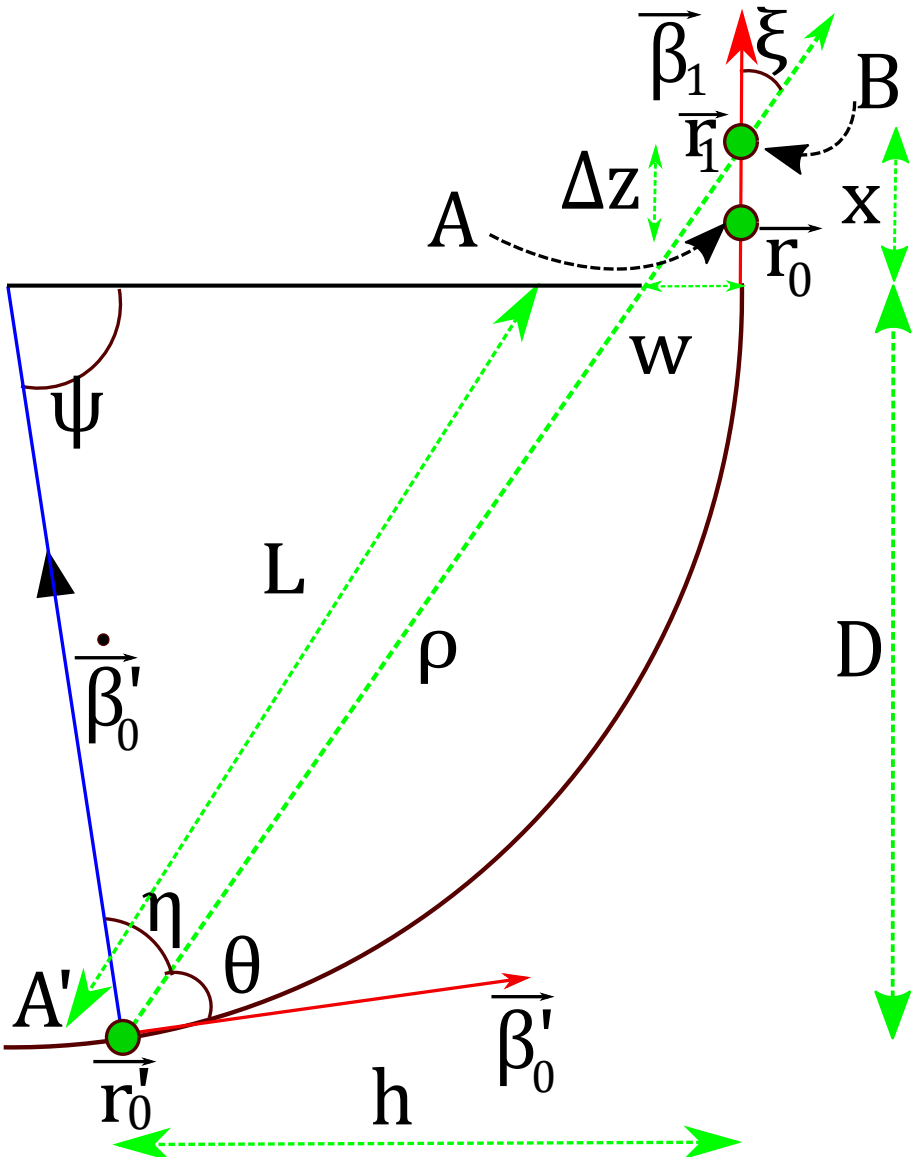

Figure 2.5: Geometry of CSR interaction between an emitting electron at $\vec{r_0}'$ inside the magnet and a receiving electron at $\vec{r_1}$ past the magnet. The distances and angles shown are derived in Appendix A.2. The colour scheme is the same as Fig. 2.2.

For the full derivation of the total CSR field after the exit of the bending magnet, see Appendix A.2. Defining the following quantities:

$$\zeta = x + R\sin(\psi) - \beta\rho\cos(\psi), \tag{2.38}$$

$$\chi = R\sin(\psi/2) + x\cos(\psi/2), \tag{2.39}$$

with ψ the angle between the emitting electron at retarded position $\vec{r_0}'$ and the exit of the magnet, we obtain the following expression for the radiation field:

$$E_{||,rad}^{exit}(z,x) = \frac{Ne\beta^2}{4\pi\epsilon_0}\int_0^{\phi_m}\left(\frac{2\sin(\psi/2)\zeta\chi}{\left(\rho-\beta\left(R\sin(\psi)+x\cos(\psi)\right)\right)^2\rho} - \frac{\sin(\psi)}{\rho-\beta\left(R\sin(\psi)+x\cos(\psi)\right)}\right)\lambda\left(z'(\psi)\right)d\psi. \tag{2.40}$$

In this expression, $x = x_c + z$ is the position of the evaluation point with respect to the exit edge of the magnet, with x_c the distance from exit edge to bunch centroid and z the position relative to the bunch centroid. In the integral, the charge density should be evaluated at z', which from Eq. A.18 is given by $z'(\psi) = -x_c - R\psi + \beta\rho$. The corresponding expression for the Coulomb field is:

$$E_{||,C}^{exit}(z,x) = \frac{Ne\beta R}{4\pi\epsilon_0\gamma^2}\int_0^{\phi_m}\frac{x-\beta\rho\cos(\psi)+R\sin(\psi)}{\left(\rho-\beta\left(R\sin(\psi)+x\cos(\psi)\right)\right)^2\rho}\times\lambda(z'(\psi))d\psi. \tag{2.41}$$

Eq. 2.40 gives the longitudinal radiation field as observed along a bunch that just passed a single bending magnet. The expression for the radiation field (Eq. 2.40) can be integrated using the ultrarelativistic and small-angle approximations (see Appendix A.2) to yield the full field:

$$E_{||,rad}^{exit}(z,x) \approx \frac{Ne}{\pi\epsilon_0}\left(\frac{\lambda(z-\Delta z_{max})}{\phi_m R+2x} - \frac{\lambda(z)}{2x} + \int_{z-\Delta z_{max}}^{z}\frac{\partial\lambda(z')}{\partial z'}\frac{dz'}{\psi(z')R+2x}\right). \tag{2.42}$$

In the integrand of Eq. 2.42, $\psi(z)$ is defined implicitly by the relation:

$$z - z' = f(\psi) = \frac{R\psi^3}{24}\frac{R\psi+4x}{R\psi+x}. \tag{2.43}$$

and $\Delta z_{max} = f(\phi_m)$. Here, it has been taken into account that source points positioned after the exit of the magnet do not contribute to the CSR radiation, and the first two terms arise because Eq. 2.42 is the result of an integration

by parts. We can now follow a similar procedure to calculate the Coulomb component of the field given by Eq. 2.41. The kernel is strongly peaked around $\psi = 0$, and so we can assume that $\lambda(z)$ is constant over the relevant range, and apply a small-angle Taylor expansion, resulting in:

$$E_{||,C}^{exit}(z,x) \approx \frac{Ne\lambda(z)}{4\pi\epsilon_0\gamma^2}\int_0^{\phi_m}\frac{2\gamma^2}{(x+R\psi)^2}d\psi = \frac{Ne}{2\pi\epsilon_0}\frac{\lambda(z)}{x}. \tag{2.44}$$

This term cancels with one of the boundary terms in Eq. 2.42, resulting in the following expression for the total CSR exit transient field:

$$\begin{aligned} E_{||}^{exit}(z,x) = E_{||,C}^{exit}(z,x) + E_{||,rad}^{exit}(z,x) \approx \frac{Ne}{\pi\epsilon_0}\Bigg(\frac{\lambda(z-z_{max})}{\phi_m R + 2x} + \\ \int_{z-\Delta z_{max}}^{z-\Delta z_{min}}\frac{\partial\lambda(z')}{\partial z'}\frac{dz'}{\psi(z')R+2x}\Bigg). \end{aligned} \tag{2.45}$$

This is equivalent to the expression for the exit transient field given in [56]. However, we have provided a full explanation of how both the Coulomb and radiation components of the Liénard-Wiechert fields complement each other to produce this result. A comparison between Eqs. 2.40, 2.42 and the full formula 2.45 is given for a benchmark case in the following Section. For a schematic representation of the Coulomb field during rectilinear motion, motion on an arc, and the transition regime upon exiting a curved trajectory, see Fig. 2.6. A physical description for the underlying mechanism behind the interaction of both the Coulomb and radiation fields can be understood as follows. The contribution from the Coulomb field is significant only within a very small range $\psi \lesssim \gamma^{-1} \ll 1$. The field lines corresponding to the Coulomb field of a relativistic particle are confined to a very flat region perpendicular to the direction of motion. An important property of the Coulomb field is that the field lines point away from a virtual source point that moves with velocity $\vec{\beta}c$ in the direction that the emitter had at the time of emission. In the figure, the retarded position of the emitter is shown, and the apparent, instantaneous source of the Coulomb field is also indicated. For a bunch moving in rectilinear motion (Fig. 2.6a), this apparent source point remains coincident with the instantaneous position of the emitter. Two particles that are at the same longitudinal position to each other barely

feel each other's field due to the pancake effect. The field lines of the upstream particle are always behind the downstream particle.

In the case of an arc (Fig. 2.6b), the path of the observer curves away from the direction that the emitter had at time of emission (denoted the 'z direction'). Therefore the z component of the velocity of the observer becomes lower than βc during the transit time in which the field travels from emitter to observer. Therefore, at time of observation, the 'pancake region' of dense field lines is in front of the observer. In either the rectilinear or arc case, the upstream particle observes a very small field. However, at the end of the arc (Fig. 2.6c), the geometry must pass from a situation with field lines in front of the observer to a situation with field lines behind the observer. Hence there must be a point where this field passes over the observer, giving a spike of CSR force. This effect is the exact analogue of the entrance effect sketched in Fig. 2.4, in which the geometry transits from a case with the Coulomb field behind the observer to a situation with the field in front of it.

The above mechanism may also explain why the contribution of the Coulomb field is only significant in the very final angular range $0 < \psi < \gamma^{-1}$ of the arc, as detailed in the previous section. This is simply the angular extent of the pancake field that needs to pass over the observing particle. It should also be noted that the field line patterns sketched in the figures are not entirely realistic, because there will only be a thin radiation shell of thickness $\Delta s/\beta$ generated from the path element Δs, and only in this thin shell the drawn pancake field line pattern exists. The subsequent path element will generate another radiation shell, and the corresponding 'pancake field' inside that shell will be slightly differently oriented due to the different orientation of the path element. The total field line pattern will be the sum of all such infinitesimal shells-with-pancake-fields, in which the concept of a pancake field will be hard to recognize at all. The main point is, however, that with any path element there is an associated region of dense field lines. Near the end of the arc, there is a point where this region will pass over the upstream particles, creating a brief but intense spike of CSR force.

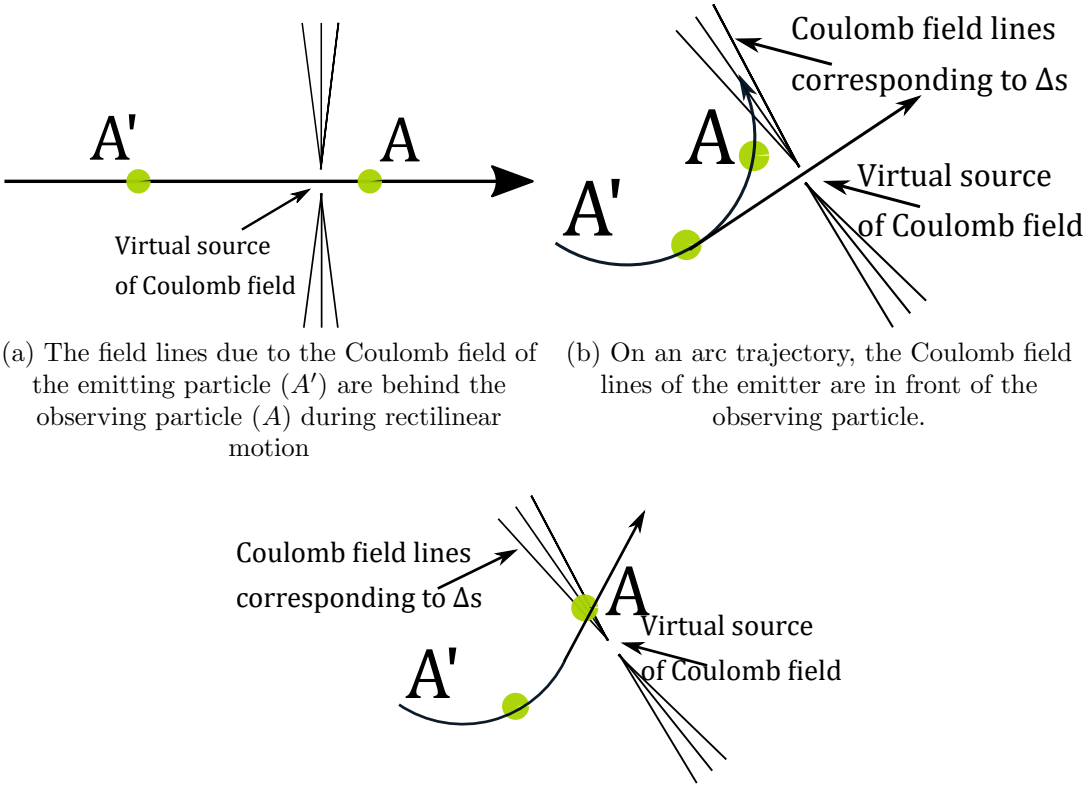

(a) The field lines due to the Coulomb field of the emitting particle (A') are behind the observing particle (A) during rectilinear motion

(b) On an arc trajectory, the Coulomb field lines of the emitter are in front of the observing particle.

(c) In the transition regime, there is a small range over which the observing particle experiences a sharp spike in the CSR force due to the emitter.

Figure 2.6: Schematic representation of the CSR exit transient field on three different trajectories.

2.2.3 Deficiencies in the 1D Model

One of the assumptions which underlies the theory outlined above is that the bunch has no transverse extent – that is, the bunch distribution is projected onto the nominal axis through a dipole magnet (see Fig. 2.7a for a simplified schematic of this model). Under this condition, all particles in front of an emitter of synchrotron radiation can be influenced by it. The validity of this expression is contingent on the length of the bunch greatly exceeding its transverse size (see Sec. 4.5 and Ref. [55]).

However, this may not be practically applicable for a bunch inside a bending magnet. The bunch will have some finite energy spread, causing the bunch to disperse within the magnet, potentially resulting in a bunch that – inside the dipole – is much wider transversely than it is longitudinally, therefore violating the approximation on which the 1D theory is based (see Fig. 2.7b). In order to

illustrate a potential issue with the 1D projection of the bunch, two particles, A and B, are shown in Fig. 2.7b: the former is lower in energy than the reference particle, and therefore takes a longer trajectory through the magnet, whereas the path of the latter particle, with a higher energy, is reduced. In the 1D approximation, particle A is behind particle B, and therefore the lower-energy particle will give a CSR kick to the higher-energy particle. However, due to the directionality of the CSR field, it may not even be causally possible that these two particles can influence each other if the transverse extent of the bunch is taken into account. In addition, if the beam has some microbunching structure (see Sec. 2.3), the length of each microbunch (the microbunching period) may be much less than the transverse beam size, which is another potential limitation to the 1D model. It could therefore be expected that there exist certain conditions under which the strength of CSR field will be overestimated in the 1D approximation.

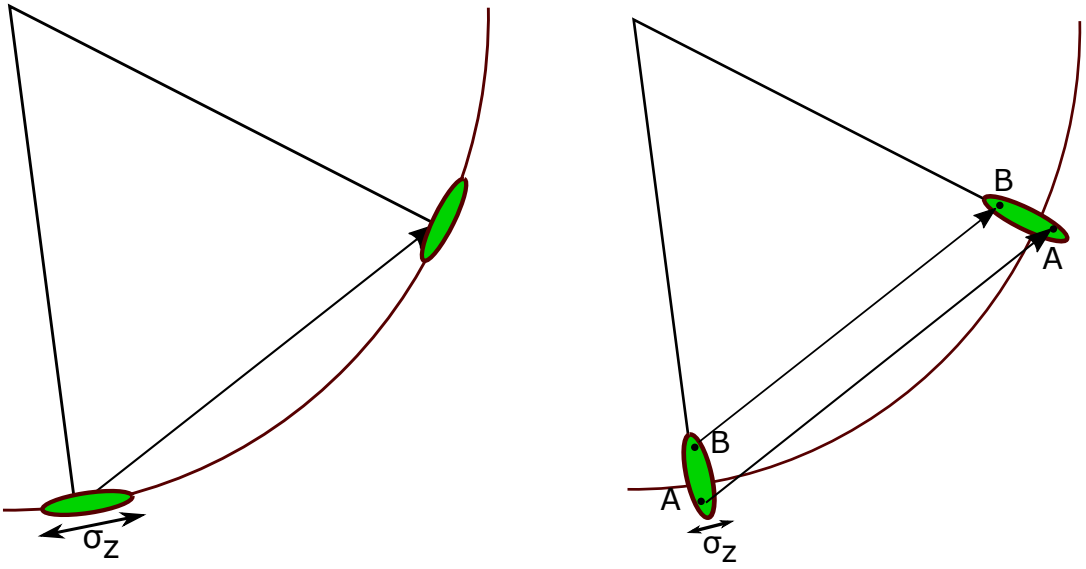

(a) Schematic representation of the CSR interaction in the 1D model.

(b) Schematic representation of the CSR interaction for a bunch with transverse extent.

Figure 2.7: Schematic representation of the CSR interaction in the 1D approximation (left), and with a more realistic picture of a dispersed bunch with a transverse extent (right).

2.2.4 Emittance Growth

The emittance growth caused by CSR can be calculated by considering the variation in transverse motion that is induced by the change in energy of a particle receiving radiation. Under dispersive conditions, the transverse motion of a particle is defined as the combination of its betatron and dispersive contributions:

$$x(s) = x_\beta(s) + R_{16}(s_0 \rightarrow s_1)\delta(s) = x_\beta + \Delta x, \tag{2.46a}$$

$$x'(s) = x'_\beta(s) + R_{26}(s_0 \rightarrow s_1)\delta(s) = x'_\beta + \Delta x', \tag{2.46b}$$

with the subscript β denoting the betatron component, δ the relative change in momentum due to CSR, and R_{16}, R_{26} the matrix components between positions s_0 and s_1, described above (see Sec. 2.1).

For dispersion functions η_x and η'_x for horizontal spatial and angular motion, respectively, and with the CSR-induced relative rms energy increase as $\sigma_{\delta,CSR}$, it follows that $\langle \Delta x^2 \rangle = (\eta_x \sigma_{\delta,CSR})^2$ and $\langle \Delta x'^2 \rangle = (\eta'_x \sigma_{\delta,CSR})^2$ [57, 58]. For a Gaussian line-charge distribution, the mean energy change of a particle due to the CSR steady-state field (right-hand side of Eq. 2.36) is [59]:

$$\langle \delta_{CSR} \rangle \approx -0.35 \; r_e \frac{N}{\gamma} \frac{\theta R^{1/3}}{\sigma_z^{4/3}}, \tag{2.47}$$

where $\sigma_{\delta,CSR} = 0.7 \times |\langle \delta_{CSR} \rangle|$, N is the number of particles, σ_z is the electron bunch length, and θ, R are the bending angle and bending radius of the dipole, respectively. The horizontal emittance increase as a result of the energy change due to CSR $\epsilon_{x,d}$ is then [57]:

$$\epsilon_{x,d} = \epsilon_{x,0} \left[\beta_x \langle \Delta x'^2 \rangle + 2\alpha_x \langle \Delta x \Delta x' \rangle + \gamma_x \langle \Delta x^2 \rangle \right] = \epsilon_{x,0} H_x \sigma^2_{\delta,CSR}, \tag{2.48}$$

with the optics function H_x defined as:

$$H_x = \frac{\eta_x^2 + (\beta_x \eta'_n + \alpha_x \eta_x)^2}{\beta_x}. \tag{2.49}$$

If, then, the Twiss parameters and $\sigma_{\delta,CSR}$ are known, it is possible to compute the steady-state CSR-induced emittance growth in a bunch compressor. The energy variation due to the entrance and exit transient electric fields (Eqs. 2.35 and 2.45) cannot be easily solved analytically, and so their contribution to the emittance can only be accounted for in simulation, or semi-analytically, by calculating the transient contribution to the horizontal deflection using simulated beam parameters.

Comparisons between these analytic formulae and some test cases are given in Chapter 3 (Sec. 3.2). The largest contribution to the CSR-induced emittance growth in a four-dipole bunch compressor, however, does come from steady-state CSR, and this analytical treatment also allows for the minimisation of this emittance growth using a careful optics balance through the bunch compressor [58]. The energy kick $\sigma_{\delta,CSR}$ is inversely proportional to the electron bunch length, which is reduced to a minimum in the fourth dipole magnet. Therefore, by minimising H_x in the vicinity of this magnet, it is possible to reduce the contribution of CSR to the final emittance of the electron beam. A similar approach is taken to lattice design for a low-emittance electron storage ring [35]: the mechanism for emittance growth from CSR is very similar to that for emittance growth from synchrotron radiation, and in both cases the emittance growth is minimised by minimising the integral of H_x in the bending magnets.

2.3 Theory of Microbunching

Microbunching in particle accelerators is defined as small-scale modulations within the longitudinal phase space of a particle bunch. Density fluctuations due to shot noise can develop in the low-energy section of an accelerator, which can then undergo amplification due to impedance effects and dispersion in magnetic chicanes, leading to a modulation in energy and/or density that can degrade the emittance and energy spread of an electron beam. This instability, first observed in numerical simulations of FELs [60], and later measured experimentally in x-ray FEL facilities [23, 61], can have a dramatic impact on the performance of an FEL. As mentioned above (Sec. 2.1.5), the slice energy spread of the bunch must be

reduced as far as possible in order to for the bunch to emit coherently in an undulator. Microbunching can increase this slice energy spread, at scales equal to or longer than the (shortest) modulation wavelength. As such, the mechanisms driving the instability have been intensely studied in recent years.

This section will outline three important collective effects known to have an impact on the production and evolution of small-scale structures within electron beams: shot noise, longitudinal space-charge and CSR. Geometric impedances due to discontinuities in the accelerator vacuum chamber in accelerating cavities are also known to have an effect on microbunching [62, 63], but these effects are small compared with those that arise due to the effects discussed in detail, and so will not be considered. A recent study [64] has highlighted the importance of small-angle Coulomb scattering, or intrabeam scattering (IBS), as a mechanism for damping the microbunching instability, and so this effect is also introduced. The amplification of modulations in the longitudinal phase space density will be discussed, and an analytic model will be introduced that illustrates the relationship between the microbunching in the bunch longitudinal phase space and its associated Fourier transform.

2.3.1 Shot Noise Model

The source of electrons used in high-brightness linear accelerators ultimately determines the quality of the final bunch. In the case of FELs, an RF photoinjector – in which a laser pulse impinges on a photocathode inside an RF cavity – is a common method for generating these bunches. The properties of the laser pulse therefore has a direct impact on the properties of the electron bunch it produces. In the simplest case, a laser with a Gaussian or flat-top profile in the transverse and longitudinal planes is assumed, but in reality this approximation does not generally hold; small perturbations in the laser intensity profile are often present due to shot noise. These perturbations are generally too small to observe experimentally for low-energy bunches, but simulations have shown that such a bunch with shot noise in its longitudinal density can experience amplified bunching further down the accelerator [65, 66]. These perturbations can then give rise to a nonlinear longitudinal density profile in the electron bunch.

2.3.2 Longitudinal Space-Charge Model

Since the space-charge field experienced by an electron in the bunch is dependent on its neighbouring electrons, these small deviations in the density profile can cause a change in energy for a given electron. This longitudinal space-charge (LSC) force can accelerate electrons towards the head of the bunch, and decelerate those behind, causing a localised clustering of the bunch in time [67]. This can give rise to a periodic density perturbation for short bunches, causing the following longitudinal electric field to be generated by summing over contributions from N point charges with coordinates (x_j, y_j, z_j) [68]:

$$E_z\left(\mathbf{X}\right) = -\frac{e}{4\pi\epsilon_0}\sum_j^N \frac{\gamma\left(z-z_j\right)}{\left[\left(x-x_j\right)^2+\left(y-y_j\right)^2+\gamma^2\left(z-z_j\right)^2\right]^{3/2}}, \tag{2.50}$$

with $\mathbf{X} = (x, y, z)$ and γ the relativistic Lorentz factor. The longitudinal Fourier transform of E_z is:

$$\tilde{E}_z(k) = -\frac{eik}{2\pi\gamma_0^2\epsilon_0}\sum_j^N e^{-ikz_j}K_0\left(\frac{k|\mathbf{r}-\mathbf{r}_j|}{\gamma}\right), \tag{2.51}$$

where $k = 2\pi/\lambda$ is the wavenumber of the modulation, $\mathbf{r} = (x, y)$ describes the transverse coordinates, and K_0 is the modified Bessel function of the second kind, of order zero. The exponential term describes the phase of the microbunching, and the Bessel function term gives its amplitude. The longitudinal space-charge impedance per unit length can be calculated – assuming a bunch with uniform transverse density – as follows [68]:

$$Z_{LSC}(k) = -\frac{\tilde{E}_z(k)}{\tilde{I}(k)}, \tag{2.52}$$

where $\tilde{I}(k)$ is the Fourier transform of the current density. For a beam with uniform transverse size $r_b \approx 1.747\left(\sigma_x+\sigma_y\right)/2$, the 1D LSC impedance is given as [26]:

$$\bar{Z}_{LSC}\left(k, r_b, \gamma\right) = \frac{iZ_0}{\pi k r_b^2}\left[1-\frac{kr_b}{\gamma}K_1\left(\frac{kr_b}{\gamma}\right)\right], \tag{2.53}$$

where K_1 is the modified Bessel function of the second kind, of order one, and $Z_0 \approx 377\,\Omega$ is the impedance of free space. Due to the mutual repulsion of electrons in a high-density region, a longitudinal space-charge force can accelerate the particles towards the front of the region and decelerate those towards the back of the region. This variation in energy then causes slippage in the longitudinal dimension. Given the initial bunching, there may be a number of such high-density regions, and with a number of particles being accelerated and decelerated from regions of high longitudinal density, this longitudinal slippage in energy can then again cause bunching in longitudinal density. This process can then repeat, giving rise to an oscillation between energy and density modulations. In the case of a relativistic beam in a drift space, this oscillation has a characteristic frequency given by [26]:

$$\omega_{LSC}\left(k_0, r_b, \gamma\right) = c\left[\frac{I_0}{\gamma^3 I_A} k_0 \frac{4\pi |Z_{LSC}(k_0, r_b, \gamma)|}{Z_0}\right]^{1/2} \lesssim \frac{2c}{r_b}\left(\frac{I_0}{\gamma^3 I_A}\right)^{1/2}, \quad (2.54)$$

for an initial peak current $I_0 = Nec$ for N electrons, an initial modulation wavenumber k_0 and $I_A \approx 17\,\mathrm{kA}$ the Alfvèn current. Since this oscillation frequency is inversely proportional to the beam energy, the period of the oscillation between energy and density modulations can become large (on the order of 10s or 100s of metres) for ultrarelativistic beams. Nevertheless, due to the long accelerating sections required to drive a short wavelength FEL, this oscillation cannot be neglected when considering the evolution of the microbunching instability in such a machine.

In order to evaluate the impact of this LSC impedance on the final bunch profile, the bunching factor $b(k)$ is introduced. In the simplest case, this is given by the Fourier transform of the current profile of the bunch:

$$b(k) = \frac{1}{Nec}\int I(z)\exp\left(-ikz\right) dz. \quad (2.55)$$

The average longitudinal bunching factor for a broad-band spectral distribution

of modulations Δk is given by:

$$|b_0(k)|^2 = \frac{2ec}{I_0}\frac{\Delta k}{k^2}. \tag{2.56}$$

Later on, this 1D analysis will be extended to cover the full longitudinal phase space, taking the microbunching in energy into account. The value of $b(k)$ is proportional to the amplitude of the modulations in density (at a given wavenumber) relative to the average current of the bunch. The final amplitude of the energy modulation at a distance L from the point of initial modulation can then be described in terms of the LSC impedance and the bunching factor [21]:

$$\Delta\gamma(k, r_b, \gamma) = -\frac{4\pi I_0}{I_A} b(k) \int_0^L \frac{Z_{LSC}(k, r_b, \gamma; s)}{Z_0} ds, \tag{2.57}$$

where Z_{LSC} is now considered as a function of s throughout the accelerator. The LSC field is strongest at low energies, since the impedance is inversely proportional to the energy of the bunch cubed. As the beam energy increases beyond a few tens of MeV, the effect of LSC becomes significant only at short wavelengths, typically on the order of a small fraction of the bunch length.

2.3.3 CSR Model

As described above in Sec. 2.2, CSR emitted by a short bunch in a magnetic compressor can interact with the bunch itself, causing an increase in both the projected emittance and correlated energy spread. In the case of a bunch with density perturbations in the longitudinal phase space, CSR can also be emitted at the wavelength of the density modulations in the bunch, inducing a modulation in energy. The linear dispersion R_{56} of the bunch compressor – which relates the path length of a particle over a beamline section to the energy of the particle (see Sec. 2.1.4) – can then convert these energy modulations into density modulations, thereby enhancing the microbunching in longitudinal density.

Omitting the shielding effect from the conducting walls of the beam pipe, the steady-state wake produced by an ultrarelativistic particle travelling through a

bending magnet (with bending radius R) has the following form [55, 69, 70]:

$$W(s) = \frac{2}{(3R(s)^2)^{1/3}} \frac{1}{s^{1/3}}. \tag{2.58}$$

This equation is valid in the regime $s > 0$ (with s the relative longitudinal position within the bunch), as the CSR wake always propagates in front of the particle. The CSR impedance can then be calculated as the Fourier transform of this wake:

$$Z_{CSR}(k,s) = \int_0^\infty W(s-s') \exp\left(-iks'\right) ds' = -\frac{ik^{1/3}A}{R(s)^{2/3}}, \tag{2.59}$$

where $A = 3^{-1/3}\Gamma\left(\frac{2}{3}\right)\left(\sqrt{3}i - 1\right) \approx 1.63i - 0.94$, and Γ is the Gamma function. These expressions are valid under the assumption that the retardation time for the coherent radiation is small compared to the length of the magnet, and considering only steady-state CSR (meaning that transient effects due to the entrance and exit fields of the dipole are neglected). In a bunch compression chicane, the longitudinal density modulation is no longer fixed, as the longitudinal motion in a dipole is coupled to the horizontal motion, and the modulation wavelength reduces with the bunch length. The final bunching factor $b_f(k(s), s)$ can be evaluated as a function of the initial bunching factor at position s_0 at the compressor entrance $b_0(k(s_0), s_0)$, and the bunch compressor transfer matrix parameters R_{51}, R_{52} and R_{56} [22]:

$$b_f(k(s), s) = b_0(k(0), s_0) + \int_0^s K(\tau, s) b(k(\tau), \tau)\, d\tau, \tag{2.60}$$

with the kernel $K(\tau, s)$ defined as:

$$K(\tau,s) = ik(s)R_{56}\frac{I(\tau)Z_{CSR}(k(\tau),\tau)}{\gamma I_A} \exp\left[\left(-\frac{k(s_0)U^2(s,\tau)\sigma_\delta^2}{2}\right)\right.$$
$$\left.\times\left(-\frac{k(s_0)\epsilon_0\beta_0}{2}\left(V(s,\tau) - \frac{\alpha_0}{\beta_0}W(s,\tau)\right)^2 - \frac{k(s_0)\epsilon_0}{2\beta_0}W^2(s,\tau)\right)\right], \tag{2.61}$$

for a bunch with initial emittance ϵ_0, energy spread σ_δ, α_0 and β_0 the initial Twiss parameters, and the parameters U, V, W for a compression factor $C(s)$

defined as follows:

$$U(s,\tau) = C(s)R_{56}(s) - C(\tau)R_{56}(\tau), \tag{2.62a}$$

$$V(s,\tau) = C(s)R_{51}(s) - C(\tau)R_{51}(\tau), \tag{2.62b}$$

$$W(s,\tau) = C(s)R_{52}(s) - C(\tau)R_{52}(\tau). \tag{2.62c}$$

Given the bunch compressor configuration, the equation 2.60 can be solved iteratively to calculate the microbunching gain.

2.3.4 Intrabeam Scattering

Coulomb scattering between particles can occur when a bunch travels through an accelerator, causing a redistribution of momentum among the particles [71, 72, 73], which results in an increase in the uncorrelated energy spread of the bunch σ_δ. This effect, known as intrabeam scattering, or IBS, can place limits on the luminosity lifetime and beam emittance of a circular accelerator, or 'storage ring', in particular those with low emittance. IBS has been studied primarily in storage rings, since the effect requires a long time to develop, meaning that the momentum spread induced by IBS is not generally expected to be observable in a linear FEL [74, 75]. However, the push towards more intense pulses of light produced by FELs, which requires a higher charge density, has now led to a study of experimental evidence for IBS in a linear FEL [64].

The growth rate of σ_δ can be calculated for a round beam with $\epsilon_x = \epsilon_y$, $\sigma_x = \sigma_y$ and $\sigma_{x'} = \sigma_{y'}$ using the approximation of Ref. [76]. This growth rate as a function of longitudinal position s is given as [76]:

$$\frac{1}{\sigma_\delta}\frac{d\sigma_\delta}{ds} = \frac{r_e^2 N_e\,[log]}{8\gamma^2\epsilon_n\sigma_x\sigma_z\sigma_\delta^2} = \frac{A}{\sigma_\delta^2}, \tag{2.63}$$

with N_e the number of electrons in the bunch, σ_z the longitudinal bunch length, γ the bunch Lorentz factor, and ϵ_n the normalised transverse emittance. The so-called 'log' factor $[log]$ is defined in terms of the maximum and minimum impact parameters of IBS scattering events (b_{max} and b_{min} respectively) [73, 77], and is

given as:

$$[log] = \ln\left(\frac{b_{max}}{b_{min}}\right) \approx \ln\left[\frac{\gamma^2 \sigma_y \epsilon_x}{r_e \beta_x}\right], \tag{2.64}$$

with β_x the horizontal beta function. As discussed in Ref. [64], there is some ambiguity in the literature regarding the choice of b_{max}, which then leads to uncertainty in the log factor. b_{max} is influenced by the particle density and beam size, and so calculations of the IBS effect must be evaluated appropriately with regard to these beam parameters. It should also be borne in mind that there is some uncertainty in the IBS effect on the beam as a result of this uncertainty.

In dispersive sections of the beam line, the growth rate must be modified [76]:

$$\frac{1}{\sigma_\delta}\frac{d\sigma_\delta}{ds} = \frac{r_e^2 N_e \,[log]\, \sigma_H}{8\gamma^2 \epsilon_n \sigma_x \sigma_z \sigma_\delta^3} = \frac{B}{\sigma_\delta^3}. \tag{2.65}$$

The horizontal and vertical dispersion H-functions H_x and H_y are used to define σ_H:

$$\frac{1}{\sigma_H} = \frac{1}{\sigma_\delta} + \frac{H_x}{\epsilon_x} + \frac{H_y}{\epsilon_y}. \tag{2.66}$$

The equations for the growth rate given above assume that the transverse position and angular co-ordinates follow a Gaussian distribution. This assumption generally holds for storage rings in equilibrium. However, this may not be the case for ultra-relativistic electron beams generated in photo-injectors and successively accelerated in linacs, and the feasibility of using this model may depend on how closely the transverse beam parameters follow a Gaussian distribution [78]. The charge distribution can be optically matched to predetermined Twiss parameters using dedicated and consecutive diagnostic regions located along the linac, as is done at FERMI [79]. This guarantees that matching is preserved all along the accelerator. The matching process itself is based on a model that relates the second order moments of the measured charge distribution in the transverse phase space (x, x') to the standard deviations (σ_x, $\sigma_{x'}$) of a two-dimensional Gaussian distribution [80].

The exact derivation for the IBS-induced uncorrelated energy spread growth rate $\frac{d\sigma_\delta}{ds}$ along the beamline will not be given here; see Ref. [64] for more details.

Given a known set of beam parameters, from simulation and/or experimental measurements, this parameter can be calculated iteratively along the beamline to solve for the increase in energy spread due to IBS. This effect is relevant to the microbunching instability in that it modifies the microbunching in energy that occurs due to LSC and CSR (see Secs. 2.3.2 and 2.3.3), causing a damping of the instability.

2.3.5 Spectral Gain

This section will provide an explanation for the amplification of microbunches as a result of the collective effects discussed above, and will show the impact that this amplification has on the energy spread of the bunch as a whole.

The amplification (or 'gain', G) of modulations in a bunch due to CSR and LSC can be quantified as the ratio between the final and initial bunching factors (b_f and b_0 respectively) as a function of wavenumber k:

$$G(k) = \frac{b_f(k)}{b_0(k)}. \tag{2.67}$$

In the case of modulations that are much shorter than the electron bunch length, and for modulation amplitudes that are much smaller than the average current – in the 'linear regime' of the instability – there is no mixing of modulation amplitudes of different wavenumber.

For a beam with an initial density modulation $b_0(k_0)$ which then induces an energy modulation given by $\Delta\gamma_i$, the longitudinal distribution function at the longitudinal position z_0 is given by:

$$\mathbf{X}(z_0, \delta) = \mathbf{X_0}(z_0, \delta - hz_0\delta_m(z_0)), \tag{2.68}$$

where $\delta = \Delta\gamma/\gamma$, $\delta_m = \Delta\gamma_i/\gamma$ are the relative energy and energy modulation parameters, respectively, and h is the linear energy chirp. After the bunch travels through the bunch compressor with a momentum compaction factor R_{56}, the longitudinal position of an electron with a relative energy deviation δ becomes:

$$z = z_0 + R_{56}\delta = z_0 + R_{56}\left(\delta_0 + hz_0 + \delta_m(z_0)\right). \tag{2.69}$$

The bunch compression process then results in a modulated bunching factor at the compressed wavenumber k_f at the exit of the bunch compressor:

$$\begin{aligned} b_f(k_f) &= \int dz\, d\delta \exp\left[-ik_f z\right] \mathbf{X}(z,\delta) \\ &= \int dz d\delta_0 \exp\left[-ik_f \left(z_0 + R_{56}\left(\delta_0 + hz_0 + \delta_m(z_0)\right)\right)\right] \mathbf{X_0}(z_0,\delta_0). \end{aligned} \quad (2.70)$$

In the limit of a small initial induced energy modulation ($|k_f R_{56}\delta_m| \ll 1$), then a first-order approximation for $b_f(k_f)$ is given by:

$$b_f(k_f) = \left[b_0(k_0) - ik_f R_{56}\delta_m(k_0)\right] \int d\delta_0 V(\delta_0) \exp\left(-ik_f R_{56}\delta_0\right), \quad (2.71)$$

where $k_f = k_0 C$ and $V(\delta_0)$ is the initial beam energy distribution. In the high-gain limit, where $b_f \gg b_0$, and inserting Eq. 2.57, the microbunching gain for an arbitrary energy distribution is given by:

$$G = \left|\frac{b_f}{b_0}\right| \approx \frac{I_0}{\gamma I_A} \left| k_f R_{56} \int_0^L ds \frac{4\pi Z_{LSC}(k_0, s)}{Z_0} \right| \int d\delta_0 V(\delta_0) \exp\left(-ik_f R_{56}\delta_0\right). \quad (2.72)$$

For a Gaussian energy distribution with an RMS relative energy spread of σ_δ, the gain can be approximated further as:

$$G \approx \frac{I_0}{\gamma I_A} \left| k_f R_{56} \int_0^L ds \frac{4\pi Z_{LSC}(k_0, s)}{Z_0} \right| \exp\left[-\frac{1}{2}\left(k_f R_{56}\sigma_\delta\right)^2\right]. \quad (2.73)$$

As a result of a small uncorrelated energy spread, particles within the same longitudinal slice of the bunch travel along different path lengths. The longitudinal slippage that occurs in the bunch compressor slightly suppresses the microbunching gain. Since this motion occurs because of uncorrelated energy differences, this process is known as energy damping, or longitudinal Landau damping, and it causes energy and density modulations to 'smear' at short wavelengths. Coupled with the IBS effect mentioned above (see Sec. 2.3.4), the gain

factor G can be calculated iteratively as a function of beam and lattice parameters.

If $Z_{LSC}(k, s)$ is approximately constant in amplitude over a wide range of wavenumbers – which is generally true, since LSC is a broadband impedance – then the LSC gain peaks at the wavelength $Ck_0R_{56}\sigma_\delta$, where C is the compression factor. There is also a natural cutoff of the microbunching gain in the limit $Ck_0R_{56}\sigma_\delta > 1$, since the gain is exponentially suppressed at short wavelengths due to the uncorrelated energy spread.

The expression Eq. 2.73 is independent of the initial modulation amplitude, and is valid in the 'high-gain' approximation. In this case, the final bunching factor is dominated by the transformation between energy and density that occurs during the bunch compression process.

The LSC-induced energy modulation amplitude is defined as:

$$|\Delta\gamma(\lambda)|^2 = |G(\lambda)b_0(\lambda)Z_{LSC}(\lambda)|^2. \tag{2.74}$$

In order to estimate the total rms energy spread induced by LSC, $\Delta\gamma(\lambda)$ must be integrated across the entire accelerator lattice, over a range of modulation wavelengths λ. Using Eq. 2.56, this value is found to be:

$$\sigma_\gamma^2 = \int |\Delta\gamma(\lambda)|^2 d\lambda = \frac{2ec}{I_0} \int \frac{|G(\lambda)Z_{LSC}(\lambda)|^2}{\lambda^2} d\lambda. \tag{2.75}$$

By choosing a suitable range of modulation wavelengths, the value of σ_γ can be computed using numerical methods, with the spectral gain and LSC impedance calculated from the accelerator lattice parameters and calculated beam properties. Since the drivers for short-wavelength FELs are typically based on long, straight accelerating sections, the microbunching gain due to LSC is often more significant than that due to CSR or other impedances. Nevertheless, the effect of magnetic bunch compression on the microbunching structure in the beam can be twofold. First, there is some amplification of structures in the bunch as a result of CSR impedance, which modulates the energy of particles inside the dipole magnets. Second, the dispersion function couples the energy of a particle to its longitudinal motion, and therefore translates a variation in energy into a

variation in density.

2.3.6 Analytic Model of a Microbunched Beam

The Fourier representation of a simple analytic model of an electron beam with density modulations in the longitudinal phase space can be useful for understanding the microbunching features observed in a real beam. This model uses a 2D Gaussian phase space, modulated by a sinusoidal density variation. In our analytic model, four parameters can be varied independently to recreate phase space distributions similar to those in a real image:

- Modulation frequency ω.
- Linear energy chirp of the bunch h.
- Skew of the microbunches with respect to the bulk rotation θ.
- Intensity profile of the microbunches, represented by the bunching factor b.

For a chirp term h, a skew term θ, a modulation frequency ω, a bunching factor b, and defining the following quantities:

$$x_n(x, y, \theta) = x\cos(2\pi\theta) + y\sin(2\pi\theta), \tag{2.76a}$$

$$y_n(x, y, \phi) = -x\sin(2\pi\phi) + y\cos(2\pi\phi), \tag{2.76b}$$

we arrive at the following definition of a sinusoidally modulated two-dimensional Gaussian function for a bunch with size σ_x and σ_y in the horizontal and vertical planes, respectively:

$$\mathbf{X}(x, y, \theta, \phi, \sigma_x, \sigma_y, b, \omega) = \exp\left[-\left(\frac{x_n(x, y, \theta)^2}{2\sigma_x^2} + \frac{y_n(x, y, \phi)^2}{2\sigma_y^2}\right)\right] \times \left(1 + b\cos[2\pi\omega x_n(x, y, \theta)]^2\right). \tag{2.77}$$

This function represents a simple model of the longitudinal phase space of an electron bunch with density modulations. The top rows of plots below (Figs. 2.8 –

2.11) show longitudinal phase spaces evaluted using Eq. 2.77, with each parameter being varied independently of the others. The associated Fourier transform of each simulated longitudinal phase space is shown in the bottom rows of Figs 2.8 – 2.11. The bunch compression schemes used in the microbunching experiments detailed below (see Chapter 5) resulted in longitudinal phase spaces with different microbunching parameters, and this model can help in understanding the Fourier representation of these bunches.

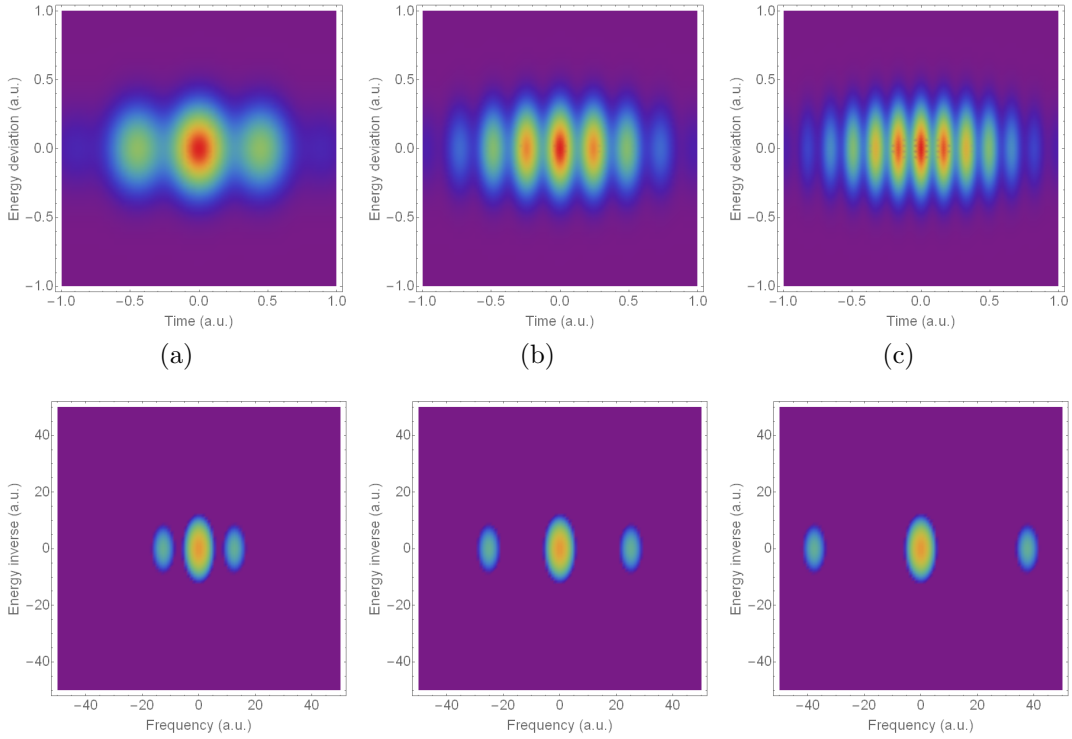

Figure 2.8: Variation of modulation frequency ω. The phase space is in the row above, and the Fourier transforms are in the row below. From left to right, $\omega = 1, 2, 3$.

It can be seen from the bottom rows of these four sets of plots (Figs. 2.8 – 2.11) that it is possible to characterise different properties of the bunch using the Fourier transform of the phase space density. In every image, the DC term is given by a bright spot in the centre of the Fourier space. This would be present even in the Fourier transform of a purely random distribution of pixels. The microbunching structure is evident in the sidebands visible in the Fourier spectrum.

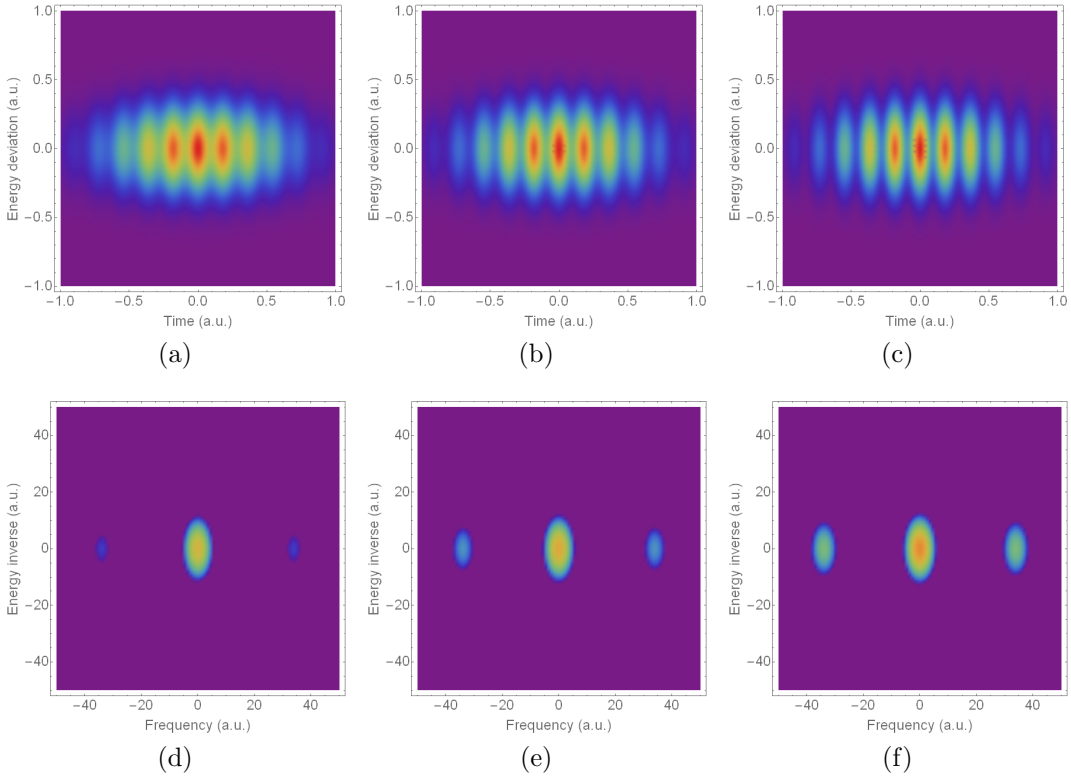

Figure 2.9: Variation of the bunching factor b. The phase space is in the row above, and the Fourier transforms are in the row below. From left to right, $b = 0.5, 1.0, 2.0$.

As seen in Fig. 2.8, as the modulation frequency ω increases, there are a greater number of microbunches present along the bunch in real space, and in the Fourier representation, the sidebands become increasingly separated from the central spot. Increasing the modulation amplitude (which is analogous to the bunching factor) causes the microbunches to become more distinct from one another, as shown in Fig. 2.9. In Fourier space, the sidebands become more intense. A bulk rotation of the bunch (corresponding to a linear energy chirp h), without changing the 'skew' term θ which controls the orientation of the microbunches, as in Fig. 2.10, causes the sidebands in the Fourier transform to rotate. If the microbunches themselves are rotated while the chirp term h is kept constant, as in Fig. 2.11, the Fourier sidebands themselves move around the DC term while their orientation remains constant.

This simple model has demonstrated that the Fourier representation of the phase space of an electron bunch should be able to reveal the properties of the

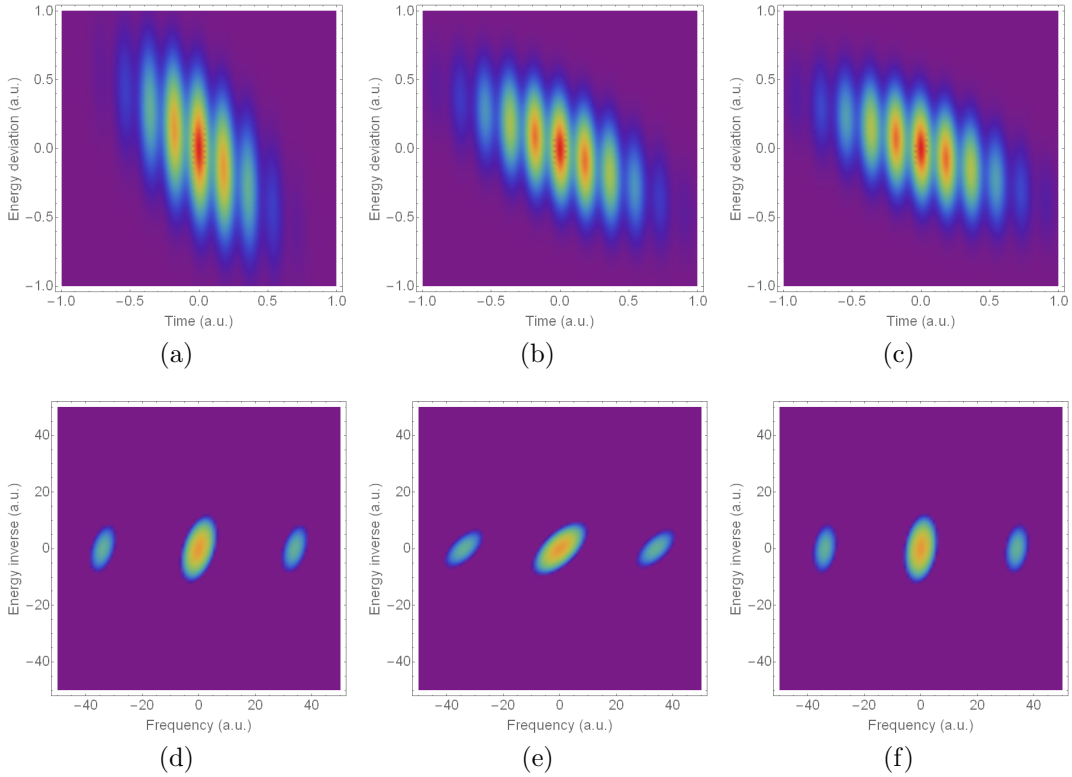

Figure 2.10: Variation of the chirp term h. The phase space is in the row above, and the Fourier transforms are in the row below. From left to right, $h = \pi/3, \pi/4, \pi/6$.

microbunching structure, allowing for a comparison with simulations and theory.

The results presented in this section demonstrate the effect that CSR, LSC and IBS can have on the longitudinal phase space of an electron beam in a linear accelerator. In Chapter 5, results from simulations and experiments will show the impact of these forces on electron bunches in the FERMI linac. In this machine, the main parameters that can be measured are the bunching factor and modulation period, and these parameters can be extracted by studing the Fourier transform of the longitudinal phase space. Various bunch compression schemes are used in order to investigate the impact of different beam parameters on these parameters, with the goal of understanding the development of the theory outlined above.

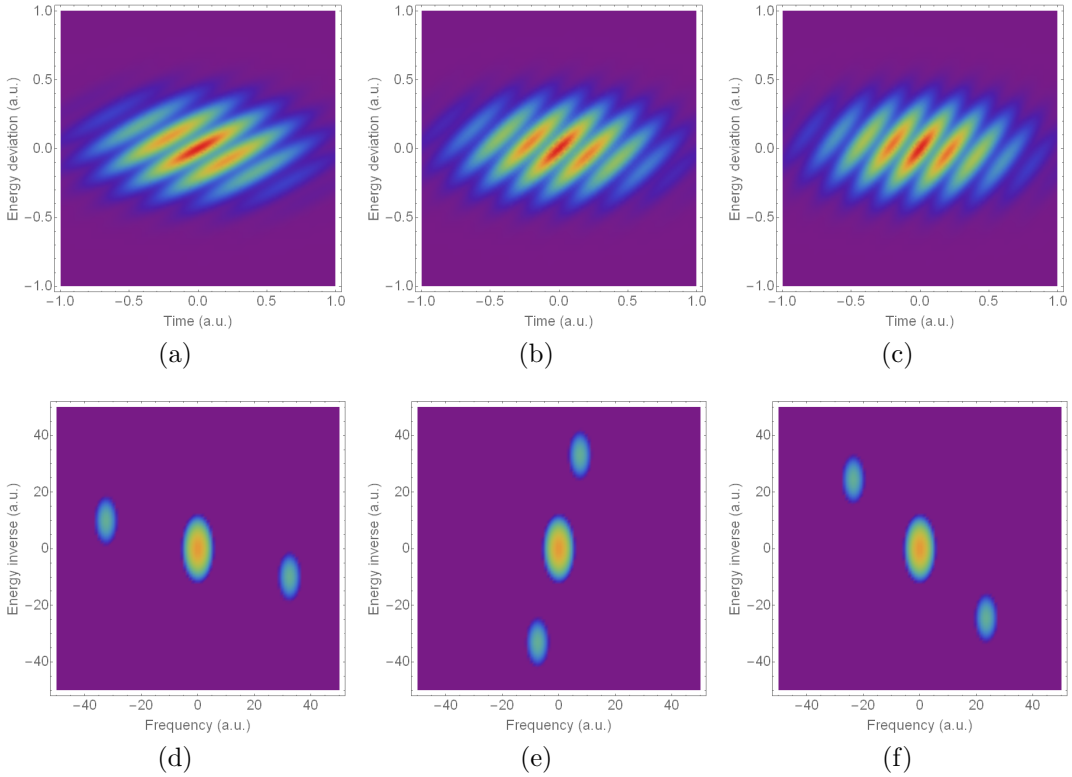

Figure 2.11: Variation of the microbunch rotation angle θ. The phase space is in the row above, and the Fourier transforms are in the row below. From left to right, $\theta = \pi/3, \pi/4, \pi/5$.

2.4 Mitigation and Generation of Microbunching

Since the microbunching instability was first recognised to be an issue for short-wavelength FELs, a number of methods have been proposed to counteract its effects on the electron bunch. Most of these techniques impose a small uncorrelated energy spread on the bunch, which prevents amplification of the modulations from taking place. The simplest, and most widely used, method for mitigating the microbunching instability is the laser heater (Sec. 2.4.1); although other potential methods have been formulated (Sec. 2.4.2), they are not routinely implemented at FEL facilities. In this section, these techniques will be reviewed in terms of their feasibility and usefulness. A discussion will follow on a method for imposing modulations on a relatively low-energy bunch through the use of a modulated laser pulse in the laser heater, thereby seeding the microbunching

instability (Sec. 2.4.3). In addition to providing the opportunity to study microbunching in detail, this technique also could lead to future applications of high-brightness electron bunches, for example in the generation of multi-colour FEL light, or for drive-witness plasma-based acceleration.

2.4.1 Laser Heater

The standard method for counteracting the gain in microbunching is the laser heater: LCLS [27], SwissFEL [30], PAL-XFEL [29], EU-XFEL [81] and FERMI [28] all have laser heaters installed. However, as this scheme irreversibly increases the slice energy spread of the bunch, this can cause issues, particularly for seeded FEL schemes that are more sensitive to this parameter.

The basic elements of the system comprise a laser, an undulator and a magnetic chicane. The undulator period and gap are set to provide the conditions for a resonant interaction between the laser and the electron beam which 'heats the beam', i.e. increases the uncorrelated energy spread, by imposing an energy spread modulation. The chicane provides a physical offset allowing the laser to be introduced along the electron trajectory. Upon leaving the second half of the laser heater chicane, any longitudinal structure in the beam is suppressed because of the variation in path length with the energy of individual particles. The interaction between the laser and the electron beam in the laser heater undulator is optimal when the electron and laser radial rms sizes are similar.

The energy spread imposed on an electron bunch in a laser heater can be calculated in the following way [26]: consider a Gaussian mode laser with rms spot size σ_r wavelength λ_L which satisfies the resonant condition for an electron bunch with relativistic factor γ_0 travelling through an undulator with period λ_u and undulator parameter K. For a laser pulse with peak power P_L, and neglecting variations in the laser and electron beam sizes during their interaction in the laser heater undulator, the amplitude of the energy modulation of an electron at radial position r is given by [26, 82]:

$$\Delta\gamma_L(r) = \sqrt{\frac{P_L}{P_0}}\frac{KL_u}{\gamma_0\sigma_r}\left[J_0\left(\frac{K^2}{4+2K^2}\right) - J_1\left(\frac{K^2}{4+2K^2}\right)\right]\exp\left(-\frac{r^2}{4\sigma_r^2}\right), \quad (2.78)$$

with $P_0 = I_A mc^2/e \approx 8.7\,\mathrm{GW}$, I_A the Alfvén current and $J_{0,1}$ are Bessel functions of the first kind.

Indirect methods of observing the damping of microbunching are informative when commissioning a laser heater system. Monitoring the FEL performance is a useful metric, and it demonstrates the importance of this device for these machines. The FEL gain length at LCLS was observed to increase by a factor of around 2.5 with an additional 100 keV energy spread added to the electron beam by the laser heater, and the FEL pulse energy could be doubled with an appropriate laser pulse energy [27]. Similar increases in FEL power across all lasing wavelengths were recorded at FERMI [28], along with an improvement in the stability, spectrum and bandwidth of the FEL pulses.

Accelerator facilities which have incorporated a laser heater system have also observed a suppression of the microbunching instability, using both direct and indirect diagnostic methods. Coherent optical transition radiation, or COTR, can cause issues when attempting to image a microbunched electron beam. Both the LCLS [23] and APS [83] have observed large increases in coherent OTR after bunch compression, making the imaging of bunches more difficult. One explanation for these strong signals at optical wavelengths is the gain in microbunching due to bunch compression. By careful tuning of the laser heater, a small energy spread imposed on the beam before compression can reduce COTR by an order of magnitude [27, 28].

2.4.2 Alternative Methods for Suppressing the Microbunching Instability

The standard laser heater system described above irreversibly increases the slice energy spread of the bunch. This can cause issues, particularly for seeded FEL schemes. Various alternatives to the laser heater have been proposed for suppressing microbunching gain in FELs. Some of these schemes have been implemented in experiments, and some have been studied only in theory and simulation. This section will provide an outline of some of these alternatives to the laser heater.

2.4.2.1 Reversible Beam Heating using TDCs

The slice energy spread requirements for a seeded FEL are more stringent than those for self-amplified spontaneous emission (SASE), and so the irreversible heating provided by a laser heater could have a detrimental effect on the FEL performance. For example, in a high-harmonic gain FEL, the energy modulation generated in the modulators must be greater than the RMS energy spread of the bunch (see, e.g., [84]), and this can become more difficult to achieve as the energy spread increases. A scheme was proposed to increase temporarily the energy spread of the electron bunch using a transverse deflecting cavity (TDC) [85] before compression with a magnetic chicane, and subsequently to remove the energy spread in a downstream TDC as a way of suppressing the microbunching instability [86].

Many accelerator facilities use an RF field with an electric component orthogonal to the direction of motion to impose a time-dependent transverse force on an electron bunch for longitudinal phase space investigations [24, 87]. This results in the temporal profile of the bunch being transformed into a transverse profile downstream. An electron in a bunch travelling through a TDC near the zero-crossing phase – that is, the point at which the sign of the electric field changes – will experience a transverse kick. The magnitude of this kick is dependent on the position of the electron within the bunch, relative to the TDC phase. Additionally, particles in the bunch will experience a change in energy based on the strength of the field in the cavity, and their position relative to the zero-crossing phase, resulting in an increase in the total energy spread. This increase, along with the compression factor in a magnetic chicane, can remove small-scale structure in the bunch. This process is reversible as the induced energy spread is uncorrelated only in the longitudinal plane, and not in the plane which experiences the transverse kick.

A TDC imposes a spatial chirp on the electron bunch, which must be removed with the second cavity. This can be achieved with careful tuning of the strength of the deflecting fields, and the betatron phase advance in the kick plane, such that the phase advance between them is an integer multiple of π. In addition, the energy spread increase imposed by the first TDC must be cancelled by the

second. As the energy spread increase depends on the mean bunch offset in the kick plane (see [86]), the offset in the second cavity can be tuned such that the overall energy spread increase due to both TDCs is zero. One potential downside of this scheme, however, is that couplings in the $y'-\delta_0$ and $y-z_0$ planes, where the y plane is that in which the transverse kick is imposed, cause a slight increase in the emittance in these planes. Simulations have shown that this scheme is almost reversible, with an overall increase in slice energy spread for a 350 MeV beam on the scale of a few keV, even when taking CSR into account. An increase in projected emittance can occur, but the slice emittance, which is of greater significance for an FEL, was mostly preserved. This removable, effective energy spread increase, which has been confirmed in simulation, also serves to mitigate the microbunching gain which would be experienced in the bunch compressor.

2.4.2.2 Reversible Beam Heating using Magnets

An alternative scheme has been proposed which could achieve a similar reversible energy spread increase without including additional TDCs into the accelerator lattice, using a combination of dipole and quadrupole magnets, and an appropriate energy chirp [88, 89]. This method is attractive as it provides a cheaper solution to that proposed in [86], without the stringent requirements on TDC tuning and timing.

The transport of a beam with an energy chirp h passing through a thin bending magnet with angle θ can be determined by combining the transfer matrices: $R_b(\theta).R_c(h)$, where $R_b(\theta)$, $R_c(h)$ are the transformations for the thin bending magnet and the acceleration that generated the energy chirp, respectively. After passing through the magnet, the longitudinal position of an electron in the bunch with horizontal position x is shifted by $-\theta x$. A magnet of opposite polarity after the bunch compressor can then reverse this shift. With the additional inclusion of a quadrupole magnet after the second bending magnet, the transfer matrix for a TDC can be replicated, thus creating the same effect described in Sec. 2.4.2.1. An undesirable corollary of this configuration is that it requires the beamline to be rotated after the dipoles, and so the kicks induced by the bends must be carefully tuned.

2.4.2.3 Electron-Magnetic Phase Mixing

For an accelerator lattice with multiple bunch compressors, with correctly tuned momentum compaction factors, it is possible to manipulate the longitudinal phase space of an electron bunch to control the bunching factor which drives the microbunching instability [25]. It has been shown [22] that, for a beam with an initial uncorrelated energy spread σ_γ, the change in the bunching factor after a compression chicane can be expressed as follows:

$$b_1(k_1) = \left(b_0(k_0) - ik_1 R_{56} \frac{\Delta\gamma(k_0)}{\gamma} \right) \exp\left[-\frac{1}{2} \left(k_1 R_{56} \frac{\sigma_\gamma}{\gamma} \right)^2 \right], \tag{2.79}$$

where R_{56} is the usual overall transfer matrix element for the chicane. In order to compress a bunch, the overall R_{56} parameter must be negative – however, the two-chicane scheme outlined in Ref. [25] shows that a second chicane with a positive R_{56}, and a sufficiently large uncorrelated energy spread, can contribute to the suppression of the increase in bunching factor. The overall compression of this scheme can be maintained provided that the momentum compaction in the first bunch compressor is increased to compensate for the positive R_{56} in the second chicane.

Bunch compression in a magnetic chicane requires a beam with a positive energy chirp, meaning that electrons at the head of the bunch have comparatively less energy than those at the tail of the bunch, and so the length of their trajectory through the chicane is greater, causing a reduction in the overall bunch length. This can be thought of as a 'rotation' in the longitudinal phase space of the bunch. After passing through the first bunch compressor, the bunch will contain spikes of current in its longitudinal profile, due to the gain in microbunching. If the energy chirp is removed by, for example, correctly tuning the accelerating cavities between the chicanes, this rotation in longitudinal phase space, coupled with the positive R_{56} in the second chicane, causes the current spikes to be removed. Experimental studies have shown [90] that this scheme can reduce the intensity on a downstream OTR screen by a two orders of magnitude, and analytical models for the microbunching gain show a reduction of three orders of

magnitude. One of the issues with this machine configuration, however, is that the CSR emitted in the second chicane, due to a very short bunch length, can cause an increase in the slice energy spread of the bunch.

2.4.2.4 Transverse Gradient Undulators

Transverse gradient undulators (TGUs) can provide a coupling between the transverse and longitudinal phase space of a beam. The path length of an electron travelling through a TGU is dependent on its transverse position at the entrance to the undulator, meaning that the effective undulator strength imposed on an electron will vary with its position. The R_{51} and R_{26} elements in the TGU transfer matrix (to first order) have the same value, but opposite sign. This causes a coupling in the transverse-longitudinal plane. For a bunch with a linear energy chirp, the path length of an electron in the TGU is dependent on x, x' and δ.

Simulations of a Gaussian bunch with a longitudinal energy chirp passing through a TGU show that a horizontally correlated energy spread is converted into a longitudinally uncorrelated energy spread, increasing the bunch slice energy spread [91]. This effect helps to reduce the overall gain in microbunching which a bunch experiences in a compression chicane. In addition to this, the coupling in the horizontal and longitudinal planes helps to reduce the bunching factor, thus further suppressing the microbunching gain.

A potential downside of this scheme, with a TGU before the bunch compressor, is that the horizontal emittance growth is considerable, and a second TGU is required to recover the emittance after the chicane. In order to prevent this growth, a small energy spread is required, and the bunch must not have an energy chirp upon entering the TGU. This means that the TGU must be placed upstream of the linac which then feeds into the chicane. As with some of the other alternative schemes outlined above, this method does not increase the slice energy spread of the bunch. An emittance growth of around 9 % has been observed in simulations [91], but this was with ideal conditions, such as a minimal energy spread.

2.4.3 Chirped-Pulse Beating as a Technique for Imposing Modulations on an Electron Beam

Laser heater systems have proven to be crucial in improving the performance of x-ray FELs [27, 28, 29]. Recent results have also shown that, through modulating the temporal profile of the laser pulse used in the laser heater, it is possible to achieve a greater degree of control over the longitudinal profile of the electron bunch, opening the possibility of novel applications in the production of multi-colour FEL beams, or the production of THz radiation via a bunch with induced microbunching [92]. This technique is similar to the echo-enabled harmonic generation scheme [93], which is used to generate high harmonics of the fundamental wavelength in an FEL undulator. This technique can achieve similar results in a shorter space, as it does not require multiple modulators before the FEL radiator section.

A schematic of the laser heater system designed for the CLARA FEL test facility [94] is shown in Fig. 2.12, and the laser heater system parameters are given in Table 2.1; further details can be found in [95]. Simulations have shown that the microbunching instability is not expected to have a large impact on the nominal CLARA modes of operation. However, it would still be useful to install a laser heater in order to investigate potential methods of utilising the laser heater in novel configurations in order to achieve flexible control of the electron bunch properties. Current profiles and longitudinal distributions up to the exit of the CLARA accelerating section, at 240 MeV, have been simulated using the `elegant` code [96] (with CSR and longitudinal space charge included). These current profiles for the nominal laser heater operating mode, and with the laser heater off are shown in Fig. 2.13. In the nominal laser heating operating mode, sufficient power will be available to damp any small-scale structure in the electron bunch. Simulations have shown that a small increase in the RMS energy spread of 25 keV, or 0.1 % of the final beam energy, should be sufficient to suppress any microbunching without greatly degrading the quality of the FEL – for this nominal operating mode of the laser heater, a pulse energy of around 48 µJ is required.

There are various ways of using modified laser pulses to modulate the longi-

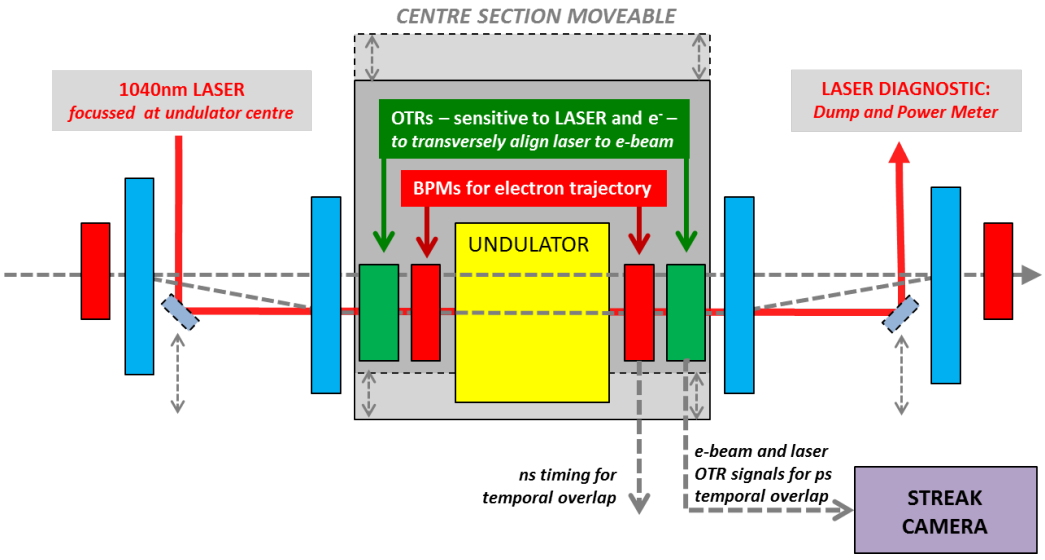

Figure 2.12: Schematic of the CLARA laser heater system. Dipoles are shown in blue.

tudinal profile of an electron bunch. One method for achieving this is through chirped-pulse beating [97] of the laser heater pulse. The pulse is stretched in both the temporal and spectral domains (or chirped), then split in a Michelson interferometer, one arm of which has a variable length. The two laser pulses are recombined, and they overlap in the temporal domain. By varying the length of the interferometer arm, a delay between the two pulses can be created, giving rise to a laser pulse with a beat frequency that is directly related to the delay τ. The intensity profile of such a laser pulse is given by [33]:

$$I_{tot}(t,\tau) = {E_0}^2 \left(\frac{\Delta t_0}{\Delta t_1}\right) \left[e^{\left(-2\frac{2\ln 2}{\Delta t_1^2}(t+\tau/2)^2\right)} + e^{\left(-2\frac{2\ln 2}{\Delta t_1^2}(t-\tau/2)^2\right)} + \left(e^{\left(-2\frac{2\ln 2}{\Delta t_1^2}(t+\tau/2)^2\right)} \cos\left(\omega_0\tau + 2\frac{2\ln 2}{\Delta t_0 \Delta t_1} t\tau\right)\right)\right], \tag{2.80}$$

with E_0 the field strength of the initial pulse, Δt_0 the Gaussian half-width of the initial pulse, Δt_1 the stretched pulse half-width, and ω_0 the centre of the optical pulse spectrum.

For a frequency chirp rate of μ, the beat frequency of the modulated laser is given by $f(\tau,\mu) \approx \mu\tau/2\pi$ [97]. We can take the parameters for the CLARA photoinjector laser pulse stretcher as an example: the initial laser pulse, with

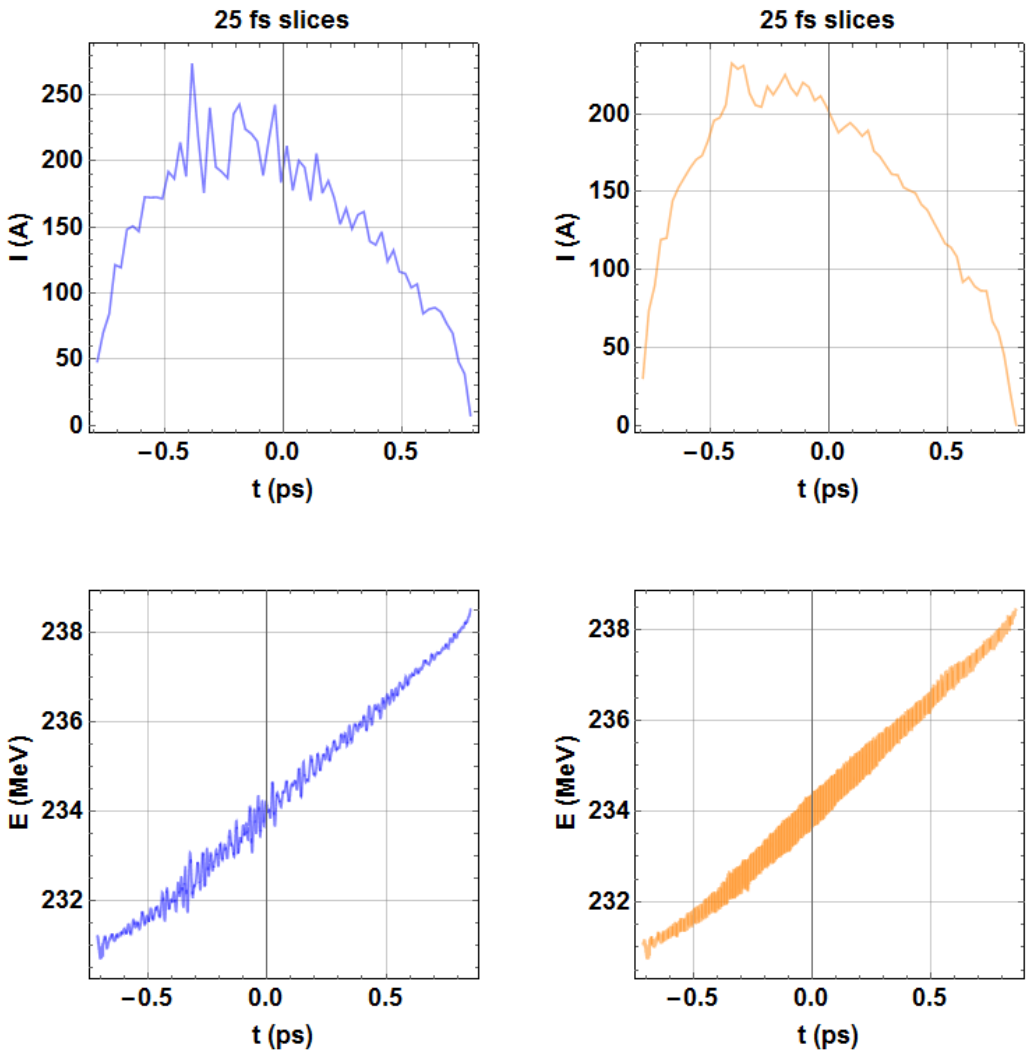

Figure 2.13: Current profiles and longitudinal phase space at full energy for: Left: laser heater off; Right: laser heater at nominal settings (25 keV added energy spread).

an rms duration of 76 fs will be stretched to a length of $1 - 8$ ps. The longer laser pulse should provide consistent overlap with the electron bunch, which has a FWHM duration of 4 ps in the laser heater section.

The interaction of such a modulated laser pulse with an electron bunch undergoing periodic motion can cause the bunch to develop longitudinal structure, thus inducing the microbunching instability. Taking the parameters for the CLARA laser heater and applying the chirped-pulse beating technique, we can obtain a range of longitudinal intensity profiles, as shown in Fig. 2.14. The flexibility of laser intensity modulations provided by this technique could lead to the generation of a range of customisable longitudinal electron beam profiles.

Table 2.1: Laser heater system parameters

BEAM TRANSPORT	
Chicane magnet length	10 cm
Chicane magnet bend angle	$0 - 5\,^{\circ}$
Beam energy	$100 - 200$ MeV
Normalised emittance	0.5 mm mrad
UNDULATOR	
Period	60 mm
Number of full periods	8
Total length including end terminations	585 mm
Minimum undulator gap	24 mm
Undulator parameter	$0.8 - 3.0$
Undulator field strength	$0.14 - 0.53$ T
LASER	
Wavelength	1040 nm
Spot size σ_{rad} at undulator centre	≤ 500 µm
Maximum pulse energy	80 µJ
Stretched pulse length (FWHM)	8 ps

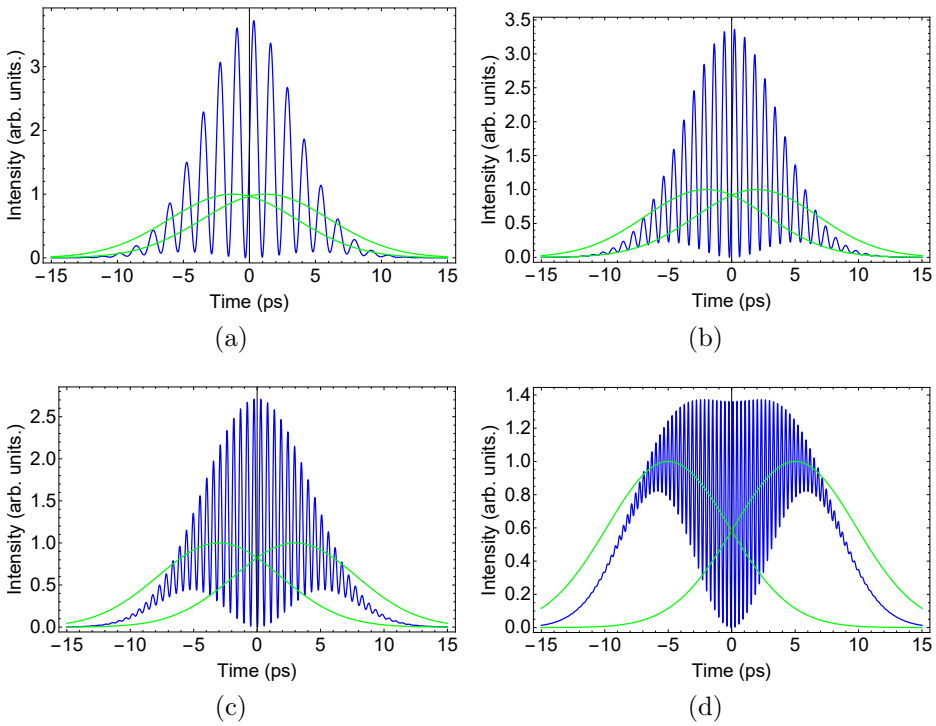

Figure 2.14: Calculated intensity profiles of modulated laser pulses for: Top left: 2.5 ps; top right: 4ps delay; bottom left: 6ps delay; bottom right: 10ps delay. These values of the delay in the laser heater interferometer correspond to modulated laser wavelengths of 383 µm, 240 µm, 160 µm and 96 µm, respectively.

2.4.3.1 Laser Heater Simulations

The interaction of a modulated laser pulse with the electron bunch in the CLARA laser heater chicane has been modelled using the `elegant` simulation code [96], which allows the user to implement custom laser fields in a laser-electron interaction (see Sec. 3.1.1 for more details on the code). Scans of a number of laser heater parameters have been performed in order to determine the optimal settings for inducing the largest density/energy variations in the bunch. After the laser heater interaction, which occurs at around 130 MeV, the bunch is shortened in a magnetic compression chicane and accelerated to its full energy of 240 MeV. As shown in [22] and Sec. 2.3.3, any perturbations in the bunch density or energy can be amplified in a bunch compressor, and so we should expect to observe a more pronounced microbunching effect after compression.

Parameter scans over modulation wavelength and bunch compressor angle have been performed in simulations in order to determine the effects of varying these parameters on the energy and longitudinal profile of the bunch. The laser intensity profiles shown in Fig. 2.14 correspond to modulation wavelengths of 383 µm, 240 µm, 160 µm and 96 µm. The bunch compressor angle was set to 104 mrad, 104.5 mrad and 105 mrad (the nominal setting for the short bunch operating mode), corresponding to compression factors of 16.3, 7.6, and 4.9, respectively. Current profiles for various bunch compression factors and modulation wavelengths are shown in Fig. 2.15.

It can be seen that, as the modulation wavelength decreases, the electrons become more tightly (micro-)bunched. As the compression factor increases, we see much larger peaks in the current profile as the bunch becomes maximally compressed. As the delay in the laser interferometer increases (thereby decreasing the modulation wavelength), the spikes in current are less discernible for the blue curve (which represents a larger compression factor) than for the others. In the upper row of plots in Fig. 2.15, all of the microbunches imposed on the bunch are preserved, whereas for the bottom row of plots, the microbunches overlap with each other in the longitudinal coordinate as the compression factor increases. This suggests that there is an optimal range of laser heater and bunch compression parameters that can be used for stimulating and propagating

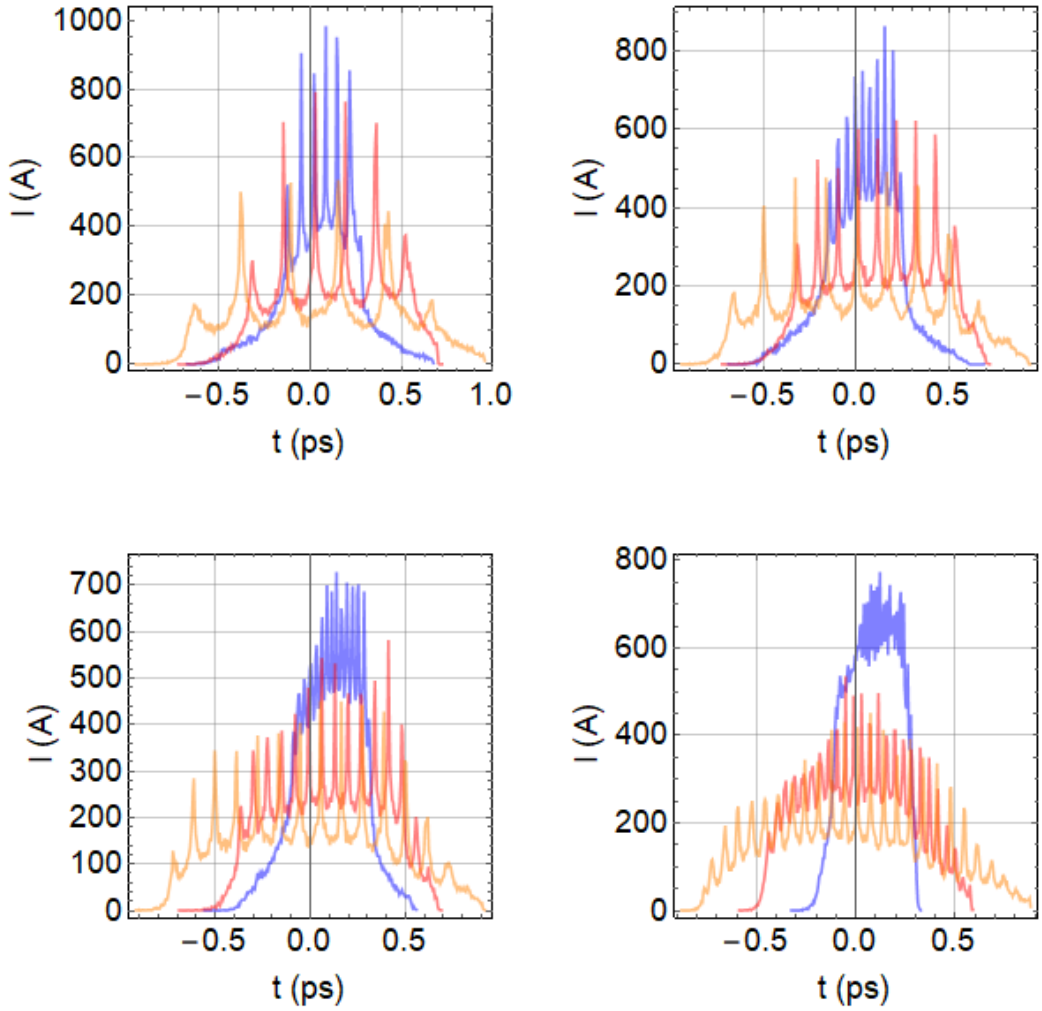

Figure 2.15: Current profiles for scans of bunch compression factor for the laser intensity profiles given in Fig. 2.14 (in the same order): Orange: 4.9; Red: 7.6; Blue: 16.3.

microbunches using this scheme.

In Fig. 2.16 we show the bunch longitudinal phase spaces only for the maximally compressed bunch at the modulation wavelengths given above. Here, it can clearly be seen that the number of microbunches present in the bunch increases as the modulation wavelength of the laser pulse decreases. These figures further illustrate the overlap of the microbunches along the longitudinal axis of the bunch, particularly at shorter modulation wavelengths. This effect will be discussed further in Sec. 5.5, where this technique is applied experimentally.

From these simulations we can see that, by varying the modulation wavelength of the laser heater, we can induce a variation in the current profile of the

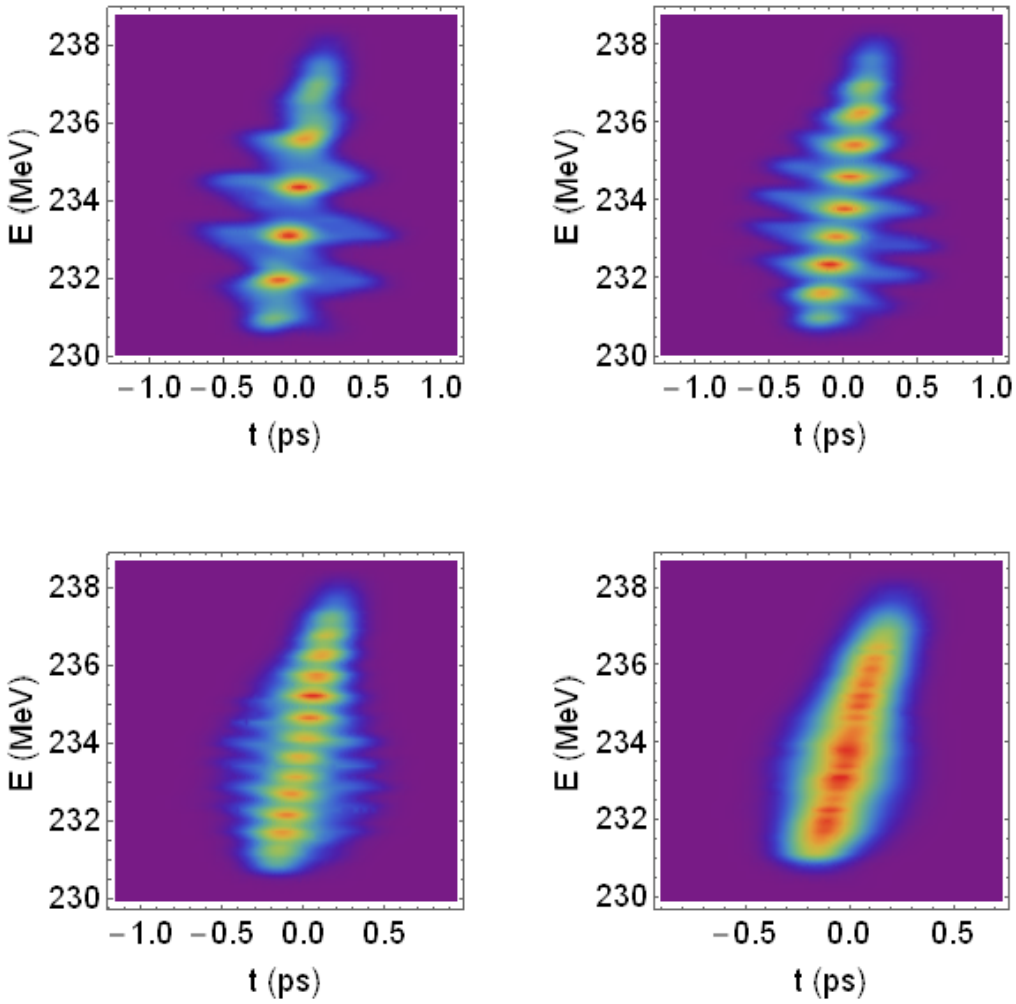

Figure 2.16: Energy profiles for the laser intensity profiles given in Fig. 2.14 near maximal bunch compression factor. The order of the figures is the same as that in Fig. 2.14.

electron bunch. The flexibility that the chirped-pulse beating technique affords in terms of the laser pulse beating frequency, in addition to the variable bunch compression factor, could increase the range of FEL pulse characteristics that CLARA can provide.

2.5 Summary

This chapter has reviewed some basic principles of accelerator physics and beam transport (Sec. 2.1). This review will be necessary in helping to understand the results from experiment and simulation presented in Chapters 4 and 5. The

two main collective effects which are investigated in this thesis, CSR and the microbunching instability, have been described theoretically in this chapter. The first of these effects – CSR – occurs when charged particles within a short bunch travel on a curved trajectory, emitting coherent radiation that can interact with other particles in the bunch and cause a change in energy. When CSR changes the energy of particles in a bunch while it is travelling through a magnetic bunch compressor, this can cause an increase in the beam emittance at the exit of the bunch compressor, which can have a negative effect on the beam quality at the entrance to an FEL undulator, for example.

The theory of CSR (Sec. 2.2) which is most widely used in the design and simulation of accelerators is based on 1D projection of the charge density of the bunch onto the longitudinal dimension. It has been shown to agree well with measurements in some cases, but the theory is expected to break down under certain conditions, such as a large bunch compression factor, or with an electron bunch with a large transverse dimension. These conditions are investigated experimentally in Chapter 4. In the current chapter, an extension to the 1D theory of CSR has been presented, which correctly takes account of the full Liénard-Wiechert field of emitting particles (Eq. 2.31). This field has both an electrostatic component and an accelerating component. It has been shown that, due to the transition regimes between a curved and straight trajectory at the entrance and exit of a bending magnet, the electrostatic component can play an important role in the CSR field in these regions. These theoretical results are compared with those from simulation in Chapter 3.

The theory of the microbunching instability, the second collective effect studied in this thesis, is also presented in this chapter (Sec. 2.3). It is characterised by a small variation in the bunch longitudinal phase space density in the injector of an accelerator, which undergoes amplification due to CSR and LSC as the bunch propagates through the machine. This instability has important implications for the operation of a machine such as an FEL, as it can reduce the FEL pulse intensity and cause shot-to-shot variation in the pulse energy. The mechanisms behind this amplification have been presented, and the instability is investigated experimentally in Chapter 5, using the 2D Fourier analysis technique described

in Sec. 2.3.6.

Methods for mitigating the microbunching instability have been summarised in this chapter (Sec. 2.4). Along with the standard method employed at a number of X-ray FEL facilities – the laser heater – alternative techniques have also been proposed and simulated. Some of these techniques, in particular those which do not increase the slice energy spread of the bunch, are favourable for an FEL when compared with the laser heater, but the majority have not been demonstrated experimentally in the context of microbunching instability suppression. The final subsection of this chapter (Sec. 2.4.3) describes a method for using the laser heater to impose modulations on an electron bunch, using a temporally modulated laser pulse. This method has been used in light sources for manipulating the bunch longitudinal phase space to produce intense pulses of radiation; in Chapter 5 it will be used to stimulate modulations in the bunch longitudinal phase space in order to investigate the microbunching instability with a known initial modulation frequency. The goal of these investigations is twofold: to provide a robust comparison between experimental measurements and simulation results in order to assess the feasibility of the latter in reproducing the physics of microbunching; and as a propadeutic to providing the first measurement of the microbunching gain curve.

Chapter 3

Simulation of CSR and Microbunching

Numerical particle tracking is an important aspect in the design of particle accelerators, and for understanding the underlying beam dynamics of such machines, particularly in experimental studies. Simulation codes are crucial in the design stage of accelerators, as they provide an insight into the feasibility of the requirements of the machine. Additionally, the simulation codes used for such studies can provide a useful supplement to the limited diagnostics in an operational accelerator. There are a wide number of such codes, ranging from codes such as MAD [98] which perform single-particle tracking through transfer matrices for the optimisation of the optics of an accelerator, through to large-scale multi-particle codes such as IMPACT [99], which include collective effects, and are capable of simulating the same number of particles as those in a real accelerator [66] (although this requires a great deal of computational power).

Self-fields which arise due to the collective interactions of many particles, such as space charge or CSR, in systems of around 10^9 particles or more, can be computationally intensive to simulate in practice, requiring hours or days to simulate on a single machine, or the use of multi-core parallel processors. Therefore, the majority of simulation codes approximate this number of particles using a smaller number of 'macroparticles', each which has a user-defined charge related to the overall charge of a real bunch, thus reducing the computational effort required to simulate the collective effects and beam dynamics within such a system.

Most codes track the temporal evolution of a bunch as it propagates through the accelerator, applying either an analytic approximation to these self-fields, or a (usually simplified) calculation of the forces between the macroparticles themselves. The choice for the number of macroparticles in a simulation, therefore, requires a balance between the computational time available, and the need to simulate collective effects with a high degree of accuracy. In order to assess the accuracy of such simulations, the computational results must be compared with other results, from either theory, experiment or other codes. Users of simulation codes often have access to computational parameters that specify the method for simulating collective interactions. A balance of these computational parameters can often be found which can lead to good agreement between the simulations and and results obtained by other methods while keeping the time required for the simulations within reasonable limits. An investigation of the parameter space of a simulation code which aims to find such a balance is often referred to as a 'convergence study'.

Three simulation codes have been used in this thesis to investigate CSR and the microbunching instability – `elegant` [96], CSRTrack [100] and GPT [101]. A brief outline of these three codes will be given in Sec. 3.1. A new module of the GPT code for the simulation of CSR has been developed for the study of extreme bunch compression scenarios, and in order to test out our new insights into the CSR entrance and exit transients derived in Sec. 2.2, benchmarking results from this code will be given (Sec. 3.2). Simulations of the microbunching instability experiments described in Chapter 5 are conducted using the `elegant` code, for the reasons outlined in Sec. 3.3.

3.1 Accelerator Simulation Codes

The codes used in this thesis to simulate CSR and microbunching have been chosen for a number of reasons. They are all able to simulate collective effects, yet they all accomplish this using slightly different methods. This provides the opportunity to study their relative merits and shortcomings, with the aim of determining which codes are more suitable given a certain bunch and accelerator

parameter regime. They have also all been under development for a number of years, and have been benchmarked against both experiment and theory (see, for example, Refs. [14, 16, 102, 103, 104, 105]). In this section, the methods employed by these three codes will be discussed, particularly with a view to explaining how they simulate CSR and LSC. Some benchmarking studies against simple test cases are also performed.

3.1.1 `elegant`

`elegant` [96] is a multi-particle 6D tracking code that utilises the standard beam transport theory, through the application of transfer matrices and multipole kicks (see, e.g. Ref. [35]), including linear and higher-order interactions. This method allows for fast simulation as compared with time-domain codes such as GPT. The code can also perform calculations of 1D LSC and CSR models [59], the latter of which is based on Ref. [18] and subsequent developments in Ref. [56]; in the cases of both LSC and CSR, it is assumed that the bunch velocity is ultrarelativistic, which is often the case for the parameter regimes studied in this thesis. As the bunch travels through an element of the lattice (a drift space, magnet or RF cavity, for example), the LSC/CSR impedance (Eqs. 2.53 and 2.59 respectively) is convolved with a histogram of the longitudinal bunch distribution a (user-specified) number of times for each element. In addition to assuming that the bunch is ultrarelativistic, a number of other approximations are made in this calculation. It is assumed, for the LSC computation, that the transverse bunch distribution is symmetric and Gaussian. In the case of CSR, some of the other approximations made include:

- Neglecting the transverse offsets of bunch particles from the reference orbit (i.e. $x, y = 0$ for particles that emit and receive CSR).
- Neglecting the electrostatic (or 'Coulomb') term of the Liénard-Wiechert field Eq. 2.31.
- Neglecting stochastic effects due to the long-range interaction between a discrete number of radiation cones [106]. Although the radiation produced

by a number of electrons can interfere constructively, there will be statistical noise in the CSR field produced as a result of the fact that every emitter is a point particle.

- Assuming that the charge density distribution moves rigidly along the nominal trajectory.
- Not taking account of shielding of CSR from the accelerator chamber [107].

The importance of these approximations can only be made clear through rigorous benchmarking with other simulation codes and with experimental measurements. Depending on the configuration of the accelerator lattice, and the bunch parameters, some of these effects may cause a more significant deviation from the above approximations than others; indeed, it may not be possible to de-convolve fully each of them separately. In addition to this, the code offers a number of computational parameters that can influence the simulated effect of LSC and CSR. Those which have the most significant impact on the bunch distribution are:

- The number of macroparticles used in the simulation.
- The number of bins used to compute the histogram of the longitudinal density distribution, which is then convolved with the LSC/CSR wake.
- High-pass filter parameters used to reduce the impact of numerical noise.

Since these parameters are computational and not determined by the physical properties of the system, there is no unique solution to inform exactly how these parameters should be set such that the code will accurately simulate the relevant effects. Given that every simulation code must make trade-offs between speed and accuracy, it is up to the user to determine the best solution that matches with theory, experiment, and other simulation codes. Nevertheless, despite all of these caveats, `elegant` has proven useful in the design of a number of accelerator facilities. In terms of CSR simulation, it has been shown to agree well with experimental measurements over a certain parameter range [14]. These measurements did show, however, an overestimation of the overall energy loss due to CSR as

the bunch compression factor approached its maximal value – this may be due to one of the above approximations not being valid. In order to reduce the noise in simulations including self-fields, large macroparticle numbers (greater than 10^6) are required, and it is expected that larger numbers are required for simulations of the microbunching instability [108].

3.1.2 CSRTrack

This code is primarily used for calculating the CSR fields generated by a bunch on a curved trajectory [100], and will be used in this thesis only for tracking through dispersive regions. CSRTrack provides a number of calculation methods for the CSR force: the 1D 'projected' method, which projects the bunch onto the longitudinal dimension and applies a fast Fourier transform (FFT) convolution of this projection with the CSR field; a full-field calculation of the Liénard-Wiechert potential onto a 3D spatial mesh; or a Green's function method. Since the latter two calculations provide the self-fields of the bunch, space charge is also included in these methods; however, they also require a much greater computational effort than the 1D method. In these two cases, the 3D bunch distribution of macroparticles is divided into Gaussian time-independent 'sub-bunches' as opposed to point-like macroparticles. The CSR process (for both emitters and receivers) is then a function of the 3D distribution of these sub-bunches.

It should also be noted that none of the simulation methods employed by CSRTrack employ the 1D approximation of Ref. [18]. Given that the nature of the 3D simulation methods require direct computation of the collective interaction, as opposed to the relatively simple method of `elegant`, simulations using CSRTrack are much more computationally intensive, but in principle they should be more accurate in calculating the effect of CSR for a real electron bunch. CSRTrack has been shown to produce good agreement with measurements of the slice emittance after bunch compression at SwissFEL [17].

3.1.3 General Particle Tracer (GPT)

GPT [101] is a time-domain particle tracking code that integrates the equations of motion of a large number of charged particles in the presence of electromag-

netic fields. Full 3D space charge calculations are included, and the transport of particles through standard accelerator components is available to users. There is also an additional option for users to write their own modules, or 'custom elements', to compile into the program, in order to model more exotic interactions. Since the CSR module in GPT was developed specifically for this study, more detail on the method of modelling CSR using this code is given below. This code is also able to simulate electron emission from photocathodes in RF photoinjectors, and so it is used in this thesis for simulating the FERMI injector (see Sec. 4.2)

3.2 CSR Calculations in GPT

In order to validate the analytical results of Sec. 2.2.2.1 and 2.2.2.2, we have numerically calculated the electromagnetic field distribution in an electron bunch in both the entrance and exit transient regimes for the simple test case of a single dipole magnet using the GPT code [101]. The code has the option to include the computation of the retarded Liénard-Wiechert fields of the tracked particles (see Eq. 2.31). Because this involves the storage of the trajectory of the particles and solution of retardation conditions, calculation of Liénard-Wiechert fields is computationally expensive. To reduce the computational cost, the GPT code does not evaluate the field of each tracked particle, but instead represents the particle bunch by a number of bunch slices (see Fig. 3.1). Each bunch slice is represented by either four or sixteen off-axis particles that are spaced according to the RMS transverse size of the slice in order to capture the impact of the transverse extent of the bunch. While integrating the equation of motion of a tracked particle, GPT evaluates the Liénard-Wiechert field resulting from the past trajectory of each of the representative particles at the longitudinal position of the tracked particle.

It is important to note that GPT uses the exact expression for the Liénard-Wiechert fields based on the numerically obtained coordinates of particles in the bunch, and does not apply any analytic approximation or presumed trajectory of the bunch. The parameters used for the test case are listed in Table 3.1.

We deliberately chose artificially small energy spread, transverse bunch size and emittance, and used hard-edged magnet fringes in the exit transient simulations to match the analytic case as closely as possible. Similarly, a small bunch charge was used in order to prevent the effects of space-charge contributing to the evolution of the beam. The dipole bend radius and magnetic length, and the beam energy, were chosen to match the design parameters of a proposed FEL facility [109].

Since this chapter will often refer back to expressions derived and discussed in Sec. 2.2.2, these equations will be given again in this section for convenience. The meanings of the terms used in the expressions are given in full in Sec. 2.2.2 and the Appendix.

Eq. 2.33 is the steady-state CSR field for a bunch that is entirely within a bending magnet:

$$E_{||}^{SS}(z) = \frac{Ne\beta^2}{8\pi\epsilon_0 R}\int_0^{\phi} \frac{\beta - \cos(u/2)}{(1-\beta\cos(u/2))^2}\lambda(z-\Delta z(u))du, \tag{3.1}$$

Eq. 2.36 represents the combined expressions for the steady-state CSR field and the contribution from the entrance transient field [18], assuming an infinitely long straight beamline section before the entrance to the magnet:

$$E_{||}^{ent} = \frac{Ne}{24^{1/3}\pi\epsilon_0 R^{2/3}}\left(\left(\frac{24}{R\phi^3}\right)^{1/3}\left[\lambda\left(z-\frac{R\phi^3}{24}\right)-\lambda\left(z-\frac{R\phi^3}{6}\right)\right] + \int_{z-R\phi^3/24}^{z}\frac{d\lambda(z')}{dz'}\frac{dz'}{(z-z')^{1/3}}\right). \tag{3.2}$$

Eq. 2.35 is a modified expression for the above expression Eq. 3.2, without the assumption of an infinitely long straight beamline section before the magnet entrance:

$$E_{||}^{ent}(z) = E_{||}^{SS}(z) + \frac{Ne}{4\pi\epsilon_0\gamma^2}\int_0^{d}\frac{(y-\beta\rho(y))\cos(\phi)+R\sin(\phi)}{(\rho(y)-\beta(y+r\sin(\phi)))^2\rho(y)}\lambda(z-\Delta(y))dy, \tag{3.3}$$

Eq. 2.40 is the expression for the CSR radiation field in the exit transient

regime, where the receiving particle has exited the bending magnet:

$$E^{exit}_{||,rad}(z,x) = \frac{Ne\beta^2}{4\pi\epsilon_0}\int_0^{\phi_m}\left(\frac{2\sin(\psi/2)\zeta\chi}{\left(\rho-\beta\left(R\sin(\psi)+x\cos(\psi)\right)\right)^2\rho} - \frac{\sin(\psi)}{\rho-\beta\left(R\sin(\psi)+x\cos(\psi)\right)}\right)\lambda\left(z'(\psi)\right)d\psi, \tag{3.4}$$

where ζ and χ are defined in the Appendix.

Eq. 2.42 is the CSR radiation field in the exit transient regime under the ultrarelativistic and small-angle approximations:

$$E^{exit}_{||,rad}(z,x) \approx \frac{Ne}{\pi\epsilon_0}\left(\frac{\lambda(z-\Delta z_{max})}{\phi_m R+2x} - \frac{\lambda(z)}{2x} + \int_{z-\Delta z_{max}}^{z}\frac{\partial\lambda(z')}{\partial z'}\frac{dz'}{\psi(z')R+2x}\right). \tag{3.5}$$

Eq. 2.45 is the total exit transient field (the sum of 3.5 and 2.44), again under the small-angle and ultrarelativistic approximations:

$$E^{exit}_{||}(z,x) \approx \frac{8Ne}{3\pi\epsilon_0}\int_0^{\phi_m}\frac{N_1(\psi)}{D_1(\psi)^2}\lambda\left(z'(\psi)\right)d\psi + \frac{Ne}{\pi\epsilon_0}\int_0^{\phi_m}\frac{N_4(\psi)}{D_2(\psi)^2}\lambda\left(z'(\psi)\right)d\psi. \tag{3.6}$$

3.2.1 Entrance Transient Effect

The CSR field was calculated initially by GPT at a point 24 cm into the magnet in order to simulate the entrance transient field. This distance is only half that of the steady-state condition D^{SS} (Eq. 2.34), and so it is expected that the general expression of the steady-state field with the entrance transient included (Eq. 3.3) will be required to calculate the fields.

In this simulation, the drift before the magnet was set to 50 m. The results from the simulation are in good agreement with Eq. 3.2, as seen in the left-hand plot of Fig. 3.2. However, if the simulation is run again, but with the drift before the bend set to 10 cm, the GPT result effectively reduces to the steady-state CSR field only (Eq. 3.2), and thereby differs from the usual approximation of

Table 3.1: Lattice and electron bunch parameters used in the GPT simulation – used for validation of the numerical study. Two different values of the drift length before the bending magnet are simulated, in order to demonstrate the impact of the Coulomb component of the Liénard-Wiechert field (Eq. 2.31).

Lattice	**Value**	**Unit**
Magnet length $R\phi_m$	1.14	m
Radius of curvature R	2.29	m
Drift length before bend	0.1, 50	m
Entrance / exit edge angle	0	rad
Fringe width (entrance)	1.7	mm
Fringe width (exit)	0	mm
Initial bunch		
Number of macroparticles	10^6	
Bunch charge	70	fC
Mean energy	380	MeV
Twiss β_x	1.34	m
Twiss β_y	3	m
Twiss α_x	0.185	rad
Twiss α_y	0	rad
$\epsilon_{N,x,y}$	5×10^{-3}	µm rad
RMS bunch length	0.6	mm
Uncorrelated energy spread	0	–
Energy chirp (dE/dz)	0	%/mm

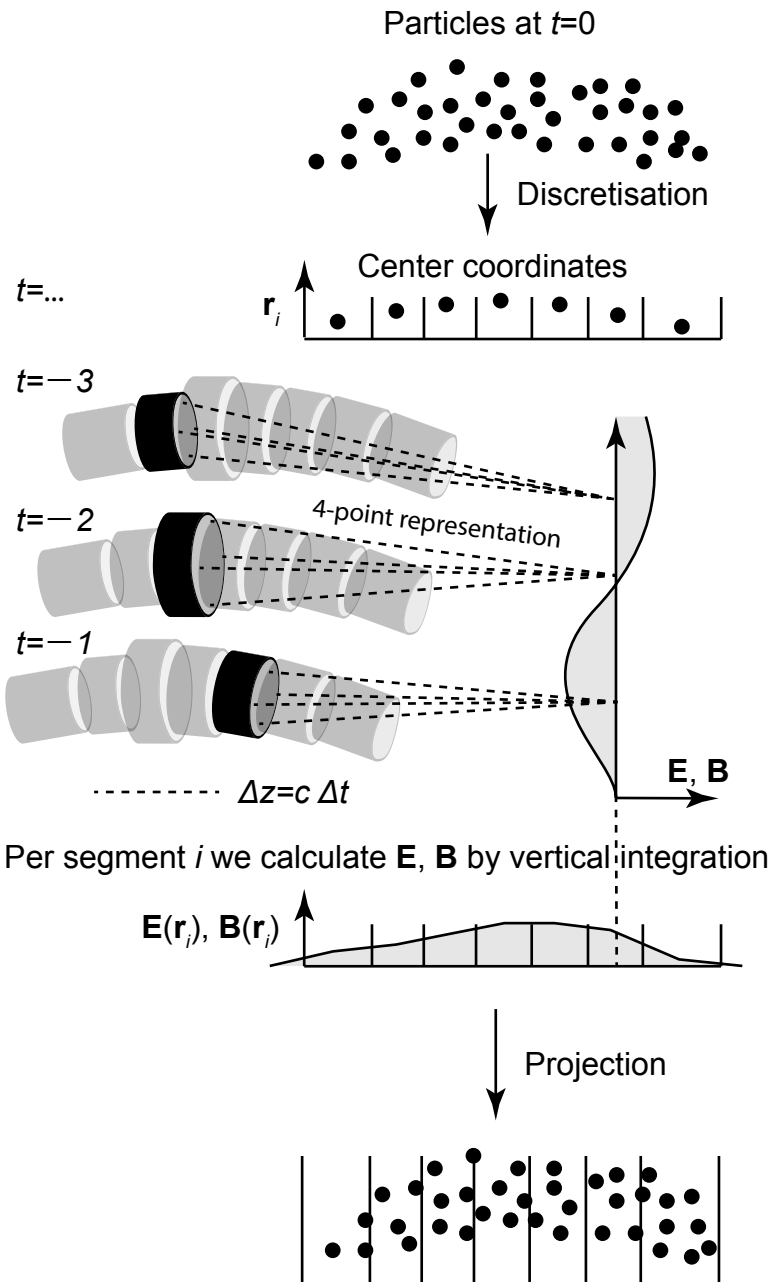

Figure 3.1: Representation of particle bunch adopted by GPT to calculate CSR forces. The particle bunch is discretised and represented by slices. The CSR force is then calculated and projected onto the bunch. [Credit: B. van der Geer, Pulsar Physics]

Ref. [18]. The second term on the right-hand side of the full entrance transient field (Eq. 3.3) is suppressed by lowering the integration boundary, showing that the approximation of an infinitely long drift before the entrance to a bending magnet may not be valid for some cases. As shown in the right-hand plot of

Fig. 3.2, the GPT simulation reflects this behaviour. Finally, it should be noted that although the term 'drift' has been used, in reality any straight section of beamline would be appropriate for the comparison of these two scenarios.

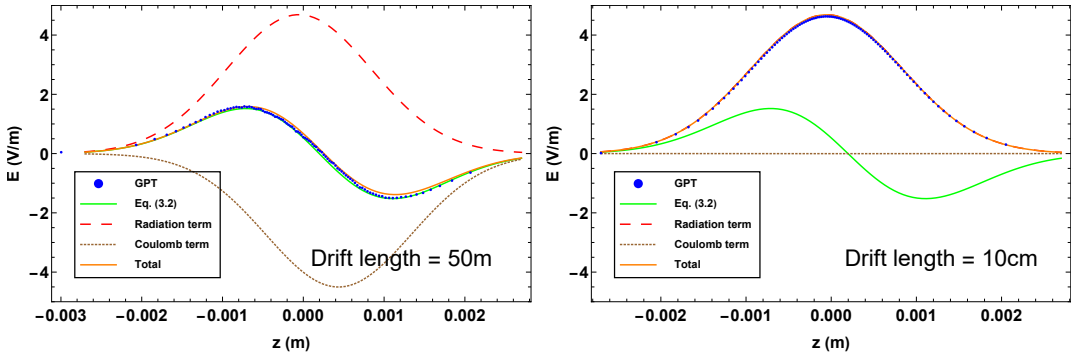

(a) (b)

Figure 3.2: Longitudinal component of CSR electric field as a function of longitudinal position in the bunch for the parameters in Table 3.1 and a drift before the magnet of: Left: 50 m; and Right: 10 cm, as simulated by GPT, against both the approximated entrance transient field (Eq.3.2) and the full entrance transient field (Eq. 3.3) – both the Coulomb and radiation terms individually, and combined. Positive values of z refer to the head of the bunch.

3.2.2 Exit Transient Effect

We now consider the simulation of the CSR exit transient field, following on from the model introduced in Sec. 2.2.2.2. The transition from the steady-state regime to the exit transient regime will also be studied. The expression for the total CSR field in the exit transient regime (Eq. 3.4) assumes that all particles follow the same reference trajectory. However, the impact of a transverse displacement of the emitting electrons on the observed electric field may be studied by including a vertical offset (out of paper) of the emitting electron shown in Fig. 2.5. Fig. 3.3 gives a side view of the resulting configuration. Due to the offset, the distance σ from emitter to observer becomes:

$$\sigma = \sqrt{\rho^2 + y^2} = \sqrt{4R^2 \sin\left(\psi/2\right)^2 + 2Rx \sin\psi + x^2 + y^2} \tag{3.7}$$

In addition, the angles θ, η and ξ are stretched somewhat, such that their cosines become smaller by a factor $\cos\delta = \rho/\sigma$. Re-evaluating the Liénard-Wiechert field

(Eq. A.23) with these modifications shows that the electric field is still given by Eq. 3.4 in the limit $\delta \to 0$ (so that $\rho \to \sigma$).

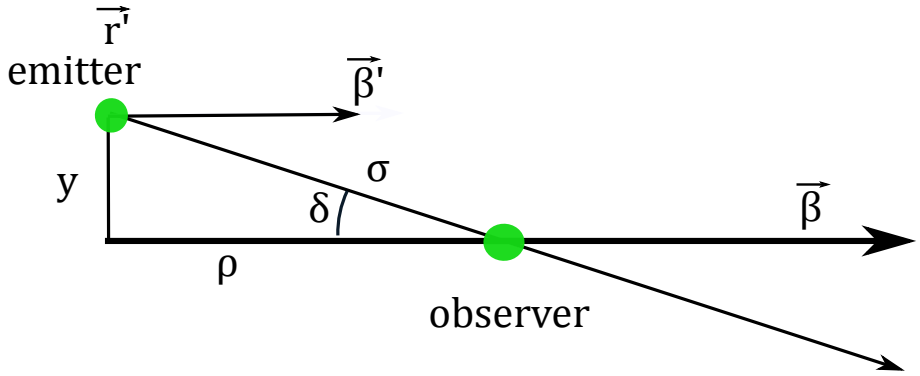

Figure 3.3: Side view of the configuration of Fig. 2.5 in the case of a vertical offset y of the emitting particle.

In Fig. 3.4 the longitudinal component of the radiation field is plotted for small values of x, the distance after the exit of the magnet. The solid blue lines again show the numerically calculated field found by GPT simulation, and the steady-state field of a bending magnet (Eq. 3.1) has been plotted as a black solid line. In the left plot, the bunch centroid is at the magnet edge, which is clearly seen by the kink in the electric field. The field in the left part of the bunch is still accurately given by the black line, while the field in the right part starts to transition to that described by the exit transient field $E_{||}^{exit}$.

The middle and right plots show the situation at 5 mm and 10 mm after the bend, which is around where the field reaches its maximum (negative) value before starting to decay. The corresponding results according to Eq. 3.4 are also plotted. For such small distances after the magnet edge, Eq. 3.4 does not reproduce the smooth transition shown by GPT, but rather predicts a sharp transition to a negative field with large amplitude as a result of the sign of the exit transient field – at the exit, all of the Coulomb fields emitted from particles within the magnet are able to interact with particles that have left it. Fig. 3.4 shows the resulting modified electric field as dashed lines. The vertical offset of the emitting charges was taken to be equal to the rms vertical bunch size at the magnet exit edge, which was only 5.8 µm.

Clearly, the match between the analytic electric field and the GPT result is much better, showing that the sudden peak in the electric field right after

the magnet edge is indeed effectively damped by a small transverse offset of the emitting charge. This explains the smooth transition observed in the simulation. Note that a transverse offset of the emitting charge, and hence the observed smooth behaviour of the field right after the magnet edge should not be dismissed as merely an artificial construct of the GPT simulation. Arguably, it should be rather seen as an effective representation of reality in which none of the particles will be exactly on-axis either. It is worth noting the significant difference between results from a model in which all emitters are all in the same horizontal plane, and the results from a model in which the emitters have some distribution in transverse position. This difference indicates that analytic 1D models are inadequate for capturing fully the physics of the CSR exit transient.

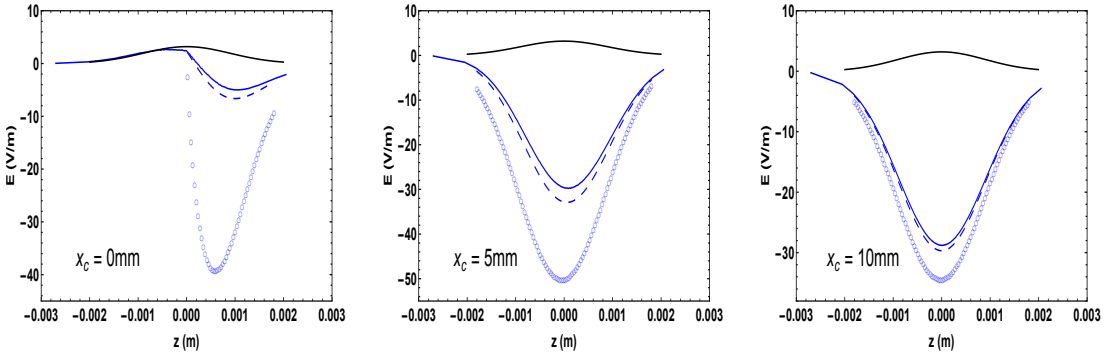

Figure 3.4: Longitudinal component of radiation field as a function of longitudinal position in the bunch, at three different distances after the exit of the bend. Solid blue: GPT simulation; Circles: Eq. 3.4; Dashed blue: Eq. 3.4, including a vertical offset $y = 5.8\,\mu\text{m}$ of the emitting particles by substituting $\rho \to \sigma$. The solid black line indicates the steady-state electric field inside the bending magnet (Eq. 3.1).

Fig. 3.5 shows the longitudinal component of the electric field as a function of longitudinal position in the bunch evaluated at 5 mm past the bending magnet. The results for the GPT simulation of both the full CSR field, and the radiation component, are compared with Eqs. 3.6 and 3.5, and Eq. 3.4 with an offset in the y plane according to Eq. 3.7. The simulation results agree well with the expression Eq. 3.4, with the inclusion of a small transverse offset. The fact that the approximation for the radiation term Eq. 3.5 differs greatly from both the exact formula for the radiation field and the simulation results demonstrate the importance of including the Coulomb term when computing CSR fields at the

exit of a bending magnet. Fig. 3.5 shows that Eq. 3.4 fully captures the actual behaviour of the field that we found both analytically and numerically.

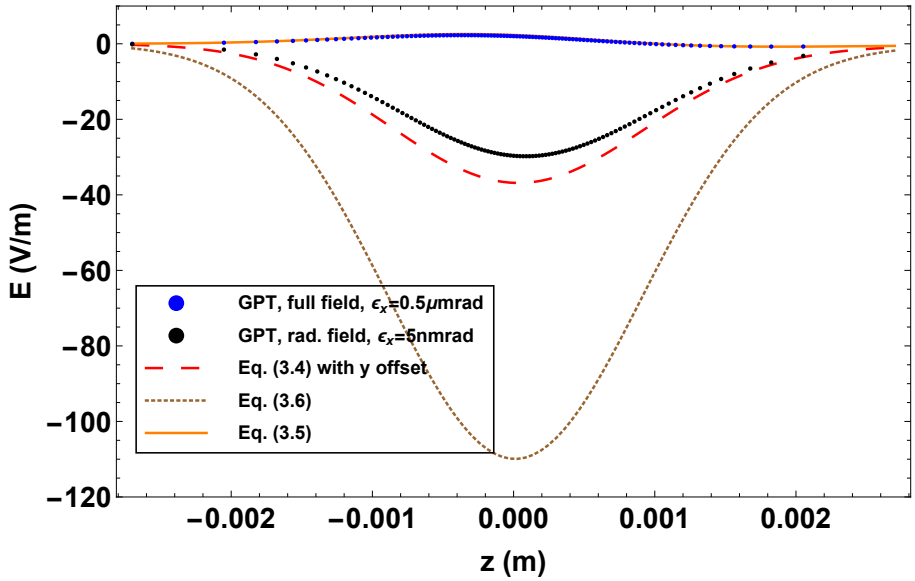

Figure 3.5: Longitudinal component of electric field as a function of longitudinal position in the bunch, at 5 mm from the exit of the dipole. Blue: GPT simulation of the full field; Black: GPT simulation of the radiation field only; Red: Eq. 3.4 with an offset in the y plane; Brown: Eq. 3.6; Orange: Eq. 3.5.

3.2.3 Convergence Study

As mentioned in the introduction to this chapter, when simulating collective effects such as CSR with codes which make some approximations with regard to the full collective interaction of the real number of particles, be it in the use of macroparticles, or in simplifying the interaction between particles – both of which apply to GPT – it is important to perform convergence studies in order to find the correct balance between accurately simulating the forces and minimising the computational cost. Before attempting to compare results from GPT and other codes with experimental data from the FERMI FEL (in Chapter 4), such a study has been undertaken. In Fig. 3.6, results are shown from GPT simulations of the CSR-induced emittance growth at the exit of the first bunch compressor of FERMI for a range of linac phases. The number of macroparticles used in the simulation was varied, from 10^5 to 10^7. In order to compare these results with another code which has undergone similar benchmarking studies [59] –

`elegant` – we also provide two sets of data for the same linac phase scans using this code. Complementing these results are simulated electron bunch lengths, in order to indicate the point of maximal bunch compression. As shown in the discussion of CSR-induced emittance growth above (Sec. 2.2.4, particularly Eqs. 2.47 and 2.48), the bunch length is inversely proportional to the energy change of a particle due to CSR, which has an impact on its emittance. The compression factor, therefore, should be proportional to the emittance growth in a bunch compressor.

As the plot shows, there is a discrepancy between the results from `elegant` and GPT, but this will be investigated in greater detail in Sec. 4.5. More interesting in the context of the convergence study are the three results from GPT for different numbers of macroparticles. There is a much better agreement for all linac phase settings for the runs with 10^6 and 10^7 macroparticles than for the runs with 10^5 macroparticles, suggesting that at least 10^6 macroparticles are required for the CSR interaction to be accurately modelled. It should also be recognised, however, that a further study would have to be conducted over a wider parameter range in order to evaluate fully the validity of this algorithm. Although a range of bunch compression factors were considered here, it may be illuminating to study a variation in emittance growth as a function of bunch charge, for example.

3.2.4 Limitations of the CSR Model

One more potential limitation of the CSR calculation in GPT is that shielding of the radiation by the vacuum chamber [107, 110] is not taken into account. Since our experimental study of CSR is concerned with the FERMI accelerator, the parameters of its bunch compressor can be taken into account. As demonstrated in [58], CSR suppression by the vacuum chamber occurs for wavelengths $\lambda \geq 2h(h/R)^{1/2}$, with h the minimum half-gap of the beam pipe, and R the bending radius. Using the parameters for the FERMI FEL, with the values $R = 3.7\,\mathrm{m}$, $h = 10\,\mathrm{mm}$, we find that the cutoff wavelength $\lambda \approx 1\,\mathrm{mm}$, which is longer than the uncompressed bunch length of 0.6 mm, and so the effect of CSR shielding is negligible for this parameter range.

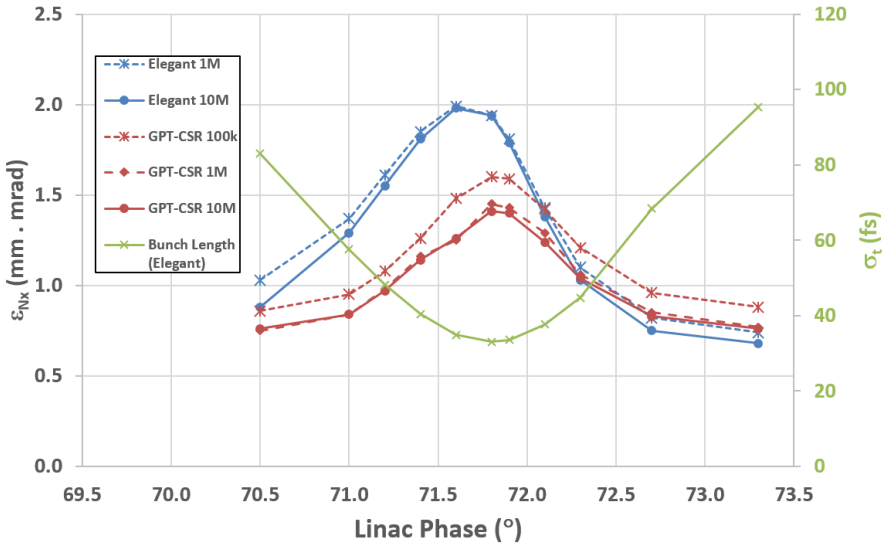

Figure 3.6: Example convergence study in `elegant` and GPT for normalised emittance after the first bunch compressor of FERMI as a function of preceding linac phase. The energy at this position is 300MeV, the bunch charge is 100 pC and the R_{56} of the bunch compressor is fixed at 57 mm.

3.3 Microbunching Simulations

As described below in Chapter 4, the GPT code is used for simulating the FERMI injector. From this GPT injector simulation, the electron bunch can be tracked through the remainder of the accelerator lattice using the `elegant` code. Among the three codes employed for simulating collective effects in this thesis, `elegant` is possibly the best-suited to simulations of the microbunching instability. The reasons for this are twofold.

1. The laser heater interaction can be simulated fully and seamlessly using an integrated beamline element: the user can specify the undulator and laser parameters, and the code tracks the electron bunch through the magnets with a co-propagating laser through numerical integration. An additional feature also allows the user to provide a file that specifies the intensity profile of the laser heater, meaning that a laser pulse that has undergone chirped-pulse beating (described by Eq. 2.80) can be simulated directly. CSRTrack is not well-benchmarked outside of bunch compressor structures, nor was it designed to simulate the interaction between laser and electron beams. While it would be possible to simulate this interaction

in GPT, the implementation would be much more complicated than in `elegant`, as the user would have to write custom elements to define the undulator and laser pulse, and the spatial and temporal overlap between the beams would require fine-tuning.

2. Since microbunching is a phenomenon that arises due to the collective interaction of large numbers of particles, the code that is used to simulate it must be able to tackle these large numbers. Again, this time thanks to the approximations that it makes by neglecting transverse collective effects, `elegant` is well-suited to the task. Once the electron bunch has become relativistic (with an energy larger than 100 MeV, or $\gamma \approx 200$), transverse space-charge forces have a smaller impact, with the longitudinal forces dominating the structure in the bunch longitudinal phase space. For this reason, GPT will be used to produce the injector simulation (as discussed in Sec. 4.2), and `elegant` will be used thereafter to simulate the various machine configurations. Despite the large parameter range investigated for the microbunching studies (discussed in full in Sec. 5.1), full simulations of the experiment can be conducted. A convergence study (described in Sec. 5.6) was run in `elegant` in order to determine the optimal settings for the LSC and CSR interactions, based on results from the experiments.

3.4 Summary

This chapter has presented a brief introduction to simulation codes used in the design of particle accelerators. A wide variety of codes exist, with some being more applicable to the simulation of collective effects than others. Three simulation codes have been used in this thesis for simulating CSR, and `elegant` is used to simulate the microbunching instability. All codes must make some approximations when simulating a large number of charged particles, and one goal of this thesis is to determine the range of applicability of these three codes by comparing experimental measurements with simulation results. In order to understand the difference in results produced by these three codes when simulating the CSR-induced emittance growth (Sec. 4.5), their methods are described

in Secs. 3.1 and 3.2.

Since the CSR module for GPT was developed specifically for this study, and because this code does not use the simplified 1D theory of CSR, but rather takes account of the full Liénard-Wiechert field (Eq. 2.31), it has been used to validate the modified theory concerning entrance and exit transient fields that occur when a bunch enters and exits a bending magnet (Sec. 2.2.2). Good agreement was found between the theoretical results and those from simulation, and a divergence between these results and the simplified 1D theory, which does not take full account of the electrostatic component of Eq. 2.31, was found. Since the divergence between these approaches occurs when there is only a short beamline section at the entrance or exit of the bending magnet, these results could have implications for machines in which there are a number of dipole magnets that are close to one another, such as in the arc of an energy recovery linac (ERL).

Chapter 4

CSR Measurements

As discussed in Section 2.2, the region of applicability of the 1D theory of CSR is limited. By projecting the electron bunch distribution onto the longitudinal dimension, the shape of the radiation cone from the emitting particles focuses the total power of CSR radiation onto a smaller area. If this 1D projection is not made, the CSR radiation will become more spread out transversely. Since the radiation cone resulting from the coherent emission of a bunch with a finite transverse extent is larger (and therefore more spread out) than that predicted by the 1D approximation, this could result in a beam emittance growth that is smaller than the theory predicts.

In order to investigate the regime of applicability of this theory, and the codes which utilise it, experimental results from the FERMI FEL facility will be compared with results from 1D CSR theory and simulation, and from codes which do not utilise the 1D approximation of Refs. [18, 55, 56]. This experiment was done over a range of electron bunch lengths and transverse beam sizes (scans of which are outlined in Sec. 4.1). The methods for simulating the initial beam distribution and these parameter scans are discussed in Sec. 4.2. The emittance measurement technique via quadrupole scan, and the analysis program written to measure this parameter, are outlined in Sec. 4.3 and Sec. 4.4 respectively. In Sec. 4.5, results from the 1D CSR theory, experimental measurements and three simulation codes are compared across a range of bunch compression parameters. Better agreement is found between experimental data and the codes which account for the transverse extent of the bunch, particularly in more extreme

compression scenarios.

4.1 CSR Parameter Scans

A schematic of the FERMI linac is shown in Fig. 4.1, and the main beam parameters during the experiment are shown in Table 4.1. The horizontal emittance was measured at the exit of the first bunch compressor, BC1, as a function of Linac 1 RF phase (i.e. energy chirp, that is, a longitudinal energy-to-position correlation along the bunch; see Sec 2.1.4), chicane bending angle, and the strength of the last quadrupole before the entrance to the bunch compressor.

The first two scans resulted in scans of the bunch length compression factor in the range $20 - 64$ and $8 - 60$ for the Linac 1 phase and chicane bending angle scans, respectively. The scan of quadrupole strength was done at a fixed compression factor of 36. The energy chirp at the entrance of the chicane was linearised using an X-band RF cavity, which approximately preserves the shape of the bunch current distribution through the chicane, as shown later in Figs. 4.8a and 4.8b [111, 112]. During the phase scan, the accelerating gradient of Linac 1 was scaled in order to keep the mean bunch energy constant at the entrance to BC1.

Measurements were taken using the single quad-scan technique [80], by varying the strength of one quadrupole magnet (Q_BC01.07), located in the straight section directly after BC1. The machine was operated with a constant bunch charge of 100 pC, and a mean energy of approximately 300 MeV at BC1. Additionally, the laser heater was configured to add around 20 keV uncorrelated energy spread to the beam, in order to suppress the microbunching instability. For each set of scans, the two other scanning parameters were kept constant. During the experimental run, the following scans were performed:

- Linac 1 phase – vary between 70.5 ° and 73.3 ° (nominal is 73 °).
- BC1 angle – vary between 100 mrad and 109 mrad (nominal is 105 mrad).
- Q_L01.04 K1 (this is the final quadrupole before the entrance to BC1) – vary between $-2.0\,\mathrm{m}^{-2}$ and $5.0\,\mathrm{m}^{-2}$ (nominal is $1.6\,\mathrm{m}^{-2}$).

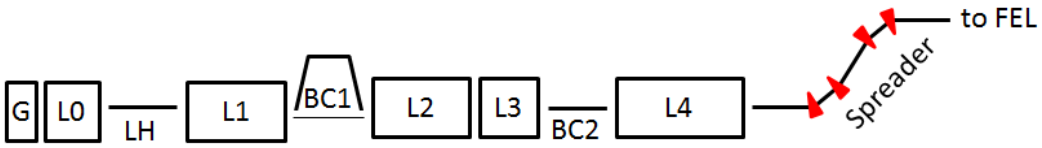

Figure 4.1: Sketch, not to scale, of the FERMI linac to FEL beam line. This study applies to the Gun (G) through the first accelerating sections (L0 and L1) and the laser heater (LH) to the exit of the first bunch compressor (BC1).

Table 4.1: Main beam and lattice parameters of the FERMI accelerator at the entrance to BC1 in the nominal configuration. The distances between the dipoles correspond to the end-to-end drift length.

Bunch and lattice parameters	**Value**	**Unit**
Bunch charge	100	pC
Mean energy	300	MeV
$\epsilon_{N,x,y}$	0.62	µm rad
RMS bunch length	0.61	mm
Relative energy spread	0.95	%
Magnet length	0.366	m
Distance between 1^{st} - 2^{nd}, and 3^{rd} - 4^{th} bend	2.5	m
Distance between 2^{nd} and 3^{rd} bend	1.0	m
Momentum compaction R_{56}	0.057	m
s-E correlation $\frac{1}{E_0}\frac{dE}{ds}$	-17.0	m^{-1}

At the diagnostic stations, both Yttrium Aluminum Garnet (YAG) and Optical Transition Radiation (OTR) screens are available. Estimates of the resolution for these screens are, respectively, 45 µm for a pixel width of 31.2 µm and 25 µm for a pixel width of 19.6 µm [113]. The majority of the measurements were initially taken with OTR screens, but coherent effects were suspected to be having an effect on the measured emittance as the bunch approached maximum compression, and so some measurements were repeated with YAG screens, whose performance is expected to suffer much less from coherent emission. The typical emittance measurement procedure consists of taking at least 5 images for between 10 and 30 settings of Q_BC01.07, and the single quad-scan technique (see, for example, [80]) is applied to calculate the transverse emittances and Twiss parameters.

4.2 Simulation Setup

Simulations of the FERMI injector (up to the exit of the first linac, see Fig. 4.1) have been produced using the GPT code. In order to match accurately the simulation to experimental conditions, the measured transverse and longitudinal profiles of the photoinjector laser were used as input parameters to the simulation (shown in Figs. 4.2 and 4.3), along with geometric wakefields from the injector linac. Full 3D space-charge effects were also included. The injector linac phase was optimised for minimal energy spread – as is done in the routine procedure of linac tuning – and good agreement was found between the simulated and experimentally measured bunch properties at the exit of the injector.

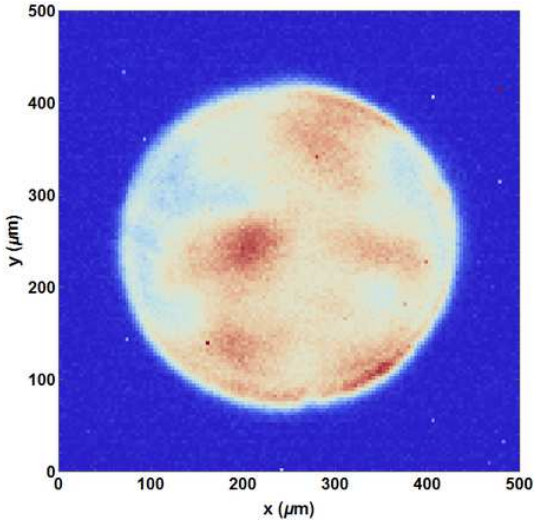

Figure 4.2: Measured transverse photo-injector laser profile used as input for GPT simulation.

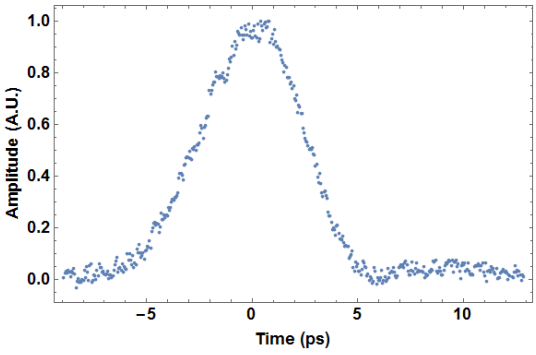

Figure 4.3: Measured longitudinal photo-injector laser profile used as input for GPT simulation.

From this injector simulation, the bunch was then tracked using the `elegant` code [96] up to the entrance of BC1, including the effects of linac wakefields,

the laser heater, CSR and space charge models. From this point, three particle tracking codes have been used to compare the emittance measurement results with simulation: `elegant`, CSRTrack and GPT – see Chapter 3 for more details on all of these codes. Briefly: in the 1D CSR simulations, `elegant` applies the calculation of Saldin *et al* [18] to calculate the energy change due to coherent radiation in a bend, and the transient effects which arise at the entrance and exit of the dipole magnet, based on [56]. In the `elegant` calculation, the dipole is split up into pieces, and the bunch is tracked sequentially through each piece. At each point, the bunch is projected onto the reference trajectory and the electric field of the bunch is computed. The projected (1D) method of CSRTrack divides the bunch up into Gaussian 'sub-bunches', smooths the longitudinal distribution, and calculates the CSR field from a convolution of the distribution with a kernel function describing the Liénard-Wiechert fields across the bunch trajectory [114]. At the exit of the bunch compressor (including a drift to account for transient CSR effects), the output from GPT or CSRTrack is then converted back into `elegant`, and tracked up to Q_BC01.07, the measurement point.

As described above in Sec. 3.2, the CSR routine in GPT does not employ the 1D approximation, but calculates the retarded Liénard-Wiechert potentials directly by slicing up the bunch longitudinally, and it does not directly project the radiating particles onto a line. Each slice contains a number of radiation emission points (typically four), and the full history of both the fields and the particle coordinates are stored for each time step. The 3D routines in CSRTrack also calculate the radiation fields directly, but in a slightly different manner. For our simulations, we have utilised the `csr_g_to_p` method, in which the particles are first replaced by Gaussian 'sub-bunches', and the radiation field is calculated via a pseudo-Green's function approach [114], with each sub-bunch having an effect on each sub-bunch in front of it.

It should be mentioned that the number of bins used for the density histogram in the CSR and longitudinal space-charge (LSC) models of `elegant`, in addition to the smoothing applied on the bunch, can have an impact on the final results [59]. Following a convergence study, by varying the number of CSR bins between 100 and 5000, and performing the parameter scans for 10^6, 5×10^6 and 10^7

macroparticles, we have determined that 500 LSC and CSR bins for an `elegant` simulation of 10^6 macroparticles is sufficient. Following previous studies [115], we set the sub-bunch size for the CSRTrack calculations to be 10 % of the rms bunch length. A similar set of simulations was run in GPT in order to achieve convergent results, for input distributions of 10^5, 10^6 and 10^7 macroparticles (see Sec. 3.2.3). To determine the significance of the Coulomb term outlined in Sec. 2.2.2.1, GPT simulations were also run with this term deactivated. Since dipole fringe fields are included in CSRTrack by default, the parameter scans were also simulated with dipole fringes in the other two codes. This should also provide the most realistic benchmark with the experimental case.

4.3 Quad Scan Technique

Quadrupole scans are a widely used technique for measuring the projected emittance and Twiss parameters of electron bunches [36]. By measuring the transverse profile of a bunch on a screen, preceded by a quadrupole and a drift, the emittance can be reconstructed by calculating the transfer matrix, $\mathbf{R}$, of these elements. To first order, between two locations in the lattice, s_0 and s_1, the covariance matrix (of second-order moments of the beam distribution) can be calculated as:

$$\Sigma_x(s_1) = \mathbf{R}_x \Sigma_x(s_0) \mathbf{R}_x^T, \tag{4.1}$$

with $\mathbf{R}_x$ the horizontal transfer matrix, and Σ_x given as:

$$\Sigma_x = \begin{pmatrix} \langle x^2 \rangle & \langle x p_x \rangle \\ \langle x p_x \rangle & \langle p_x^2 \rangle \end{pmatrix} = \epsilon_x \begin{pmatrix} \beta_x & -\alpha_x \\ -\alpha_x & \gamma_x \end{pmatrix}. \tag{4.2}$$

The rms emittance is given by (see Sec. 2.1.2):

$$\epsilon_x = \sqrt{\det(\Sigma_x)} = \sqrt{\langle x^2 \rangle \langle p_x^2 \rangle - \langle x p_x \rangle^2}. \tag{4.3}$$

Here, it is assumed that $\langle x \rangle = \langle p_x \rangle = 0$ – that is, the mean values are subtracted before taking the second-order moments. Note that this approximation is not

sufficient to describe the transport of space-charge dominated beams. For these measurements, which were taken at 300 MeV, the space-charge is expected to be sufficiently suppressed such that this effect can be neglected. The Twiss parameters relate the second-order moments of the bunch distribution to the emittance through the formulae:

$$\langle x^2 \rangle = \beta_x \epsilon_x, \tag{4.4a}$$

$$\langle x p_x \rangle = -\alpha_x \epsilon_x, \tag{4.4b}$$

$$\langle p_x^2 \rangle = \gamma_x \epsilon_x. \tag{4.4c}$$

For now, we will use the thin-lens approximation for the quadrupole matrix, giving us the following horizontal transfer matrix elements for a quadrupole, **Q** with length l and integrated strength Kl and a drift, **S** with length d:

$$\mathbf{Q} = \begin{pmatrix} 1 & 0 \\ Kl & 1 \end{pmatrix}, \mathbf{S} = \begin{pmatrix} 1 & d \\ 0 & 1 \end{pmatrix}. \tag{4.5}$$

The transfer matrix **R** of the quadrupole followed by a drift is then given as follows:

$$\mathbf{R} = \mathbf{S} \cdot \mathbf{Q} = \begin{pmatrix} 1 + Kld & d \\ Kl & 1 \end{pmatrix}. \tag{4.6}$$

Given that $x_1 = R_{11} x_0 + R_{12} p_{x,0}$, the square of the horizontal beam size at the screen $\langle x_1^2 \rangle$ can be calculated as follows [36]:

$$\langle x_1^2 \rangle = R_{11}^2 \langle x_0^2 \rangle + (2 R_{11} R_{12} \langle x_0 p_{x,0} \rangle) + R_{12}^2 \langle p_{x,0}^2 \rangle. \tag{4.7}$$

Measuring $\langle x_1^2 \rangle$ as a function of K and applying a parabolic fitting function yields three coefficients:

$$\langle x_1^2 \rangle = A(Kl)^2 + B(Kl) + C. \tag{4.8}$$

with the fit parameters obtained by substituting the elements of the transfer

matrix $\mathbf{R}$ and rearranging Eq. 4.7:

$$A = d^2\langle x_0^2\rangle \tag{4.9a}$$

$$B = 2\left(d\langle x_0^2\rangle + d^2\langle x_0 p_{x,0}\rangle\right) \tag{4.9b}$$

$$C = \langle x_0^2\rangle + 2d\langle x_0 p_x\rangle + d^2\langle p_{x,0}^2\rangle. \tag{4.9c}$$

Given the results of the fit, and the transfer matrix parameters, the values of $\langle x_0^2\rangle$, $\langle x_0 p_{x,0}\rangle$ and $\langle p_{x,0}^2\rangle$ can be calculated. These values can then be used to calculate the emittance at the location of the quadrupole s_0 using Eq. 4.3.

4.4 Image Analysis for Emittance Measurement

The FERMI online emittance procedure produces files consisting of the images taken during the quad scan, and the quad strengths, along with metadata containing various machine settings. This metadata includes:

- Quadrupole current and K values.
- Region of interest (pixel array size in x and y).
- Quad length and drift space in between quad and screen.
- Beam energy.
- Screen image calibration factor (pixels per mm).

A Python application has been written to iterate through each image, to fit a 1D Gaussian projection of each image onto the horizontal and vertical axes, and to calculate the emittance and Twiss parameters as described above – a screenshot of the graphical user interface (GUI) is given in Fig. 4.4. The experimental data is recorded using a Matlab application, and a conversion procedure is necessary to make this readable by Python. The algorithm executed by the Python application then runs as follows:

1. Select a quad scan file.

2. Load data into the image viewer. Each group of images for a given quad setting are keyed by an index; this index can also be used to determine the quadrupole settings for this group.

3. The set of images for one quadrupole setting consists of a 1D array; based on the pixel array sizes in the metadata and the length of this array, the number of shots for each group of images can be calculated and transposed into a set of 2D images. The user can also crop these images to select a particular region of interest.

4. Get projections in the horizontal and vertical axes. For each image, each row/column is iterated through, and the sum of the pixel intensity in each slice is calculated. A Gaussian fit is then applied to these intensity arrays in the horizontal and vertical directions, discarding any values below 1 standard deviation of the total slice array, in order to minimise the noise level. This may cause some issues when fitting with low-intensity bunches (i.e. not correctly focused). To counteract this, the user can choose to crop a region of the image to focus only on the area where a beam is visible.

5. The fits can then be used to determine the rms beam size (in terms of pixels); by using the screen image calibration factor (pixels per mm) the beam distribution can be calculated.

6. The parabola generated by processing the mean beam size of each group of images for all quad settings can then be used to determine the fit parameters given in Eq. 4.9. The emittance and Twiss parameters in x and y are then displayed and saved.

4.5 Discussion of Results

During the experimental run, the parameter scans detailed in Sec. 4.1 were performed, and the emittance was measured by the quad scan technique using the FERMI online emittance tool. Measurements were also processed using the Python script outlined above. Plots comparing the emittance measurements

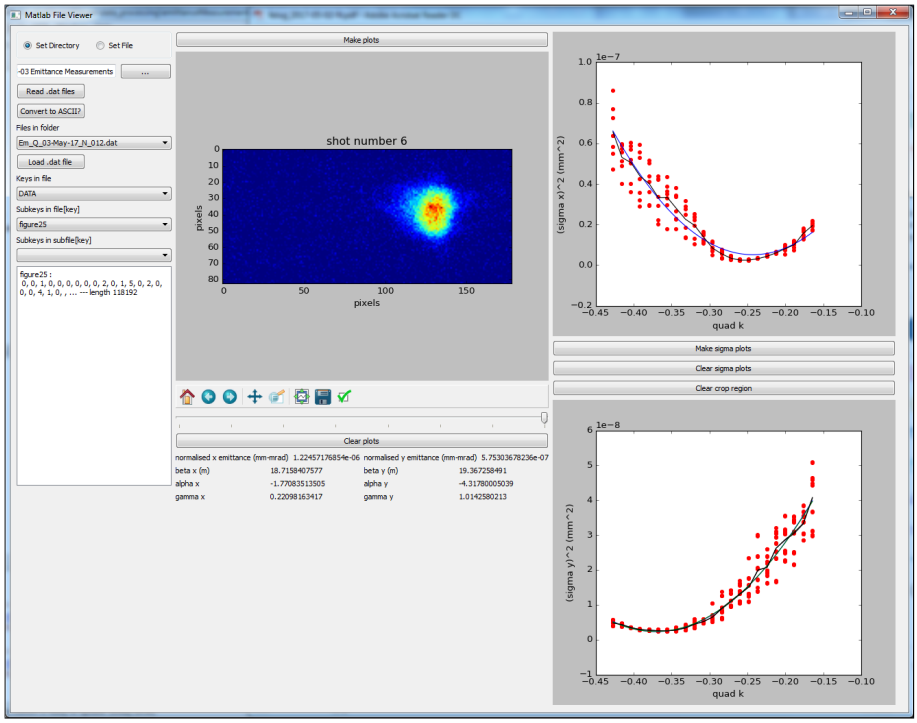

Figure 4.4: Screenshot of the Python emittance GUI.

with simulation results from the three codes are given in Figs. 4.5a,4.6a and 4.7a. There was good agreement between the two measurement methods, and so only the results from the Python script are given in the plots. The CSR-induced emittance growth in these regimes has also been calculated, based on the analytic theory given in [116], and updated in [117]. The emittance growth corresponding to the longitudinal and transverse CSR wake with the entire bunch travelling on a circular orbit are given as:

$$\Delta\epsilon_N^{long} = 7.5\times10^{-3}\frac{\beta_x}{\gamma}\left(\frac{r_e N {L_b}^2}{R^{5/3}\sigma_z^{4/3}}\right)^2 \tag{4.10a}$$

$$\Delta\epsilon_N^{trans} \approx 2.5\times10^{-2}\frac{\beta_x}{\gamma}\left(\frac{r_e N L_b}{R\sigma_z}\right)^2, \tag{4.10b}$$

with β_x the horizontal beta function, γ the relativistic Lorentz factor, r_e the classical electron radius, N the number of particles in the bunch, L_b and R the length and radius of the dipole magnet, respectively, and σ_z the electron bunch length. The total emittance growth is the sum of these two expressions. These formulae are the result of considering the longitudinal *and transverse* forces that

arise due to the steady-state CSR wake field for a bunch with a transverse radius that is finite, but small compared with the bunch length. The emittance increase occurs due to the CSR wake causing a change in the energy of the bunch, and therefore its horizontal deflection angle as it travels through the compressor. It is shown in Ref. [117] that the transverse force depends on the bunch radius, although the contribution from $\Delta\epsilon_N^{trans}$ is smaller than that from $\Delta\epsilon_N^{long}$. For Figs. 4.5a and 4.6a the emittance increase was calculated using simulation results for the beam parameters at each dipole as an input for Eqs. 4.10 and adding these values to the simulated beam emittance without CSR included.

We also provide calculations of the Derbenev parameter D_{par} [55] in Figs. 4.5b, 4.6b and 4.7b, in order to illustrate that the validity range of the CSR theory outlined in Chapter 2 [18] is violated when approaching maximal compression, or in cases where the transverse beam size is large. According to the theory, for the analytical calculations to be valid, the condition $D_{par} \ll 1$ should be fulfilled. This parameter is given by:

$$D_{par} = \sigma_\perp \sigma_z^{-2/3} R^{1/3}. \tag{4.11}$$

The values for the transverse beam size $\sigma_\perp$ and bunch length are taken from `elegant` simulations with CSR switched off.

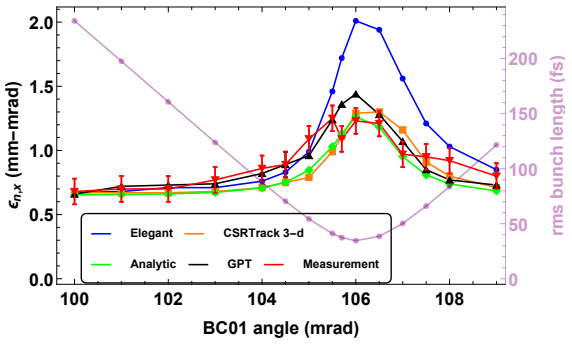

(a) Results from the BC01 angle scan.

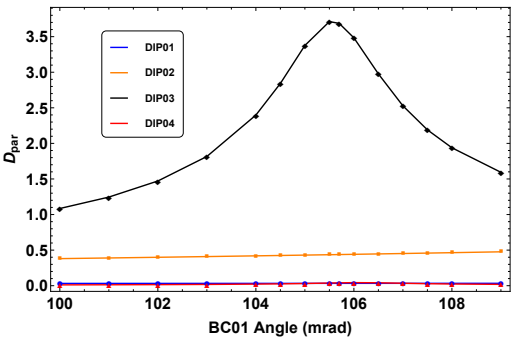

(b) D_{par} at the exit of each bunch compressor dipole for the BC01 angle scan scan.

Figure 4.5: Horizontal emittance as a function of BC01 bending angle, with the corresponding bunch length as simulated by `elegant`. The analytic results are calculated using Eq. 4.10.

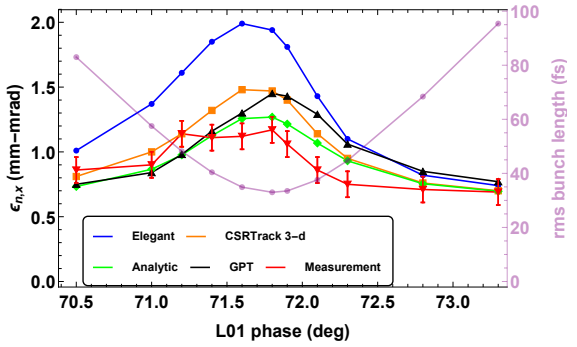

(a) Results from the L01 phase scan.

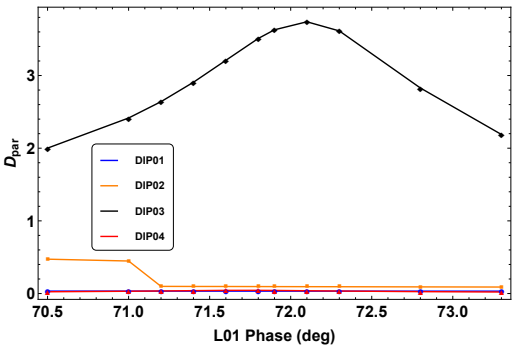

(b) D_{par} at the exit of each bunch compressor dipole for the linac phase scan.

Figure 4.6: Horizontal emittance as a function of Linac 1 phase, with the corresponding bunch length as simulated by `elegant`. The analytic results are calculated using Eq. 4.10.

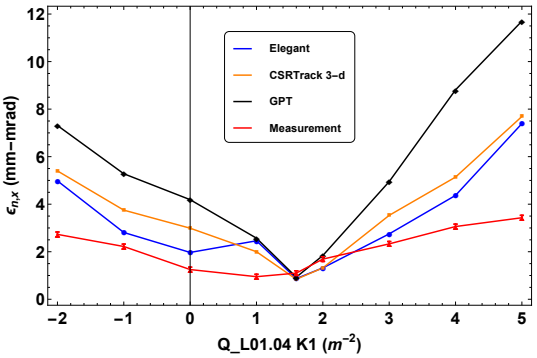

(a) Results from the Q_L01.04 scan.

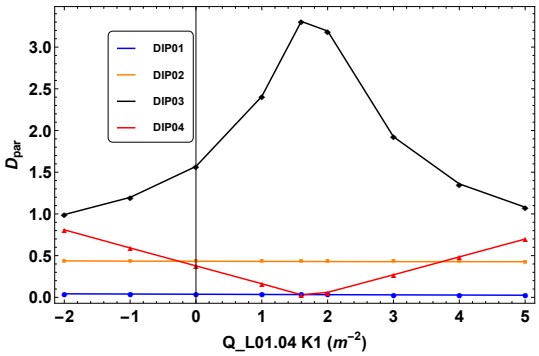

(b) D_{par} at the exit of each bunch compressor dipole for the scan of Q_L01.04 strength.

Figure 4.7: Horizontal emittance as a function of Q_L01.04 strength

As seen from the plots, there is a general agreement between the measurement procedure, simulation results and analytic calculations, at least in terms of the trends. For the scans of Q_L01.04 strength (Fig. 4.7a) in particular, some post-processing was necessary in order to crop some of the images – for a strongly mismatched bunch, some of the bunches were barely visible above the noise. The discrepancy between simulation and experiment in the peak around $71.6 - 72.1°$ in Fig. 4.6a can possibly be attributed to coherent OTR emission (COTR). It has been demonstrated that intense COTR emission can lead to an underestimation of the transverse beam size [23, 118], and thereby to lower measured emittance values. In both sets of experimental data for varying compression factor, there

is a slight dip around the point where a peak in emittance is seen in simulation, which may be evidence for COTR affecting the emittance measurement.

This interpretation is supported by the observation that the largest mismatch between the `elegant` simulation and the two sets of experimental results for this data set occur where the bunch length is around 40 fs or less – this is the point where coherent emission is expected to be maximised. This was corroborated with measurements taken using the YAG screen (not shown in the plots), which followed a similar trend to the measurements taking using the OTR screen. Although the absolute value of the emittance was larger across the range of bunch compression factors (as a result of the YAG screen having lower resolution compared to the OTR screen), the largest emittance growth measured using the YAG screen was found at the point where the compression factor was largest.

A similar apparent overestimation of emittance growth can be observed for the bunch compressor angle scan in Fig. 4.5a for the `elegant` simulation. The difference between the analytical calculations made using Eq. 4.10 and the `elegant` simulations is due to the fact that the simulation neglects the transverse size of the bunch, whereas the theory takes this parameter into account. The transverse extent of the bunch results in a wider radiation cone than that which would result from an infinitely thin bunch, and so the CSR force experienced by a particle will be reduced. GPT and CSRTrack 3D are able to capture both the emittance trend and its absolute value more accurately than `elegant` over the entire range of bunch lengths. It is also possible, however, that shielding of CSR by the vacuum pipes in the bunch compressor could contribute to the mismatch between the simulated and experimental results – this was not a factor included in any of the simulations (although see Sec. 3.2.4 for an explanation of why shielding of CSR is not expected to be significant for this experiment).

One further notable aspect of Figs. 4.5a and 4.6a is the trend of the simulated emittances on either side of maximum compression (the point of minimum bunch length). This point is located at a bunch compressor angle of 106 mrad and around 71.6 ° for the linac phase scan. For larger bending angles, or lower values of the linac phase, the bunch is over-compressed. This means that the bunch has undergone maximum compression in the final dipole magnet, and it exits

the bunch compressor with a bunch length longer than the minimum. Since the minimum bunch length is reached in the magnet, the CSR emission will reach a maximum in the final magnet. Since the `elegant` code appears to overestimate the effect of CSR on the beam emittance, this overestimation will be larger for bunches that have undergone a minimum in bunch length, when compared with under-compressed bunches.

The simulated current profiles for the bunch compressor and linac phase scans are shown in Fig. 4.8. For the linac phase scan, the largest discrepancies between the experimental data and the CSRTrack and GPT simulations occur between linac phase settings of $71.6 - 72.1\,^\circ$ – in this range, the maximum current is greater than 1.3 kA. Comparing the results from simulation and experiment with D_{par}, we observe the most appreciable overestimation of the effect of CSR in the 1D simulation when D_{par} is greater than 2.5 at any point across the chicane. When the value D_{par} is smaller than this value, as during configurations with more moderate compression as in Fig. 4.5a, the agreement between all of the simulations and experimental results is good.

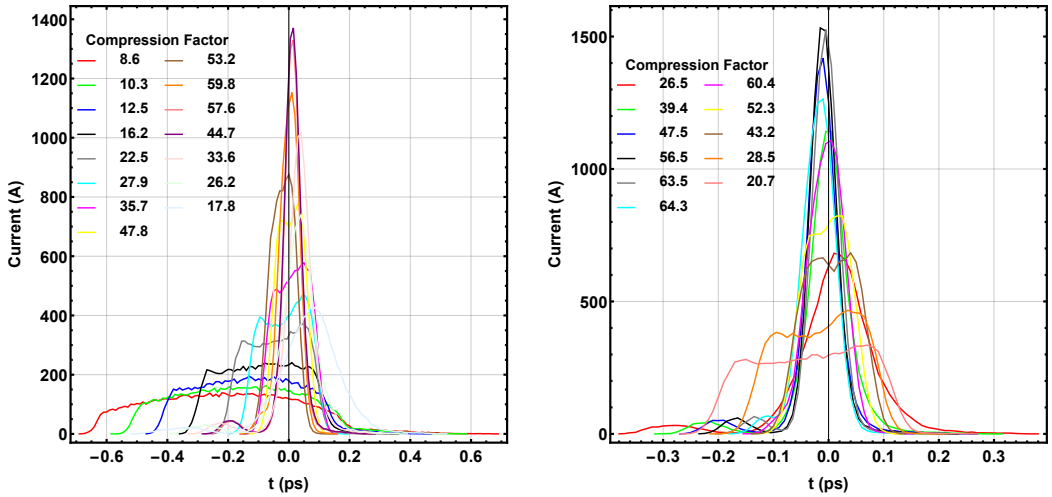

(a) Bunch compressor angle scan.

(b) Linac phase scan.

Figure 4.8: `elegant` simulation of the current profiles for compression factor scans.

The differences between the `elegant` results and those from CSRTrack and GPT simulations are also noteworthy. It appears that, when the bunch undergoes maximum compression (as seen from the minimal bunch length in

Figs. 4.5a and 4.6a), the discrepancy between the 1D and 3D codes is largest, with `elegant` returning an emittance value around 40 % larger than CSRTrack at the peak. GPT does return a slightly higher value for the emittance than CSRTrack and the experimental data around maximal compression. In order to rule out LSC in `elegant` accounting for this difference, the parameter scans were simulated with LSC switched on and off in `elegant`, with only a maximum reduction of 5 % in the projected emittance without LSC. Little variation was seen in the GPT results with space-charge switched off. Comparisons between CSR simulations and experimental data have been studied previously [14, 16, 17], but only for moderate compression factors (up to around 15 at a given bunch compressor).

Indeed, at moderate compression factors – up to around $15 - 20$, at which point the bunch length approaches 100 fs, we see relatively good agreement between the codes and experimental data to within 10 %. It can also be seen that the analytic calculations of Eq. 4.10 reflect the experimental measurements and the GPT and CSRTrack simulations quite well, despite the Derbenev criterion being violated for large bunch compression factors. The fact that the codes which calculate the CSR fields directly from the retarded potentials give a closer agreement with experimental data further suggests that there are limits to the applicability of 1D simulations of CSR.

As the compression factor is increased – up to a maximum value of 64 – more significant discrepancies between the simulation results appear. It appears that there is an overestimation of the effects of CSR in `elegant`. By comparing the simulated slice properties for various compression factors, we can try to observe where the discrepancies arise. In order to isolate the effects of CSR, the parameter scans were run in `elegant` and CSRTrack 1D with CSR switched off (see Figs. 4.9a and 4.10a). The agreement between the codes in this case is good, and from this we can conclude that CSR *is* the dominant process causing the projected emittance growth.

Now, if the same set of parameter scans are run again with CSR switched on, (see Figs. 4.9b and 4.10b), it can be seen that, towards maximal compression, the `elegant` simulation returns a higher value for the horizontal slice emittance in the

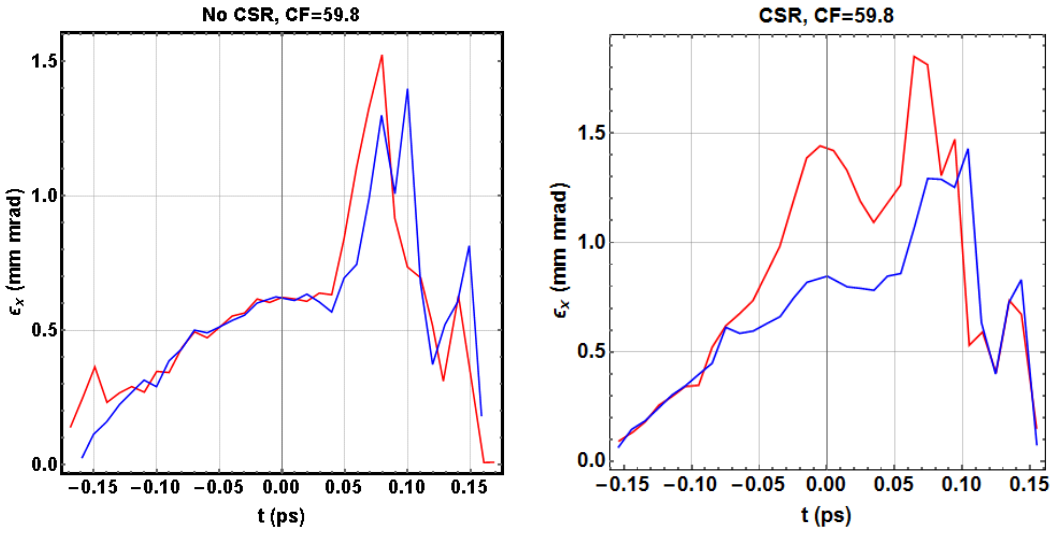

(a) (b)

Figure 4.9: Slice emittance for maximum compression in the bunch compressor angle scan as simulated by `elegant` (Red) and CSRTrack 1D (Blue), without, and with, CSR.

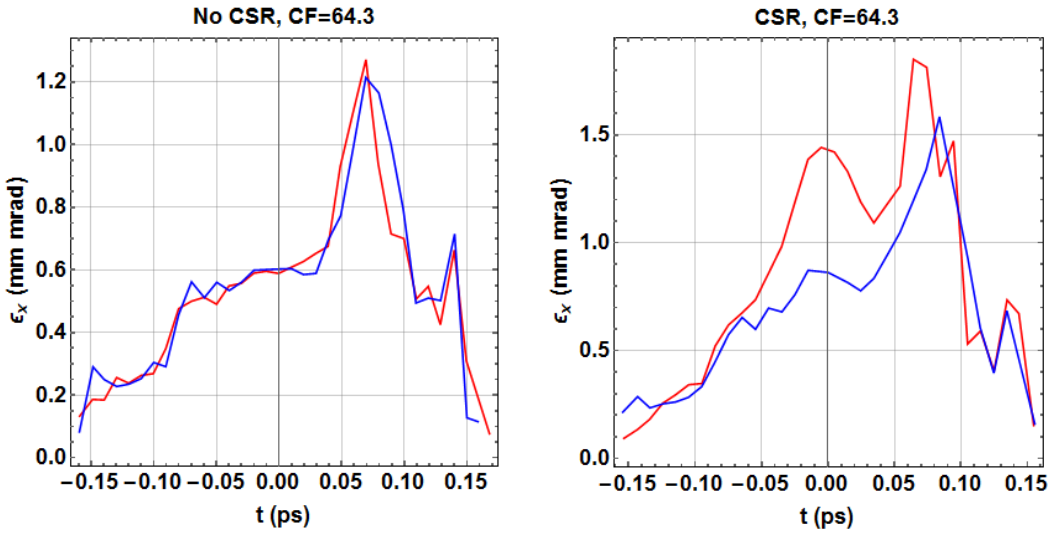

(a) (b)

Figure 4.10: Slice emittance for maximum compression in the linac phase scan as simulated by `elegant` (Red) and CSRTrack 1D (Blue), without, and with, CSR.

central portions of the bunch as compared with the results from the CSRTrack 1D simulation. This is the region where, for a bunch with a Gaussian longitudinal distribution, the steady-state CSR wake is largest, due to the greater density of particles in this region. Slice emittance values at lower compression values (on either side of the maximum) show good agreement between the codes. The vertical emittance and current profiles are almost identical in all compression

scenarios.

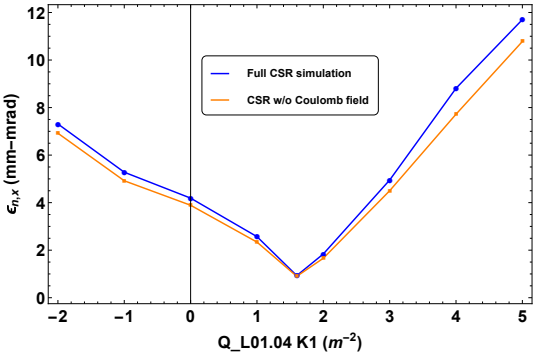

(a) Q_L01.04 scan.

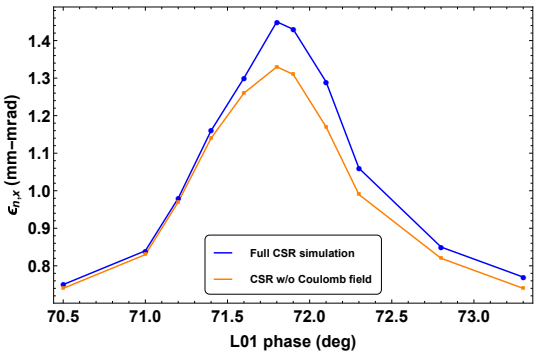

(b) Linac phase scan.

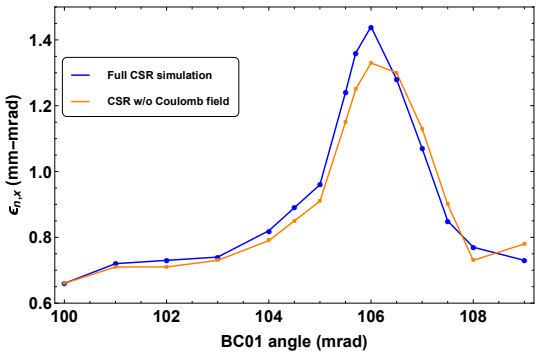

(c) Bunch compressor angle scan.

Figure 4.11: GPT simulation of emittance growth in the three scans with and without the Coulomb term of the Liénard-Wiechert field.

Another noteworthy effect of the Liénard-Wiechert potentials in strong compression scenarios is revealed by the GPT simulation. Plots comparing the final projected emittance as simulated by GPT for the three parameter scans are shown in Figs. 4.11a, 4.11b and 4.11c, with the Coulomb term switched on and off. It can be seen that, approaching maximal compression, or largest transverse bunch size, the Coulomb term can have a considerable impact (up to 10 %) on the final CSR-induced emittance growth. In the case of a larger bending angle in the chicane, this can be understood as the catch-up distance for the Coulomb term being shorter, and similarly for a bunch with minimal chirp around the linac phase for maximal compression. When the bunch has a larger transverse size due to the focusing into the chicane, the radiating cone is also larger, and so the Coulomb interaction between the tail and head of the bunch will also make a larger contribution. It is also likely that this neglected term will have a more significant impact for accelerator configurations with a higher density of

bends, such as in arcs in energy recovery linacs (ERLs). These results give further evidence of the importance of correctly simulating CSR effects in dispersive regions.

4.6 Summary

This chapter has presented a study of CSR-induced emittance growth in the first bunch compressor of the FERMI linac across a range of beam parameters. As described in Chapters 2 and 3, finding an agreement between measurement, theory and simulation in the field of collective effects in this field has been a long-standing issue. The measurements presented in this chapter, and the corresponding simulations and analytic calculations, show good agreement for a range of bunch compression factors (a factor of almost an order of magnitude). The experimental measurements show that, as the bunch length decreased to the minimum value across the scans of bunch compression factor, the projected emittance after compression reached a maximum. This is in good agreement with the theory of CSR (see Sec. 2.2), which states that the radiated CSR power is inversely proportional to the bunch length. Three simulation codes have been used to simulate these experimental measurements – two of which (GPT and CSRTrack) calculate the CSR interaction between emitting and receiving particles directly using the Liénard-Wiechert potentials (Eq. 2.31), with some simplifications to reduce the computational load, and one which uses the 1D CSR theory (`elegant`), neglecting the transverse extent of the bunch. As expected, the codes which are not limited by the 1D approximation provide better agreement with the experimental measurements.

One further aspect of this study aimed to investigate the limits of the theory of CSR, whose validity is limited by the ratio between the transverse and longitudinal bunch size, and the bending radius of the dipole magnets in the bunch compressor. The theory should be invalidated if the transverse size of the bunch becomes considerable when compared with the bunch length (i.e. if D_{par} is not much less than 1, see Eq. 4.11). This invalidation condition was met during the experiment for the largest values of the bunch compression factor, reaching a

maximum value of $D_{par} \approx 3$. The predicted emittance growth for the beam and lattice parameters of this experiment has been calculated and compared with the results from simulation and experiment, and good agreement was found between all of these (except for the results from the `elegant` code), suggesting that the theory described in Sec. 2.2 may be more robust than expected, at least in terms of describing the projected growth in beam emittance due to CSR.

Chapter 5

Microbunching Measurements

Laser heaters have proven to be invaluable components of high-energy free-electron lasers (FELs) [27, 28, 29], utilised in order to suppress the microbunching instability [22, 25, 61], a collective effect that can develop due to shot noise [66] in the injector of such a machine, and undergo amplification due to space-charge [68] and coherent synchrotron radiation effects [22] (see Sec. 2.3). Any small-scale structure in an electron bunch can develop and amplify during acceleration, leading to deleterious effects in the FEL process at the high-energy end of the machine. The laser heater in its nominal configuration consists of a small dispersive chicane, in the centre of which is an undulator (see Sec. 2.4.1). Propagating simultaneously with the electron beam in the undulator is a laser pulse which imposes an energy modulation on the beam. Since the wavelength of the laser is much shorter than the electron bunch length, the paths travelled by particles with different energies through the second half of this chicane will then overlap in longitudinal phase space. This process therefore removes the modulation, also causing a slice energy spread increase across the bunch, which prevents the development of the microbunching instability in the remainder of the accelerator lattice.

Recent experiments at the FERMI FEL [13] have investigated the possibility of using a non-uniform laser pulse to impose modulations on the bunch, thereby seeding the microbunching instability (see Sec. 2.4.3 and Ref. [92]). This is achieved through chirped-pulse beating of the laser heater pulse, in which the pulse is chirped and separated, then recombined with a variable delay [97]. The

beating frequency of this chirped pulse is then proportional to the delay between the two pulses, and the wavelength of the pulse can approach the same order as the electron bunch length. The imposition of such a laser pulse onto the electron bunch leads initially to an energy modulation, which is then converted into a density modulation at the exit of the laser heater chicane. Due to longitudinal space-charge forces, there is a plasma oscillation between energy and density modulations that develops along the machine (see Sec. 2.3.2 and Ref. [19]), and so the final orientation of the microbunches in the bunch longitudinal phase space will be a function of this plasma oscillation frequency. (See Sec. 2.3.6 for an analytic model of a microbunched beam with varying microbunch orientation angles.)

The ability of computational codes to simulate microbunching is an active area of research, and this chapter will also present simulations of the experiments outlined above. By using the `elegant` simulation code (see Sec. 3.1.1), it is possible to simulate the large numbers of particles required to reproduce the effects of microbunching. As mentioned in Sec. 2.4.3, the code can also simulate the electron-laser interaction within the laser heater, and the user can define a custom laser pulse corresponding to the intensity profile produced by chirped-pulse beating.

In this chapter, results will be presented from an experiment which aimed to develop an understanding of the development, mitigation, and stimulation of, the microbunching instability. The machine and experimental parameter range, and the method for analysing the beam longitudinal phase space, are outlined in Sec. 5.1. The image analysis techniques, and measurements of the bulk longitudinal phase space, are given in Sec. 5.2. These techniques are applied in Sec. 5.3 to analyse the measured slice energy spread increase on the bunch due to the use of the laser heater. Studies of the 'natural' microbunching, which develops without the intervention of a laser heater, and of the laser heater in its nominal configuration, are given in Sec. 5.4. In order to study the microbunching parameters of interest, in particlar the modulation frequency and bunching factor, we have developed a novel method of analysing the longitudinal phase space of such beams using two-dimensional Fourier analysis. This method has the added

benefit of providing two more parameters of interest: the energy chirp of the bunch (that is, a measure of the correlation between the position of an electron in the bunch and its energy – see Sec. 2.1.4), and the angle of orientation of the microbunches with respect to the total bunch. This latter parameter is of interest for understanding the plasma oscillations undergone by the bunch due to longitudinal space-charge forces (see Sec. 2.3.2). In Sec. 5.5, this analysis technique will be applied to study induced microbunching, in which the chirped-pulse beating technique (see Sec. 2.4.3) was used on the laser heater pulse to seed microbunching in the electron beam, over a range of laser and lattice parameters. Example measurements of the longitudinal phase space of these experiments are shown, and in Sec. 5.6, along with analysis and discussion of the microbunching parameters of these beams. Simulations of these experiments have also been conducted. The bunching factor, modulation period in energy and time, and plasma oscillation phase produced by these simulations are the main parameters of interest to provide a benchmark between simulation and experiment.

5.1 Introduction to Microbunching Studies

Electron bunch compression in the accelerating section of the FERMI FEL can be achieved using two four-dipole chicanes. The bending angles of these chicanes can be varied, meaning that three possible bunch compression scenarios are available: using the first or second chicanes only (BC1 or BC2, respectively: the 'single compression' schemes), or using both in tandem (BC1+BC2: 'double compression'). The evolution of small-scale structure in a bunch is highly dependent on the LSC and CSR interactions during transport through the accelerator (see Sec. 2.3), and so the point(s) at which the bunch is compressed can influence the microbunching gain, frequency and plasma oscillation phase. These parameters can be investigated experimentally by studying the longitudinal phase space of electron beams at the exit of the accelerating section of the FERMI linac. The longitudinal phase space can be measured through the use of a transverse deflecting cavity (TDC) and a dipole magnet [85, 119].

A TDC, or vertical RF deflector (VRFD), acts to streak the beam along the

desired plane. In the case of the FERMI vertical deflector, the deflecting phase is set such that the voltage is zero in the centre of the bunch (its 'centroid') and gives a vertical deflection that varies (approximately) linearly from the head to the tail of the bunch. Since the vertical trajectory of an electron in the bunch then depends on its longitudinal position, the temporal profile of the bunch can be observed on a screen at a downstream location. When coupled with a dipole magnet, which deflects particles horizontally according to their energy, it is possible to obtain an image representing the distribution of particles in longitudinal phase space.

The vertical position of a particle on the observation screen depends on its deflection in the TDC through the element R_{34} of the transfer matrix from the cavity to the screen. This can be controlled through the optics of the beamline, to optimise the temporal resolution of the longitudinal phase space measurement. In order to calculate this accurately, errors due to the screen pixel size, to the beam non-zero vertical emittance ϵ_y, and to the TDC-induced energy spread (defined below) must be taken into account when calculating the slice energy spread (SES). The spread of longitudinal momentum $\sigma_{\delta,\mathrm{TDC}}$ is dependent on the vertical position of particles within the cavity, and so it can therefore provide a measurement of the bunch length. Given the beam mean energy $E \approx \bar{p}_z c$, where $\bar{p_z}$ is the beam central longitudinal momentum, evaluated at a distance of σ_z from the bunch centroid, the rms value of $\sigma_{\delta,\mathrm{TDC}}$ is [120]:

$$\sigma_{\delta,\mathrm{TDC}} \approx \frac{eV_{\mathrm{rf}}k_{\mathrm{rf}}}{2\bar{p}_z c}\sqrt{\left(\frac{eV_{\mathrm{rf}}k_{\mathrm{rf}}}{2\bar{p}_z c}\right)\frac{L}{3}^2\sigma_z^2 + \epsilon_y\beta_{y,\mathrm{TDC}}}, \tag{5.1}$$

with $V_{\mathrm{rf}} \approx 19\,\mathrm{MV}$, $k_{\mathrm{rf}} = 62.8\,\mathrm{m}^{-1}$ the voltage and wavenumber of the TDC with length $L = 3.5\,\mathrm{m}$, and $\beta_{y,\mathrm{TDC}} \approx 25\,\mathrm{m}$ the average vertical betatron function in the TDC. Measurements of the beam optics parameters, of the SES vs. the deflector RF power attenuation factor, and the evaluation of the effective peak deflecting voltage, led to estimated temporal and energy resolutions of $\approx 10\,\mathrm{fs}$ and $70\,\mathrm{keV}$, respectively.

The FERMI energy spread measurements produce files consisting of the images taken during the measurements, along with metadata containing various machine settings. This metadata includes:

- Pixels per mm.
- Laser heater actuator (intensity).
- Magnet / RF settings and measured parameters.
- Measurements from diagnostic devices.

The final goal for this measurement procedure is to be able to correlate the machine parameters with the measured microbunching parameters. The details of this post-processing of images will be presented throughout the remainder of this chapter. The algorithm for analysing images and extracting microbunching parameters executes the following operations:

1. **Image Fitting**:
   (a) Calculate, based on the TDC parameters, the dipole current and the pixel size, the calibration factors in the longitudinal and energy axes.
   (b) Select a rectangular portion of the full image based on a Gaussian fit in the horizontal and vertical directions.
   (c) Extract from these fits the current and energy profile, and the bunch length and total energy spread.
2. **Fourier transform and Region of Interest selection**:
   (a) Calculate the Fourier transform of the bunch image.
   (b) From the calibration factors measured in real space, calculate the pixel resolution in Fourier space.
   (c) Normalise the intensity of this image such that the maximum value (in the centre) is equal to 1.
   (d) Select a portion of this image that contains the region of interest; in this case, the satellites around the central (DC) term that represent the modulations on the bunch.
3. **Microbunching parameter extraction**

(a) From this portion of the image, the bunching factor (Fourier transform image intensity) as a function of frequency (in either the energy or longitudinal dimension) is measured, along with the plasma oscillation angle (the arctangent of the ratio between these two frequencies at a given point). See Sec. 5.4 below for more details.

This procedure is then repeated for a number of shots, and statistical analysis is performed. Save for step 2.(d), which requires some user intervention to determine the region of interest, this routine is automated. The details concerning a number of the steps in this procedure are given throughout the remainder of this chapter.

Nine different accelerator lattice and laser heater configurations were used during this experiment for the purposes of investigating the longitudinal phase space microbunching at the exit of the FERMI linac – see Table 5.1 for a summary of the beam parameters for each lattice configuration. The point at which the compression occurs, and the relative strength of the compression, has an influence on both the final predicted bunching factor and the microbunching gain as a function of initial modulation, and so it is instructive to compare the microbunching across these three lattice configurations. The theory of microbunching (see Sec. 2.3) predicts the largest amplification of bunch modulations for a double compression scheme over the single compression cases, and so the three lattice configurations investigated in this chapter will aim to validate this prediction (see Secs. 5.4 and 5.6 below). The chirped-pulse beating method applied to the laser heater (see Sec. 2.4.3) can also be used to investigate the microbunching gain in more detail (see Sec. 5.5 below): by applying a modulation with a known frequency on the bunch, and observing the final bunching factor, it is possible in principle to experimentally reconstruct the microbunching gain curve.

For each of these bunch compression scenarios, three different laser heater configurations were employed. Firstly, in order to study the 'natural' microbunching, the laser was switched off. Secondly, the laser heater was used in its nominal configuration: the laser pulse – Gaussian in both transverse and longitudinal dimensions – co-propagated with the beam travelling through the laser heater undulator, adding an uncorrelated energy spread to the entire beam. This was

Table 5.1: Main measured beam parameters of the FERMI accelerator for the three compression schemes. Except where stated, the values correspond to the bunch parameters at the end of Linac 4.

Bunch parameters	**Unit**	**BC1 only**	**BC2 only**	**BC1+BC2**
Bunch charge	pC	100	100	100
Final beam energy	MeV	787	713	754
Beam energy at bunch compressor	MeV	297	427	307, 707
Bunch length (rms)	fs	54	37	62
Chicane bending angle	mrad	105	90	$105 + 85$
R_{56}	mm	-62.5	-40.9	$-62.5, -40.9$
Peak current	A	550	800	480
Relative σ_δ (rms)	%	0.1	0.15	0.3
Energy chirp at BC	m^{-1}	≈ -15.5	≈ -23.8	$\approx -11.9, -21.5$
Energy chirp at DBD	m^{-1}	≈ -20	≈ -85	≈ -110

done for a range of laser pulse energies. Thirdly, the chirped-pulse beating technique (see Sec. 2.4.3) was applied to the laser heater pulse, in order to impose modulations on the bunch longitudinal phase space. This was done for all three lattice configurations, over a range of laser pulse energies and chirped-pulse beating delays, which varied the intensity profile and beating wavelength of the laser pulse.

5.2 Image Analysis

This section gives a description of the methods used to analyse the longitudinal phase space images. A system consisting of a vertical RF deflector together with a horizontally bending dipole can provide a measurement of the distribution of particles in longitudinal phase space, showing the particle density as a function of longitudinal position (with respect to the centroid of the bunch) and particle energy. The microbunching instability is known to affect the beam distribution in terms of both the longitudinal profile and the energy profile (see Sec. 2.3), and so a measurement of these beam properties proves to be useful in quantifying the modulations in the bunch. Such measurements are also useful for filtering out images whose longitudinal phase space properties diverge largely from the average, due primarily to jitter in the RF linacs in the machine. In this section, the methods used for measuring the bulk properties of the longitudinal phase space (bunch length and slice energy spread) are described and applied.

5.2.1 Current Profile Measurements

The bunch compression process is strongly dependent on the relative RF phase that the bunch experiences before compression, as this has an influence on the chirp of the bunch (see Eq. 2.29). In particular, during the experiment it was observed that the phase jitter of the X-band linearising cavity was causing bunch-to-bunch variation in the bunch length. As a result of the larger electric field gradient in this cavity (11.9 GHz as compared with the 2.9 GHz S-band cavities in the accelerating linacs), phase jitter in the X-band cavity leads to a larger change in the RF field, which then results in a larger bunch length variation.

Fig. 5.1a shows the correlation between a number of RF phase parameters at each of the FERMI klystrons and the final bunch length for bunches compressed using BC1-only. It can be seen clearly that klystron number 4 (K04) is most strongly correlated with the bunch length – this klystron is the driver for the X-band lineariser. In Fig. 5.1b the bunch length is plotted as a function of the measured phase. A correlation can be seen here, with the bunch length varying by up to a factor of two from shot to shot. There is not a one-to-one correlation here between bunch length and X-band cavity phase, as a number of other parameters also contribute to a variation in the compression, but this RF phase provided by far the most significant contribution to bunch length jitter during the experiment.

The final microbunching modulation wavelength depends on the ratio between an initial (i.e. pre-compressed) modulation in the bunch and the compression factor. For this reason, the experimental data was filtered based on the current profile of the measured bunches. Given a total bunch charge Q of 100 pC – which did not vary greatly during the experiment – the current profile $I(t)$ can be determined using the following formula:

$$I(t) = \frac{Q \cdot \Sigma\mathbf{X}(t)}{\Delta t \cdot \Sigma\mathbf{X}}, \tag{5.2}$$

where $\mathbf{X}$ represents the intensity of a pixel in the bunch, $\Sigma\mathbf{X}(t)$ represents the total intensity of a slice along the temporal axis, $\Sigma\mathbf{X}$ gives the total pixel intensity of the image, and Δt is the temporal resolution of the image (around 10 fs, as

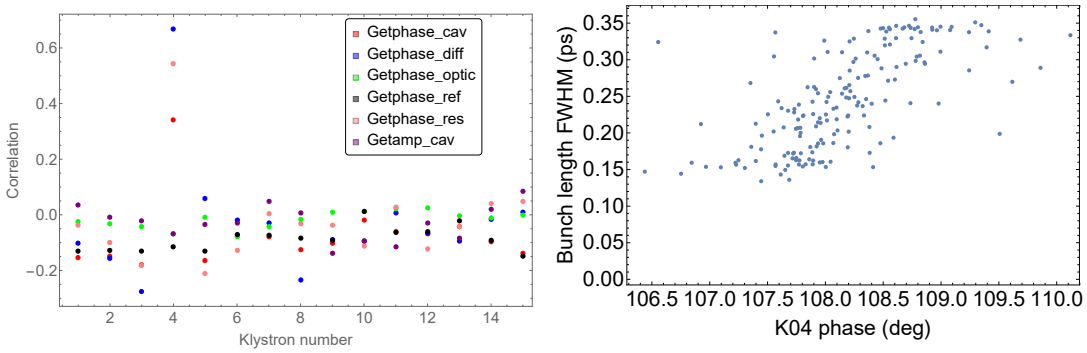

(a) Correlation between a number of phase parameters at all klystrons used to drive the FERMI RF structures and the measured final bunch length. The parameters in the legend refer to the parameters labelled in the metadata associated with the measurement set.

(b) Final measured bunch length as a function of K04 phase – this is the klystron used to drive the X-band linearising cavity.

Figure 5.1: Correlation between RF phase parameters and final measured bunch length for the BC1-only lattice configuration.

described above in Sec. 5.1). The bunch length is calculated as the FWHM of the current profile $I(t)$.

During the experiment, the goal was to maintain the bunch compression factor such that the final bunch length was the same across all three bunch compressor configurations. The current in the centre of the bunch was in the range 500–700 A. Fig. 5.2a shows a histogram of the measured FWHM bunch length over 200 shots. In order to analyse only those bunches with a similar compression factor (assuming the same initial bunch length), therefore maintaining the same final bunching period, the microbunching analysis performed below (Sec. 5.4) was performed only on those bunches whose bunch length fell within 10 % of the mean value. Fig. 5.2b shows the distribution of bunch lengths in this range.

The reason for choosing only the images corresponding to bunches within this range is to ensure a flat-top current profile in the bunch core, in addition to attempting to preserve the microbunching period across a number of images, as this period is dependent on the compression factor. As shown in Fig. 5.2a, there was a significant variation in the bunch length, with a considerable number of bunches that were compressed 1.5–2 times as much as others. Fig. 5.3 shows the averaged current profiles for both the full set of measurements and the reduced subset; it can be seen that the latter set of measurements better preserves the

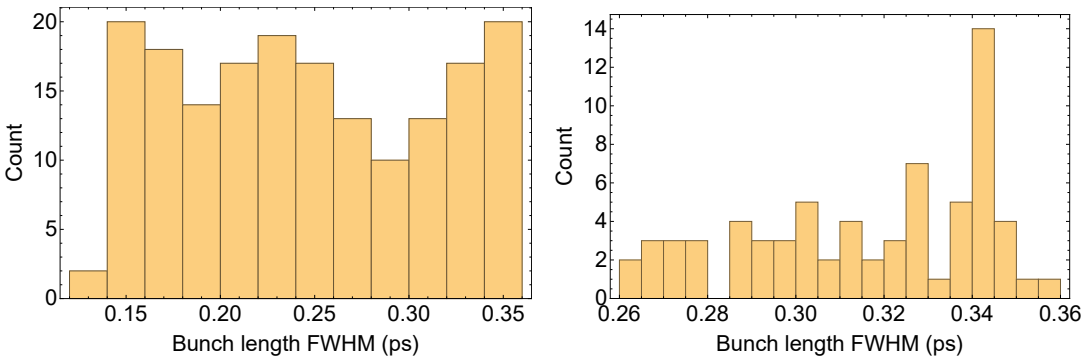

(a) All 200 images.

(b) Subset of shots with the desired current profile (70 images).

Figure 5.2: Histogram of measured bunch length (FWHM) for bunches compressed using BC1-only.

flat-top current profile desired for this experiment.

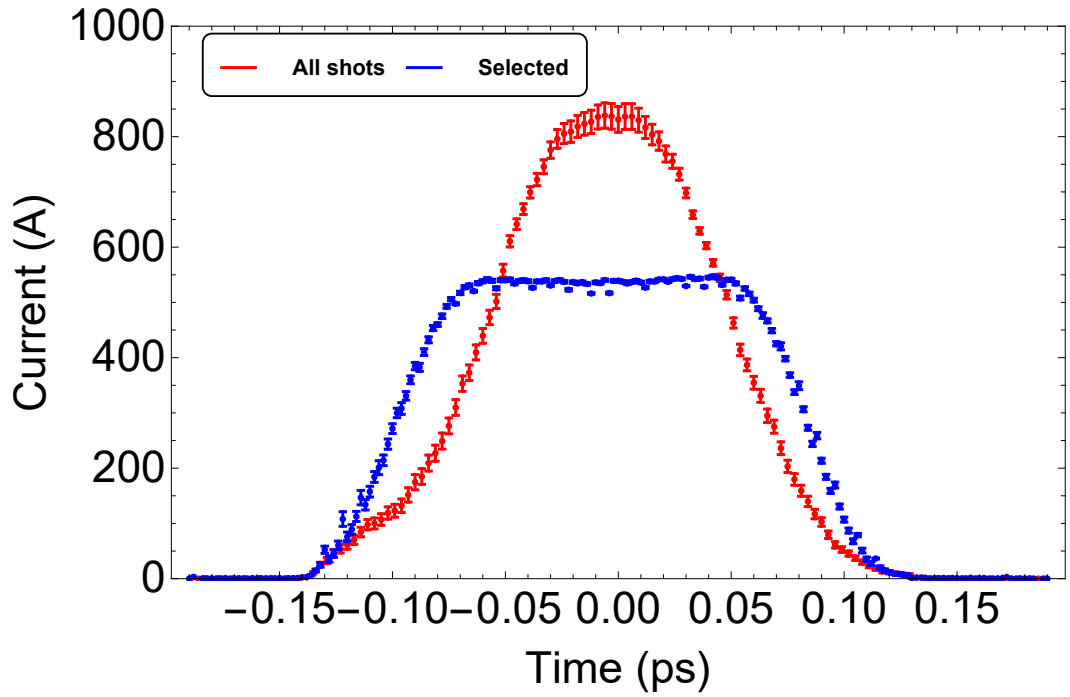

Figure 5.3: Current profile (measured) for bunches compressed using BC1-only. The curve in red shows the mean current profile across all 200 shots, whereas the blue curve gives the mean over the selected subset of bunches with the desired current profile. The error bars represent the standard error across the measurement sets.

For sets of measurements corresponding to the two other bunch compressor configurations, the jitter was not as pronounced, as the compression process is not as strongly dependent on the phase of the linearising cavity, which is slightly

upstream of the entrance to BC1. In order to ensure that the microbunching and energy spread analysis gave consistent results – that is, for cases where the bulk longitudinal phase spaces did not largely diverge from one another – only bunches whose current profile fell within the specified range were analysed. This shot selection procedure is more complicated in the case of strong microbunching, as the current profile is not smooth. In this case, a Gaussian fit was applied to the measured bunch length, and shots were analysed if the width of this Gaussian fit fell within one standard deviation of the mean bunch length across all measurements.

5.2.2 Slice Energy Spread Measurements

A similar process to that described above in Sec. 5.2.1 can be used to determine the slice energy spread of the bunch. Since the transverse deflecting cavity provides a full single-shot measurement of the bunch longitudinal phase space, the energy spread of the bunch as a function of longitudinal position can be determined.

The slice energy spread $\sigma_E(t)$ at some position in time along the bunch t can be measured by fitting a Gaussian to a 1D projection of the bunch along the slice. The measured slice energy spread along the bunch for the case of BC1-only compression without the laser heater is shown in Fig. 5.4. The bunch images used to produce this figure were in the same subset as those shown above in Fig. 5.3.

It can be seen that, throughout the core of the bunch – within the region $\approx \pm 0.05\,\text{ps}$ from the centre – the mean slice energy spread is $0.187 \pm 0.004\,\text{MeV}$. As shown in Fig. 5.3, outside of this range, the current profile drops sharply. This means that the fitting of the slice energy spread is no longer reliable, and so the measured slice energy spread at the head and tail of the bunch increases. Within the region of interest (the core of the bunch), there is little variation in slice energy spread across the bunch core.

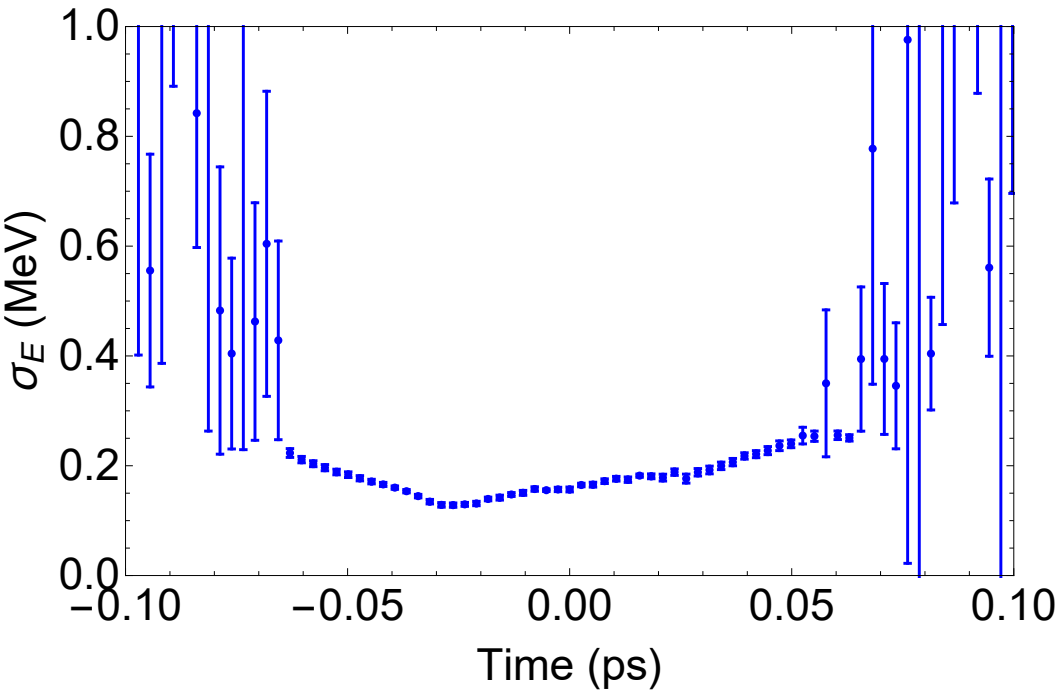

Figure 5.4: Slice energy spread (measured) for bunches compressed using BC1-only. The images analysed for this plot are the same as those used to produce the blue curve in Fig. 5.3. The error bars represent the standard error across the measurement set.

5.3 Energy Spread Induced by the Laser Heater

The energy spread and the temporal resolution of the diagnostic system, considering limitations from beam optics, calibration error of the beam stretching and screen spatial resolution, was estimated respectively to be 70 keV and 10 fs (rms values). According to particle tracking runs using GPT [101] (see Sec. 4.2), the uncorrelated (slice) beam energy spread out of the injector – once the space charge forces internal to the bunch are mostly suppressed by the ultra-relativistic motion – is predicted to be approximately 2 keV rms in the bunch core (see Fig. 5.5).

The laser heater parameters are given in Table 5.2. For more details on the system, see Ref. [28]. The slice energy spread (SES) measured at the DBD screen as a function of the laser heater energy added is shown in Fig. 5.6 for all three compression scenarios. In this case, only the mean SES of the bunch core has been calculated. This is for two reasons: strong nonlinear compression in the head and tail of the bunch can sometimes lead to the generation of current

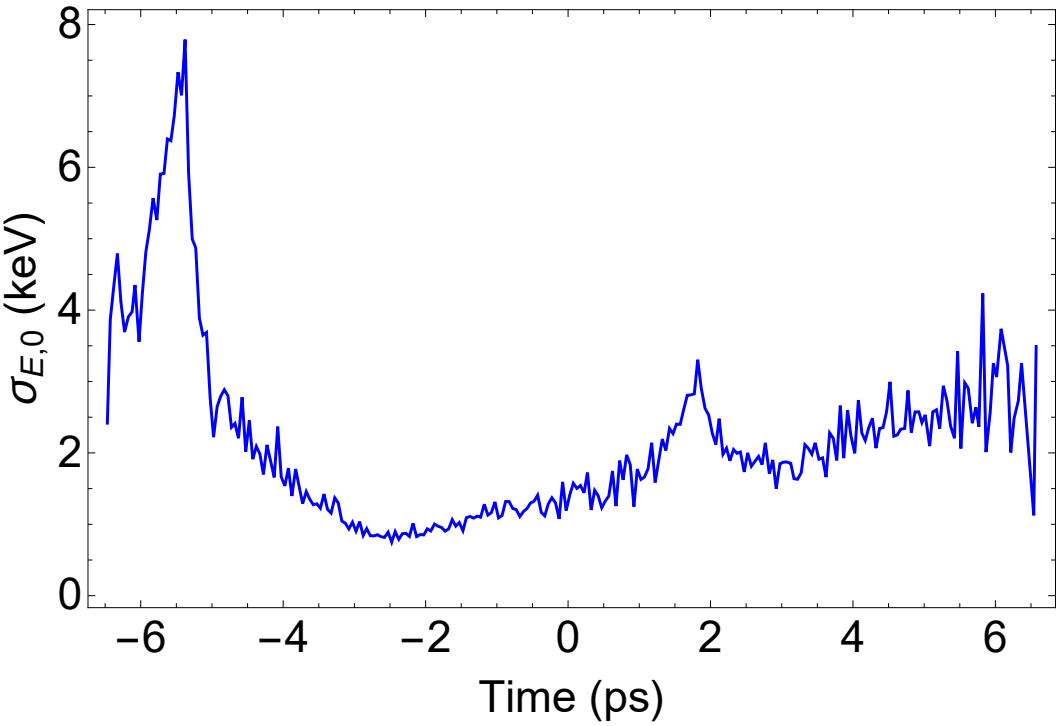

Figure 5.5: Slice energy spread at the exit of the FERMI injector as simulated by GPT.

Table 5.2: FERMI laser heater system parameters

BEAM TRANSPORT	
Chicane magnet bend angle	3.5 °
Transverse offset in chicane	30 mm
Dispersion	60 cm
Beam energy	96 MeV
Emittance	0.35 mm − mrad
Transverse beam size	70 µm
UNDULATOR	
Period	40 mm
Number of full periods	12
Undulator parameter K	0.88
LASER	
Wavelength	783 nm
Spot size	120 µm
Pulse length (FWHM)	16.5 ps
Pulse length (stretched)	7.02 ps
Pulse energy (maxmimum)	16.7 µJ
Spectral bandwidth	5 nm
Linear chirp coefficient	$-1.5 \times 10^{23}\,\mathrm{s}^{-2}$
Delay between pulses	4–30 ps

spikes, which distorts the measurement; and, as mentioned above (Sec. 5.2.1), if the current profile drops off at the head and tail of the bunch, then the fitting of the SES is not as reliable.

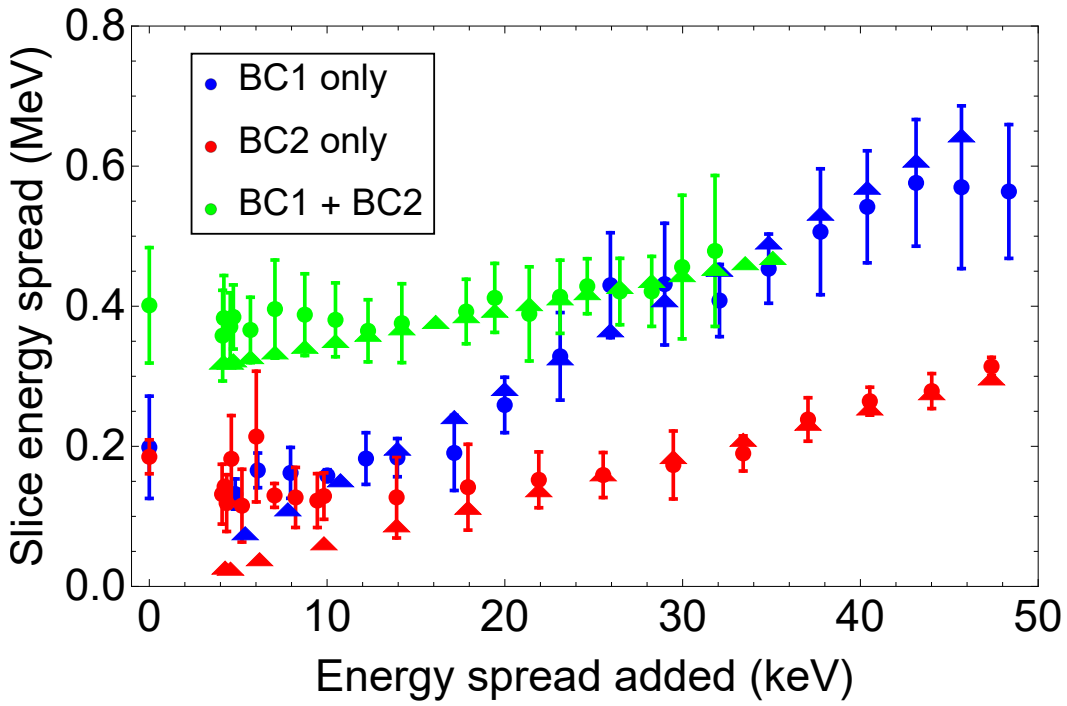

Figure 5.6: Slice energy spread at the bunch core, measured at the end of the linac, as a function of the energy spread added by the laser heater for all three compression scenarios. Circles show the measured values, and the triangles use Eq. 2.78, taking into account the decompression by the spectrometer dipole.

First, we notice that the SES associated with null or weak LH action (up to 10 keV of added energy spread) is comparable in the BC1 and BC2 schemes, and much larger in the BC1+BC2 scenario, in spite of the lower total compression factor compared to the single stage compressions. This is consistent with theoretical predictions of the microbunching gain, according to which, once the peak current is partially increased by the first compressor, the second compressor then causes the energy modulation cumulated upstream to be converted into amplified bunching [121, 22]. This in turn drives larger energy modulations, resulting in a larger SES at the linac end. In that sense, the larger SES of the double compression is a clear signature of stronger instability gain.

At the same time, in spite of a higher final peak current in the BC2-only scheme with respect to BC1-only, the SES is comparable in these two cases.

This is explained by the fact that, in the former scheme, a much lower peak current (around 18 A) propagates through the injector-to-BC2 linac section than in the latter. Therefore, the naturally low bunching factor of the initial beam generates much lower energy modulation at the entrance of BC2 than the already compressed beam in BC1 does. This way, the degrading effect of a higher peak current at the exit of BC2 is counterbalanced by the lower amount of energy modulation cumulated up to that point. This allows one to conclude that a high final peak current is not the only factor leading to a higher instability gain. Instead, the evolution of the beam properties along the entire beam line should be considered.

Second, we note that at very strong heating (from 20 keV and higher added energy spread) the instability is expected to be partly or fully suppressed, and therefore the SES should follow a linear dependence from the LH-induced energy spread, where the proportionality should be just the linear compression factor [46]. Though a linear dependence of the SES on the LH-induced energy spread is apparent in the figure, the slope is not as high as expected. The reason for this is that the bunch length increases as the beam passes through the DBD spectrometer magnet, in the presence of a relatively large linear energy chirp (see Table 5.1). In this case, the bunch length can be reconstructed from the beam image at the screen as it was at the deflector location (i.e. at the nominal compression factor).

The SES, instead, is decreased by the same amount the bunch is lengthened in the dipole magnet. The analysis of the images for the three compression schemes confirms that the energy chirp at the dipole is approximately 20 m^{-1}, 85 m^{-1} and 110 m^{-1} for the BC1, BC2 and BC1+BC2 scheme, respectively. Once coupled to the dipole longitudinal dispersion, $R_{56} = 0.12$ m, that chirp reduces the nominal compression factor, and therefore the SES cumulated up to that point, by factors of approximately 3, 13 and 16 respectively. This scaling only holds in the region of strong beam heating, which allows the longitudinal emittance to be approximately preserved during magnetic (de-)compression. For heating level lower than 20 keV, the microbunching instability is still playing a role. In fact, a minimum of the SES is barely visible for the single compression schemes, for

the LH set at around 5–8 keV. Also plotted in Fig. 5.6 is a theoretical evaluation of the slice energy spread added by the laser heater, using Eq. 2.78, taking this decompression effect into account. It can be seen that the predicted values match up well with the measured SES. Eq. 2.78 does not take microbunching into account, and so the fact that there is a linear trend in the SES for increasing laser heater pulse energy above 10 keV suggests that the microbunching has been removed beyond this point.

Theoretical evaluations of the gain curve associated with the CSR impedance only as introduced in [121, 22] (Sec. 2.3.3), indicate that, for all the three compression schemes, the CSR-induced microbunching is negligible compared to the effect of the LSC impedance [26]: the peak CSR gain is typically around unity, and is one or two orders of magnitude lower than that associated with LSC. Consequently, the impact of CSR on the final SES is also very small (for an estimate of the SES and its dependence on the total gain, see e.g., Eq. 17 in [61]). The gain in microbunching as a function of initial modulation wavelength is plotted for the three compression schemes in Fig. 5.7, taking into account the beam and lattice parameters through the machine. The calculation takes into account CSR and LSC effects, and additionally the effect of intrabeam scattering (IBS) [64] (Sec. 2.3). It can be seen that maximum gain for the single compression schemes are around half that of the double compression scheme, in which case the IBS effect substantially damps the microbunching upon entrance to BC2.

Particle tracking runs for the FERMI injector have been conducted with the GPT code [101] (for more details on these simulations, see Sec. 4.2). These simulations have provided an estimate for the uncorrelated (slice) beam energy spread out of the injector, once the space charge forces internal to the bunch are mostly suppressed by the ultra-relativistic motion, predicted to be approximately 2 keV rms in the bunch core. In the presence of a total compression factor of 35 as in the BC1-only case, for example, and in the absence of the instability, the preservation of the beam longitudinal emittance predicts a final value around 70 keV. The measured minimum SES is larger than this, as a signature of residual instability action in the longitudinal phase space at low heating levels. It is only once the microbunching has been removed (above approximately 10 keV of heating)

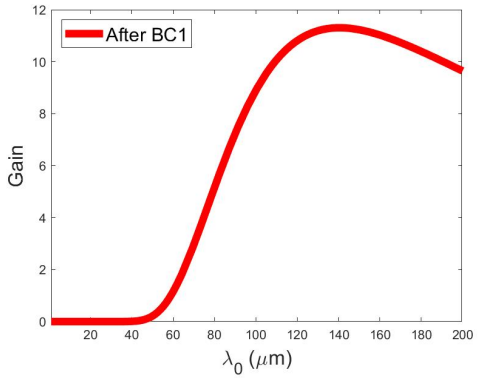

(a) BC1 only.

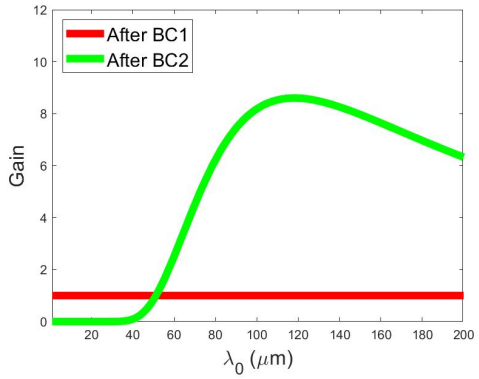

(b) BC2 only.

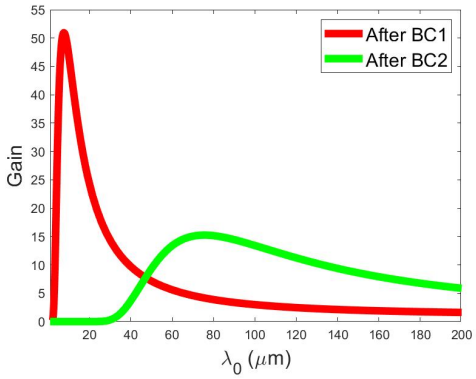

(c) BC1 + BC2.

Figure 5.7: Calculated microbunching gain as a function of initial modulation wavelength λ_0, including the effects of LSC, CSR and IBS.

that good agreement between the measured SES and Eq. 2.78 can be seen clearly. The slice energy spread added by the deflector (see Eq. 5.1) is a systematic contribution which adds in quadrature to the actual beam energy spread, and so it was subtracted from the measured quantity as shown in Fig. 5.6. The error bars are dominated by the uncertainty on the measurement reproducibility.

5.4 Fourier Analysis of Longitudinal Phase Space

Two-dimensional Fourier analysis of the longitudinal phase space of a beam can reveal, in addition to the microbunching frequency and amplitude, the phase of the plasma oscillation between bunching in energy and in time. By comparing these three parameters for measured bunches, it is possible to demonstrate experimentally the interplay between collective effects in electron beams, and

to address the accuracy of the models used in simulation. In this section, the procedure for measuring the modulations on the bunch will be described, some representative examples of these measurements for BC1-only compression will be shown, and the suppression of the microbunching with the laser heater will be discussed. The measured modulation period and bunching factor for all three bunch compression schemes is also presented and discussed; finally, the plasma oscillation phase at the end of the linac is measured and compared with semi-analytical predictions.

5.4.1 Measurement Procedure

A procedure has been developed and implemented in order to extract the aforementioned microbunching parameters. The algorithm, implemented in Mathematica [122], runs as follows:

1. Select an area of the bunch image to remove low-frequency components on the order of the bulk scale of the bunch, and apply an intensity threshold to suppress noise.

2. Apply a 2D Fourier transform to this image and convert from frequency/inverse energy space (in units of THz/MeV^{-1}) to wavelength/energy modulation space (in units of µm/keV).

3. Select, by eye, a region of interest based on the position of the satellites around the DC term in frequency space.

4. Remove wavelength/energy modulation values corresponding to frequencies smaller than half the Fourier transform of the bunch length and energy spread.

5. Find the maximum bunching factor as a function of wavelength/energy modulation.

The fourth step in this procedure is necessary to ensure that only truly periodic features contribute to the microbunching analysis. Artefacts associated with noise in the imaging system cannot be removed completely without artificially manipulating the longitudinal phase space image of the bunch itself, but a

low-intensity threshold is sufficient to remove some of the persistent noise in the Fourier transform. One other possible method for reducing noise would be the application of smoothing algorithms. Mathematica [122] includes in-built functions for Gaussian [123], Wiener [124], mean [125] and band-pass [126] filters, all of which were applied to the longitudinal phase space images. However, a great deal of fine-tuning was found to be necessary in order to arrive at similar results to a simple low-intensity threshold. Since this method should be applicable to a range of modulation periods in 2D space, and a range of depths of modulation, fine-tuning of smoothing filters were not found to be useful in this case.

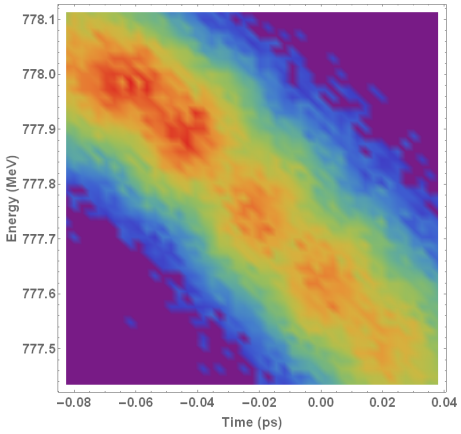

(a) Longitudinal phase space.

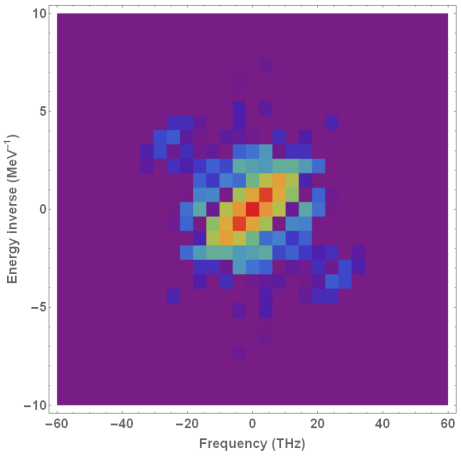

(b) Fourier spectrum of Fig. 5.8a in frequency space.

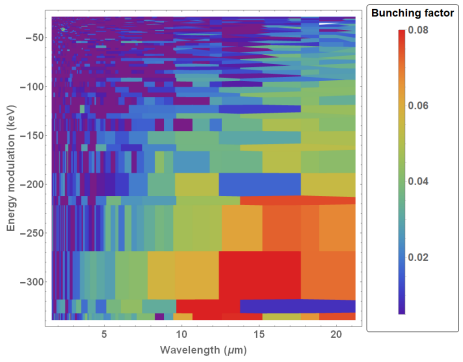

(c) Selected region of the Fourier spectrum of Fig. 5.8a in wavelength space – mean of 20 images of the Fourier spectrum.

Figure 5.8: Example of 2D microbunching analysis for a bunch compressed using BC1 only, with the laser heater off. The two satellites located around $[\pm 25\text{–}30\,\mathrm{THz}, \mp 3.5\,\mathrm{MeV}^{-1}]$ in Fig. 5.8b represent the modulations in intensity in Fig. 5.8a.

The normalised amplitude of a satellite in Fourier space yields the bunching factor and the distance from the central term gives the microbunching period along both axes. The arctangent of the ratio between these values represents the plasma oscillation phase – we normalise the units in this case such that the phase is dimensionless (see Sec. 5.4.4). The physical origin of this parameter is a combination of a periodic oscillation between energy and density modulations and the shearing of microbunches due to the magnetic bunch compression process, as mentioned above (Sec. 2.3). Therefore, the term 'phase' may not be strictly applicable. Nevertheless, since these two effects combine to produce a periodic variation in the longitudinal phase space, we reserve the term 'phase' to refer to the direction of orientation of the microbunching in longitudinal phase space.

An analytic model of a modulated Gaussian bunch has been constructed for the purposes of demonstrating the influence of these beam parameters on the Fourier transform – see Sec. 2.3.6 for examples. Both low- and high-frequency peaks in intensity are of less interest than peaks at intermediate frequencies, since the former relate to structure on the scale of the bunch (including current spikes at the head and tail of the bunch), and the latter arise primarily due to the resolution of the imaging system.

5.4.2 Example Case: BC1 only

An example of how the 2D microbunching analysis procedure is applied to a single set of images is shown in Fig. 5.8. From the original image of the longitudinal phase space of the bunch – in this case, compressed using BC1 only, and with the laser heater switched off – the Fourier transform in frequency space is then calculated. In this case, the modulation on the bunch is represented by the points at $\approx [\pm 25\,\mathrm{THz}, \mp 3.5\,\mathrm{MeV}^{-1}]$ in Fig. 5.8b – this can be confirmed by applying a low-intensity threshold to Fig. 5.8b and performing an inverse Fourier transform, in which case only the DC term in the Fourier transform remains, and the modulations on the bunch disappear. The symmetric properties of Fourier analysis mean that it is arbitrary which of the two satellites in Fourier space we choose to analyse.

By inverting the dimensions Fig. 5.8b into wavelength/energy space, averag-

ing over 20 shots, and selecting the region of interest, the microbunching features in both dimensions can be clearly seen – see Fig. 5.8c. Since the dimensions of Fig. 5.8c are the inverted dimensions of the initial Fourier transform, the pixels in this plane become larger as the wavelength and energy modulation increase. The region between 10 and 15 µm and −250 and −350 keV represent the strongest modulations on the longitudinal phase space of these bunches.

As the laser heater is activated, the modulations on the bunch become smeared out due to a larger uncorrelated energy spread along the bunch. This results in a suppression of the satellites in the Fourier space that represent the modulations on the bunch, meaning that the bunching has been effectively suppressed. Examples of images of bunches that have interacted with the laser heater are shown in Fig. 5.9. It can be seen that, even with a small added energy spread, the microbunching has been suppressed by around a factor of 2, while for a much larger laser heater power, the slice energy spread of the bunch has blown up, although the microbunching level has essentially been suppressed to the noise level. The colour scale on Figs. 5.8c, 5.9c and 5.9f is the same, to enhance the visibility of the suppression of modulations. Due to noise in the imaging system, the measured bunching of a background image still exhibits a maximum value of around 0.01 – 0.02 (see colour scale on Fig. 5.9f), and so this can be said to demonstrate cases where there is no measurable microbunching in a real beam image. The value of the bunching factor represents the variation in depth of modulations along the bunch at some given frequency, and so the minimum value observed for larger laser heater energies represent a value of around 1 – 2 %.

5.4.3 Analysis of All Compression Schemes

In order to provide a comparison between the longitudinal phase space of a beam that has not been heated and beams which have, we can project the 2D bunching onto the wavelength axis or the energy axis for increasing values of the laser heater energy. Such a projection onto the wavelength axis is shown in Fig. 5.10a for the BC1-only case, both for a beam that has not been heated, and for beams heated with various laser heater energy settings. Due to the inherent noise associated with microbunching, this plot represents the mean microbunching

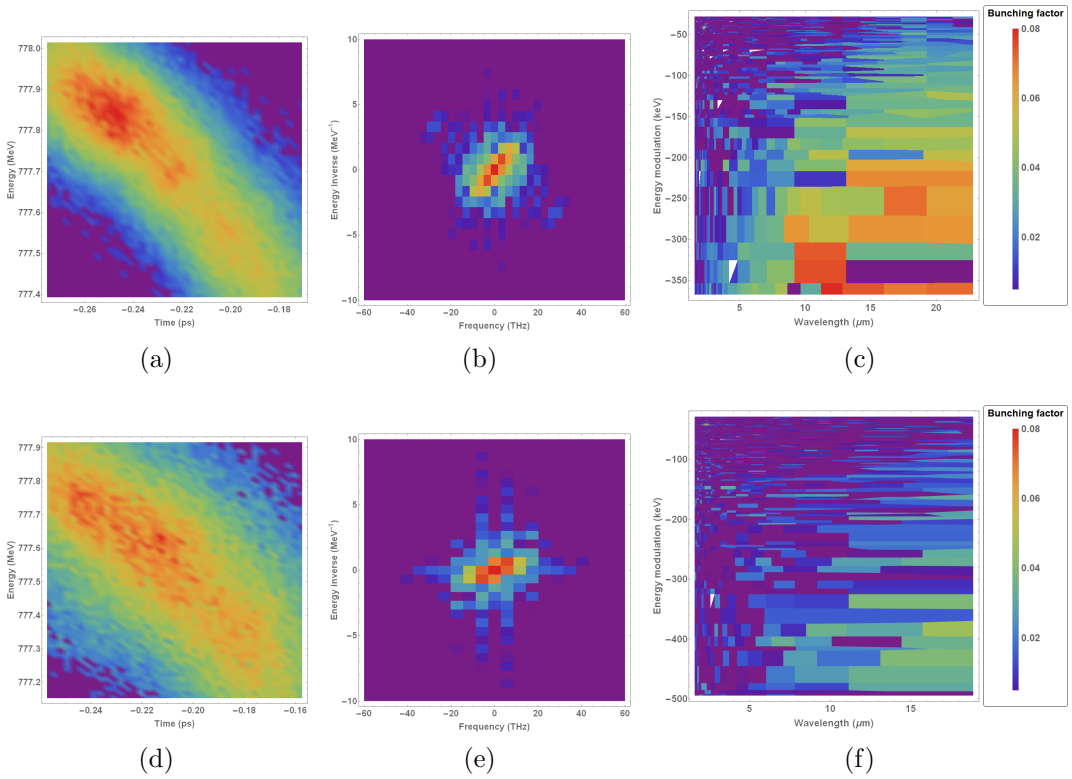

Figure 5.9: Examples of 2D microbunching analysis for a bunch compressed using BC1 only, with the laser heater on, adding: Top row: 5 keV; Bottom row: 26 keV. The order of the plots from left to right is the same as that of Fig. 5.8.

over a subset of 20 shots whose current profile fell within the correct range. Each point along the horizontal axis represents the maximum bunching of the Fourier spectrum, averaged over 20 shots. The trend towards decreasing bunching as the laser heater energy increases is clear, and it approaches the noise floor of the measurement for a relatively small added energy spread.

Similar effects can be observed in the analysis of the longitudinal phase space in other compression scenarios; see Fig. 5.10b for the reduction in bunching in the wavelength axis for a bunch compressed using BC2 only. As with the case for BC1 only, the bunching is strongest for low laser heater energy settings, eventually decreasing to the noise level as the laser heater-induced energy spread increases. In this case, however, the maximum bunching with the laser heater off is slightly smaller than that observed in the BC1-only configuration. Additionally, a slightly larger energy spread must be added by the laser heater in order to reduce the bunching down to the noise floor of the measurement.

An analogous set of measurements corresponding the double compression

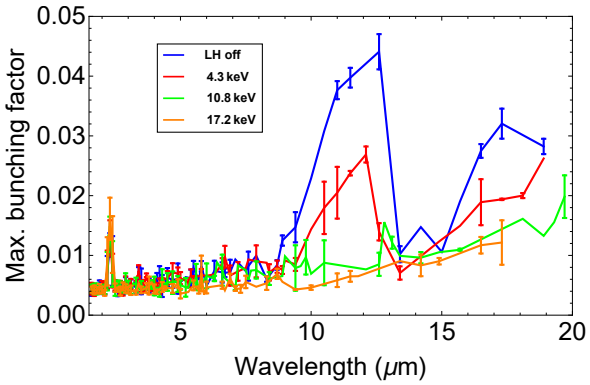

(a) BC1 only.

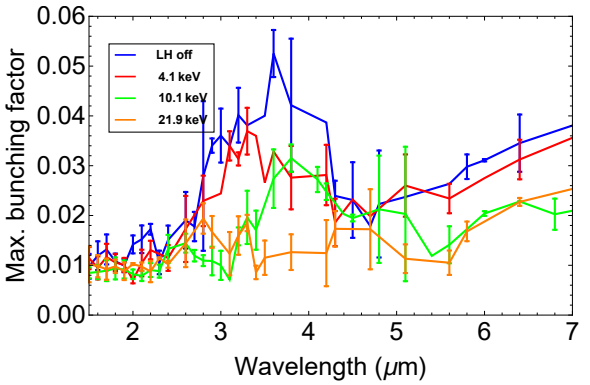

(b) BC2 only.

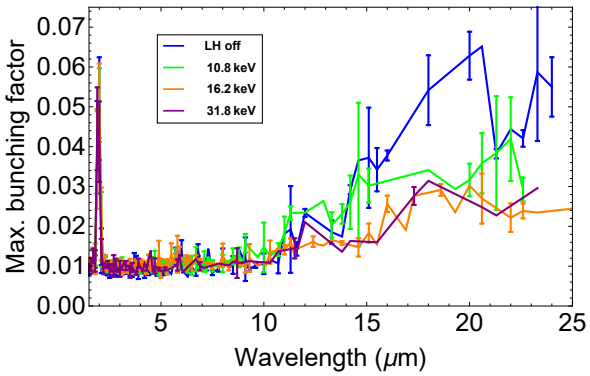

(c) BC1 + BC2.

Figure 5.10: Maximum measured bunching factor in the wavelength axis for bunches compressed using all three machine configurations, for a number of laser heater energy settings (average of 20 shots).

scheme is shown in Fig. 5.10c. In this case, the strongest bunching is seen in the wavelength axis at around 17 µm, and the influence of the laser heater can be observed as with the other machine configurations. The peak occurs at a longer wavelength than that predicted by the theory in this case (see Fig. 5.7),

which suggests that the final maximum bunching period should be of a similar order to the other two cases. The reason for this is that the plasma oscillation causes a stronger mixing between energy and density modulations than in the single-compression cases, and so a simple 1D projection of the bunching onto the frequency axis presents a distorted picture of the actual case in the full longitudinal phase space. In the cases of BC1-only compression and the double compression scheme, there is some short-wavelength (high-frequency) bunching measured at around 1 µm. This is not observed for the BC2-only compression case. This was measured for portions of the image in which there was not any beam, and so it can most likely be attributed to noise in the imaging system. The phase space imaging setup was slightly different for each compression scheme, and so the value of the bunching factor for this high-frequency component is different in each of the plots.

The absolute value of the maxmium bunching factor with the laser heater off is largest for the double compression scheme, in agreement with the theoretical predictions (see Fig. 5.7). The modified theory of microbunching gain, with the effect of IBS included (see Secs. 2.3.4 and 2.3.5), predicts a microbunching gain for the double compression scheme of less than a factor of 2 larger than the single compression schemes; this result is more consistent with experimental measurements than the theory without IBS, which predicts a gain of around a factor of 5 larger.

If the maximum bunching factor is then calculated as a function of the energy spread added (as shown in Fig. 5.11), it can clearly be seen that the microbunching level has been suppressed completely for a relatively low added energy spread for all three compression scenarios. On comparing this increase in energy spread with the results given in Fig. 5.6, it can be seen that the microbunching can be suppressed by operating the laser heater at low power, leading to only a small increase in the energy spread. For a compression factor of 35, an added energy spread of 10 keV means increasing the overall energy spread of the bunch by around 0.5 %. As shown in Ref. [127], an added energy spread of approximately this magnitude (albeit with a smaller compression factor) was able to increase the photon intensity of FERMI FEL-2 by two orders of magnitude.

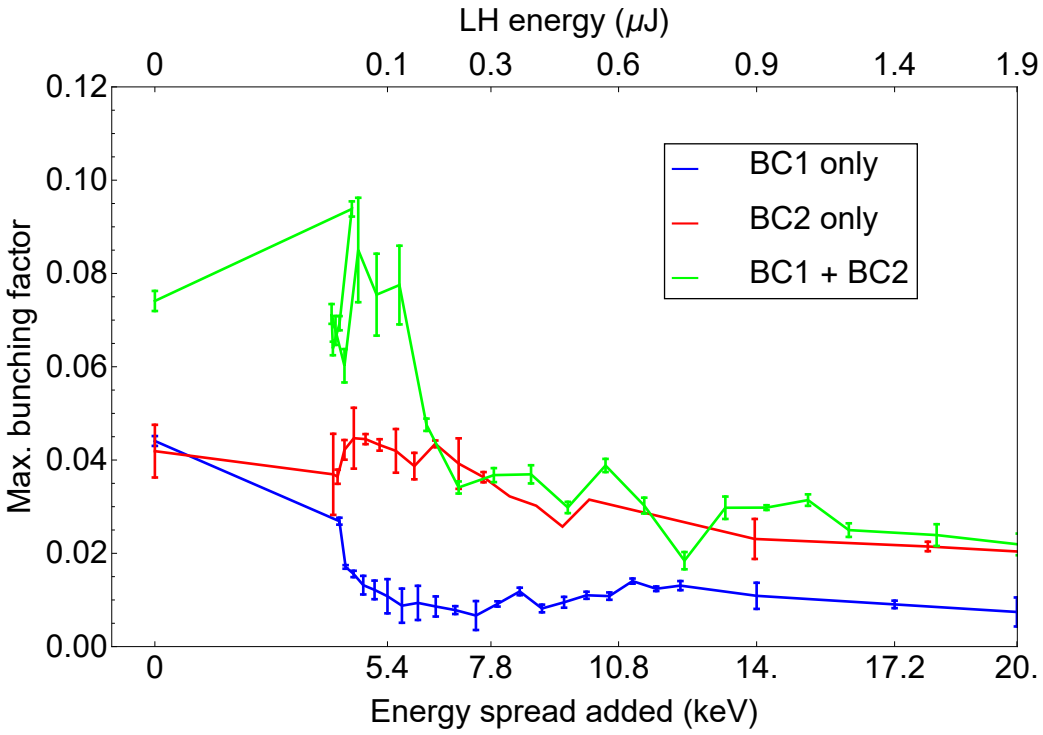

Figure 5.11: Maximum bunching factor as a function of laser-heater induced energy spread for all three compression scenarios.

5.4.4 Plasma Oscillation Phase

Since the modulation period in energy is on the order of 100s of keV, while the modulation period along the length of the bunch is on the order of 10s of µm at the peak bunching factor, we have measured the 'normalised' plasma oscillation phase as $\theta_{P,N} = \arctan\left(\bar{E}^i_{mod}/\bar{f}_{mod}\right)$, where $\bar{E}^i_{mod}, \bar{f}_{mod}$ denote the normalised modulation period along the energy-inverse and frequency axes in Fourier space, respectively. This normalised phase for the maximum bunching factor across the three compression schemes is shown in Fig. 5.12a. It can be seen that the mixing between energy and density modulations is most significant in the case of double compression, since the peak bunching factor is at a phase of $\pi/4$ between a pure energy modulation and a pure density modulation. This explains why the projected modulation wavelength in Fig. 5.10c is longer than in the single compression cases: the distance of the satellite in Fourier space from the DC term is fixed for a given modulation period, and it rotates in a circle around the centre as the plasma oscillation evolves. Taking a 1D projection along the

frequency axis, for example, will present a distorted picture of the modulation period if there is not a pure density modulation in the bunch.

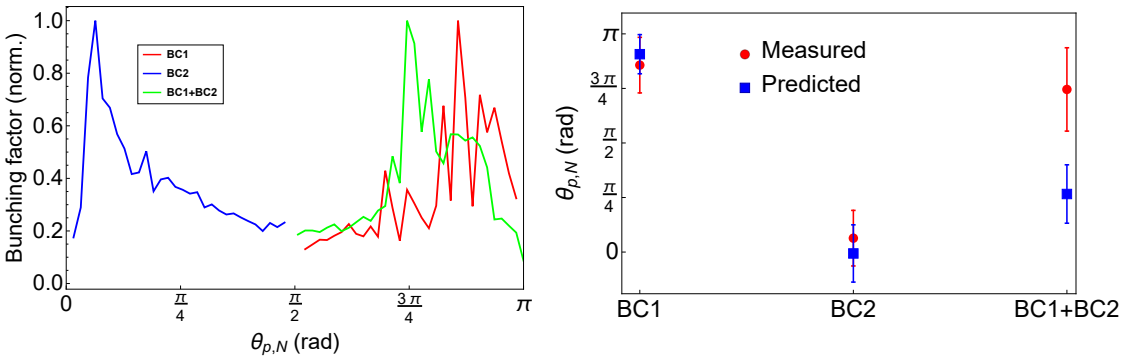

(a) Normalised plasma oscillation phase – average of 20 shots.

(b) Measured and theoretical plasma oscillation phase at the DBD location.

Figure 5.12: Bunching factor as a function of plasma oscillation phase (normalised, left) and a comparison between measured and predicted final plasma oscillation phase for all three compression scenarios.

In order to compare the measured plasma oscillation phase at the DBD location with theoretical predictions, a semi-analytic model has been developed to track the evolution of the plasma oscillation through the machine. Particle tracking runs of the post-injector lattices for the three compression schemes have been conducted using the `elegant` code [96] to compute the beam size, peak current and beam energy throughout the lattice. These parameters can be fed into Eq. 2.54 to calculate, piece-wise, the evolution of the plasma oscillation frequency ω_P throughout the machine as a function of initial modulation wavelength λ_0, also taking into account the shearing of the microbunches due to the bunch compression process as described above. The change in the plasma oscillation phase θ_P through a beamline component or drift space of length L is calculated as $\omega_P L \pmod{\pi}$.

Since any initial modulations on the bunch arising due to shot noise in the injector will be broad-band, we suppose that θ_P at the injector exit is zero for all λ_0. A comparison between the predicted and measured values for θ_P is shown in Fig. 5.12b. Here, the error bars on the measured values represent the FWHM of the curves in Fig. 5.12a, and the errors in the predictions represent the variation in ω_P across a range of λ_0 given by the theoretical curves in Fig. 5.7. It can be

seen that the predictions match up well with the measured values in both single compression schemes, whereas there is a larger discrepancy in the case of double compression. It is also noted here that little variation in the plasma phase was observed when increasing the energy spread imposed by the laser heater.

A plot of the semi-analytical calculations of the evolution of $\theta_{p,N}$ across the three bunch compression schemes is shown in Fig. 5.13. A range of values for λ_0 were considered in each case, showing the range of expected final values for $\theta_{p,N}$ in each case. The smaller values of λ_0 correspond to a larger $\theta_{p,N}$, since shorter-wavelength modulations correspond to a higher plasma oscillation frequency ω_P. The spread of values in each case can be interpreted physically as the angular spread of the microbunches in Fourier space, given that the initial modulation on the bunch has a broad-band shot noise profile. Each element in the `elegant` lattice has a finite length, with some elements (such as the linacs) being quite long, hence the step changes in $\theta_{p,N}$. The model does not consider impedance due to CSR or geometric wakefields from the linac structures, but these effects are expected to be relatively small compared with the LSC impedance.

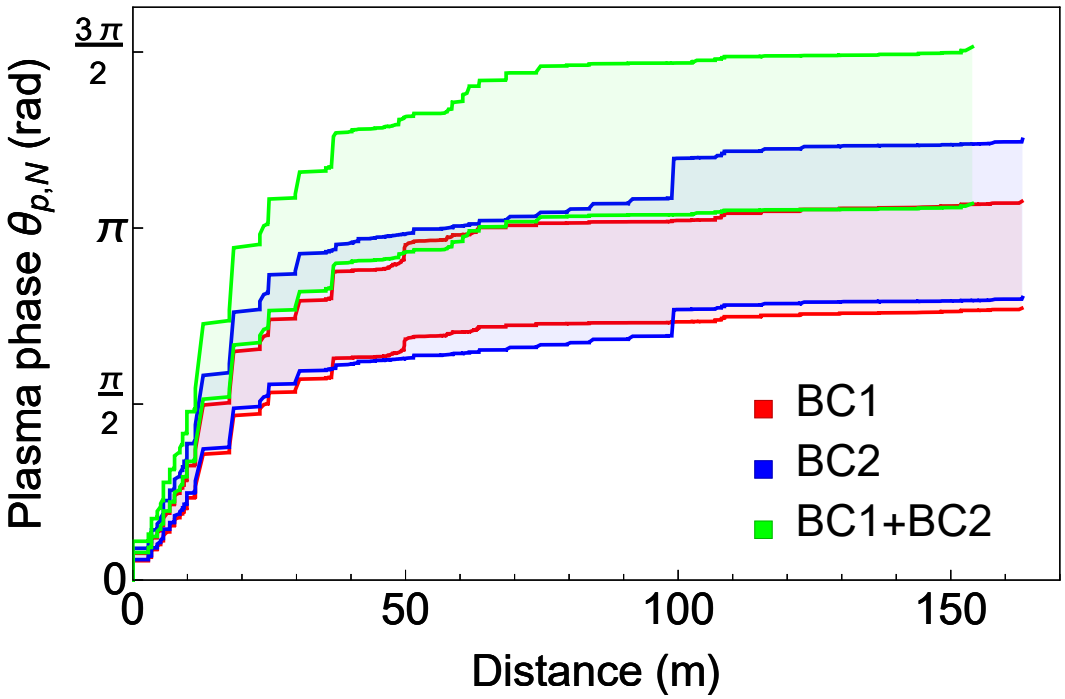

Figure 5.13: Evolution of plasma oscillation phase $\theta_{p,N}$ through the FERMI linac (from the exit of the injector) up to the DBD location for the three compression schemes. The range of values for each scheme denote a range of initial modulation wavelengths λ_0 around the peak of the gain curves in Fig. 5.7.

5.5 Inducing Microbunching with the Laser Heater

The electron beam longitudinal phase space was measured for a number of machine configurations: in addition to varying the bunch compression process using combinations of the two variable bunch compressors, the microbunching was seeded in the laser heater for a range of initial modulation wavelengths and laser pulse energies. This seeding was achieved using chirped-pulse beating of the laser pulse in the laser heater (see Sec. 2.4.3). The timing between the electron beam and the laser in the laser heater chicane can also be varied, allowing for timing scans that provided the largest amplification of the microbunches. For a fixed laser pulse energy, the largest final bunching factor as a function of initial seed wavelength in the laser heater is related to the largest microbunching gain. In this section, some examples of longitudinal phase space distributions for the three compression schemes will be given, and the influence of different laser heater beating wavelengths on the electron bunch will be shown. The following section will present quantitative analysis of the microbunching and simulations of the experiment.

In order to cross-check the measured electron bunch modulation period with the beating wavelength of the laser pulse, measurements of the variation in energy spread along the bunch were taken at the low-energy RF deflecting cavity, located at the exit of BC1. In this case, the bunch was uncompressed. The modulation period along the length of the bunch was extracted for a range of values of the laser beating delay τ. Fig. 5.14 shows the variation of delay between pulses and the corresponding modulation period on these bunches, along with values for the beating wavelength of the laser pulse from the theory. It can be seen that the measurements agree well with the predictions.

With a variation of the delay τ between 4 ps and 30 ps – corresponding to initial modulations imposed on the bunch in the range 0.6–4.5 THz – a wide range of modulated longitudinal phase spaces can be probed. Some example intensity profiles of these modulated laser pulses are shown in Fig. 5.15.

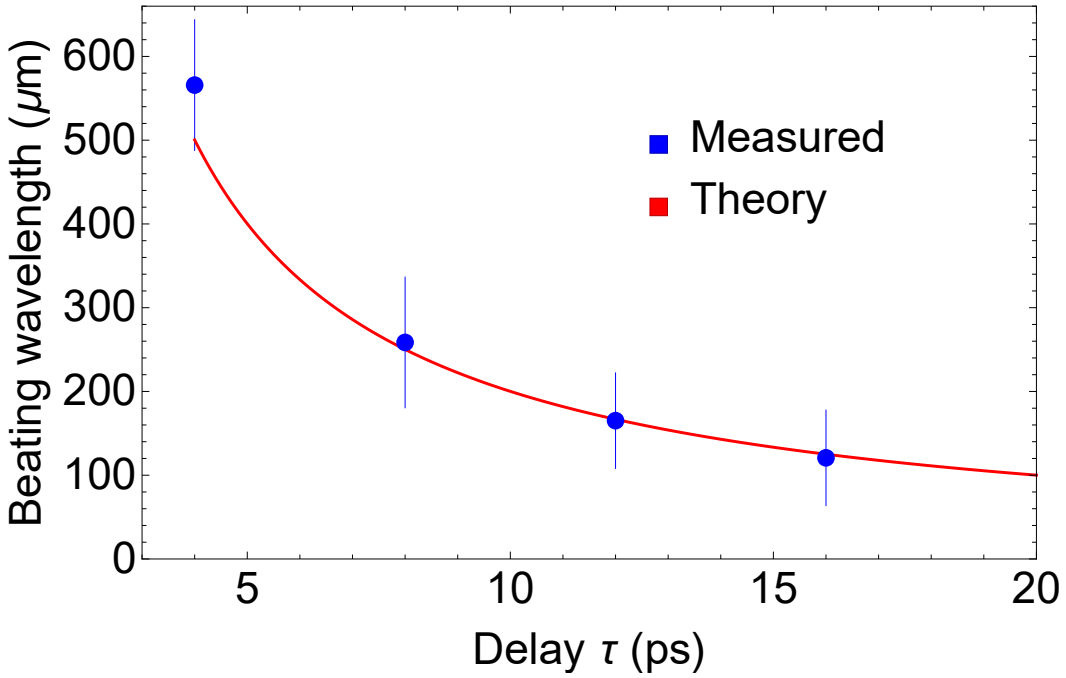

Figure 5.14: Measured (blue) and predicted (red) modulation period on the electron bunch as a function of interferometer delay τ, with an uncompressed bunch.

5.5.1 Double Compression

We begin by analysing the features in the longitudinal phase space for a bunch compressed with the BC1 angle set to 105 mrad – the 'nominal' configuration – and with a variable, though modest, compression in BC2 – the angle of the second compressor was set in the range 17.1–35.2 mrad. This was done in order to accentuate the microbunching features in the beam. The results given below are for a fixed BC2 angle of 28.5 mrad.

A range of longitudinal phase space measurements the double compression scheme are shown in Fig. 5.16. In this case, the delay between the two laser pulses in the laser heater was set to 12 ps (final beating wavelength $\lambda_f = 8.3\,\mu$m for compression factor $C = 23$), and the initial laser pulse energy (before splitting and recombination) was varied between 0.1 µJ and 10 µJ, corresponding to an added energy spread (in the single pulse mode) between 5 and 50 keV. Qualitatively, it can be seen that, as the laser pulse energy increases, the longitudinal density modulations in the bunch become increasingly pronounced, and for the largest laser pulse energy shown (Fig. 5.16d), the uncorrelated energy spread in

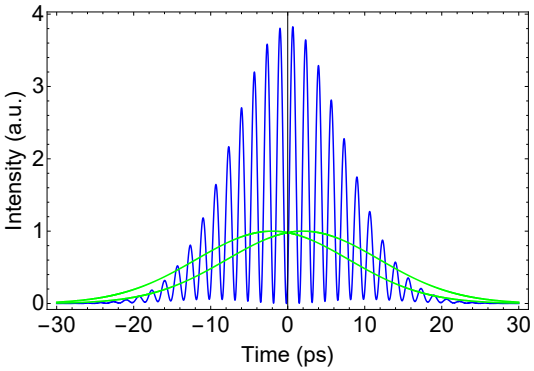

(a)

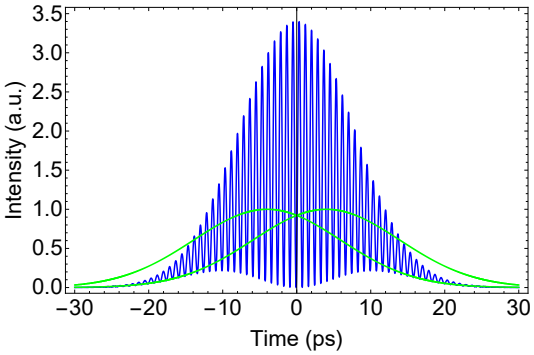

(b)

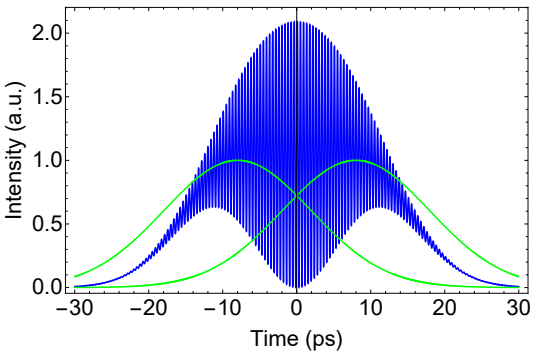

(c)

Figure 5.15: Calculated intensity profiles (blue) of modulated laser pulses (from Eq. 2.80) for delays between pulses of: above: 4 ps (0.6 THz frequency); middle: 8ps (1.2 THz frequency); bottom: 16ps (2.4 THz frequency). The intensity profiles for the two separated laser pulses before recombination are shown in green.

the bunch core becomes more prominent. These images are representative of the majority of measurements taken over 20 shots, although there was some variation in the bunch length due to jitter in the RF structures. As a result, the statistical analysis done below (Sec. 5.6) was performed only for those bunches whose current profile was close to the nominal value of around 600–650 A in the

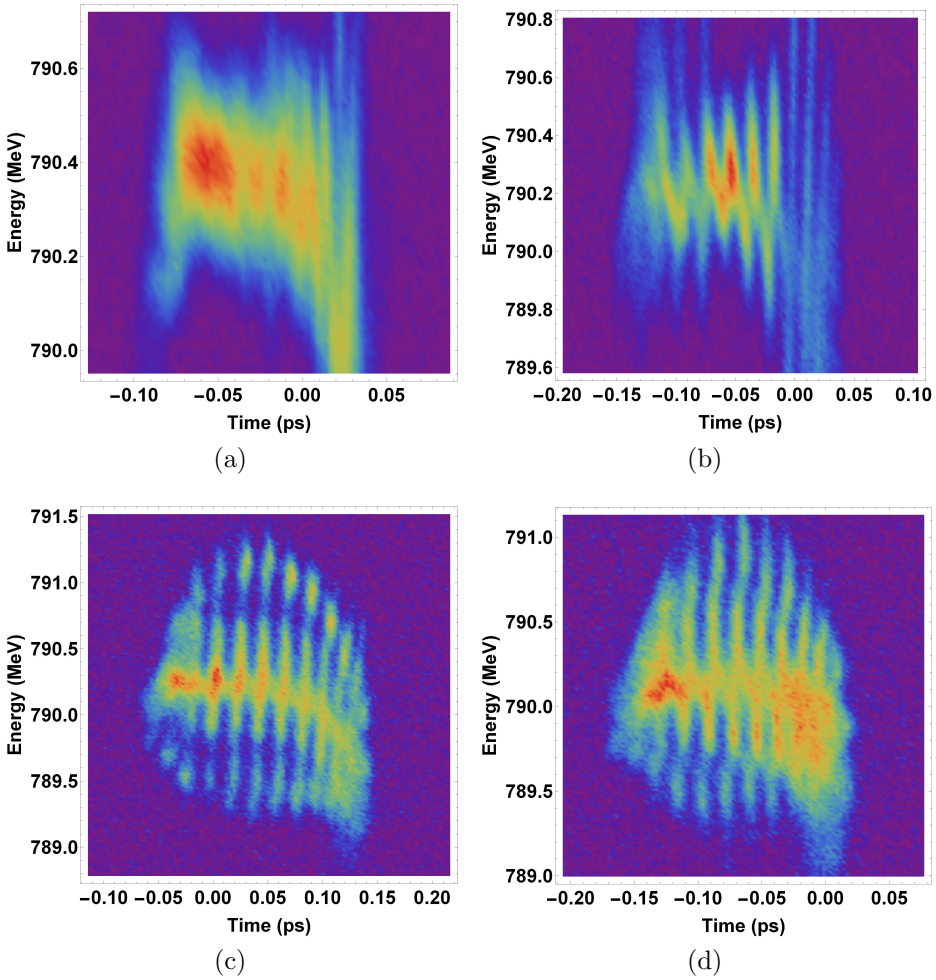

Figure 5.16: Single-shot measured longitudinal phase space for BC1 and BC2 bending angles set to 105 and 28.5 mrad, respectively, for a laser heater beating frequency of 1.8 THz. The initial laser pulse energy from was set to: 0.08 (top left), 0.6 (top right), 2.9 (bottom left) and 6.8 µJ (bottom right).

bunch centroid.

The bunching factor has been measured along both axes of the longitudinal phase space simultaneously using the 2D Fourier analysis method described above (Sec. 5.4). The variation in modulation frequency and bunching factor as a function of laser heater energy can be quantified by measuring the Fourier transform of these images (shown in Fig. 5.17, each of which represents the mean of a number of shots for each setting). There is some small variation in the plasma oscillation phase for different settings of the laser heater pulse energy, although this is small, and is difficult to distinguish from the angular spread of the satellites in Fourier space.

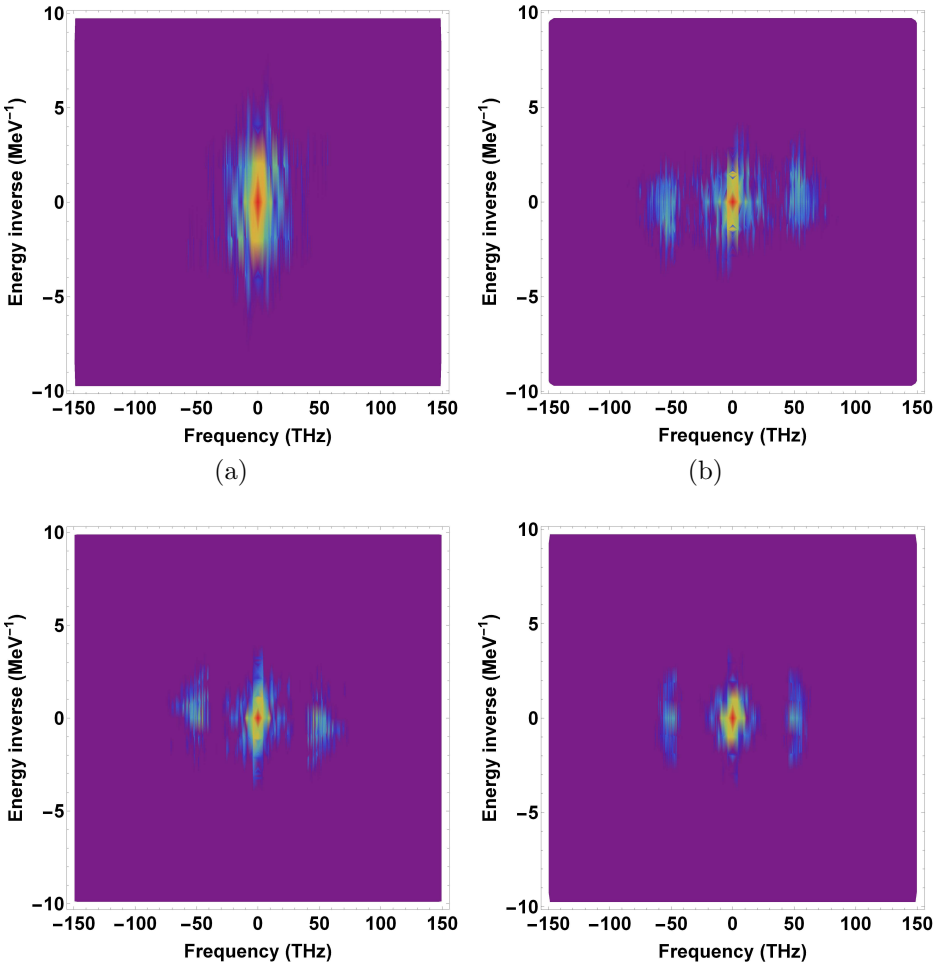

Figure 5.17: Measured Fourier transform (averaged over 20 shots) for the same machine settings as in Fig. 5.16.

In the case of a 12 ps initial beating delay, corresponding to an initial modulation frequency of 1.8 THz, the final measured bunching period is in the range 40–45 THz. This matches up well with the compression factor $C \approx 23$. By normalising the pixel intensity in Fourier space to the maximal value (at the centre), a measurement of the bunching factor as a function of frequency in both planes can be obtained (see below, Sec. 5.6.2).

The relationship between the initial bunching frequency imposed by the modulated laser in the laser heater, the compression factor, and the final bunching frequency has been measured for one laser heater setup; we can now begin to analyse the development of microbunching for a range of different cases. The beating delay τ was varied between 8 and 20 ps for this compression scheme.

Some example longitudinal phase space measurements for two settings of the initial beating frequency $\nu_i = 1.2$ and 2.4 THz – are shown in the top row of plots in Fig. 5.18. In this case, the initial laser pulse energy was set to 3.5 µJ. In the longitudinal phase spaces, it can be seen that the number of microbunches present in the bunch increases with the beating frequency.

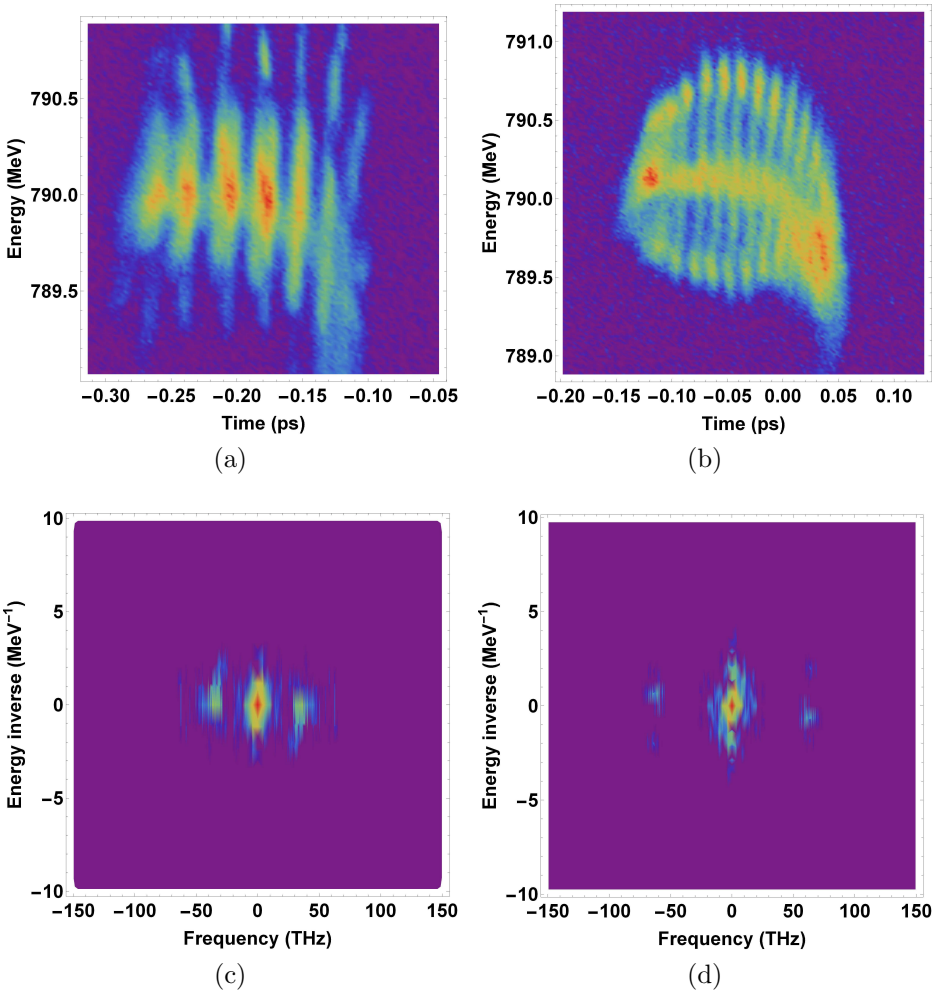

Figure 5.18: Single-shot measured longitudinal phase space (above) and Fourier transform (averaged over 20 shots, below) for the same lattice settings as in Fig. 5.16, but with initial beating frequencies of 1.2 (left) and 2.4 (right) THz, and an initial laser pulse energy of 3.5 µJ.

For a compression factor of 23, these delays correspond to a predicted final bunching frequency of 30 and 55 THz, respectively. In the longitudinal phase space, it can be seen that the number of microbunches present in the bunch longitudinal phase space increases with the beating delay. This relationship can also be demonstrated by measuring the position of the satellites relative

to Fourier space from the DC term, as shown in the bottom row of plots in Fig. 5.18, where the separation varies as a function of the initial modulation. This relationship is characterised for all three compression schemes below (Sec. 5.6.3).

5.5.2 Single Compression

A similar set of measurements to those detailed above were taken for bunches compressed using only BC2, the second bunch compressor. This resulted in the electron beam propagating with uncompressed imposed modulations across a longer distance, meaning that short-range collective effects between the microbunches were relatively suppressed as compared with a scheme in which the bunch is compressed at an earlier point in the lattice. In this machine configuration, a beam scraper was applied in the bunch compressor in order to suppress a large current spike at the head of the bunch (due to strong nonlinear compression), without having a measurable effect on the modulations in the rest of the bunch. The beam scraper in the FERMI bunch compressor [15] consists of two moveable copper rods that can be inserted into the path of the beam in the centre of the bunch compressor chicane. Due to the dispersive path in this region, which transforms the longitudinal phase space coordinates ($[E, z]$) into spatial co-ordinates ($[z, x]$), portions of the beam can be selected in order to remove current spikes.

In the case of bunches compressed using BC1 only, the longitudinal charge density of the bunch was high during the remainder of the acceleration process. This higher charge density enhances collective effects, suppressing the induced microbunching, and so the range of viable settings of the laser heater power was smaller than in the other two compression schemes: for 1 µJ laser pulse energy and above, no significant modulation was observed on the bunch at the end of the linac. Example images of the measured longitudinal phase spaces for these two configurations – with an initial beating frequency of 1.8 THz – are shown in Fig. 5.19. Across all three compression schemes, the final bunching periods observed agree very well with the wavelength of the modulated laser heater pulse (see Sec. 5.6.3 for further analysis), demonstrating the flexibility of this technique for producing strongly modulated bunches over a range of bunching periods.

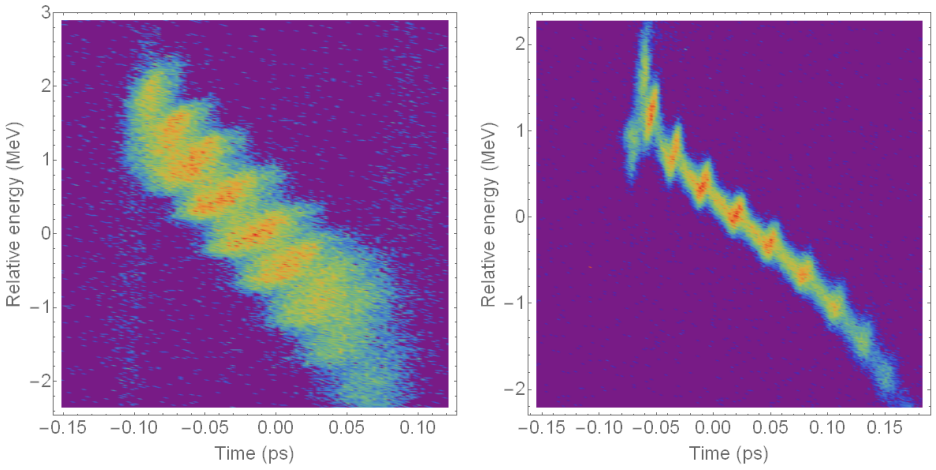

(a) (b)

Figure 5.19: Single-shot measured longitudinal phase space for bunches compressed using BC1-only (left) and BC2-only (right), with an initial beating frequency of 1.8THz.

On comparing the longitudinal phase spaces from the double compression scheme (Fig. 5.16) with those from the single compression schemes (Fig. 5.19), it can be seen that the linear energy chirp is more prominent in the latter cases than in the former. Due to the requirements on both the bunch compression factor and the final beam energy, it was not possible to remove fully this chirp for the single compression schemes, since the parameter range for these experiments were quite different to the nominal operation mode of FERMI [13]. Nevertheless, as discussed in Sec. 2.3.6, the energy chirp on the bunch does not affect the microbunching parameters of interest in the Fourier transform of the longitudinal phase space images.

5.6 Comparison Between Measurements and Simulations

As explained above (Sec. 5.4), there are a number of parameters that can be extracted from both the measurements and simulations of the longitudinal phase space of modulated beams. In addition to the longitudinal phase space itself, microbunching parameters such as the modulation period on the bunch, the bunching factor, and the plasma oscillation phase can be measured using 2D Fourier

analysis. In this section, these parameters will be characterised and compared between measurement and simulation for the laser heating beating experiment outlined above (Sec. 5.5). A wide range of initial modulation frequencies are imposed across multiple bunch compression schemes, and so we can study the development of the microbunching instability in detail.

5.6.1 Simulated Longitudinal Phase Space Measurements

Having measured the effect of the modulated laser heater pulse on the electron beam for a range of pulse energies, it is instructive to compare these measurements with those from simulation. `elegant` simulations were performed using the same parameters as were used in the measurements shown in Fig. 5.16. Collective effects and the modulated laser pulse in the laser heater were included (using the analytical expression for the laser pulse modulation Eq. 2.80). By including the effect of the deflecting cavity at the end of the linac, and using the same calibration factors as the measurement (mm to ps and MeV), the complete measurement can be simulated. In order to determine the accuracy of the simulated measurement, the bunch length, energy spread and linear energy chirp of the simulated screen image can be cross-checked with the simulated longitudinal phase space before the bunch is streaked by the deflecting cavity. Good agreement was found for these parameters. The longitudinal phase space images produced by the simulation are shown in Fig. 5.20.

Due to the large number of machine configurations, laser heater pulse energies and modulation wavelengths, the majority of simulations were run for only 10^5 macroparticles – a relatively small number compared with the real number of particles in the bunch. A convergence study was conducted for a subset of the experimental parameters using up to 10^7 macroparticles, and varying the number of longitudinal density bins used for the CSR and LSC calculations. More details on this convergence study are given in the discussion of the measurements of the bunching factor below (Sec. 5.6.2). It was found that even this lower number of particles was able to reproduce the measured bunching factor. In cases where the modulation frequency on the bunch is smaller than that used in this experiment, it is expected that it would be necessary to run a simulation with a greater num-

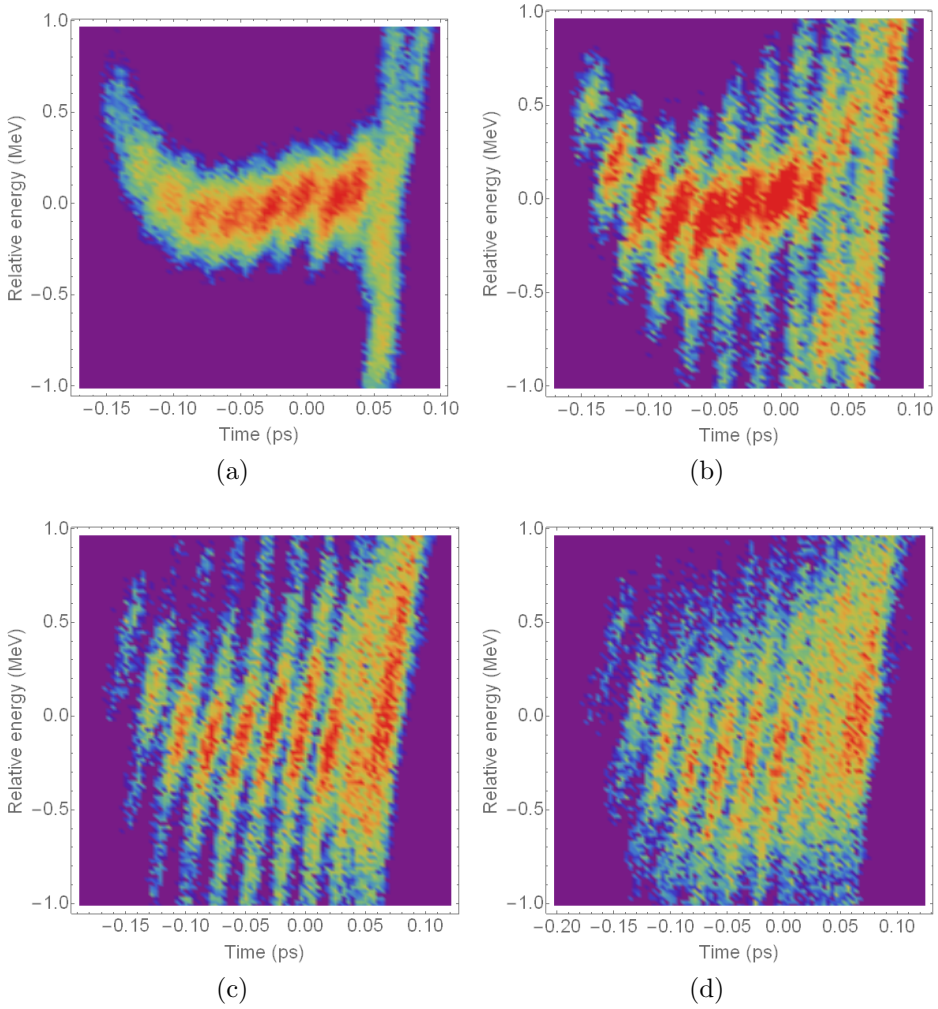

Figure 5.20: Simulated longitudinal phase spaces for the same machine settings as Fig. 5.16.

ber of macroparticles. Nevertheless, it can be seen that the simulation is able to reproduce the microbunching effects observed in the measured data: the final longitudinal phase space with a low-energy laser pulse exhibits similar macroscopic properties (in terms of total bunch length and energy spread); and the microbunching in the phase space becomes more prominent as the laser pulse energy increases. There is not an exact match between the simulated and experimentally measured distributions, in particular at the head and tail of the bunch, but there is some agreement between the bulk bunch parameters (slice energy spread, bunch length and energy chirp in the bunch core), and the periodicity of the modulations on the bunch (discussed below, Sec. 5.6.3). A quantitative comparison of the measured and simulated microbunching parameters is given

in the sections below.

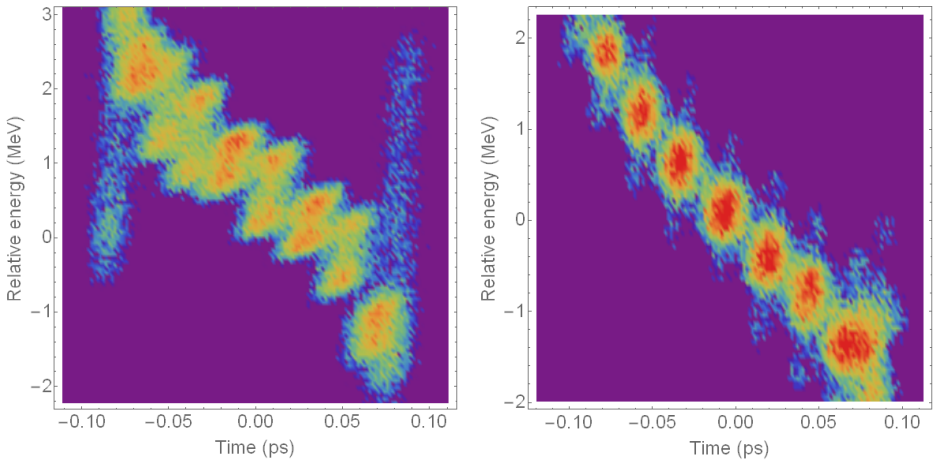

(a) (b)

Figure 5.21: Single-shot simulated longitudinal phase space for bunches compressed using BC1-only (left) and BC2-only (right), with an initial beating frequency of 1.8THz. These simulations correspond to the measurements in Fig. 5.19.

Examples of the simulated longitudinal phase space for the two single-compression configurations – with an initial beating frequency of 1.8 THz – are shown in Fig. 5.21. It can be seen in both of these cases that the simulation is able to reproduce the experimentally measured macroscopic bunch properties (see Fig. 5.19), in terms of bunch length and energy spread, and that the modulations imposed have a similar periodicity. The bunching period and bunching factor are characterised in the subsections below.

5.6.2 Bunching Factor

Firstly, the maximum bunching factor as a function of laser pulse energy is measured for each of the initial beating wavelength settings – see Fig. 5.22. This plot shows the bunching factor for the double compression scheme. It can be seen that, in most cases, as the initial laser pulse energy increases, the maximum bunching measured reaches a peak for each setting of the initial beating, eventually falling to a lower level as the energy spread induced in the laser heater undulator reduces the amplitude of the modulations in the bunch. We also note that the results from simulation are able to capture the trends observed across

the full range of modulation wavelengths, although there are discrepancies in terms of the absolute values of the bunching factor in some cases. This is due to a combination of factors: the statistical variation in the experimental results arise both from the fact that microbunching is inherently a noisy phenomenon, which may not be completely overridden by imposing a modulation using the laser, and from jitter in the RF system causing bunch length variation from shot to shot; additionally, the simulations do not account for the full 3D collective effects for the actual number of particles in the bunch.

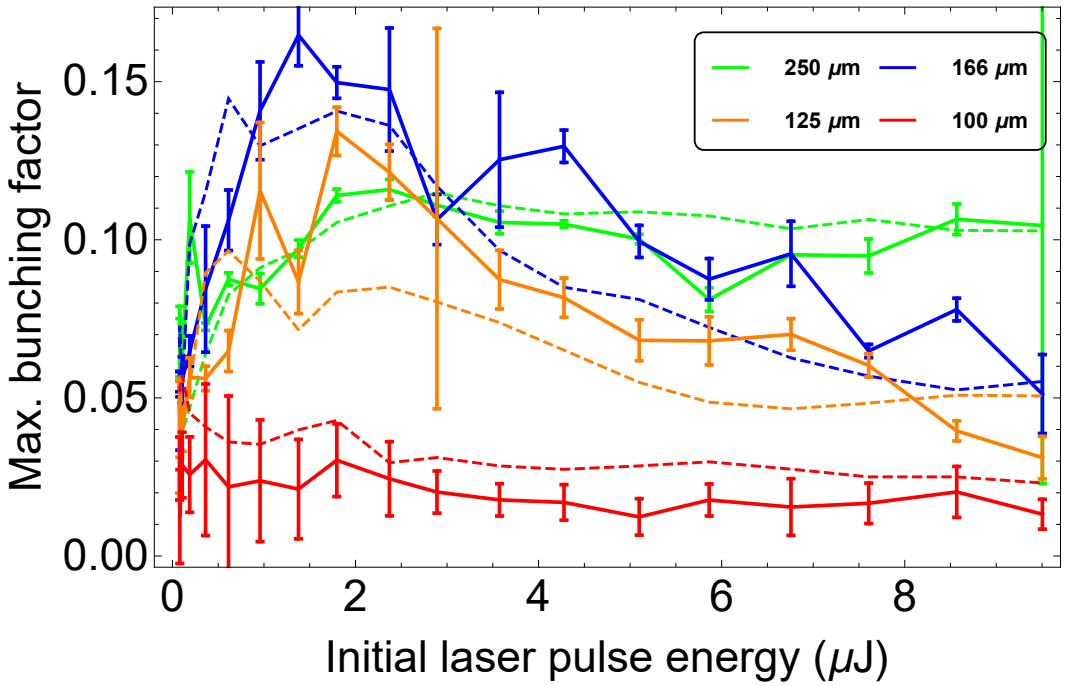

Figure 5.22: Maximum bunching factor as a function of initial laser pulse energy for a range of initial beating wavelengths. The lattice settings are the same as in Fig. 5.16. Measured bunching factor is shown by solid lines, and dashed lines show the simulated values. The error bars represent the standard deviation in maximum bunching factor over 20 shots.

A comparison between the simulated and measured maximum bunching factor across all three bunch compression schemes is shown in Fig. 5.23. The results shown cover the ranges of initial laser beating frequencies used for each configuration. A general trend of higher levels of bunching at shorter beating frequencies is observed (resulting in a longer bunching period on the bunch at the end of the linac). This is a result of the fact that the maximum intensity of the laser pulse for a given initial pulse energy decreases as the beating frequency increases

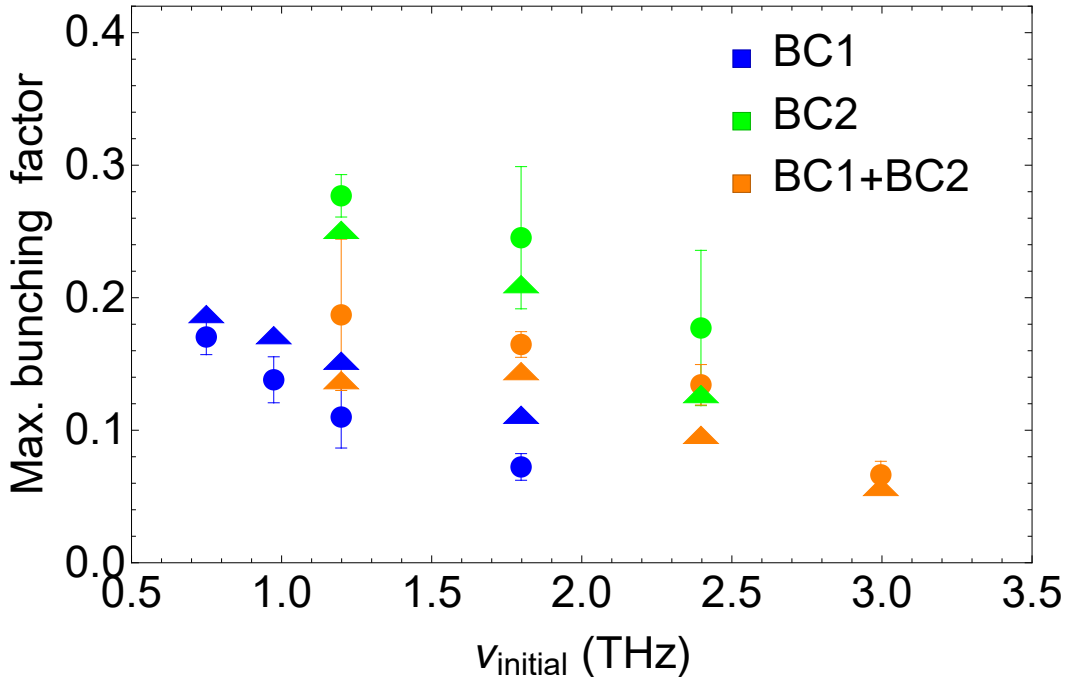

Figure 5.23: Maximum bunching factor – measured (circles) and simulated (triangles) as a function of initial modulation frequency ν_i for the three compression schemes (given in the legend)..

(see Fig. 5.15). There is some discrepancy between measurement and simulation in terms of the absolute value of the maximum bunching factor in some cases, but our results show that the code is able to reproduce the trend observed experimentally.

As mentioned above (Sec. 3.1.1), microbunching is simulated by the `elegant` code based on a histogram of the bunch current density, with a user-specifed number of bins for both LSC and CSR interactions. There is no exact method to determine *a priori* the number of bins to simulate microbunching accurately (although some hints are given in Refs. [108, 128]), and the optimal solution will vary depending on the bunch and lattice properties, and the wavelength of the interaction that is to be simulated.

Therefore, a convergence test was run to produce simulated bunching factors were consistent for a range of simulation parameters. For a test case, the scan of bunching factor as a function of initial laser pulse energy for the double compression scheme, with an initial beating frequency of 1.8 THz, was run over a range of macroparticle numbers and longitudinal binning histogram values. The number of macroparticles simulated ranged from 10^5 to 5×10^7, and the number

of LSC/CSR bins were varied together, from 20 bins to 500 bins.

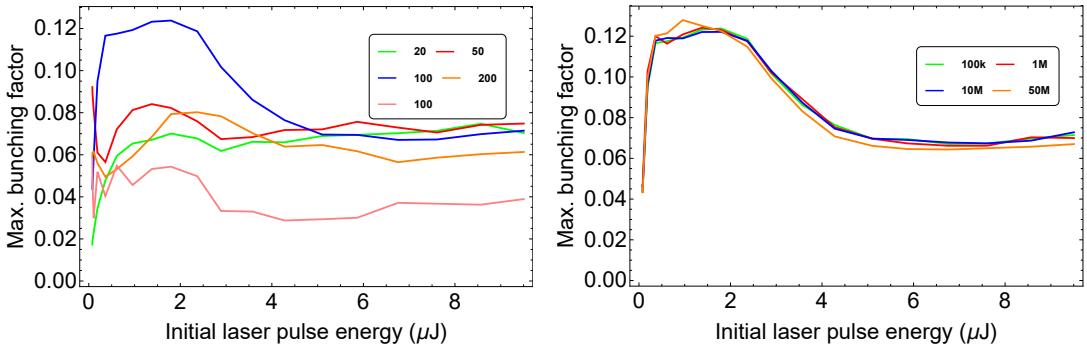

(a) Variation of the number of LSC/CSR bins (see the legend). The number of macroparticles is fixed at 10^5.

(b) Variation of the number of macroparticles (see the legend). The number of LSC/CSR bins is fixed at 100.

Figure 5.24: Simulations of the blue curve in Fig. 5.22 (double compression scheme, initial beating frequency 1.8 THz) for a range of simulation parameters.

The curves produced for varying numbers of bins and macroparticles are shown in Fig. 5.24. The peak in the bunching is observed in the scan over the number of bins for 10^5 macroparticles (Fig. 5.24a) for a similar initial laser pulse energy ($\approx$ 1.5–2 µJ) in all cases. The peak value of the bunching, however, varies with the number of bins. When the number of bins is lower than 100, the amplification of the modulation depth of microbunches is relatively small, whereas for a bin number higher than this value, the effect of CSR increases the bunch energy spread to the point where the modulations become less prominent, and so the peak bunching value decreases. This value for the binning histogram was consistent with that used for the simulations of CSR-induced emittance growth for the `elegant` simulations presented in Chapter 4.

Therefore, a following set of scans were performed for this fixed number of bins, with varying numbers of macroparticles (Fig. 5.24b). In this case, there is little variation in either the shape of the curve, or the maximum bunching factor, and so it can be concluded that this is the optimal number of bins for this range of bunch, lattice and simulation parameters. This was the value used for the simulations of the other bunch compression schemes and laser heater beating frequencies.

5.6.3 Modulation Period

The periodicity of microbunching in the electron bunch can be quantified as a function of either the longitudinal or energy density modulations. This can be achieved by projecting the 2D Fourier representation of the bunch images shown, for example, in Fig. 5.25 onto the energy or time axis. By doing this, we lose information concerning the correlative relationship between the microbunching along both axes, but this 1D information can provide a useful benchmark for simulation and theory – additionally, one quantity may be more pertinent than another, for example when multi-colour FEL pulses are desired (in which case the bunching in energy is more significant), or for cases in which multiple bunches separated by time are required (and so longitudinal density modulations are important).

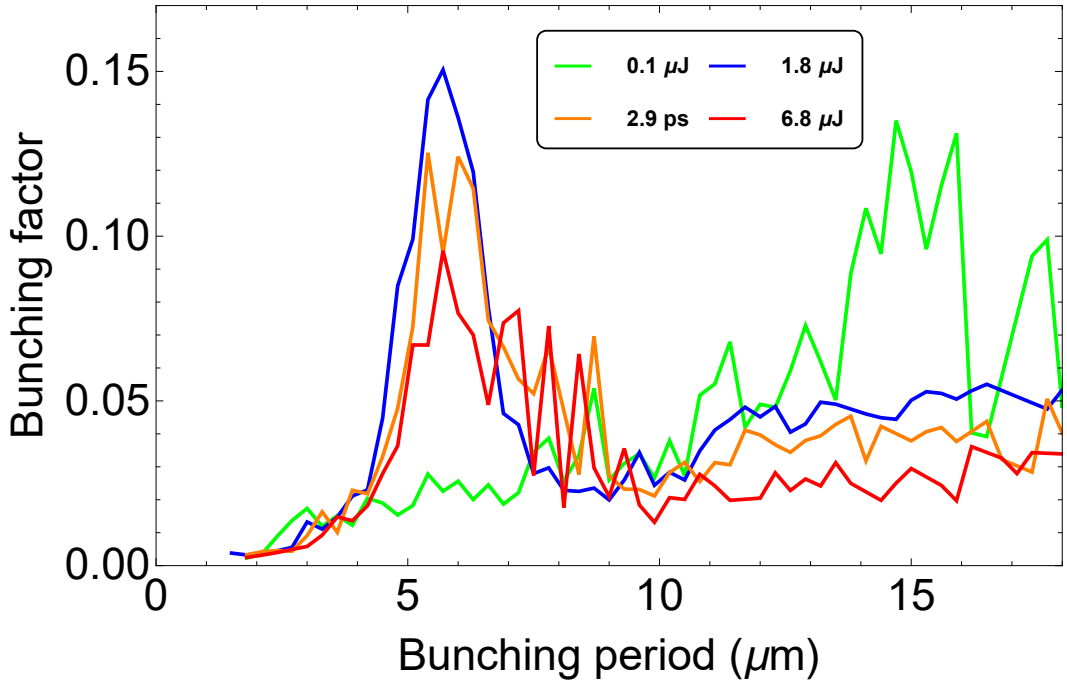

Figure 5.25: Measured final modulation period of the bunch longitudinal profile for a range of laser heater pulse energies, for the same machine settings as Fig. 5.16.

Bunching factors obtained by projecting the 2D Fourier space distribution onto the time axis are shown as functions of bunching period and for different laser heater pulse energies in Fig. 5.25. The data shown are for the case outlined in Sec. 5.5.1 (1.8 THz initial beating frequency, BC1 and BC2 angles 105

and 28.5 mrad respectively). In this case, we analyse on one of the satellites in Fourier space, and focus only on modulations above a specified frequency, so as not to include the DC term in our analysis, as this only provides information about the bulk structure of the bunch. We also measure the maximum projected bunching as a function of frequency, and transform this quantity into wavelength, or bunching period (through the relationship $\lambda = c/f$, with f the frequency, c the speed of light, and λ the resulting period). It can be seen that, while the initial bunching for a low laser pulse energy (0.1 µJ) is relatively small, it grows to a peak of around 0.14 for a laser pulse energy of around 1.8 µJ, eventually decreasing in amplitude as the bunch slice energy spread becomes larger. The peak in the bunching observed at a period of $\lambda_f \approx 15$ µm for the lowest setting of the laser heater energy is most likely due to the 'natural' microbunching that occurs purely as a function of the collective effects in the machine, rather than being induced in the laser heater.

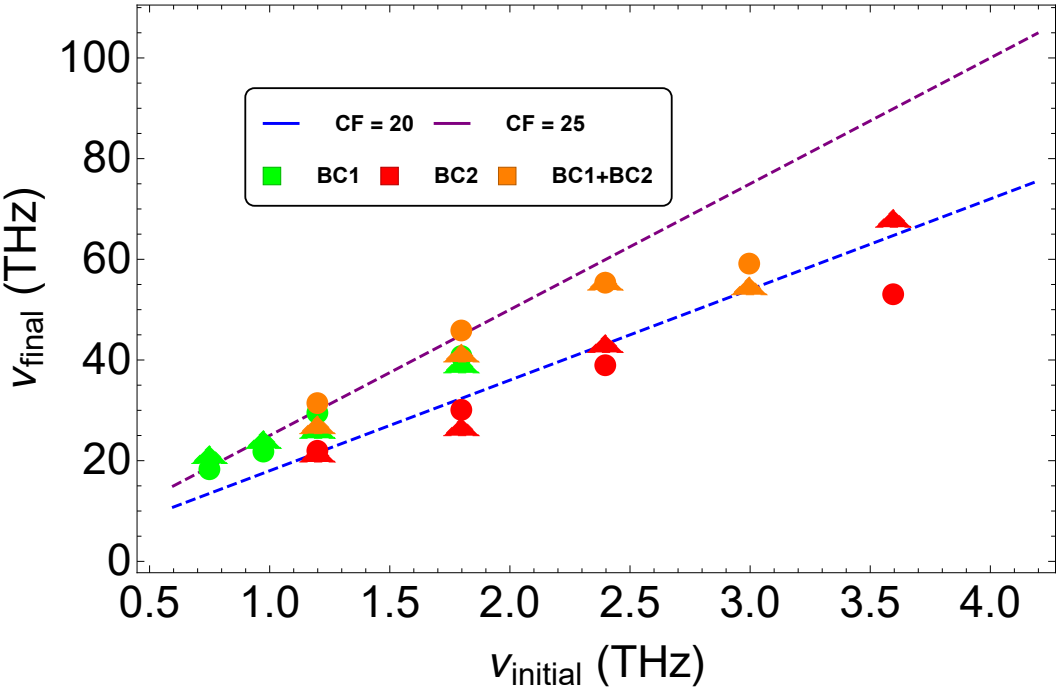

Figure 5.26: Final measured modulation frequency ν_f as a function of initial laser heater beating frequency ν_i for all three compression schemes. The dashed lines show a simple correlation between the initial and compressed laser frequency at two different compression factors ($CF \approx 20$ for BC2-only; $CF \approx 23$–25 for BC1-only and BC1+BC2); solid circles show measured values and solid triangles show simulated values.

A full summary of the relationship between the initial beating frequency and the final measured modulation period for all three compression schemes is shown in Fig. 5.26. By calculating the compressed frequency of the laser pulse in the laser heater, and comparing this with the measured frequency of the modulation on the bunch, it can be seen that, across all three compression schemes, the agreement is good. Each point on this plot represents the mean modulation frequency across a range of laser heater pulse energies – this parameter varied little over a wide range of values. A measurement of the compression factor that is independent of the modulation wavelength is the peak current of the bunch, which can be obtained by calculating the charge density in the bunch core (see Sec. 5.2.1). We found excellent agreement between these two measurements of the bunch compression factor.

Two different lines are presented for the compressed laser wavelength in Fig. 5.26. This is due to the fact that the bunch compression was not exactly the same for all three lattice configurations; namely, the bunch was slightly longer in the BC2-only configuration (see Table 5.1). This presents a simple linear correlation between the initial laser beating frequency and its compressed value. There is some divergence between this simple model and the measured/simulated final modulation frequency on the bunch itself for larger initial beating frequency. This might be due to nonlinear effects impacting the modulation on the bunch, or the fact that the laser pulse energy was not sufficiently strong to imprint significant modulations on the bunch at these values of ν_i.

We also compare the measured values with those produced by simulation, and it can be seen that the agreement here is good in most cases. By varying either the initial beating frequency or the compression factor, this technique could easily produce modulations on the bunch over an even wider range.

Due to the limitations of the pixel resolution of the measurement system, it was not possible to resolve microbunching at periods shorter than around 2 µm, as this approaches the Nyquist limit of the system. In addition to this limitation, the pulse energy of the modulated laser decreases in amplitude as the beating frequency increases (see Fig. 5.15), and therefore a larger initial pulse energy would be required to reproduce exactly the energy spread modulation

achieved for a shorter beating frequency. For smaller values of the initial beating frequency, only a small initial laser pulse energy ($< 2\,\mu J$) was required to override the 'natural' microbunching such that the period at which the peak bunching factor is measured corresponds to the modulation imposed in the laser heater. It can also be seen that the simulated values of the bunching period generally agree well with the measurements. Future work in this direction could involve running the same sets of measurements and simulations with different values of the bunch charge – this could help in deducing the extent to which the initial seed modulation is actually amplified by the collective effects.

5.6.4 Energy Modulation

As in the previous case of bunching in longitudinal density, the bunching in energy can also be studied (as shown in Fig. 5.27). We restrict this analysis only to the single-compression schemes, which exhibited significant bunching in both energy and time, since in the case of double compression, the bunches were separated only in time, with the mean slice energy remaining constant. As such, we can project our 2D Fourier transform of the longitudinal phase space onto the energy axis, revealing the point of maximal bunching in energy. It can clearly be seen that, as the initial LH beating frequency is increased, the measured energy modulation period is reduced. This bunching in energy is of interest for FELs, in particular schemes which aim to produce multi-colour pulses of light [32].

We also show, in Fig. 5.28, a plot of energy modulation period as a function of laser pulse energy. In this case, the measurements were performed for bunches compressed using BC1-only, with an initial beating frequency of 1.8 THz. As with the analogous case for a projection onto the longitudinal axis shown above for the double compression scheme (Fig. 5.25), the modulation in energy is prominent for low settings of the laser heater energy, and eventually decays as Landau damping reduces the depth of the modulations in the bunch. Having demonstrated this analysis extended from the initial 2D Fourier transform into either plane, this technique has shown to be flexible in analysing a range of longitudinal phase spaces.

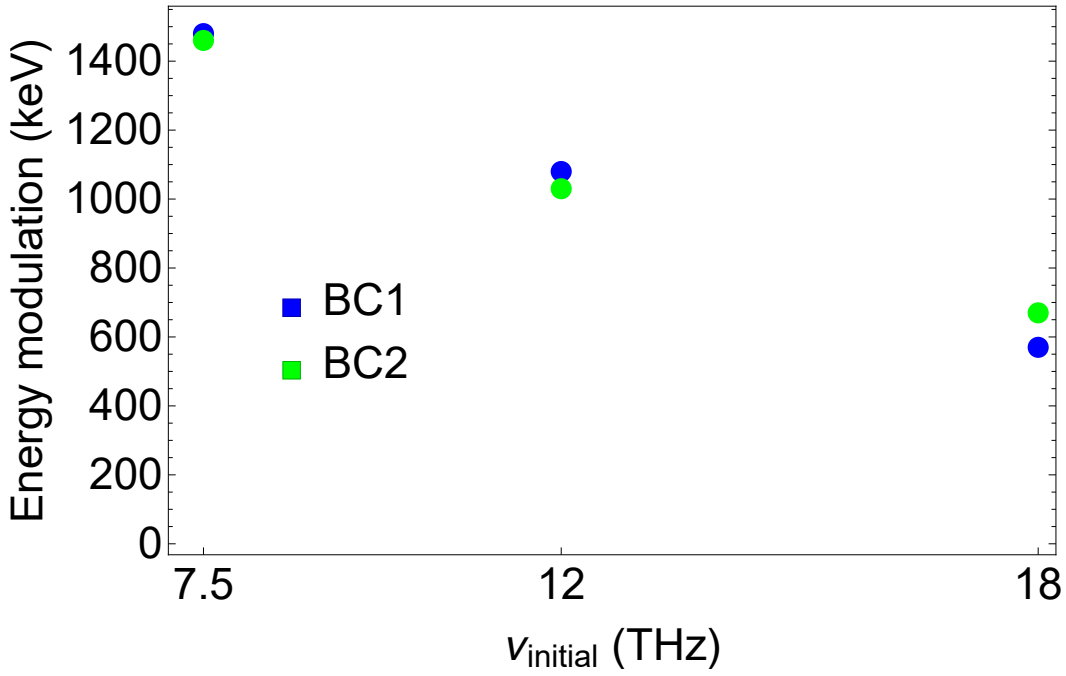

Figure 5.27: Measured energy modulation at the peak bunching factor as a function of initial beating frequencies for a fixed laser heater power. Results for BC1-only and BC2-only compression schemes are shown, since for the case of BC1+BC2 the bunches exhibited modulations purely in longitudinal density.

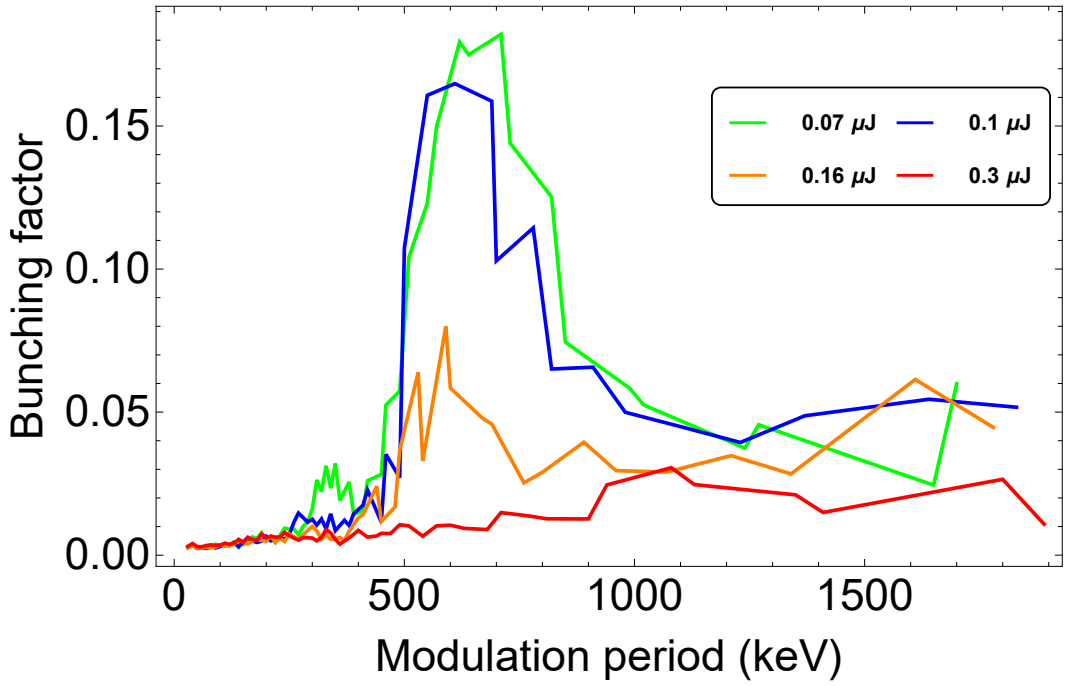

Figure 5.28: Measured bunching factor as a function of final modulation in energy for a range of laser heater pulse energies, for bunches compressed using BC1-only, with an initial laser beating frequency of 1.8 THz.

5.6.5 Microbunching Phase

One feature of a microbunched beam that can only be parameterised by analysing the full longitudinal phase space is the angle of rotation of the microbunches. As mentioned above (Sec. 2.3), the LSC forces within the bunch can cause a plasma oscillation between microbunching in energy and longitudinal density over a sufficiently long distance. This manifests itself as a rotation of the microbunches in longitudinal phase space [129]. This process of rotation is further enhanced by bunch compression, which causes a rotation and a shearing in the phase space. In the context of light source operation, the plasma oscillation phase can be of vital importance for optimising the quality of the electron beam, and so its characterisation can provide useful information. For example, if the electron beam has some finite energy spread that follows a Gaussian distribution, then (ignoring shot noise effects) the FEL pulse will have a similar distribution; if the beam is bunched in energy, there will be spikes in FEL intensity that correlate with the distribution of microbunches along the energy axis.

The plasma oscillation phase (θ_p) of a microbunched beam can be measured using the 2D Fourier transform of the bunch image, using the method shown in Sec. 5.4.4. Measurements of the bunching factor as a function of (normalised) plasma oscillation phase are shown in Fig. 5.29 for all three compression schemes. The simulated values for this parameter are also shown, with quite good agreement for all three compression schemes, in particular the case of BC1-only compression. In the other two cases, there is a difference in the location of the peak bunching factor of approximately 100 mrad, although the distributions are similar. This discrepancy could perhaps be a result of an oversimplification in the code that does not take full account of the LSC forces in the bunch. In each case, the initial beating frequency was set to 1.8 THz, but $\theta_{p,N}$ at the location of maximum bunching remained similar regardless of the initial modulation wavelength imposed on the bunch. This is because the plasma frequency depends only on the beam energy and current, and both of these parameters are fixed only by the compression scheme.

It can be seen from the figure that, in the case of the double compression scheme, the bunch exhibited a modulation almost entirely in longitudinal den-

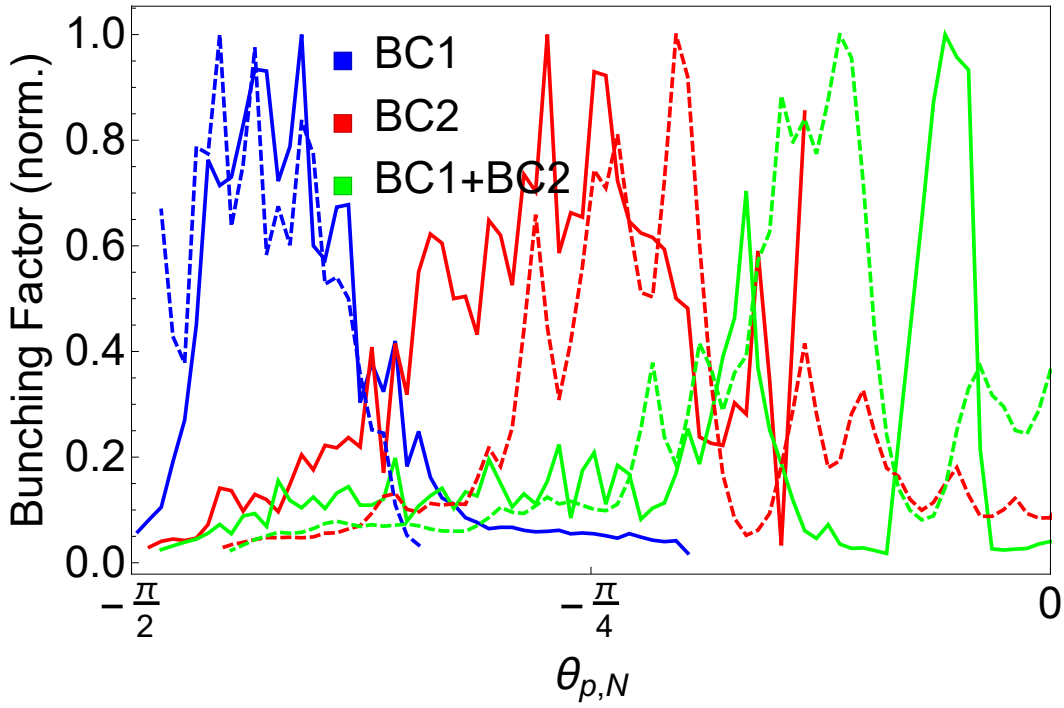

Figure 5.29: Bunching factor as a function of plasma oscillation angle $\theta_{p,N}$ for all three bunch compression schemes, each with an initial laser heater beating frequency of 1.8 THz. Each curve represents the mean bunching factor over 20 shots; solid lines show the measured bunching factor, and dashed lines show the corresponding simulations.

sity (given that the maximum bunching factor is located around $\theta_{p,N} \approx 0$). This can be seen in the longitudinal phase space plots (Fig. 5.16), in which the orientation of the microbunches results in a density modulation. In the case of single compression with BC1-only and BC2-only, there is a clear mixing between energy and density modulations, given that $\theta_{p,N}$ at the location of maximum bunching factor has a non-zero value. In such a case, the Fourier transforms of these bunches exhibit clear modulations in both energy and longitudinal density, demonstrating that a purely 1D analysis would be insufficient to describe the microbunching for these more complex structures.

5.7 Summary

This chapter has presented measurements and simulations of microbunching across a range of bunch compression schemes and laser heater configurations. A method based on 2D Fourier analysis was used to study structure within the

bunch longitudinal phase space, with the goal of measuring bunching in both time and energy simultaneously. This technique was applied to study natural microbunching, its suppression with the laser heater, and also the stimulation of microbunching with modulations of a known frequency. One goal of this study was to determine the bunch compression scheme which is most appropriate for producing bunches with a lower level of microbunching at the end of the FERMI linac. The theory of microbunching (Sec. 2.3) suggests that – at least in the case of FERMI – the amplification of modulations is lower if the bunch is compressed only once, rather than twice (Fig. 5.7). This was indeed found to be the case (see Fig. 5.11 and Sec. 5.4.3), as the measured bunching factor for the double compression scheme with the laser heater switched off was found to be approximately twice that measured for the single compression schemes.

The suppression of microbunching through the use of the laser heater in single-pulse operation mode has also been demonstrated. It was found that, even with a small increase in energy spread added by the laser heater ($< 10\,\mathrm{keV}$), the measured bunching factor decreased to the noise level for BC1-only compression. The required energy spread added was slightly larger for the other compression schemes. These results further corroborate the applicability of the 2D Fourier analysis technique to measure microbunching.

One further feature of microbunched beams that can be revealed by this analysis is the plasma oscillation phase of the microbunches. The ability to measure this feature is useful because it can provide a benchmark of theory and simulation, in order to determine their accuracy when compared with experimental measurements. The validity of microbunching theory and plasma oscillations has been a long-standing issue [19, 130], with implications for the generation of light via the FEL interaction [131]. The technique described in this chapter has been used to measure the plasma oscillation phase of a microbunched beam directly for the first time, and good agreement between measurements and semi-analytical calculations of this phase was shown for the single-compression schemes (Fig. 5.12b). These results imply that the theory of plasma oscillations can be relied upon for the development of further experimental schemes which seek to exploit this plasma oscillation.

Two other long-standing issues in the field are the validity of the theoretical microbunching gain curve, and the ability of simulation codes to reproduce accurately the microbunching that is measured experimentally, since simulation codes are vitally important when designing and commissioning an accelerator. The results presented in Secs. 5.5 and 5.6 provide a step towards an experimental measurement of the microbunching gain curve for the first time, and a corresponding set of simulations of these experiments. By stimulating modulations on the beam in the laser heater, through the use of a temporally modulated laser pulse, and measuring the bunching factor at the end of the FERMI linac (Sec. 5.5), we can begin to investigate the theoretical microbunching gain. Although the range of wavelength modulations imposed in this experiment do not cover a sufficiently wide range to provide a full measurement of the gain curve, these results, and the technique used to investigate them, can be used to pave the way towards this measurement. The pulse energy of the modulated laser becomes relatively weak when approaching frequencies near the peak of the theoretical microbunching gain curve. A future investigation of a similar nature to that described in Sec. 5.5 which could probe these short frequencies with sufficient laser intensity could provide measurements of the microbunch amplification around the peak of this curve.

Finally, these measurements of beams with imposed modulations have been simulated, and the microbunching features have been compared, along with sample images of the beam longitudinal phase space. Although some differences between measurement and simulation could be seen, good agreement was found between the microbunching features, in terms of bunching factor, modulation period, and plasma oscillation phase. The range of bunch compression schemes and use of imposed modulations extend previous studies making comparisons between simulation and experiment [66]. The results of the comparisons presented here, in addition to the previous studies, indicate that the simulation codes used in this chapter (`elegant` and GPT) can simulate accurately the microbunching that is observed experimentally, although some discrepancies remain. Therefore, it is expected that these codes can be used reliably for the design of experiments and machines in which microbunching is expected to play a significant role. How-

ever, fine-tuning of the simulation models was required in order to converge on the results which most consistently reproduced the experimental measurements, and even then the agreement was not perfect, and so these codes should be used carefully when simulating microbunching.

Chapter 6

Conclusions

6.1 CSR Investigations

By extending the 1D CSR theory, it has been found that the longitudinal electric field as observed in the CSR interaction before the entrance to, and after the exit of, a bending magnet has a qualitatively different behaviour than is commonly assumed. In particular, the contribution to the CSR field from the Coulomb field of the Liénard-Wiechert potential cannot be neglected when calculating entrance transient effects, and in order to model this interaction correctly, these fields must be taken into account. The importance of the transient effects of CSR are significant in terms of minimising the projected emittance growth in bunch compressor systems, and therefore in optimising the accuracy of beam optics matching to the undulator line for high-gain UV and X-ray FELs [132, 133]. These observations are interesting technologically because they suggest that it may be possible to design an optimized magnet (or system of magnets) in which the CSR impact of the magnet itself is partially cancelled by that of the drift directly after it, thereby reducing adverse effects like emittance growth and microbunching gain, particularly in more complex transport systems such as compressive arcs in energy recovery linacs (ERLs). It may also be possible to extend the analytical treatment in the case of two bending magnets limiting a straight drift, providing an extension of the validity range of the formulae.

A comparison between experimental measurements and simulation results to determine the effect of CSR on projected emittance growth has been demon-

strated. The simulation codes `elegant`, GPT and CSRTrack have been employed for this comparison. Good agreement between the simulations and FERMI measurements is seen when the bunch compression, RF parameters, and matching are closest to their nominal settings. As the compression ratio increases, the differences between the simulation methods become more clear. As expected, the 1D simulation results diverge more significantly both from the experimental data, and from simulations results with codes which take the transverse extent of the bunch into account in situations where the condition (in terms of the Derbenev parameter) given in Eq. 4.11 is strongly violated, and the 1D CSR approximation breaks down. The breakdown of this condition has been studied experimentally; the theory suggested that the condition is valid only in the parameter regime $D_{par} \ll 1$, whereas it has been demonstrated that up to $D_{par} \approx 3.5$, the commonly used CSR theory remains valid – at least in terms of predicted emittance growth, and under the parameters of the FERMI experiment – and so this condition can potentially be relaxed.

High-brightness FELs benefit from tight control of beam emittance throughout the machine. A more accurate and realistic prediction of beam brightness degradation/preservation, also in proximity of points of full compression, would allow an optimized design from the very first stages. A recent study has been conducted to investigate the CSR interaction across two dipole magnets in an ERL, in which the CSR interaction between two particles can be carried from one magnet to another, as a result of their close proximity [134]. An investigation of the impact of transient CSR fields in a case such as this would be an interesting point of study for future work.

6.2 Microbunching Investigations

An in-depth analysis of the microbunching instability in the longitudinal phase space of high-brightness electron beams has been undertaken. This instability, resulting from a combination of collective effects, can have a strong adverse impact on the electron bunch properties, and must be understood in order to improve the quality of future accelerators. As such, the work completed in this thesis has

focused on developing new analysis methods for diagnosing the instability by measuring the frequency of modulation in the full 2D longitudinal phase space.

By measuring the amplitude of the density modulations in these bunches, and their frequency in time and in energy, the development of the instability has been quantified, providing a useful benchmark for theoretical predictions and simulations. The instability was parametrised through studying various properties of the longitudinal phase space and its associated Fourier transform in 2D. The amplitude of the density modulations provide a measurement of the bunching factor, demonstrating the strength of the instability. The period of these modulations can be compared with theoretical calculations of the microbunching gain, which predict the amplification in density modulation as a function of initial modulation wavelength. Finally, the 2D Fourier analysis reveals the orientation of the microbunching in phase space, giving a deeper insight into the effect than that which can be provided by measurement of the microbunching just in energy or in longitudinal density. The measured tilt angle, which is exhibited in the Fourier transform of the beam image as the position of the microbunching satellite with respect to the central term, gives the phase of the plasma oscillation between microbunching in energy and longitudinal density.

The instability is mitigated at FERMI and a number of similar machines through the use of a laser heater, which adds a small uncorrelated energy spread to the electron bunch in the low-energy section of the machine. The technique of 2D Fourier analysis developed in this thesis was applied to both unheated and heated bunches, and the damping of the instability was clearly shown, even when the energy spread added by the laser heater was relatively small, thus preserving the low slice energy spread necessary for optimal FEL operation.

In addition to this study, a novel technique was applied to stimulate the microbunching instability. This was achieved through the use of chirped-pulse beating of the laser heater pulse – a technique that chirps the initial laser pulse, separates it into two pulses, then recombines them with a variable delay between the pulses in an interferometer. This method produced laser pulses with a controllable wavelength which could approach the same order of magnitude as the electron bunch length. Therefore, modulations in energy spread could

be imposed onto the electron bunch, which was then transformed into a density modulation through the use of a dispersive magnetic chicane. The amplitude of the modulation could be controlled through varying the intensity of the laser pulse, and the wavelength of the final pulse could be varied by changing the length of the interferometer arm for one of the separated laser pulses.

The flexibility of this technique provided a range of modulated electron bunches which were then characterised using the analysis technique described above. By measuring the bunching factor for a range of modulated laser pulse energies and wavelengths, the microbunching instability could be studied in unprecedented detail, and compared with simulation and theory. In addition to allowing detailed tests of the theory and simulation codes, this technique could have wide-ranging applications in the production of multi-colour FEL light, the production of light in the THz range – an area which has previously been difficult to reach with conventional accelerator techniques – or as the basis for future plasma-based accelerators which rely on multiple bunches separated in time.

Future avenues of research for this technique could include producing bunches with a longitudinal density or energy modulation with a view to their application in light-source generation. Additionally, under the right conditions, the ability to quantify the bunching factor as a function of imposed modulation frequency could result in an experimental study of the microbunching gain for the first time. In the case of the experiments analysed for this thesis, the initial modulation wavelengths imposed by the laser pulse did not cover a sufficiently wide range for the microbunching gain to be studied in this way; nevertheless, the results presented here suggest the possibility of measuring this parameter in future.

Appendix A

A.1 Derivation of CSR Entrance Transient

We begin by calculating a number of distances shown in Fig. 2.3. The angle ϕ is the angle between the receiving particle at position $\vec{r_1}$ and the entrance of the arc. The two orthogonal directions of this arc (h, D) are given by $h = 2R\sin(\phi/2)$ and $D = R\sin(\phi)$, and therefore the distance ρ between the emitter at the retarded position $\vec{r_0}'$, at a distance y before the entrance to the magnet, and the receiver at $\vec{r_1}$ is:

$$\rho = \sqrt{h^2 + (y+D)^2} = \sqrt{4R^2\sin^2(\phi/2) + 2Ry\sin(\phi) + y^2}. \tag{A.1}$$

The time taken by electromagnetic signals to travel from emitter to observer is $t - t' = \rho/c$. During this same time, the bunch must have traveled a distance $R\phi + y - \Delta z$ along the path in order to have the observing electron at the position sketched in Fig. 2.3 at time t, where $\Delta z = z - z'$ is the instantaneous distance between both electrons. Therefore $t - t' = (R\phi + y - \Delta z)/(\beta c)$, from which follows the retardation condition:

$$\Delta z = y + R\phi - \beta\rho. \tag{A.2}$$

Two more useful lengths sketched in Fig. 2.3 are:

$$w = \frac{y}{y+D}h = \frac{2yR\sin^2(\phi/2)}{y + R\sin(\phi)} \tag{A.3}$$

and

$$L = \frac{D}{y+D}\rho = \frac{R\sin(\phi)}{y+R\sin(\phi)}\rho, \tag{A.4}$$

where L is the distance between the entrance to the magnet and the observation point $\vec{r_1}$. These lengths can be used to derive the cosine and sine of the angles ξ and θ between the vectors $\vec{n}$, $\vec{\beta}$ and $\vec{\beta}'$ which are required to evaluate Eq. 2.31. The triangle defined by the emitter and the endpoints of h gives:

$$\cos(\theta) = \frac{y+D}{\rho} = \frac{y+R\sin(\phi)}{\rho} \tag{A.5}$$

and

$$\sin(\theta) = \frac{h}{\rho} = \frac{2R\sin^2(\phi/2)}{\rho}. \tag{A.6}$$

In order to calculate ξ we need to use its complementary angle η. Using the cosine and sine rules on the triangle defined by η and ϕ gives:

$$\cos(\xi) = \sin(\eta) = \frac{R-w}{L}\sin(\phi) = \frac{R\sin(\phi)+y\cos(\phi)}{\rho} \tag{A.7}$$

and

$$\sin\xi = \cos\eta = \frac{R^2+L^2-(R-w)^2}{2RL} = \frac{2\sin(\phi/2)(R\sin(\phi/2)+y\cos(\phi/2))}{\rho}. \tag{A.8}$$

Having these angles available, we can now calculate the point-to-point Liénard-Wiechert field of the emitter $\vec{E}^{PP}$ at the position of the receiver. Since we require only the parallel component, we can take the inner product $\vec{\beta}\cdot\vec{E}^{PP}$. Additionally, because the emitter is in uniform motion, its retarded electric field is given only by the Coulomb term of the Liénard-Wiechert field, yielding:

$$E_{||}^{PP,ent} = \frac{e}{4\pi\epsilon_0\gamma^2}\frac{\vec{n}\cdot\vec{\beta}-\vec{\beta}'\cdot\vec{\beta}}{(1-\vec{n}\cdot\vec{\beta})^3\rho^2}. \tag{A.9}$$

These inner products can be expressed in terms of the angle ϕ as follows:

$$\vec{n} \cdot \vec{\beta} = \beta \cos(\xi) = \beta \frac{R \sin(\phi) + y \cos(\phi)}{\rho}, \tag{A.10}$$

$$\vec{n} \cdot \vec{\beta}' = \beta \cos\theta = \beta \frac{y + R \sin(\phi)}{\rho} \tag{A.11}$$

and

$$\vec{\beta} \cdot \vec{\beta}' = \beta^2 \cos(\phi). \tag{A.12}$$

Substituting into Eq. A.9 gives:

$$E_{||}^{PP,ent}(y) = \frac{e}{4\pi\epsilon_0\gamma^2} \frac{(y - \beta\rho)\cos(\phi) + R\sin(\phi)}{(\rho - \beta(y + R\sin(\phi)))^3}. \tag{A.13}$$

This is the field observed by a single point particle at an angle ϕ into the arc, produced by another single point particle at a distance y before the entrance of the arc. In order to obtain the field due to a bunch of particles, the bunch with a charge density $Ne\lambda(z)$ should be thought of as a number of point particles at positions $s = s_c + z$, each with charge $Ne\lambda(z)dz$, where s is the absolute position along the path, z is the position within the bunch relative to the bunch centroid and s_c the position of the centroid. Summing up the contributions from all the fields of these point particles gives:

$$E_{||}^{ent}(z, y) = Ne \int_{-\infty}^{z_{max}} E_{||}^{PP,ent}\left(y(z')\right) \lambda(z') dz' + E_{||}^{SS}, \tag{A.14}$$

where the first term represents the field contribution at the position of the receiver due to the part of the bunch that is still before the magnet entrance at the time of emission, $E_{||}^{SS}$ is the contribution to the field due to the part of the bunch that is inside the magnet at the same time, and z_{max} is the position in the bunch giving the boundary between these two parts. In order to evaluate Eq. A.14 directly, an explicit relation between the current position of the emitter z' and its position at the time of emission y is required. This can be done by changing the integration

variable from z' to y, and so we can use Eq. A.2 to calculate dz'/dy:

$$\frac{dz'}{dy} = -\frac{\rho - \beta(y + R\sin(\phi))}{\rho}. \tag{A.15}$$

Given this relation and that from Eq. 2.33, we have an equation for $E_{||}^{SS}$, and the total CSR entrance field thus becomes:

$$\begin{aligned} E_{||}^{ent}(z,y) &= Ne \int_{-\infty}^{z_{max}} E_{||}^{PP,ent}(y)\lambda(z'(y))\frac{dz'}{dy}dy + E_{||}^{SS} \\ &= E_{||}^{SS} + \frac{Ne}{4\pi\epsilon_0\gamma^2}\int_0^d \frac{(y-\beta\rho(y))\cos(\phi) + R\sin(\phi)}{(\rho(y) - \beta(y + R\sin(\phi)))^2\rho(y)}\lambda(z - \Delta(y))dy, \end{aligned} \tag{A.16}$$

where $\Delta(y) = y + R\phi - \beta\rho(y)$, and d the length of the drift before the magnet taken into account for the calculation of the CSR field. The upper integration boundary of this expression arises due to the finite length of the straight section before the entrance to the magnet.

A.2 Derivation of CSR Exit Transient

This derivation will parallel that given above in A.1 for the entrance transients. To evaluate Eq. 2.31, we first calculate a number of lengths indicated in Fig. 2.5. The angle ψ is the angle between the emitter and the end of the arc. The lengths (h, D) along two orthogonal directions associated with this arc are given by $h = 2R\sin(\psi/2)$ and $D = R\sin(\psi)$. Therefore ρ is equal to:

$$\rho = \sqrt{h^2 + (x + D)^2} = \sqrt{4R^2\sin^2(\psi/2) + 2Rx\sin(\psi) + x^2}, \tag{A.17}$$

where x is the distance from the exit edge of the magnet to the observing electron. The time taken by electromagnetic signals to travel from emitter to observer is $t - t' = \rho/c$. During this same time, the bunch must have traveled a distance $R\psi + x - \Delta z$ along the path in order to have the observing electron at the position sketched in Fig. 2.5 at time t, where $\Delta z = z - z'$ is the instantaneous distance between both electrons. Therefore $t - t' = (R\psi + x - \Delta z)/(\beta c)$, from which

follows the retardation condition:

$$\Delta z = x + R\psi - \beta\rho. \tag{A.18}$$

Two more useful lengths sketched in Fig. 2.5 are:

$$w = \frac{2xR\sin^2(\psi/2)}{(x + R\sin(\psi))} \tag{A.19}$$

and

$$L = \frac{R\rho\sin(\psi)}{(x + R\sin\psi)}, \tag{A.20}$$

where L is the distance between the emitting electron at $\vec{r'}$ and the exit of the magnet. These lengths can be used to derive the angles ξ and θ between the three vectors $\vec{n}, \vec{\beta}$ and $\vec{\beta'}$ indicated in Fig. 2.5. The triangle defined by $\vec{r}$ and the endpoints of h gives $\cos(\xi) = (x + R\sin(\psi))/\rho$ and $\sin(\xi) = (2R/\rho)\sin^2(\psi/2)$. Using the cosine and sine rules on the triangle defined by η and ψ gives:

$$\cos\theta = (R\sin(\psi) + x\cos(\psi))/\rho \tag{A.21}$$

and

$$\sin\theta = 2\sin(\psi/2)(R\sin(\psi/2) + x\cos(\psi/2))/\rho. \tag{A.22}$$

Since we are interested only in the component of the field parallel to the direction of $\vec{\beta}$, we take the inner product $\vec{\beta}\cdot\vec{E}$. As it turns out, both the radiation term and the Coulomb term of the Liénard-Wiechert field make a significant contribution, even in the ultrarelativistic limit. Expanding the triple vector product in the radiation term of the field (Eq. 2.31) and taking the inner

product of the full Liénard-Wiechert field with $\vec{\beta}$ gives:

$$E_{\parallel}^{PP} = \frac{\vec{\beta}\cdot\vec{E}}{\beta} = \frac{e}{4\pi\epsilon_0\beta}\left(\frac{\left(\vec{n}.\vec{\beta}-\vec{\beta}\cdot\vec{\beta}'\right)}{\gamma^2\left(1-\vec{n}\cdot\vec{\beta}'\right)^3\rho^2}\times \frac{\left(\vec{n}\cdot\vec{\beta}-\vec{\beta}\cdot\vec{\beta}'\right)\left(\vec{n}\cdot\dot{\vec{\beta}}'\right)-\left(1-\vec{n}\cdot\vec{\beta}'\right)\left(\vec{\beta}\cdot\dot{\vec{\beta}}'\right)}{c\left(1-\vec{n}\cdot\vec{\beta}'\right)^3\rho}\right). \tag{A.23}$$

The superscript PP indicates that Eq. A.23 gives the field of a point particle. We can calculate the inner products in this expression as follows:

$$\vec{n}\cdot\vec{\beta} = \beta\cos(\xi) = \beta\frac{x+R\sin(\psi)}{\rho}, \tag{A.24}$$

$$\vec{n}\cdot\vec{\beta}' = \beta\cos(\theta) = \beta\frac{R\sin(\psi)+x\cos(\psi)}{\rho}, \tag{A.25}$$

$$\vec{n}\cdot\dot{\vec{\beta}}' = \frac{\beta^2 c}{R}\sin(\theta) = \frac{\beta^2 c}{R}\frac{2\sin(\psi/2)\left(R\sin(\psi/2)+x\cos(\psi/2)\right)}{\rho}, \tag{A.26}$$

$$\vec{\beta}\cdot\vec{\beta}' = \beta^2\cos(\psi), \tag{A.27}$$

$$\vec{\beta}\cdot\dot{\vec{\beta}}' = \frac{\beta^3 c}{R}\sin(\psi). \tag{A.28}$$

Substituting these expressions into Eq. A.23 and separating the first and second terms into the Coulomb and radiation components, respectively, results in the single-particle longitudinal components of the CSR field:

$$E_{||,C}^{PP,exit}(z,x) = \frac{e\beta}{4\pi\epsilon_0\gamma^2}\frac{x+R\sin(\psi)-\beta\rho\cos(\psi)}{\left(\rho-\beta\left(R\sin(\psi)+x\cos(\psi)\right)\right)^3}, \tag{A.29}$$

$$E_{||,rad}^{PP,exit}(z,x) = \frac{e\beta^2}{4\pi\epsilon_0 R}\times \left(\frac{2\sin(\psi/2)\left(x+R\sin(\psi)-\beta\rho\cos(\psi)\right)\left(R\sin(\psi/2)+x\cos(\psi/2)\right)}{\left(\rho-\beta\left(R\sin(\psi)+x\cos(\psi)\right)\right)^3} - \frac{\rho\sin(\psi)}{\left(\rho-\beta\left(R\sin(\psi)+x\cos(\psi)\right)\right)^2}\right). \quad \text{(A.30)}$$

These are the contributions of the Coulomb and radiation terms to the field observed by a single electron at distance x after the exit of the arc, produced by another single electron at angle ψ before the exit of the arc. Which particular electron of the bunch distribution actually is at angle ψ at the required time of emission is governed by the retardation condition Eq. A.18. One may be tempted to neglect the Coulomb term $E_{||,C}^{PP}$ in the ultrarelativistic limit on account of the factor γ^{-2}. However, the radiation term contains an additional small factor $\sin(\psi/2)$ in the numerator, and so in the end both terms are comparable in size. The combined field E due to all electrons between the tail of the bunch and the observing electron is obtained by adding the fields E^{PP} of the individual particles. This results in:

$$E_{||}^{exit}(z,x) = Ne\int_{-\infty}^{z} E_{||}^{PP,exit}\left(\psi(z')\right)\lambda(z')dz', \quad \text{(A.31)}$$

where N is the number of particles in the bunch and $\lambda(z')$ is the charge distribution normalised such that $\int_{-\infty}^{+\infty}\lambda(z')dz' = 1$. To evaluate this integral directly, an explicit relation $\psi(z')$ between the current position of the emitter z' and the position at time of emission given by ψ is necessary. To avoid this complication, we change the integration variable from z' to ψ. This requires the derivative $dz'/d\psi$, which from Eq. A.18 is $-R\left(1-\beta\left(R\sin(\psi)+x\cos(\psi)\right)/\rho\right)$. Eq. A.31 thus becomes:

$$E_{||}^{exit}(z,x) = Ne\int_{0}^{\phi_m} E_{||}^{PP,exit}(\psi)\lambda\left(z'(\psi)\right)\frac{dz'}{d\psi}d\psi = E_{||,C}^{exit}(z,x) + E_{||,rad}^{exit}(z,x), \quad \text{(A.32)}$$

and the Coulomb and radiation terms are defined as:

$$E^{exit}_{||,C}(z,x) = \frac{Ne\beta R}{4\pi\epsilon_0\gamma^2}\int_0^{\phi_m} \frac{x + R\sin(\psi) - \beta\rho\cos(\psi)}{\left(\rho - \beta\left(R\sin(\psi) + x\cos(\psi)\right)\right)^2\rho}\lambda\left(z'(\psi)\right)d\psi, \quad \text{(A.33)}$$

and

$$E^{exit}_{||,rad}(z,x) = \frac{Ne\beta^2}{4\pi\epsilon_0}\times \int_0^{\phi_m}\left(\frac{2\sin(\psi/2)\left(x + R\sin(\psi) - \beta\rho\cos(\psi)\right)\left(R\sin(\psi/2) + x\cos(\psi/2)\right)}{\left(\rho - \beta\left(R\sin(\psi) + x\cos(\psi)\right)\right)^2\rho} - \frac{\sin(\psi)}{\rho - \beta\left(R\sin(\psi) + x\cos(\psi)\right)}\right)\lambda\left(z'(\psi)\right)d\psi. \quad \text{(A.34)}$$

In this expression, $x = x_c + z$ is the position of the evaluation point s with respect to the exit edge of the magnet, with x_c the distance from exit edge to bunch centroid and z the position in the bunch where the field is evaluated relative to the bunch centroid. In the integral, the charge density should be evaluated at z', which from Eq. A.2 is given by $z'(\psi) = x_c + z - x_c - z' = -x_c - R\psi + \beta\rho$.

The expressions for $E^{exit}_{||,C}$ and $E^{exit}_{||,rad}$ give the Liénard-Wiechert field of a bunch exiting a circular arc, without any ultrarelativistic or small-angle approximations. However, through applying these approximations we can arrive at a simpler form for these fields. Given that the integrands in these expressions are strongly peaked around a small range of $\psi \ll 1$, approximations can be made using Taylor expansions – although it should be noted that the approximation $\psi \ll x/R$ cannot be used, as the post-bend distance x may also be small. First, we re-evaluate the distance ρ (Eq. A.17) between the emitter at the retarded time and

the receiver at the current time:

$$\begin{aligned}\rho &\approx \sqrt{4R^2\left(\frac{1}{4}\psi^2-\frac{1}{48}\psi^4\right)+2Rx\left(\psi-\frac{1}{6}\psi^3\right)+x^2} \\ &= R(\psi+x_n)\sqrt{1-\frac{\frac{1}{12}\psi^4+\frac{1}{3}x_n\psi^3}{(\psi+x_n)^2}} \\ &\approx R\left(\psi+x_n-\frac{\psi^2}{24}\frac{\psi^2+4\psi x_n}{\psi+x_n}\right),\end{aligned} \tag{A.35}$$

where $x_n = x/R$. This approximation can now be applied to Eqs. A.33 and A.34. Expanding all the trigonometric functions results in:

$$E^{exit}_{||,C}(z,x) \approx \frac{8Ne}{3\pi\epsilon_0}\int_0^{\phi_m}\frac{\gamma^{-2}N_1(\psi)+\psi^2N_2(\psi)+...}{\left(\gamma^{-2}D_1(\psi)+\psi^2D_2(\psi)\right)^2}\gamma^{-2}\lambda\left(z'(\psi)\right)d\psi, \tag{A.36}$$

$$E^{exit}_{||,rad}(z,x) \approx \frac{Ne}{\pi\epsilon_0}\int_0^{\phi_m}\frac{\gamma^{-2}N_3(\psi)+\psi^2N_4(\psi)+...}{\left(\gamma^{-2}D_1(\psi)+\psi^2D_2(\psi)\right)^2}\psi^2\lambda\left(z'(\psi)\right)d\psi, \tag{A.37}$$

where (to quadratic order in ψ and x_n):

$$N_1(\psi) = 3\left(\psi+x_n\right)^2+... \tag{A.38a}$$

$$N_2(\psi) = \left(\psi+x_n\right)\left(2\psi+3x_n\right)+... \tag{A.38b}$$

$$N_3(\psi) = 4\left(\psi+x_n\right)^2+... \tag{A.38c}$$

$$N_4(\psi) = \left(\psi+2x_n\right)^2+... \tag{A.38d}$$

$$D_1(\psi) = 4\left(\psi+x_n\right)^2+... \tag{A.38e}$$

$$D_2(\psi) = \left(\psi+2x_n\right)^2+... \tag{A.38f}$$

There are two important results in Eqs. A.36 and A.37. Firstly, the velocity field is suppressed by a factor γ^{-2}, so in many cases this field is negligible with respect to the radiation field. However, the integrand of the radiation field also contains the factor ψ^2, which suppresses this field at small angles. Therefore,

there is a small part of the integration interval $\psi \lesssim \gamma^{-1}$ in which the Coulomb field dominates, rather than the radiation field, and vice versa for the regime $\psi \gtrsim \gamma^{-1}$. Secondly, in both the Coulomb field and the radiation field individually, the same two regimes can be distinguished when considering the importance of the terms proportional to γ^{-2} against those proportional to ψ^2. Therefore, in the regime where the Coulomb field dominates, the significant terms are N_1 and D_1, and in the regime with the dominant radiation field, the significant terms are N_4 and D_2. Combining these results, we can make a further approximation:

$$E_{||}^{exit}(z,x) \approx \frac{8Ne}{3\pi\epsilon_0}\int_0^{\phi_m}\frac{N_1(\psi)}{D_1(\psi)^2}\lambda\left(z'(\psi)\right)d\psi + \frac{Ne}{\pi\epsilon_0}\int_0^{\phi_m}\frac{N_4(\psi)}{D_2(\psi)^2}\lambda\left(z'(\psi)\right)d\psi. \tag{A.39}$$

An approximation to $dz/d\psi$ (from Eq. A.2) can be made in the ultrarelativistic limit, as $\gamma \to \infty$:

$$\frac{dz'}{d\psi} = -\frac{R}{\rho}\left(\rho - \beta\left(R\sin(\psi) + x\cos(\psi)\right)\right) \approx -\frac{R\psi^2\left(\psi+2x_n\right)^2}{8\left(\psi+x_n\right)^2}. \tag{A.40}$$

Given that the Coulomb term is only significant in a small range $\psi \lesssim \gamma^{-1} \ll 1$ for sufficiently high beam energy, and that over this range the charge density will not vary significantly, we can approximate the field as follows:

$$\begin{aligned} E_{||,C}^{exit}(z,x) &\approx \frac{8Ne}{3\pi\epsilon_0}\int_0^{\phi_m}\frac{N_1(\psi)}{D_1(\psi)^2}\lambda(z'(\psi))d\psi \\ &\approx \frac{Ne}{2\pi\epsilon_0}\lambda(z'(0))\int_0^{\phi_m}\frac{d\psi}{\left(\psi+x_n\right)^2} = \frac{Ne}{2\pi\epsilon_0}\frac{\lambda(z'(0))}{x_n}. \end{aligned} \tag{A.41}$$

Integrating the second term on the right-hand side of Eq. A.39 (the radiation component) by parts gives:

$$E_{||,rad}^{exit}(z,x) \approx \frac{Ne}{\pi\epsilon_0}\left(\frac{\lambda(z-\Delta z_{max})}{\phi_m R + 2x_n} - \frac{\lambda(z)}{2x_n} + \int_{z-\Delta z_{max}}^{z-\Delta z_{min}}\frac{\partial\lambda(z')}{\partial z'}\frac{dz'}{\psi(z')R+2x_n}\right). \tag{A.42}$$

In the integrand of this expression, $\psi(z)$ is defined implicitly by the relation:

$$z - z' = f(\psi) = \frac{R\psi^3}{24}\frac{R\psi + 4x}{R\psi + x}. \tag{A.43}$$

and $\Delta z_{max} = f(\phi_m)$. Now, it can be seen that there is an exact cancellation between the second term of $E^{exit}_{||,rad}$ and $E^{exit}_{||,C}$, leading to a final approximation for the exit transient field:

$$E^{exit}_{||}(z,x) \approx \frac{Ne}{\pi\epsilon_0}\left(\frac{\lambda(z-\Delta z_{max})}{\phi_m R + 2x_n} + \int_{z-\Delta z_{max}}^{z} \frac{\partial\lambda(z')}{\partial z'}\frac{dz'}{\psi(z')R + 2x_n}\right), \tag{A.44}$$

This is an equivalent result to that derived in [56], but for a qualitatively different reason: the cancellation of terms between the Coulomb and radiation fields in the exit transient regime.

Bibliography

[1] J. D. Jackson. *Classical Electrodynamics*. Wiley, 1962.

[2] H. Motz. Applications of the radiation from fast electron beams. *J. Appl. Phys.*, 22(527), 1951.

[3] H. Motz, W. Thon, and R. N. Whitehurst. Experiments on radiation by fast electron beams. *J. Appl. Phys.*, 24(826), 1953.

[4] D. H. Bilderback, P. Ellaume, and E. Weckert. Review of third and next generation synchrotron light sources. *J. Phys. B*, 38(9):S773, 2005.

[5] J. M. J. Madey. Stimulated emission of Bremsstrahlung in a periodic magnetic field. *J. Appl. Phys.*, 42(1906), 1971.

[6] P. Finetti, H. Höppner, E. Allaria, C. Callegari, F. Capotondi, P. Cinquegrana, M. Coreno, R. Cucini, M. B. Danailov, A. Demidovich, G. De Ninno, M. Di Fraia, R. Feifel, E. Ferrari, L. Fröhlich, D. Gauthier, T. Golz, C. Grazioli, Y. Kai, G. Kurdi, N. Mahne, M. Manfredda, N. Medvedev, I. P. Nikolov, E. Pedersoli, G. Penco, O. Plekan, M. J. Prandolini, K. C. Prince, L. Raimondi, P. Rebernik, R. Riedel, E. Roussel, P. Sigalotti, R. Squibb, N. Stojanovic, S. Stranges, C. Svetina, T. Tanikawa, U. Teubner, V. Tkachenko, S. Toleikis, M. Zangrando, B. Ziaja, F. Tavella, and L. Giannessi. Pulse duration of seeded free-electron lasers. *Phys. Rev. X*, 7:021043, Jun 2017.

[7] C. Bostedt, S. Boutet, D. M. Fritz, Z. Huang, H. J. Lee, H. T. Lemke, A. Robert, W. F. Schlotter, J. J. Turner, and G. J. Williams. Linac Coherent Light Source: The first five years. *Rev. Mod. Phys.*, 88:015007, 2016.

[8] E. L. Saldin, E. A. Schneidmiller, and M. V. Yurkov. *The Physics of Free Electron Lasers*. Springer, 2000.

[9] P. Schmüser, M. Dohlus, J. Rossbach, and C. Behrens. *Free-Electron Lasers in the Ultraviolet and X-ray regime*. Springer, 2014.

[10] R. Bonifacio, L. De Salvo Souza, P. Pierini, and E.T. Scharlemann. Generation of XUV light by resonant frequency tripling in a two-wiggler FEL amplifier. *Nucl. Instrum. Meth. A*, 296(1):787, 1990.

[11] R. Bonifacio, C. Pellegrini, and L.M. Narducci. Collective instabilities and high-gain regime in a free electron laser. *Opt. Commun.*, 50(6):373, 1984.

[12] L. H. Yu. Generation of intense UV radiation by subharmonically seeded single-pass free-electron lasers. *Phys. Rev. A*, 44:5178, 1991.

[13] E. Allaria, R. Appio, L. Badano, W. A. Barletta, S. Bassanese, S. G. Biedron, A. Borga, E. Busetto, D. Castronovo, P. Cinquegrana, S. Cleva, D. Cocco, M. Cornacchia, P. Craievich, I. Cudin, M. Dal Forno, M. B. Danailov, G. D'Auria, R. De Monte, A. Demidovich, G. De Ninno, P. Delguisto, S. Di Mitri, B. Diviacco, A. Fabris, R. Fabris, W. M. Fawley, M. Ferianis, E. Ferrari, S. Ferry, L. Fröhlich, P. Furlan, G. Gaio, F. Gelmetti, L. Giannessi, M. Giannini, R. Gobessi, R. Ivanov, E. Karantzoulis, M. Lonza, A. Lutman, B. Mahieu, M. Milloch, S. V. Milton, M. Musardo, I. Nikolov, S. Noe, F. Parmigiani, G. Penco, M. Petronio, L. Pivetta, M. Predonzani, F. Rossi, L. Rumiz, A. Salom, C. Scafuri, C. Serpico, P. Sigalotti, S. Spampinati, C. Spezzani, M. Svandrlik, C. Svetina, S. Tazzari, M. Trovò, R. Umer, A. Vascotto M. Veronese, R. Visintini, M. Zaccaria, D. Zangrando, and M. Zangrando. Highly coherent and stable pulses from the FERMI seeded free-electron laser in the extreme ultraviolet. *Nat. Photon.*, 6:699, 2012.

[14] K. L. F. Bane, F.-J. Decker, Y. Ding, D. Dowell, P. Emma, J. Frisch, Z. Huang, R. Iverson, C. Limborg-Deprey, H. Loos, H.-D. Nuhn, D. Ratner, G. Stupakov, J. Turner, J. Welch, and J. Wu. Measurements and modeling

of coherent synchrotron radiation and its impact on the Linac Coherent Light Source electron beam. *Phys. Rev. ST Accel. Beams*, 12:030704, 2009.

[15] S. Di Mitri, E. M. Allaria, P. Craievich, W. Fawley, L. Giannessi, A. Lutman, G. Penco, S. Spampinati, and M. Trovò. Transverse emittance preservation during bunch compression in the FERMI free electron laser. *Phys. Rev. ST Accel. Beams*, 15:020701, 2012.

[16] C. C. Hall, S. G. Biedron, A. L. Edelen, S. V. Milton, S. Benson, D. Douglas, R. Li, C. D. Tennant, and B. E. Carlsten. Measurement and simulation of the impact of coherent synchrotron radiation on the Jefferson Laboratory energy recovery linac electron beam. *Phys. Rev. ST Accel. Beams*, 18:030706, 2015.

[17] S. Bettoni, M. Aiba, B. Beutner, M. Pedrozzi, E. Prat, S. Reiche, and T. Schietinger. Preservations of low slice emittance in bunch compressors. *Phys. Rev. Accel. Beams*, 19:034402, 2016.

[18] E. L. Saldin, E. A. Schneidmiller, and M. V. Yurkov. On the coherent radiation of an electron bunch moving in an arc of a circle. *Nucl. Instrum. Meth. A*, 398(2):373, 1997.

[19] J. B. Rosenzweig, C. Pellegrini, L. Serafini, C. Ternieden, and G. Travish. Space-charge oscillations in a self-modulated electron beam in multi-undulator free-electron lasers. *Nucl. Instrum. Meth. A*, 393(2):376, 1997.

[20] E. L. Saldin, E. A. Schneidmiller, and M. V. Yurkov. An analytical description of longitudinal phase space distortions in magnetic bunch compressors. *Nucl. Instrum. Meth. A*, 483(1):516, 2002.

[21] E. L. Saldin, E. A. Schneidmiller, and M. V. Yurkov. Longitudinal space charge-driven microbunching instability in the TESLA Test Facility linac. *Nucl. Instrum. Meth. A*, 528(1):355, 2004.

[22] Z. Huang and K.-J. Kim. Formulas for coherent synchrotron radiation microbunching in a bunch compressor chicane. *Phys. Rev. ST Accel. Beams*, 5:074401, 2002.

[23] R. Akre, D. Dowell, P. Emma, J. Frisch, S. Gilevich, G. Hays, Ph. Hering, R. Iverson, C. Limborg-Deprey, H. Loos, A. Miahnahri, J. Schmerge, J. Turner, J. Welch, W. White, and J. Wu. Commissioning the Linac Coherent Light Source injector. *Phys. Rev. ST Accel. Beams*, 11:030703, 2008.

[24] M. Röhrs, C. Gerth, H. Schlarb, B. Schmidt, and P. Schmüser. Time-resolved electron beam phase space tomography at a soft x-ray free-electron laser. *Phys. Rev. ST Accel. Beams*, 12:050704, 2009.

[25] S. Di Mitri, M. Cornacchia, S. Spampinati, and S. Milton. Suppression of microbunching instability with magnetic bunch length compression in a linac-based free electron laser. *Phys. Rev. ST Accel. Beams*, 13:010702, 2010.

[26] Z. Huang, M. Borland, P. Emma, J. Wu, C. Limborg, G. Stupakov, and J. Welch. Suppression of microbunching instability in the Linac Coherent Light Source. *Phys. Rev. ST Accel. Beams*, 7:074401, 2004.

[27] Z. Huang, A. Brachmann, F.-J. Decker, Y. Ding, D. Dowell, P. Emma, J. Frisch, S. Gilevich, G. Hays, Ph. Hering, R. Iverson, H. Loos, A. Miahnahri, H.-D. Nuhn, D. Ratner, G. Stupakov, J. Turner, J. Welch, W. White, J. Wu, and D. Xiang. Measurements of the Linac Coherent Light Source laser heater and its impact on the x-ray free electron laser performance. *Phys. Rev. ST Accel. Beams*, 13:020703, 2010.

[28] S. Spampinati, E. Allaria, L. Badano, S. Bassanese, S. Biedron, D. Castronovo, P. Craievich, M. B. Danailov, A. Demidovich, G. De Ninno, S. Di Mitri, B. Diviacco, M. Dal Forno, E. Ferrari, W. M. Fawley, L. Fröhlich, G. Gaio, L. Giannessi, G. Penco, C. Serpico, C. Spezzani, M. Trovò, M. Veronese, S. V. Milton, and M. Svandrlik. Laser heater commissioning at an externally seeded free-electron laser. *Phys. Rev. ST Accel. Beams*, 17:120705, 2014.

[29] J. Lee, J.-H. Han, S. Lee, J. Hong, C. H. Kim, C. K. Min, and I. S. Ko. PAL-XFEL laser heater commissioning. *Nucl. Instrum. Meth. A*, 843:39, 2016.

[30] M. Pedrozzi, M. Calvi, R. Ischebeck, S. Reiche, C. Vicario, B. D. Fell, and N. R. Thompson. The laser heater system of SwissFEL. *Proceedings of FEL'14, Basel, Switzerland*, 2014.

[31] E. Roussel, C. Evain, M. Le Parquier, C. Szwaj, S. Bielawski, M. Hosaka, N. Yamamoto, Y. Takashima, M. Shimada, M. Adachi, H. Zen, S. Kimura, and M. Katoh. Transient response of relativistic electron bunches to wavenumber selected perturbations near the micro-bunching instability threshold. *New J. Phys.*, 16(6):063027, 2016.

[32] E. Roussel, E. Ferrari, E. Allaria, G. Penco, S. Di Mitri, M. Veronese, M. Danailov, D. Gauthier, and L. Giannessi. Multicolor high-gain free-electron laser driven by seeded microbunching instability. *Phys. Rev. Lett.*, 115:214801, 2015.

[33] P. Ungelenk, M. Höner, H. Huck, S. Khan, C. Mai, A. Meyer auf der Heide, C. Evain, C. Swzaj, and S. Bielawski. Continuously tunable narrowband pulses in the THz gap from laser-modulated electron bunches in a storage ring. *Phys. Rev. Accel. Beams*, 20:020706, 2017.

[34] Z. Zhang, L. Yan, Y. Du, W. Huang, C. Tang, and Z. Huang. Generation of high-power, tunable terahertz radiation from laser interaction with a relativistic electron beam. *Phys. Rev. Accel. Beams*, 20:050701, 2017.

[35] A. Wolski. *Beam Dynamics In High Energy Particle Accelerators*. Imperial College Press, 2015.

[36] H. Wiedemann. *Particle Accelerator Physics*. Springer, 2007.

[37] K. L. Brown. A first- and second-order matrix theory for the design of beam transport systems and charged particle spectrometers. *SLAC-R-75*, 1982.

[38] B. D. Muratori, J. K. Jones, and A. Wolski. Analytical expressions for fringe fields in multipole magnets. *Phys. Rev. ST Accel. Beams*, 18:064001, 2015.

[39] E. D. Courant and H. S. Snyder. Theory of the alternating-gradient synchrotron. *Annals of Physics*, 3(1):1, 1958.

[40] FERMI@Elettra Conceptual Design Report. 2007.

[41] Linac Coherent Light Source Conceptual Design Report. 2002.

[42] European XFEL Technical Design Report. 2007.

[43] Pohang Accelerator Laboratory PAL-XFEL Technical Design Report. 2014.

[44] SwissFEL Conceptual Design Report. 2011.

[45] A. W. Chao. *Physics of collective beam instabilities in high energy accelerators*. Wiley, 1993.

[46] S. Di Mitri. Bunch length compressors. *CERN Yellow Reports: School Proceedings*, 2018.

[47] I. Zagorodnov and M. Dohlus. Semianalytical modeling of multistage bunch compression with collective effects. *Phys. Rev. ST Accel. Beams*, 14:014403, 2011.

[48] Y. Sun, P. Emma, T. Raubenheimer, and J. Wu. x-band rf driven free electron laser driver with optics linearization. *Phys. Rev. ST Accel. Beams*, 17:110703, 2014.

[49] Z. Huang and K.-J. Kim. Review of x-ray free-electron laser theory. *Phys. Rev. ST Accel. Beams*, 10:034801, 2007.

[50] K.-J. Kim. An analysis of self-amplified spontaneous emission. *Nucl. Instrum. Meth. A*, 250(1):396, 1986.

[51] K.-J. Kim. Three-dimensional analysis of coherent amplification and self-amplified spontaneous emission in free-electron lasers. *Phys. Rev. Lett.*, 57:1871, 1986.

[52] B. W. Zotter and S. A. Kheifets. *Impedances and wakes in high-energy particle accelerators*. World Scientific, 1998.

[53] K. L. F. Bane and P. B. Wilson. Wake fields and wake field acceleration. *SLAC-PUB-3528*, 1984.

[54] Y. Cai. Coherent synchrotron radiation by electrons moving on circular orbits. *Phys. Rev. Accel. Beams*, 20:064402, 2017.

[55] Ya. S. Derbenev, J. Rossbach, E. L. Saldin, and V. D. Shiltsev. Microbunch radiative head-tail interaction. *TESLA FEL Reports 1995-05*, 1995.

[56] G. Stupakov and P. Emma. CSR wake for a short magnet in ultrarelativistic limit. *SLAC-PUB-9242*, 2002.

[57] S. Di Mitri and M. Cornacchia. Electron beam brightness in linac drivers for free-electron-lasers. *Phys. Rep.*, 539:1, 2014.

[58] S. Di Mitri, M. Cornacchia, and S. Spampinati. Cancellation of coherent synchrotron radiation kicks with optics balance. *Phys. Rev. Lett.*, 110:054801, 2013.

[59] M. Borland. Simple method for particle tracking with coherent synchrotron radiation. *Phys. Rev. ST Accel. Beams*, 4:070701, 2001.

[60] M. Borland, Y. C. Chae, P. Emma, J. W. Lewellen, V. Bharadwaj, W. M. Fawley, P. Krejcik, C. Limborg, S. V. Milton, H.-D. Nuhn, R. Soliday, and M. Woodley. Start-to-end simulation of self-amplified spontaneous emission free electron lasers from the gun through the undulator. *Nucl. Instrum. Meth. A*, 483(1):268, 2002.

[61] D. Ratner, C. Behrens, Y. Ding, Z. Huang, A. Marinelli, T. Maxwell, and F. Zhou. Time-resolved imaging of the microbunching instability and

energy spread at the Linac Coherent Light Source. *Phys. Rev. ST Accel. Beams*, 18:030704, 2015.

[62] R. L. Gluckstern. Longitudinal impedance of a periodic structure at high frequency. *Phys. Rev. D*, 39:2780, 1989.

[63] Z. Huang, M. Borland, P. Emma, and K.-J. Kim. Effects of linac wakefield on CSR microbunching in the Linac Coherent Light Source. *Proceedings of PAC'03, Portland, OR, USA*, 2003.

[64] S. Di Mitri, G. Perosa, A. D. Brynes, I. Setija, S. Spampinati, P. H. Williams, A. Wolski, E. Allaria, S. Brussaard, L. Giannessi, G. Penco, P. R. Rebernik, and M. Trovò. Experimental evidence of intrabeam scattering in a free-electron laser driver. *New J. Phys.*, 22(8):083053, 2020.

[65] M. Venturini and A. Zholents. Modeling microbunching from shot noise using Vlasov solvers. *Nucl. Instrum. Meth. A*, 593(1):53, 2008.

[66] J. Qiang, Y. Ding, P. Emma, Z. Huang, D. Ratner, T. O. Raubenheimer, M. Venturini, and F. Zhou. Start-to-end simulation of the shot-noise driven microbunching instability experiment at the Linac Coherent Light Source. *Phys. Rev. Accel. Beams*, 20:054402, 2017.

[67] J. Rosenzweig, C. Pellegrini, L. Serafini, C. Ternienden, and G. Travish. Space-charge oscillations in a self-modulated electron beam in multi-undulator free-electron lasers. *TESLA FEL Reports 1996-15*, 1996.

[68] M. Venturini. Models of longitudinal space-charge impedance for microbunching instability. *Phys. Rev. ST Accel. Beams*, 11:034401, 2008.

[69] J. B. Murphy, S. Krinsky, and R. L. Gluckstern. Longitudinal wakefield for an electron moving on a circular orbit. *Part. Accel.*, 57, 1997.

[70] G. Stupakov and S. Heifets. Beam instability and microbunching due to coherent synchrotron radiation. *Phys. Rev. ST Accel. Beams*, 5:054402, 2002.

[71] A. Piwinski. Intrabeam scattering. *Proceedings of 9th International Conference on High Energy Accelerators, Stanford, CA, USA*, 1974.

[72] J. D. Bjorken and S. K. Mtingwa. Intrabeam scattering. *Part. Accel.*, 13, 1982.

[73] K. Kubo, S. K. Mtingwa, and A. Wolski. Intrabeam scattering formulas for high energy beams. *Phys. Rev. ST Accel. Beams*, 8:081001, 2005.

[74] Z. Huang. Intrabeam scattering in an X-ray FEL driver. *SLAC-TN-05-026*, 2005.

[75] S. Di Mitri. Intrabeam scattering in high brightness electron linacs. *Phys. Rev. ST Accel. Beams*, 17:074401, 2014.

[76] K. L. F. Bane. A simplified model of intrabeam scattering. *Proceedings of EPAC'02, Paris, France*, 2002.

[77] A. Piwinski. Intrabeam scattering in presence of linear coupling. *DESY Internal Reports*, 90(113), 1990.

[78] S. Di Mitri and M. Cornacchia. Merit functions for the linac optics design for colliders and light sources. *Nucl. Instrum. Meth. A*, 735:60, 2013.

[79] S. Di Mitri, M. Cornacchia, C. Scafuri, and M. Sjöström. Electron beam optics and trajectory control in the fermi free electron laser delivery system. *Phys. Rev. ST Accel. Beams*, 15:012802, 2012.

[80] M. G. Minty and F. Zimmermann. Beam techniques -- Beam control and manipulation. *SLAC-R-621*, 2003.

[81] M. Hamberg, F. Brinker, and M. Scholz. First heating with the European XFEL laser heater. *Proceedings of IBIC'16, Barcelona, Spain*, 2016.

[82] T.M. Tran and J.S. Wurtele. TDA - A three-dimensional axisymmetric code for free-electron-laser (FEL) simulation. *Comput. Phys. Commun.*, 54(2):263, 1989.

[83] A. H. Lumpkin, N. S. Sereno, W. J. Berg, M. Borland, Y. Li, and S. J. Pasky. Characterization and mitigation of coherent-optical-transition-radiation signals from a compressed electron beam. *Phys. Rev. ST Accel. Beams*, 12:080702, 2009.

[84] D. J. Dunning, N. R. Thompson, B. W. J. McNeil, R. Bartolini, Z. Huang, and H. Geng. Optimisation of an HHG-seeded harmonic cascade FEL design for the NLS project. *Proceedings of IPAC'10, Kyoto, Japan*, 2010.

[85] P. Emma, J. Frisch, and P. Krejcik. A transverse RF deflecting structure for bunch length and phase space diagnostics. *LCLS-TN-00-12*, 2000.

[86] C. Behrens, Z. Huang, and D. Xiang. Reversible electron beam heating for suppression of microbunching instabilities at free-electron lasers. *Phys. Rev. ST Accel. Beams*, 15:022802, 2012.

[87] Y. Ding, C. Behrens, P. Emma, J. Frisch, Z. Huang, H. Loos, P. Krejcik, and M.-H. Wang. Femtosecond x-ray pulse temporal characterization in free-electron lasers using a transverse deflector. *Phys. Rev. ST Accel. Beams*, 14:120701, 2011.

[88] G. Stupakov and P. Emma. Reversible electron beam heater without transverse deflecting cavities. *Proceedings of FEL'15, Daejon, Korea*, 2015.

[89] J. Qiang, C. E. Mitchell, and M. Venturini. Suppression of microbunching instability using bending magnets in free-electron-laser linacs. *Phys. Rev. Lett.*, 111:054801, 2013.

[90] S. Di Mitri and S. Spampinati. Microbunching instability suppression via electron-magnetic-phase mixing. *Phys. Rev. Lett.*, 112:134802, 2014.

[91] C. Feng, D. Huang, H. Deng, Q. Gu, and Z. Zhao. Suppression of microbunching instability via a transverse gradient undulator. *New J. Phys.*, 17(7):073028, 2017.

[92] E. Roussel, E. Allaria, M. B. Danailov, S. Di Mitri, E. Ferrari, D. Gauthier, L. Giannessi, G. Penco, and M. Veronese. New scenarios of microbunching

instability control in electron linacs and free electron lasers. *Proceedings of IPAC'17, Copenhagen, Denmark*, 2017.

[93] G. Stupakov. Using the beam-echo effect for generation of short-wavelength radiation. *Phys. Rev. Lett.*, 102:074801, 2009.

[94] J. A. Clarke, D. Angal-Kalinin, N. Bliss, R. Buckley, S. Buckley, R. Cash, P. Corlett, L. Cowie, G. Cox, G. P. Diakun, D. J. Dunning, B. D. Fell, A. Gallagher, P. Goudket, A. R. Goulden, D. M. P. Holland, S. P. Jamison, J. K. Jones, A. S. Kalinin, W. Liggins, L. Ma, K. B. Marinov, B. Martlew, P. A. McIntosh, J. W. McKenzie, K. J. Middleman, B. L. Militsyn, A. J. Moss, B. D. Muratori, M. D. Roper, R. Santer, Y. Saveliev, E. Snedden, R. J. Smith, S. L. Smith, M. Surman, T. Thakker, N. R. Thompson, R. Valizadeh, A. E. Wheelhouse, P. H. Williams, R. Bartolini, I. Martin, R. Barlow, A. Kolano, G. Burt, S. Chattopadhyay, D. Newton, A. Wolski, R. B. Appleby, H. L. Owen, M. Serluca, G. Xia, S. Boogert, A. Lyapin, L. Campbell, B. W. J. McNeil, and V. V. Paramonov. CLARA conceptual design report. *JINST*, 9(05):T05001, 2014.

[95] A. D. Brynes, S. P. Jamison, B. D. Muratori, N. R. Thompson, and P. H. Williams. Laser heater design for the CLARA FEL test facility. *Proceedings of IPAC'17, Copenhagen, Denmark*, 2017.

[96] M. Borland. elegant: A flexible SDDS-compliant code for accelerator simulation. *Proceedings of ICAP'00, Darmstadt, Germany*, 2000.

[97] A. S. Weling and D. H. Auston. Novel sources and detectors for coherent tunable narrow-band teraherz radiation in free space. *J. Opt. Soc. Am. B*, 13(12):2783, 1996.

[98] CERN. MAD-X. `http://mad.web.cern.ch/mad/`.

[99] J. Qiang, R. D. Ryne, S. Habib, and V. Decyk. An object-oriented parallel particle-in-cell code for beam dynamics simulation in linear accelerators. *J. Comp. Phys.*, 163(434), 2000.

[100] M. Dohlus and T. Limberg. CSRTrack: Faster calculation of 3-d CSR effects. *Proceedings of FEL'04, Trieste, Italy*, 2004.

[101] Pulsar Physics. General Particle Tracer. `http://www.pulsar.nl/gpt`.

[102] S. Di Mitri, C. Venier, R. Vescovo, and L. Sturari. Wakefield benchmarking at a single-pass high brightness electron linac. *Phys. Rev. Accel. Beams*, 22:014401, 2019.

[103] V. Sajaev, R. Lindberg, M. Borland, and S. Shin. Simulations and measurements of the impact of collective effects on dynamic aperture. *Phys. Rev. Accel. Beams*, 22:032802, 2019.

[104] K. Hacker, R. Molo, S. Khan, L. L. Lazzarino, C. Lechner, Th. Maltezopoulos, T. Plath, J. Rossbach, S. Ackermann, J. Bödewadt, M. Dohlus, N. Ekanayake, T. Laarmann, and H. Schlarb. Measurements and simulations of seeded electron microbunches with collective effects. *Phys. Rev. ST Accel. Beams*, 18:090704, 2015.

[105] I. V. Bazarov, B. M. Dunham, C. Gulliford, Y. Li, X. Liu, C. K. Sinclair, K. Soong, and F. Hannon. Benchmarking of 3D space charge codes using direct phase space measurements from photoemission high voltage dc gun. *Phys. Rev. ST Accel. Beams*, 11:100703, 2008.

[106] B. Garcia, T. O. Raubenheimer, and R. Ryne. Stochastic effects from classical 3D synchrotron radiation. *Proceedings of FEL'17, Santa Fe, NM, USA*, 2017.

[107] J. S. Nodvick and D. S. Saxon. Suppression of coherent radiation by electrons in a synchrotron. *Phys. Rev.*, 96:180, 1954.

[108] M. Borland. Modeling of the microbunching instability. *Phys. Rev. ST Accel. Beams*, 11:030701, 2008.

[109] P. W. Smorenburg and B. van der Geer. Sign change of the CSR force after the exit of a bending magnet. *Unpublished*, 2016.

[110] C. Mayes and G. Hoffstaetter. Exact 1D model for coherent synchrotron radiation with shielding and bunch compression. *Phys. Rev. ST Accel. Beams*, 12:024401, 2009.

[111] P. Emma. X-band RF harmonic compensation for linear bunch compression in the LCLS. *LCLS-TN-01-1*, 2001.

[112] G. D'Auria, M. El Ashmawy, A. Rohlev, M. Scafaru, C. Serpico, A. Turchet, and D. Wang. The x-band system for the FERMI@Elettra FEL projects. *Proceedings of IPAC'10, Kyoto, Japan*, 2010.

[113] G. Penco, E. Allaria, L. Badano, P. Cinquegrana, P. Craievich, M. Danailov, A. Demidovich, R. Ivanov, A. Lutman, L. Rumiz, P. Sigalotti, C. Spezzani, M. Trovò, and M. Veronese. Optimization of a high brightness photoinjector for a seeded FEL facility. *JINST*, 8(05):P05015, 2013.

[114] M. Dohlus. Two methods for the calculation of CSR fields. *TESLA FEL Reports 2003-05*, 2003.

[115] C. P. Prokop, P. Piot, and M. Church. Beam dynamics simulations for the low-energy magnetic bunch compressor at ASTA. *FERMILAB-TM-2533*, 2012.

[116] G. Stupakov. Effect of centrifugal transverse wakefield for microbunch in bend. *SLAC-PUB-8028*, 2006.

[117] G. Stupakov. Centripetal transverse wakefield in relativistic beam. *arXiv*, 1901:10745, 2019.

[118] A. H. Lumpkin, R. J. Dejus, and N. S. Sereno. Coherent optical transition radiation and self-amplified spontaneous emission generated by chicane-compressed electron beams. *Phys. Rev. ST Accel. Beams*, 12:040704, 2009.

[119] P. Craievich, M. Petronio, S. G. Biedron, D. Castronovo, M. D. Forno, S. Di Mitri, N. Faure, D. L. Civita, G. Penco, L. Rumiz, L. Sturari, R. Vescovo, and D. Wang. Implementation of radio-frequency deflecting devices for

comprehensive high-energy electron beam diagnosis. *IEEE Trans. Nucl. Sci.*, 62(1):210, 2015.

[120] K. Floettmann and V. V. Paramonov. Beam dynamics in transverse deflecting RF structures. *Phys. Rev. ST Accel. Beams*, 17:024001, 2014.

[121] S. Heifets, G. Stupakov, and S. Krinsky. Coherent synchrotron radiation instability in a bunch compressor. *Phys. Rev. ST Accel. Beams*, 5:064401, 2002.

[122] Wolfram Research, Inc. Mathematica, Version 12.0. Champaign, IL, 2019.

[123] Wolfram Research, Inc. Mathematica -- GaussianFilter. `https://reference.wolfram.com/language/ref/GaussianFilter.html`.

[124] Wolfram Research, Inc. Mathematica -- WienerFilter. `https://reference.wolfram.com/language/ref/WienerFilter.html`.

[125] Wolfram Research, Inc. Mathematica -- MeanFilter. `https://reference.wolfram.com/language/ref/MeanFilter.html`.

[126] Wolfram Research, Inc. Mathematica -- BandpassFilter. `https://reference.wolfram.com/language/ref/BandpassFilter.html`.

[127] S. Spampinati, G. De Ninno, E. Allaria, D. Castronovo, M. B. Danailov, A. Demidovich, S. Di Mitri, B. Diviacco, W. M. Fawley, L. Fröhlich, G. Penco, C. Spezzani, M. Trovò, M. Dal Forno, E. Ferrari, and L. Giannessi. Progress with the FERMI laser heater commissioning. *Proceedings of FEL'13, New York, NY, USA*, 2013.

[128] M. Borland. Controlling noise and choosing binning parameters for reliable CSR and LSC simulation in Elegant. *OAG Technical Notes*, OAG-TN-2005-27, 2005.

[129] A. D. Brynes, I. Akkermans, E. Allaria, L. Badano, S. Brussaard, G. De Ninno, D. Gauthier, G. Gaio, L. Giannessi, N. S. Mirian, G. Penco, P. Rebernik, I. Setija, S. Spampinati, C. Spezzani, M. Trovò, P. H. Williams,

A. Wolski, and S. Di Mitri. Characterisation of microbunching instability with 2D Fourier analysis. *Sci. Rep.*, 10:5059, 2020.

[130] P. Musumeci, R. K. Li, and A. Marinelli. Nonlinear longitudinal space charge oscillations in relativistic electron beams. *Phys. Rev. Lett.*, 106:184801, 2011.

[131] E. A. Schneidmiller and M. V. Yurkov. Using the longitudinal space charge instability for generation of vacuum ultraviolet and x-ray radiation. *Phys. Rev. ST Accel. Beams*, 13:110701, 2010.

[132] S. Di Mitri and S. Spampinati. Estimate of free electron laser gain length in the presence of electron beam collective effects. *Phys. Rev. ST Accel. Beams*, 17:110702, 2014.

[133] P. Baxevanis, Z. Huang, and G. Stupakov. Effect of an angular trajectory kick in a high-gain free-electron laser. *Phys. Rev. Accel. Beams*, 20:040703, 2017.

[134] W. Lou and G. H. Hoffstaetter. Coherent synchrotron radiation wake expressions with two bending magnets and simulation results for a multiturn energy-recovery linac. *Phys. Rev. Accel. Beams*, 23:054404, 2020.